

Structural changes in the eye lens during accommodation

Thesis submitted to Cardiff University for the degree of Doctor of Philosophy

March 2019

Submitted by:

Saleha Keder Al-atawi

Structural Biophysics Research Group

School of Optometry and Vision Sciences

Cardiff University

Abstract

Aim: The main aim of this thesis was to investigate the changes in the lens crystallin molecular spacing and ordering, the lens suture confluence area, and the lens fibre widths, during the accommodation.

Methods: The molecular spacing and ordering of crystallin proteins were analysed using small angle X-ray scattering (SAXS) in Atlantic salmon, European squid and porcine lenses, and additionally in stretched and unstretched porcine lenses. Confocal microscopy was used to image anterior and posterior lenses to quantify changes in the lens suture confluence areas and lens fibre widths. In serial cryosections of porcine lenses, accommodative changes in lens fibre widths were analysed in both the nucleus and cortex.

Results: The molecular spacing of crystallins within the porcine lens nucleus was significantly less than in the Atlantic salmon and European squid lenses. As a case in point, the Bragg spacing in the porcine nucleus area, at 1mm along the horizontal meridian, decreased from 18.9 ± 0.3 nm to 15.9 ± 0.3 nm. Furthermore, significant accommodative changes in the average spacing between crystallin proteins in all vertical and horizontal meridians ($p < 0.05$) were determined. For instance, at the 1 mm vertical meridian, Bragg spacing in an unstretched lens increased from 16.6 ± 0.6 nm to 20.9 ± 2.8 nm in a stretched lens. The suture confluence area also changed following stretch at some depths. A significant increase in lens fibre widths in stretched lenses was observed in the nucleus (43.3 ± 10.2 μm versus 47.1 ± 8.6 μm , $p = 0.001$), the anterior cortex (67.4 ± 16.8 μm versus 72.9 ± 17.8 μm , $p = 0.000$), and the equatorial cortex (90.5 ± 11.2 μm versus 96.5 ± 11.9 μm , $p = 0.002$). However, a significant reduction in the posterior cortical lens fibre widths (69.3 ± 12.4 μm versus 59.6 ± 9.4 μm , $p = 0.0000$) in stretched lenses.

Conclusion: The accommodation, as characterised in a porcine model, involves significant structural changes within lens crystallins and fibre widths. To the researcher's knowledge, the novel data is provided herein. This study contributes to future research in this area by offering enhanced fixation protocols that preserve lens shape, in both accommodated and unaccommodated state, particularly important for 2D SAXS grid scans and microscopy-based analyses.

Dedication

I dedicate this thesis to my loving parents, for their constant encouragement and untiring support. I am especially grateful to my dotting parents-in-law; whose kindness still fills my heart long after they left to be with the Lord. I will forever cherish their memories.

I am particularly grateful to Allah for my beloved husband, Abdullah Al-atawi, who has never let me down, and whose bright light shined on my way even at the darkest hours of this journey. Thank you for your counsel and support. I am also thankful to my cheerleaders who have inspired me to be the best I could ever be, Yousef, Mohammed, and Salem. Mom loves you.

Finally, to my siblings, I dedicate this to you too, for never leaving my side. It is especially comforting to know that I can always count on your support.

Acknowledgment

This has been an extraordinarily exacting journey and one that I could never have made without the constant guidance and support of those I came across every step of the way. They helped me, each in their own way, big and small, to be the success that I am today.

First of all, I would like to thank Allah for the strength that he has given me throughout my journey. It fills my heart with immeasurable comfort knowing that I can always draw strength from you whenever I wobble. Thanks, Allah for everything that I have, and will ever have.

I owe a debt of gratitude to my tireless supervisors, Dr. Justyn Regini and Prof. Keith Meek, for the guidance and support they afforded me throughout my course and study. Without their constant feedback, this journey would never have been possible. I am especially thankful to my third supervisor, the ever-cheerful Dr. Julie Albon, for her kindness, encouragement, understanding, and patience with international students. My weekly meetings with her were instrumental in keeping me on the right path. I thank you from the bottom of my heart and hope you know that my singular purpose in life today is to become half the person (as teacher) that you are.

I am equally grateful to my Ph.D. advisors, Prof. Tom Margrain and Jonathan Erichsen, for their friendly advice and encouragement. I will always cherish the hearty discussions we had together and your invaluable suggestions that helped me overcome great obstacles throughout my Ph.D. journey. In the same breath, I would like to extend my gratitude to David Whitaker, my part-time advisor, for his kind support.

I also wish to thank Nick White for going beyond the call of duty to be of help to me. Even as I write this today, I still remember your invitation to always seek you out whenever I needed help. You had an uncanny way of making everything complex seem really simple.

It would be impossible to end this section without expressing my sincerest gratitude to Dr. Rob Young, for his assistance in the lab, during my first year. The same goes for the entire Biophysics Structural Research group, academics, and students, both past and present, for the support and advice that they afforded me. Studying at the School of Optometry and Vision Sciences afforded me the great fortune of meeting a great,

bighearted and welcoming people. I particularly remember Mrs. Susan Hobbs' kind heart not just for me, but for all postgraduate students. In the same vein, I thank Gregg Morrish and Philip Booth, both for helping with the technical issues and for ensuring that I never wanted for anything in the way of animal specimens. I also wish to thank all the support staff, who worked with and assisted me throughout this time.

I would never have started this journey in the first instance, without my sponsor, Al-Baha University and the Saudi Ministry of Higher Education, thank you.

Lastly, but of course, not least, I would like to thank the rest of my family members and friends, particularly my parents and siblings, especially Nora and Abdullaziz. There are many more, to whom I am eternally grateful, but for whom I could not make space here to thank them individually. I hope you all know that I am thankful. May God grant you the desires of your hearts.

I am thankful for each moment in PhD journey, sad and happy, that taught me new things about life.

TABLE OF CONTENTS

| | |
|--|------------|
| Abstract | i |
| Dedication | ii |
| Acknowledgment | iii |
| List of Figures | xii |
| List of Tables | i |
| Abbreviations: | i |
| Chapter One | 1 |
| 1 Introduction and background | 2 |
| 1.1 The ocular lens | 2 |
| 1.2 Lens gross anatomy | 3 |
| 1.2.1 The lens capsule and epithelium | 3 |
| 1.2.2 The cortex | 4 |
| 1.2.3 The nucleus | 5 |
| 1.3 Lens development | 5 |
| 1.3.1 Types of lens zones during fibre formation | 7 |
| 1.3.2 Fibre elongation | 7 |
| 1.3.3 Lens suture and composition | 8 |
| 1.4 Lens proteins | 10 |
| 1.5 Change of crystalline lens with ageing | 14 |
| 1.5.1 The lens shape | 14 |
| 1.5.2 Ageing of lens proteins | 15 |
| 1.5.3 Fibre cells compaction | 16 |
| 1.6 Lens functions | 17 |

| | | |
|-------------------------|--|-----------|
| 1.6.1 | Refraction | 17 |
| 1.6.2 | Gradient refractive index..... | 17 |
| 1.6.3 | Lens transparency | 18 |
| 1.7 | Eye lens disorders | 18 |
| 1.7.1 | Cataracts..... | 18 |
| 1.7.2 | Presbyopia | 20 |
| 1.8 | Accommodation..... | 21 |
| 1.8.1 | Internal lens changes during accommodation | 24 |
| 1.9 | Porcine lenses as a model of accommodation | 25 |
| 1.9.1 | Lens stretching devices to imitate accommodation | 27 |
| 1.10 | Research problems, and objectives of the present study..... | 28 |
| 1.10.1 | Aims and objectives..... | 31 |
| Chapter Two..... | | 32 |
| 2 | Ultrastructure of Atlantic Salmon, European squid, and porcine lenses | 33 |
| 2.1 | Introduction | 33 |
| 2.2 | Materials and methods | 40 |
| 2.2.1 | Tissue source and sample preparation..... | 40 |
| 2.2.2 | Small angle X-ray scattering (SAXS)..... | 41 |
| 2.2.3 | Mounting of samples for small angle X-ray scattering..... | 45 |
| 2.2.4 | Small angle x-ray scattering | 46 |
| 2.2.5 | Data analysis..... | 47 |
| 2.2.6 | Bragg spacing and H/FWHM ratio | 51 |
| 2.2.7 | Rotation of the anisotropic reflections | 52 |

| | | |
|----------------------------|---|-----------|
| 2.2.8 | Statistical analysis | 53 |
| 2.3 | Results | 54 |
| 2.3.1 | Individual X-ray scattering patterns and montages of patterns of the lens in pig, Atlantic salmon, and European squid..... | 54 |
| 2.3.2 | The X-ray scattering intensity of the lens in pig, European squid, and Atlantic salmon | 61 |
| 2.3.3 | Bragg spacing and H/FWHM ratio for European squid, Atlantic salmon and porcine lenses | 63 |
| 2.4 | Discussion..... | 71 |
| 2.4.1 | The intensity profile of the lens in pig, European squid, and Atlantic salmon | 71 |
| 2.4.2 | Bragg spacing and H/FWHM ratio for European squid, Atlantic salmon and porcine lenses | 74 |
| 2.4.3 | Rotation of the anisotropic reflection of the European squid and Atlantic salmon lenses | 76 |
| 2.5 | Conclusion..... | 78 |
| Chapter Three | | 80 |
| 3 | Measuring the crystallin proteins spacing and ordering between the in the accommodated and unaccommodated lens | 81 |
| 3.1 | Introduction | 81 |
| 3.2 | Materials and methods | 83 |
| 3.2.1 | Tissue sourcing | 83 |
| 3.2.2 | Simulation of accommodation using a lens stretcher device | 84 |
| 3.2.3 | Samples preparation..... | 86 |

| | | |
|--------------------------|--|------------|
| 3.2.4 | Mounting of samples for small angle X-ray scattering..... | 87 |
| 3.2.5 | Small angle x-ray scattering | 88 |
| 3.2.6 | Statistical analysis..... | 88 |
| 3.2.7 | Hypothesis | 89 |
| 3.3 | Results | 90 |
| 3.3.1 | Individual X-ray scattering patterns and montages of patterns of fresh and fixed lenses..... | 90 |
| 3.3.2 | Bragg spacing and H/FWHM ratio for fresh and fixed lenses in both unstretched and stretched positions | 96 |
| 3.3.3 | Fresh and fixed lenses Bragg spacing in accommodated and unaccommodated states..... | 115 |
| 3.4 | Discussion..... | 117 |
| 3.4.1 | The intensity profile of the lens in fresh and fixed lenses..... | 117 |
| 3.4.2 | Bragg spacing and H/FWHM ratio for fresh and fixed lenses | 118 |
| 3.4.3 | Scattering of the fresh and fixed lenses in accommodated and unaccommodated states..... | 119 |
| 3.5 | Conclusion..... | 121 |
| Chapter Four..... | | 123 |
| 4 | The lens curvature and microstructural changes between the accommodated and unaccommodated state..... | 124 |
| 4.1 | Introduction | 124 |
| 4.2 | Materials and methods | 126 |
| 4.2.1 | Source of tissues | 126 |

| | | |
|-------|---|------------|
| 4.2.2 | Measurement of superficial lens fibre widths and suture angle using light microscopy..... | 130 |
| 4.2.3 | Measurement of lens fibre widths and suture intersection area within the anterior and posterior lens using confocal laser scanning microscopy | 132 |
| 4.2.4 | Determination of lens fibre widths throughout the full depth of unstretched and stretched porcine lenses..... | 136 |
| 4.3 | Results | 140 |
| 4.3.1 | The radius of curvature of the lens surface in simulations of the accommodated and unaccommodated state..... | 140 |
| 4.3.2 | Lens Fibre widths and suture angle in the superficial lens..... | 141 |
| 4.3.3 | Lens fibre widths and suture intersection area within the anterior and posterior lens using confocal laser scanning microscopy | 143 |
| 4.3.4 | Lens Fibre Widths throughout the full depth of the porcine lens | 150 |
| 4.3.5 | General observations of the porcine lens throughout the full depth .. | 153 |
| 4.4 | Discussion..... | 154 |
| 4.4.1 | The behaviour of the lens curvature radii during the accommodated and unaccommodated states as seen under optical coherence tomography..... | 155 |
| 4.4.2 | Individual lens fibre widths | 156 |
| 4.4.3 | The lens fibre width as a function of depth and areas..... | 156 |
| 4.4.4 | Lens fibre widths in accommodated and unaccommodated states | 157 |
| 4.4.5 | Lens suture angles..... | 164 |
| 4.5 | Conclusion..... | 167 |
| | Chapter Five..... | 169 |

| | | |
|----------|--|------------|
| 5 | General discussion | 170 |
| 5.1 | Crystallin proteins and their ordering in different groups of animals | 171 |
| 5.2 | Crystallin proteins in accommodated and unaccommodated states..... | 172 |
| 5.3 | The change of other lens features as a function of the lens depths | 174 |
| 5.4 | The change of lens fibre widths during accommodation | 176 |
| 5.5 | Conclusion..... | 179 |
| 5.5.1 | The study limitations..... | 181 |
| 5.5.2 | Future work | 181 |
| 6 | References | 183 |
| 7 | Appendixes..... | 198 |
| 7.1 | Appendix 1: Preparation of pig lenses for serial block face scanning electron microscopy (SBFSEM)..... | 198 |
| 7.1.1 | Primary fixation | 198 |
| 7.1.2 | Embedding techniques | 198 |
| 7.1.3 | Microwave Tissue Processing | 200 |
| 7.1.4 | Serial block face protocol attempted..... | 201 |
| 7.2 | Appendix 2: Protocol for preparation of artificial aqueous humor..... | 207 |
| 8 | Submitted abstracts and Future publications..... | 209 |
| 8.1 | Abstracts (1): Changes in the X-ray diffraction pattern of porcine lens before and after simulated accommodation | 209 |
| 8.1.1 | Abstract (2): Internal lens structure changes during simulated accommodation..... | 211 |
| 8.1.2 | Ultrastructure of aquatic mammal and porcine lenses | 213 |
| 8.1.3 | Changes in the X-ray diffraction pattern of porcine lens before and after simulated accommodation..... | 213 |

8.1.4 Internal lens structure changes during simulated accommodation 213

9 Figure Permissions.....214

List of Figures

| | |
|--|----|
| Figure 1-1: The vertebrate eye and lens. | 2 |
| Figure 1-3: Lens fibre structure. | 5 |
| Figure 1-4: Lens development in the embryonic stage | 6 |
| Figure 1-5: The different lens zones. | 7 |
| Figure 1-6: Scanning electron micrograph showing the opposite-end fibre curvature | 9 |
| Figure 1-7: Species-specific suture patterns. | 10 |
| Figure 1-8: The protein structure shapes in the eye lens. | 12 |
| Figure 1-9: Schematic representation of age-related growth in the zones C1-C3 | 15 |
| Figure 1-10: A mature cortical cataract (Jesse, 2014)..... | 19 |
| Figure 1-11: Lens behaviour in the accommodation and unaccommodation states .. | 23 |
| Figure 1-12: Slit-lamp Scheimpflug photography set-up..... | 25 |
| Figure 2-1: Anatomical structures of the cephalopoda, fish, and human eye | 34 |
| Figure 2-2: The eye of a Japanese flying squid (<i>Ommastrephes pacificus</i>) | 35 |
| Figure 2-3: A schematic planar view of a synchrotron facility | 43 |
| Figure 2-4: The x-rays are diffracted by two planes of crystalline lattice | 44 |
| Figure 2-5: The process for preparing fresh lenses and clamping onto the front incident X-ray beam. | 46 |
| Figure 2-6: Small angle X-ray diffraction from a porcine lens. | 47 |
| Figure 2-7: Montages of all X-ray patterns for a fresh porcine lens in an un-stretched position | 49 |
| Figure 2-8: Montages of all X-ray patterns from Atlantic salmon and European squid lenses..... | 50 |
| Figure 2-9: X-ray patterns from the porcine lens and the location of the horizontal and vertical meridian locations..... | 50 |

| | |
|--|----|
| Figure 2-10: Typical individual SAXS patterns for squid, salmon, and porcine lenses..... | 55 |
| Figure 2-11: A 2D Grid scan montage of SAXS patterns from a squid lens. | 57 |
| Figure 2-12: A 2D Grid scan montage of SAXS patterns from a squid lens | 58 |
| Figure 2-13: 2D Grid scan montage of SAXS patterns of a salmon lens..... | 59 |
| Figure 2-14: A 2D Grid scan montage of SAXS patterns from a porcine lens..... | 60 |
| Figure 2-15: The intensity profile for the species lens through the middle meridian | 62 |
| Figure 2-16: The average Bragg spacing in squid, salmon and porcine lenses..... | 65 |
| Figure 2-17: The average Bragg spacing derived from SAXS along the vertical meridians of a 2D scan. | 66 |
| Figure 2-18: The average of H/FWHM ratio derived from SAXS along the horizontal meridians of a 2D scan | 69 |
| Figure 2-19: The average H/FWHM ratio derived from SAXS along the vertical meridians of a 2D scan..... | 70 |
| Figure 2-20: TEM image from the anterior segment of a squid lens | 78 |
| Figure 3-1: Correct positioning for attachment of the eyeball to the lens stretcher .. | 84 |
| Figure 3-2: Posterior eye dissection. | 85 |
| Figure 3-3: Corneal dissection and visible iris after cornea tissue removed. | 86 |
| Figure 3-4: Typical individual SAXS patterns from un-stretched fresh porcine lens and un-stretched fixed porcine lens. | 91 |
| Figure 3-5: A 2D Grid scan montage of SAXS patterns with a magnified view of individual patterns from an un-stretched fresh porcine lens and from an un-stretched fixed porcine lens. | 92 |
| Figure 3-6: The middle meridian for the lens crystalline density plotted I versus q for the fresh lens | 94 |

| | |
|--|-----|
| Figure 3-7: The middle meridian for the lens crystalline density plotted q vs I for fixed lens | 95 |
| Figure 3-8: Typical Bragg spacing derived from SAXS patterns along the Horizontal meridians in a 2D scan. | 98 |
| Figure 3-9: Typical Bragg spacing derived from SAXS patterns along the Vertical meridians in a 2D scan. | 99 |
| Figure 3-10: The average Bragg spacing derived from SAXS patterns along the Horizontal meridians in a 2D scan. | 100 |
| Figure 3-11: The average Bragg spacing derived from SAXS patterns along the Horizontal meridians in a 2D scan..... | 101 |
| Figure 3-12: Typical Bragg spacing derived from SAXS patterns along the Horizontal meridians in a 2D scan. | 104 |
| Figure 3-13: Typical Bragg spacing derived from SAXS patterns along the Vertical meridians in a 2D scan for a fixed lens. | 105 |
| Figure 3-14: The average Bragg spacing derived from SAXS patterns along the Horizontal meridians | 106 |
| Figure 3-15: The average Bragg spacing derived from SAXS patterns along the Vertical meridians | 107 |
| Figure 3-16: Typical H/FWHM ratio derived from SAXS patterns along the Horizontal meridians in a 2D scan. | 109 |
| Figure 3-17: Typical H/FWHM ratio derived from SAXS patterns along the Vertical meridians in a 2D scan. | 110 |
| Figure 3-18: Typical H/FWHM ratio derived from SAXS patterns along the Horizontal meridians in a 2D scan for fixed lenses..... | 113 |

| | |
|--|-----|
| Figure 3-19: Typical H/FWHM ratio derived from SAXS patterns along the Vertical meridians in a 2D scan for fixed lenses..... | 114 |
| Figure 4-1: Lens fibres within the suture junction region of an unstretched lens (ie. accommodated lens)..... | 131 |
| Figure 4-2: Suture angles within the centre ROI in the unstretched and stretched porcine lens..... | 132 |
| Figure 4-3: Confocal imaging of the porcine lens. | 134 |
| Figure 4-4: The z-profile of the anterior lens up to 300µm depth for the unstretched and stretched lens..... | 134 |
| Figure 4-5: WGA labelled lens fibres in lens cryosection | 139 |
| Figure 4-6: Anterior and posterior average lens curvature radii..... | 140 |
| Figure 4-7: Regional mean lens fibre widths in stretched and un-stretched states..... | 142 |
| Figure 4-8: The lens fibre widths in both anterior and posterior surfaces. | 144 |
| Figure 4-9: The suture confluence area in both the anterior and posterior surfaces | 145 |
| Figure 4-10: The anterior lens suture at different depths. | 147 |
| Figure 4-11: The posterior lens suture at different depths | 148 |
| Figure 4-12: Orthogonal of the suture pattern at a depth of 300 µm | 149 |
| Figure 4-13: Lens fibre widths measured in 25µm tissue sections at 1mm depth intervals | 153 |
| Figure 4-14: Lens fibre widths in nuclear and cortical areas in unstretched and stretched. | 153 |
| Figure 4-15. Vertical and horizontal measurements diameters. | 153 |
| Figure 4-16: Diagrammatic representation of the origin and insertion of the zonules with lens capsule.. | 162 |
| Figure 4-17: The axial thickness decreases in the unaccommodated states..... | 162 |

List of Tables

| | |
|--|-----|
| Table 1-1: The three main crystallin types (α , β and γ) | 11 |
| Table 2-1: The refractive indices in the cortex and nucleus areas of squid, atlantic salmon and porcine lenses | 36 |
| Table 2-2: Averages and standard deviations of the interference functions' Bragg spacing from meridians in the horizontal and vertical grids within the squid, salmon, and porcine lenses. | 64 |
| Table 2-3: The p-value of Bragg spacing difference between the central nuclear and cortex areas | 68 |
| Table 2-4: Average and standard deviation of the H/FWHM ratio from patterns in the Horizontal and vertical grids within the three groups of animals..... | 68 |
| Table 3-1: Average and standard deviation of the interference functions Bragg spacing's from patterns in the horizontal (H) and vertical (V) grids within the fresh porcine lenses in both un-stretched and stretched positions..... | 96 |
| Table 3-2: Average and standard deviation of the interference functions Bragg spacings from patterns in the horizontal (H) and vertical (V) grids within the fixed porcine lenses..... | 103 |
| Table 3-3: Average and standard deviation of the interference functions H/FWHM ratio from patterns in the horizontal (H) and vertical (V) grids within typical fresh porcine lens..... | 108 |
| Table 3-4: Average and standard deviation of the interference functions of H/FWHM ratio from patterns in the horizontal (H) and vertical (V) grids within the typical fixed porcine lenses..... | 112 |
| Table 3-5: The p-value of Bragg spacing difference in the horizontal (H) and vertical (V) grids between fresh un-stretched and stretched lenses, and fixed un-stretched and stretched lenses. | 112 |
| Table 4-1: Average and standard deviations lens widths for the various lenses/areas | 143 |
| Table 4-2: Anterior and posterior suture confluence area..... | 145 |
| Table 4-3: Mean and standard deviations of lens fibre widths in five areas. | 150 |
| Table 5-1: Summary of results of crystallin proteins..... | 177 |

Table 5-2: Summary of results of curvature radii and lens fibre widths during the accommodation.180

Abbreviations:

| | |
|---------|--|
| Cz | the central zone |
| Pgz | the pre-germinative zone |
| Tz | the transitional zone |
| 3D | three-dimensional |
| sHSP | small heat shock proteins |
| GRIN | gradient refractive-index |
| NUC | nuclear cataract |
| COR | cortical cataract |
| PSC | posterior sub-capsular cataract |
| TEM | transmission electron microscopy |
| SBF SEM | serial block-face scanning electron microscopy |
| DDSA | dodeceny succinic anhydride |
| BDMA | benzyl dimethylamine |
| PBS | phosphate-buffered saline |
| ROI | region of interest |
| WGA | wheat germ agglutinin. |
| SAXS | small angle x-ray scattering |

Chapter One

1 Introduction and background

1.1 The ocular lens

The crystalline lens, which plays an important role in contributing to the eye's refractive power for both distant and near sight, is situated posterior to the iris, between the vitreous humour and aqueous humour (see Figure1-1), suspended in ciliary muscles (Augusteyn, 2008). The lens grows throughout life and is able to maintain its transparency, depending on its protein structures within lens fibre (Lovicu & Robinson, 2004; Augusteyn, 2007; Schachar, 2012). The mammalian lens is also capable of assuming different shapes. In order to provide a background to the lens (and this thesis), this chapter will focus on the lens's anatomy and its development.

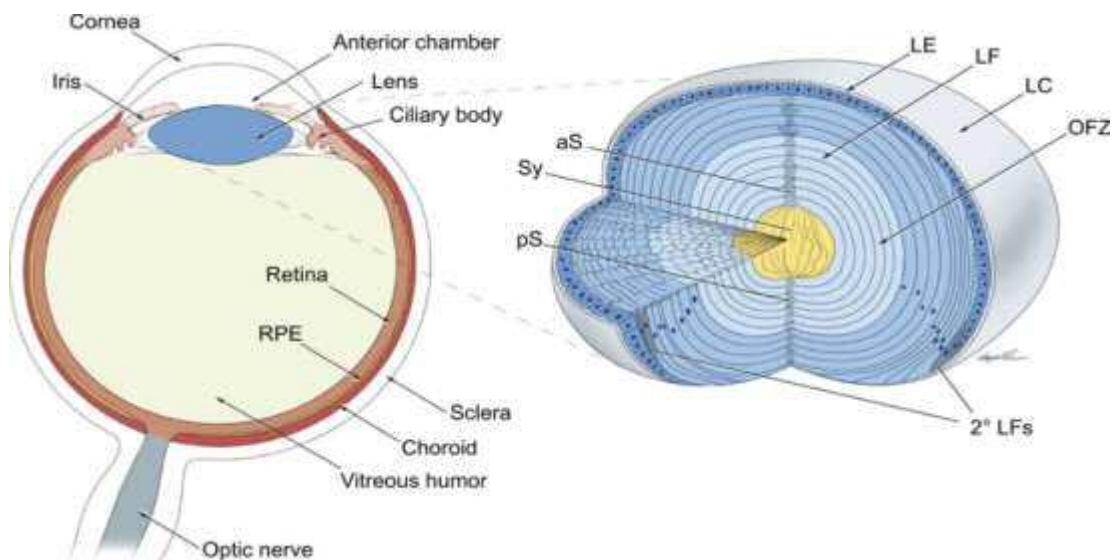


Figure 1-1: The vertebrate eye and lens. The lens consists of the capsule LC, epithelium, LE, and lens fibres LFs. Newly formed fibres deposit on top of existing fibres to form hexagonally packed concentric shells and radially aligned cells. aS, anterior suture, pS posterior suture, OFZ, organelle-free zone, LFs, secondary lens fibres, Sy, syncytium. This is adapted from Shi et al. (2009) and Cvekl and Ashery-Padan (2014).

1.2 Lens gross anatomy

While it is outside the scope of this present study to offer a more comprehensive anatomical account, it is necessary, for the purposes of setting the context of this study, to provide understanding of the lens' three histological structures: the lens capsule, lens epithelium, and the lens fibres (subdivided into the cortex and nucleus).

1.2.1 The lens capsule and epithelium

The lens capsule is a thin transparent membrane that encloses the lens (Cohen, 1965) (Figure 1-2). It consists of transparent laminated sheets (of collagen IV, nidogen and perlecan) that run in parallel directions to the capsule's surface (Cohen, 1965).

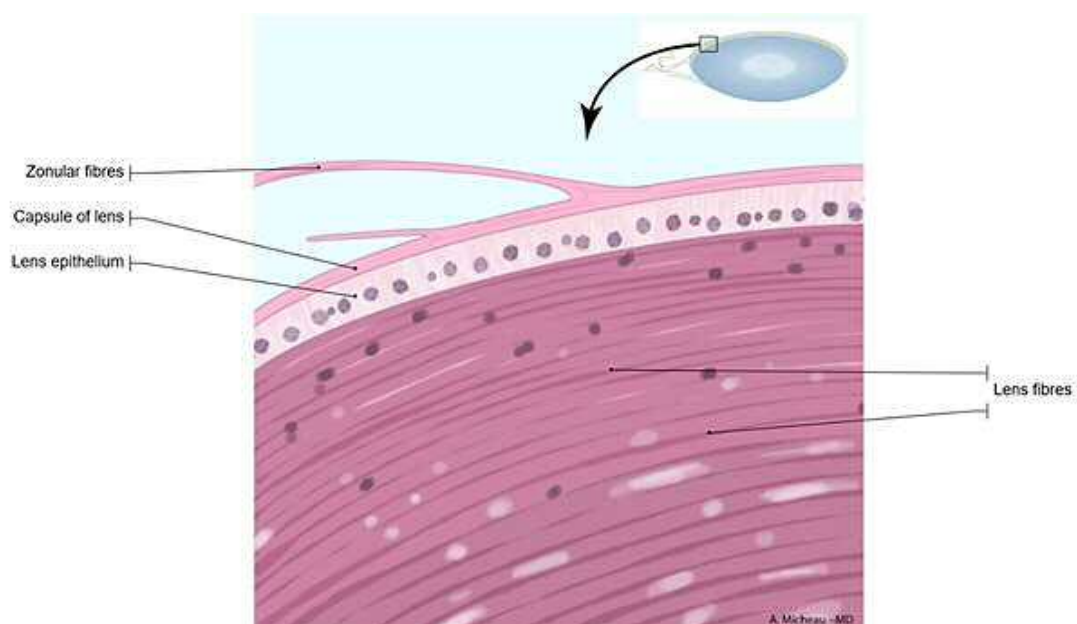


Figure 1-2: The lens capsule, lens epithelium and lens fibres (Copeid from IMAIOS, 2014)

The lens epithelium lies directly beneath the lens capsule, from where the transparent ocular lens fibre cells are generated (Garland et al., 1996; Andley, 2008; Cvekl &

Ashery-Padan, 2014). This layer only occurs on the anterior surface and is responsible for the growth and development of lens fibres. It comprises a single layer of cuboidal-shaped cells that have a relatively high metabolic activity, necessary for lens cell growth and transparency (Andley, 2008). The lens' continual growth throughout life and its fibre cells are never replaced, as they need to maintain their transparency and functionality for a human lifetime (Andley, 2008). This following section demonstrates two of the most distinctive regions of the lens: the cortex and the nucleus.

1.2.2 The cortex

The cortex comprises the outer part of the internal structure of the eye lens (Kuszak et al., 2004a). The literature shows a lack of agreement on what constitutes the boundary of the lens cortex and nucleus in different species and lens types (Al-Ghoul, et al., 2001; Kuszak, et al., 2006). However, it is appropriate, according to Lovicu & Robinson (2004), to consider the lens as consisting of both a cortex (comprising cortical fibres) and a nucleus (comprising nuclear fibres). Garland et al. (1996) argue that the nucleus has a highly characteristic protein pattern (such as a high protein concentration and protein type within the nucleus) that differentiates it from that in the cortex area. Meanwhile, Kuszak et al. (2004a) support factors such as age, time of development, and state of maturation to be used to distinguish between the cortical and nuclear fibres. Anatomically, however, lens fibres are typically hexagonal in shape and arranged in radial cell columns when viewed cross-sectionally (Figure 1-3) (Lovicu & Robinson, 2004).

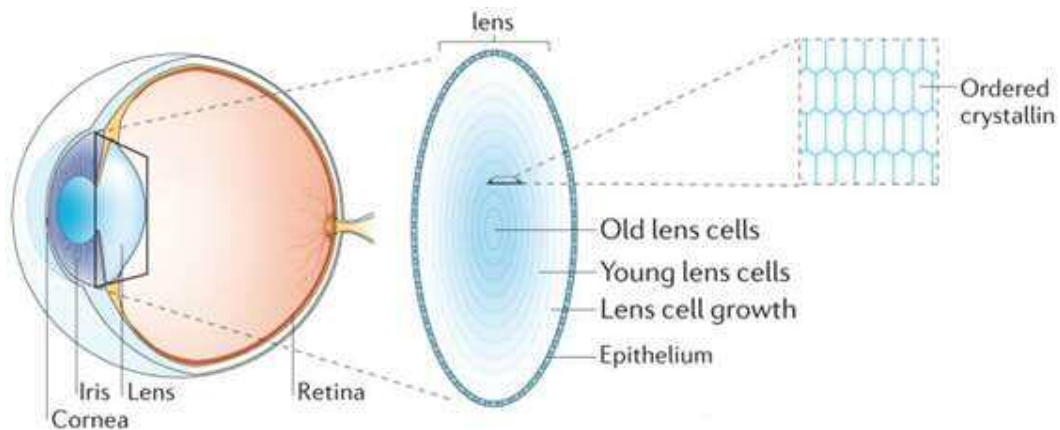


Figure 1-3: Lens fibre structure. A cross-section of the eye lens shows radial growth of lens fibre; the older lens fibre cells exist in the nucleus and the younger cells on the cortex (adapted from Toyama and Hetzer, 2013).

1.2.3 The nucleus

The primary fibres at the centre of the lens are the lens' original nuclear fibres (Kuszak, 1995; Kuszak, 2004). Since lens growth continues throughout life, all secondary fibres become a part of the nucleus fibres once they complete the maturation process i.e. as soon as they are completely elongated (Figure 1-3). The embryonic, as well as foetal nuclei, consist of all the fibres created during the embryonic and foetal development, respectively (Kuszak, 1984). The development of the lens through life offers important insight into, amongst others, its structure/shape, fibre composition, and functionality.

1.3 Lens development

The eye's basic structure develops from two main components that interact during development: the lens and the retina (Fuhrmann, 2010). The human eye is formed from three parts of primordial tissue: the neural tube ectoderm (that gives rise to, for instance, the retina, the ciliary body epithelia, the iris, and the optic nerve), the surface ectoderm (that gives rise to, the lens, the eyelids, and both the conjunctival and corneal

epithelia) and the mesoderm (West-Mays et al., 2010, Chow and Lang, 2001, Lovicu and McAvoy, 2005). Once the embryonic lens has formed, it mostly maintains its basic architecture and polarity by interacting with surrounding ocular media (West-Mays et al., 2010, Chow and Lang, 2001, Lovicu and McAvoy, 2005) (Figure1-4).

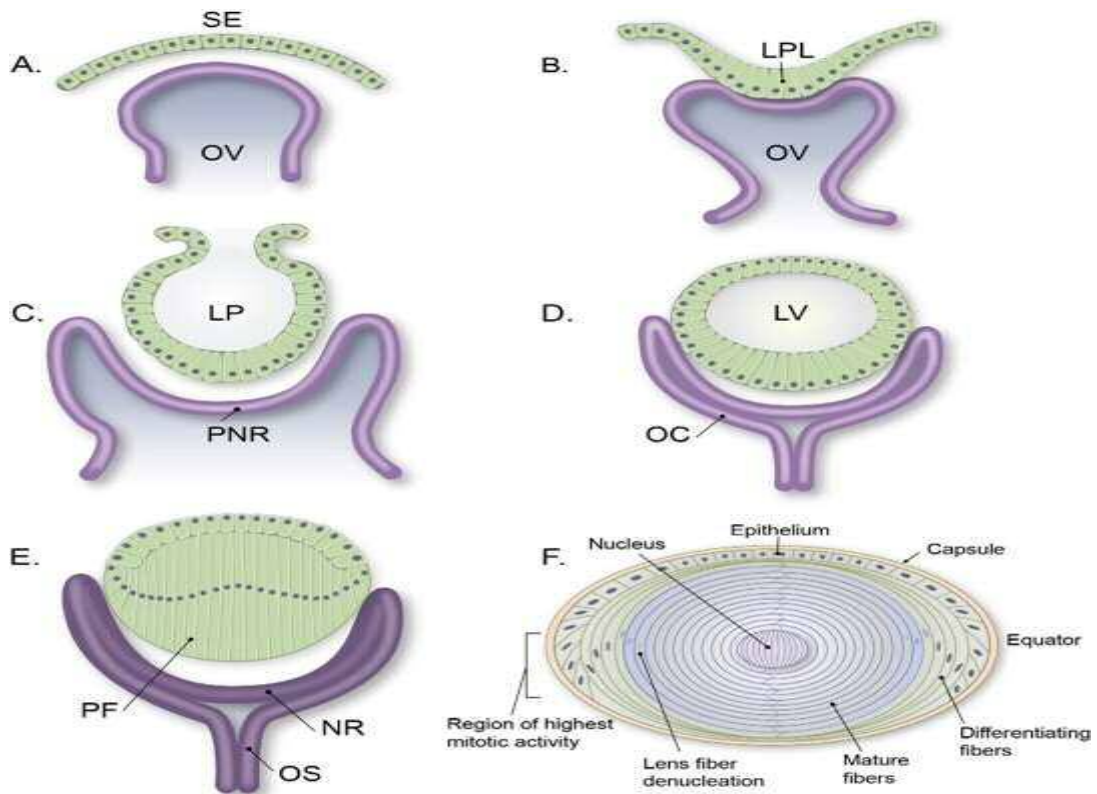


Figure 1-4: Lens development in the embryonic stage - SE: surface ectoderm; OV: optic vesicle; LPL: lens placode; LP: lens pit; PNR: presumptive neuroretina; LV: lens vesicle; OC: optic cup; PF: primary fibres; NR: neuroretina; OS: optic stalk. The schematic drawings from A to F illustrate the key stages in the development of the lens: (A) early surface ectoderm and the optic vesicle; (B) the ectoderm establishing the lens placode by touching the optic vesicle; (C) further development of the ectodermal layer continuing to form the lens pit; (D) the lens placode forming the lens vesicle and the optic vesicle-forming the optic cup; (E) the elongation of the primary fibres to fill the lens vesicle, coupled with the formation of both the neuro-retina and optic stalk; and (F) the fully formed lens internal structure (Chun-hong Xia, 2011, p. 364).

1.3.1 Types of lens zones during fibre formation

The post-mitotic lens epithelium forms the basal layer and the remaining lens epithelial cells originate from the germinative zone (Kuszak et al., 2004b; Kuszak et al., 2004a). The remaining lens epithelial cells differentiate into three other zones: the central zone (cz), within which the epithelial cells extend over about 80% of the anterior surface of the lens; and the pre-germinative zone (pgz); and the transitional zone (tz). The pgz and tz cover almost 5% of the periphery of the cz and approximately 5% of the periphery of the gz of the lens epithelium, respectively (Kuszak, 1995a; Kuszak et al., 2004a), (Figure 1-5).

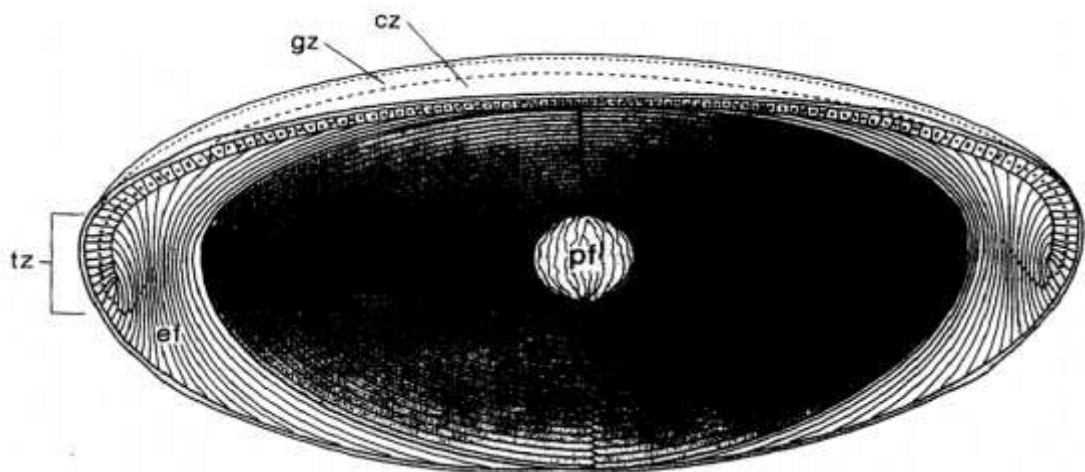


Figure 1-5: The different lens zones. cz: central zone; gz: germinative zone; tz: transitional zone; pf: primary fibre mass; and ef: elongation fibres (Copied from Kuszak, 1995).

1.3.2 Fibre elongation

The secondary fibres derived from cuboidal cells in the epithelial membrane form into layers (Kuszak, 1995). The transitional cells migrate posteriorly and start elongating bi-directionally (Lovicu & Robinson, 2004). As fibre elongation proceeds, the anterior

ends locate between the primary fibre mass and the lens epithelium while the posterior ends locate between the lens capsule and the primary fibre mass (Kuszak & Brown, 1994; Kuszak, et al., 2004b). As soon as posterior and anterior ends of the freshly formed fibres break contact with the capsule posteriorly and the epithelium anteriorly, respectively, the elongation ends (Lovicu & Robinson, 2004). There is, therefore, an overlap between mature secondary fibres and new mature fibres, called the lens suture (Kuszak, 1995a; Kuszak et al., 2004a).

Kuszak and Costello (2004) show that the final secondary fibres are not arranged from end-to-end around the anterior and posterior parts of the lens' polar axis. First, the lens fibre ends are more than three times wider than their mid portions in primate lenses. Moreover, there are two types of fibre curvature: convex-concave curvature (exhibiting a crescent shape) and the opposite-end curvature (which has a three-dimensional (3D) S-shape), as shown in Figure 1-6. The 3D curvature is formed by both anterior and posterior fibre segments curling in opposite directions inside a growth shell (Kuszak, 1995a; Kuszak, 1995b; Kuszak et al., 2004b).

1.3.3 Lens suture and composition

The fibres, whose length is approximately one-half of the polar border, overlap to form suture branches (Kuszak, 1995a; Kuszak, et al., 2004b). Suture patterns result from a combination of a number of suture branches which have different types of fibre ends, giving rise to different suture pattern shapes in different species of animal, including umbilical-, line-, Y- and star-shaped. The line-shaped suture, for example, is found in rabbit lenses, while the Y-shaped suture is found in feline and porcine lenses. Human

lenses, on the other hand, exhibit a Y-shaped suture throughout the embryonic development stage, which does however, become more complex (progressively forming a six, nine- and then twelve-branched star) during adolescence, through the combination of straight and curved fibre ends (See Figure 1-7) (Kuszak, 1995a; Kuszak, 1996; Kuszak, et al., 2004b; Lovicu & Robinson, 2004). The primate and non-primate lenses have specific suture shapes, which have a directly significant relationship to the lens optical quality (Kuszak et al., 1994, Sivak et al., 1994).

Through the visual axis, the suture pattern in primate lenses does not extend from the embryonic nucleus to the periphery. In non-primate lenses, however, the suture pattern aligns along the visual axis, effectively increasing the spherical aberration (Kuszak et al., 2006).

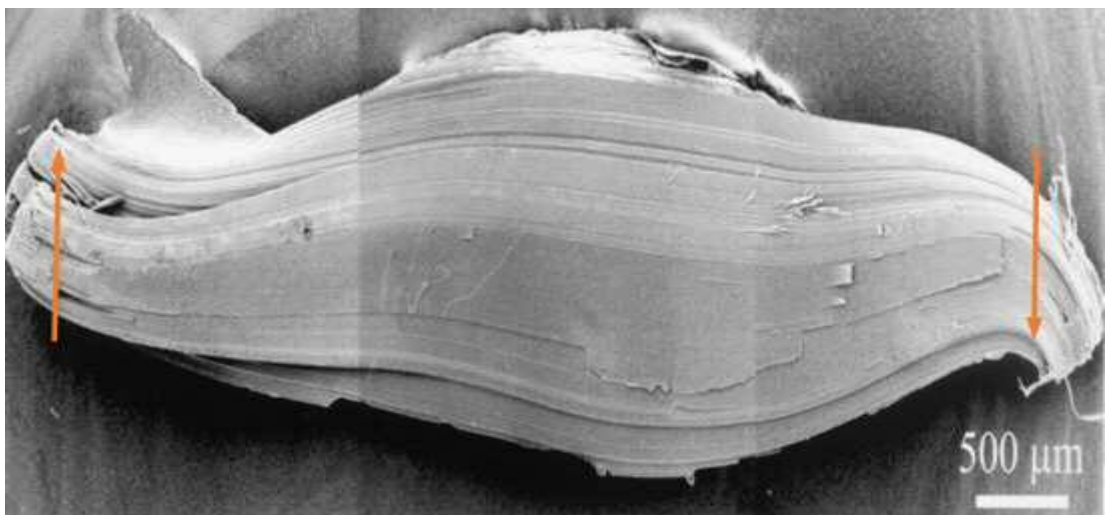


Figure 1-6: Scanning electron micrograph showing the opposite-end fibre curvature (orange arrows) (Kuszak et al., 2004b).

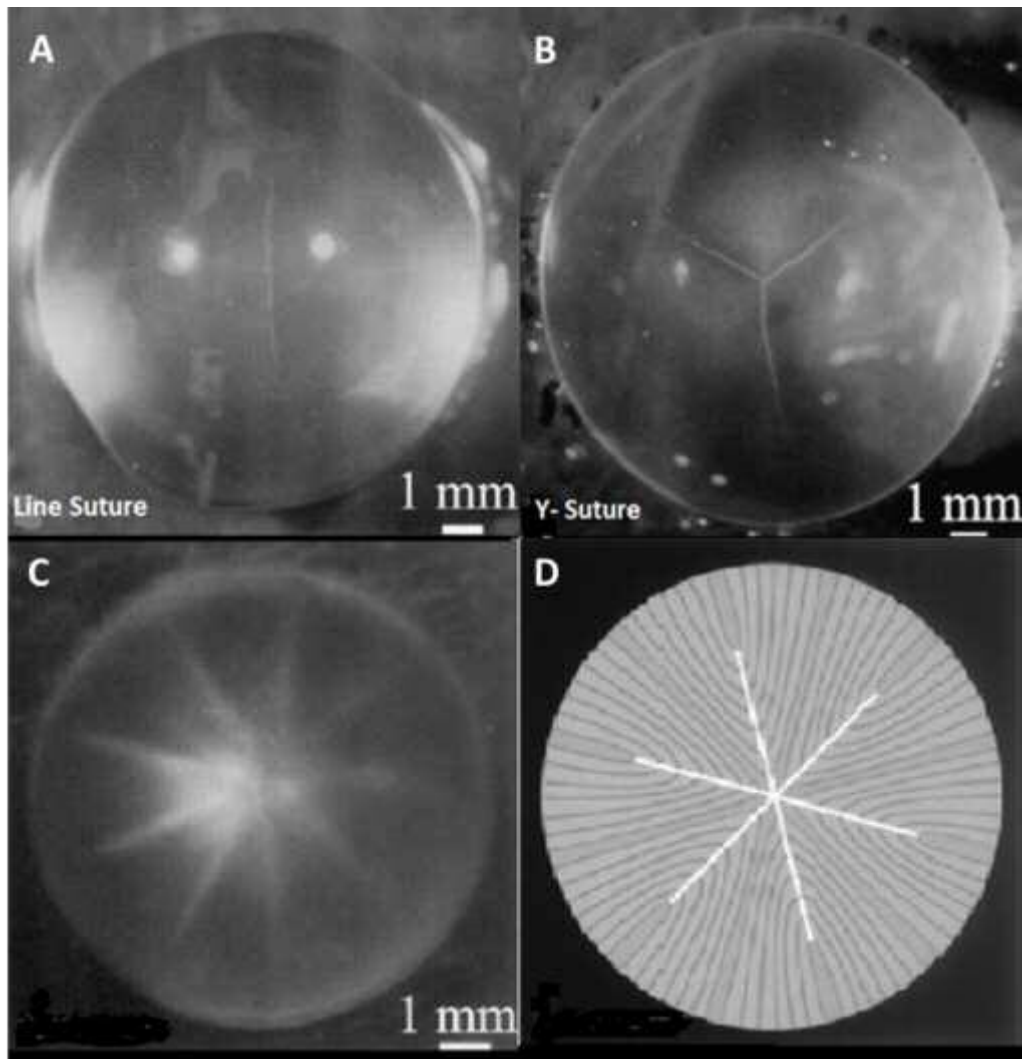


Figure 1-7: Species-specific suture patterns: the line-shaped suture pattern in a rabbit lens (A), the Y-shaped suture pattern in a cat lens (B), the star-shaped suture pattern in a primate lens (C) and a diagram of star-shaped suture pattern in a primate lens (D) (Al-Ghoul, 2003; Kuszak, 1995).

1.4 Lens proteins

The composition of the lens is approximately 35% by weight protein, while the remaining 65% is water (Davison, 1990; Paterson et al., 1992). Water-soluble proteins—the crystallin family—comprise in excess of 90% of all the lens protein, (Bloemendal, 1977; Bloemendal et al., 2004)

The lens fibres contain three crystallin types (α , β , and γ), which give the lens transparency and refractive power (Bassnett et al., 2011; Roquemore et al., 1992).

Recent experimental techniques indicate that for each type of crystallin, there are numerous isoforms. An alpha-crystallin is an oligomer that primarily comprises 20 to 40 subunits of two types, α A- and α B-crystallin (Horwitz, 1992; Inoue et al., 2016). α A-crystallin and α B-crystallin, both have molecular masses of \sim 20 kDa, with a 3:1 molar value (Augusteyn, 2004, Harding, 1991). Further, the α A-crystallin is found only in lens tissue, with trace amounts in other body organs (Horwitz, 1992, Horwitz, 2003, Duncan et al., 2004). The γ crystallins, on the other hand, vary dramatically between vertebrates and have eight monomeric isoforms (γ A, γ B, γ C, γ D, γ E, γ F, γ N, and γ S) (Bloemendal et al., 2004; Greiling and Clark, 2012; Wistow et al., 2005). The Greek key motif is an evolutionarily preserved super-secondary structural protein of the β - and γ -crystallins. Its ($\beta\gamma$ -crystallin) structural fold, which comprises an N- and C-terminal domain, provides high structural compactness as well as intrinsic stability against stress (Lapatto et al., 1991; Vendra et al., 2013). The resulting compactness also ensures lens transparency (See Table 1-1 and Figure 1-8) (Fischer et al., 2008; Wistow et al., 2005; Vendra et al., 2013).

| Crystallin | Subdivision | Subunit (kDa) | Aggregate (kDa) | State | Secondary structure | Tertiary structure |
|------------|--|---------------|-----------------|----------|----------------------|---|
| α | α A, α B | 20 | 700 | Oligomer | Some β sheet | Unknown |
| β | β A3, β B1, β A4, β B1, β B2, β B3 | 23-35 | 40-200 | Oligomer | Mostly β sheet | Two separate domains, each consisting of two Greek-key motifs |
| γ | γ A, γ B, γ C, γ D, γ E, γ F, γ N, γ S | 20 | 20 | Monomer | Mostly β sheet | Two self-associating domains, each consisting of two Greek-key motifs |

Table 1-1: The structural features of three main crystallin types (α , β and γ).

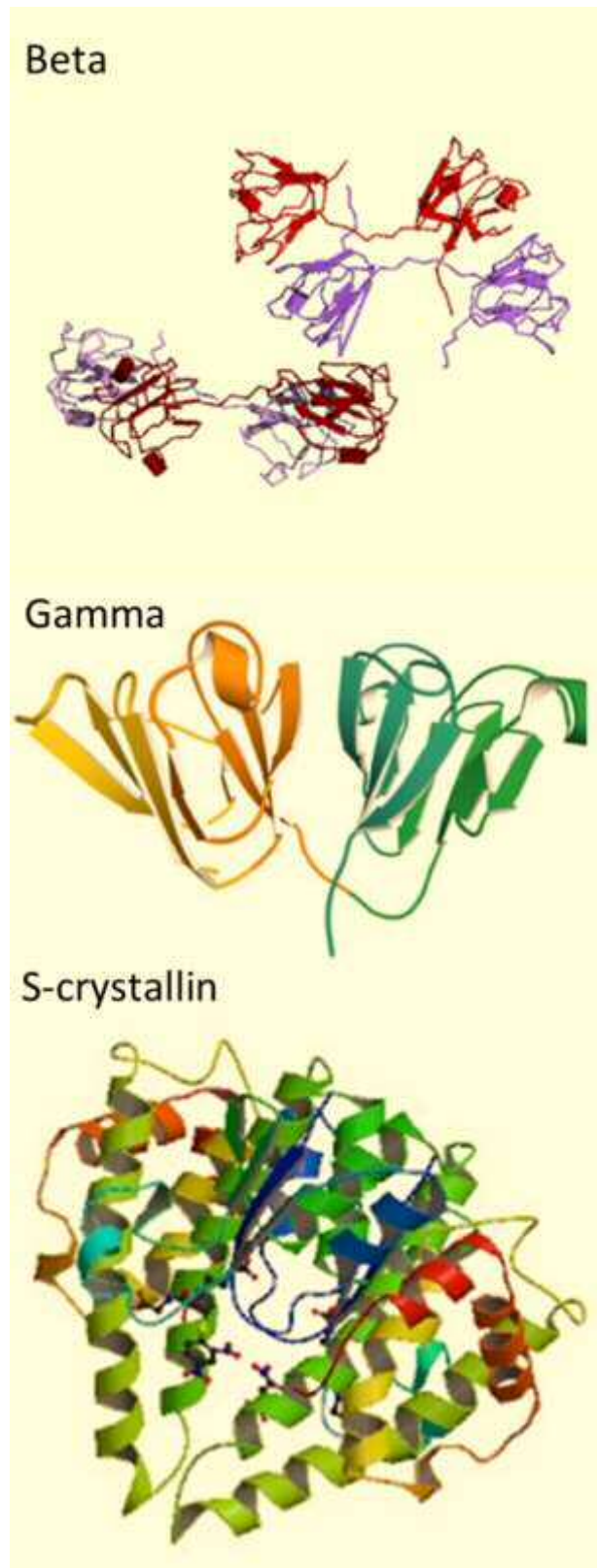


Figure 1-8: The protein structure shapes in the eye lens. Beta and Gamma which can be found in most lens species, while S-crystallin can be found in squid lenses (updated from Moreau and King, 2012, van Montfort et al., 2003, Chuang et al., 1999).

Alpha-crystallins belong to a family of small heat shock proteins (sHSP), thought to be instrumental in the proper folding of emerging polypeptide chains by inhibiting their aggregation if protein misfolding processes occur (Driessen, 1996, Kuszak et al., 1984, Piatigorsky, 1993, Duncan et al., 2004, Andley, 2007). Small heat shock proteins act to bind an equal weight of non-native protein, not just to minimise or reverse their aggregation, but also to facilitate consequent refolding (Basha et al., 2012). Alpha-crystallins within the lens are frequently exposed to UV light and age-related factors, which contribute to the development of lens opacity. Alpha-crystallin helps maintain lens transparency and prevent cataract formation throughout life (Ingolia and Craig, 1982, de Jong et al., 1993, Piatigorsky, 1993, Duncan et al., 2004).

The concentration and distribution of crystallins in the lens largely depends on the species and its visual environment, and while the concentration of α - and β -crystallins is highest in most vertebrate lenses, γ -crystallin concentrations are higher in the aquatic animal lens to increase the refractive index (Delaye & Tardieu, 1983; Wistow, 1993; Wistow et al., 2005; Zhao, 2011). Studies into the nature, concentration, and characteristics of crystallins in squid lens have shown that the refractive index gradient in squid lens is achieved through a radial variation in the density of the lens-forming s-crystallin proteins, which are relatively denser at the centre than the periphery (Figure 1-8). The s-crystallins are near variants of the glutathione s-transferase enzyme (Cai et al., 2017; Chang, 2017; Sweeney et al., 2007). Cells at varied radial positions in the lens, generate different ratios for 40 slightly different variants of s-crystallin. Further, during the development of squid eyes, the lens cells expel both their nuclei and ribosomes, leaving s-crystallins, which comprise 95% of the residual non-water mass (Sweeney et al., 2007; Chang, 2017).

1.5 Change of crystalline lens with ageing

1.5.1 The lens shape

With age, the human lens becomes more convex and thickens in the sagittal direction at a rate of ~ 0.024 mm/year (Dubbelman & Van der Heijde, 2001). The different anatomical regions in the lens generally fall into: the cortex and the nucleus. The point of sudden change in brightness on the Scheimpflug image (an effective instrument for anterior eye segment imaging) is often taken as the dividing line between the nucleus and the cortex. This is, in part, is the reason why a number of studies use Scheimpflug images to measure the increase in the nucleus and cortex of normal lenses (in-vivo studies). The growth of the cortex is estimated between 1.5 and 3.0 times that of the nucleus (Brown, 1976; Shibata et al., 1984; Kashima et al., 1993; Dubbelman & Van der Heijde., 2001).

Cook et al. (1994) measured a $3 \mu\text{m}/\text{year}$ reduction in the nucleus thickness with aging. More studies indicated that alternating dark and light zones can be distinguished within the anterior and posterior cortex (Goldmann, 1964; Dubbelman & Van der Heijde, 2001). Sparrow et al. (1987) developed a zoning system by which the cortex could be divided into four zones, namely C1-C4. As shown in figure 1-9, C1 is situated behind the anterior and slightly in front of the posterior capsule, while C3 comprises zones of high light scatter. Both C2 and C4 are low light scatter zones. Measurements of age-related changes in the respective thicknesses of the four zones indicate that most of the growth happened in C2, with C3 showing negligible changes particularly after the second decade of life. Zone C1's thickness appeared to reduce with age, while the thickness of C4 could not be measured with reasonable accuracy (Dubbelman & Van der Heijde, 2001).

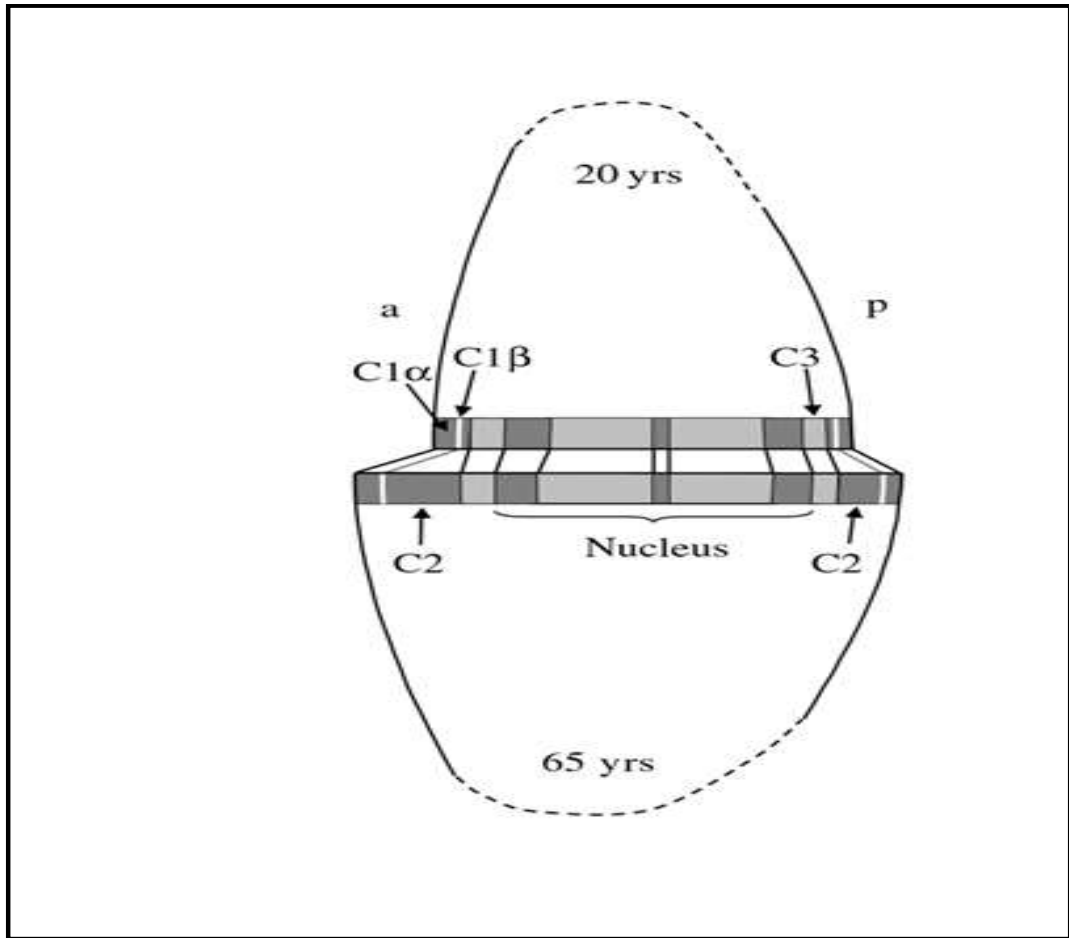


Figure 1-9: Schematic representation of age-related growth in the zones C1-C3; upper part denotes the lens of a 20-year-old and the lower part represents the lens of a 65-year-old. The change in lens thickness is mostly attributed to the expansion in the anterior and posterior of C2 (Dubbelman & Van der Heijde, 2001).

1.5.2 Ageing of lens proteins

The lens transparency is dependent on its ability to maintain, over a lifetime, its native tertiary structures and solubility of crystallin proteins. Ageing is associated with cumulative covalent protein damage due to oxidation, exposure to UV radiation, and truncations (Boscia, 2000). The crystallins, which comprise almost 90% of the total protein content of the lens, accumulate and show many age-related oxidative changes (Bloemendal, 1977; Bloemendal et al., 2004). The aggregation of proteins is associated

with protein chaperone content, which may similarly be responsible for crystallin aggregation in ageing lenses (Sharma and Santhoshkumar, 2009). A full understanding of the protein aggregation mechanism is necessary and relevant for research efforts into inhibiting or delaying cataract development, including inhibition of protein aggregation (Moreau & King, 2012).

1.5.3 Fibre cells compaction

The elongating fibre cells form flattened hexagons with an average width, as measured along regular radial cell columns in the equatorial plane, of about 3 μm . Inside the cortex, ~ 0.2 mm from the capsule, the cells become irregularly-shaped and their width reduces (Gilliland et al., 2009). Within the adult nucleus, at ~ 1 mm from the capsule, the average cell width ranges between 0.6 and 0.8 μm (Gilliland et al., 2009). This is coupled with a corresponding reduction in the average cross-sectional area of about a factor of $3\times$ between the outer cortex and the adult nucleus (Gilliland et al., 2009). Examinations of 23- and 60-year-old nuclear fibres shows evidence of compaction, which is higher in older lenses. The lens fibre compaction rate, however, reduces with age (Costello et al. 2013a). Empirical evidence shows that the lens fibre widths in samples obtained from the same area of the lens are $\sim 1.1\mu\text{m}$, $\sim 0.8\mu\text{m}$, and $\sim 0.4\mu\text{m}$ in 22-, 55- and 92-year-olds, respectively (Al-Ghoul, et al., 2001; Costello, et al., 2013b; Costello, et al., 2013a).

1.6 Lens functions

1.6.1 Refraction

Other than the cornea, the lens makes the most important contribution to the eye's total refractive power (Cvekl & Ashery-Padan, 2014). According to Gullstrand's schematic eye model, the human lens provides about 58.20 dioptres (i.e. approximately 19.11 dioptres in the unaccommodated lens and 33.06 dioptres in the full accommodated lens) of the eye's refractive power (Khurana, 2009). The lens refractive power largely depends on its surface curvature and its medium's refractive index. Both the surface curvature and medium affect the sharpness of focusing light, and therefore, affect the quality of the resulting image (Pierscionek and Regini, 2012). The gradient index, which is dependent on the lens material, the crystallins, has a major role in inducing light refraction (Zhao, et al., 2011). The lens structural proteins, the crystallins, are highly concentrated within the lens fibre cells in order to ensure transparency and generate a high refractive index (Wang et al., 2004).

1.6.2 Gradient refractive index

The concentration of proteins in the lens has a direct relationship with the resultant gradient of the refractive index (GRIN). This is not least because refraction does not only occur at the lens surface but also within its medium (Harding, 1991; Pierscionek & Regini, 2012). The gradient distribution of the refractive index results from the various distribution of protein concentrations inside the lens. In human lenses, the GRIN in the central and peripheral regions is estimated at 1.40 and 1.37, respectively (Delaye & Tardieu, 1983; Pierscionek & Chan, 1989; Wistow, 1993; Wistow et al., 2005).

1.6.3 Lens transparency

Lens transparency is critical for sight. The aqueous humour is a diluted solution of nutrient-rich molecules, with a few macromolecules which may interfere with the light's pathway (Harding, 1991). The vitreous humour, on the other hand, consists of 99% water, with a few thin collagen fibrils, hyaluronic acid, glucose, anions, cations and ions (Trokel, 1962; Harding, 1991). Lens transparency is dependent on the absorption and scattering of light. Absorption converts incident light to other forms of energy. In the normal lens, absorption is neglected when the light is in the visible wavelength. The scattering of light may be due to differences in the refractive index of lens fibres (Trokel, 1962).

1.7 Eye lens disorders

1.7.1 Cataracts

A cataract refers to opaqueness in the lens, which causes blurred vision. General symptoms of this condition include poor vision, reading difficulty, haloes around light sources, and general discomfort in bright light. Severe conditions present with an inability to distinguish between objects (Stevenson, 1839).

There are different types of cataract conditions, including nuclear cataract (NUC), cortical cataract (COR), and posterior subcapsular cataract (PSC) (Thylefors, 2002).

A NUC is defined as clouding in the central part of the lens and is the most prevalent type of age-related cataract. This type of cataract progresses gradually and may take years to have an effect on the eyesight. A COR occurs when the lens cortex becomes cloudy from the periphery towards the centre and appears as wedge-shaped spokes (Figure 1-10). The PSC, on the other hand, refers to an opacity which appears on the

posterior of the lens, as its name implies, beneath the lens capsule (Thylefors, et al., 2002).

Cataracts, whose prevalence gradually increases with age, is the main of the cause of blindness worldwide (World Health Organisation, 2010). In developed countries, the prevalence of cataracts doubles every ten years after the age of 40, which means that nearly everyone in their 90s is afflicted by some type of cataract disease (Brian, 2001). In developing countries, however, while the incidence of cataracts also increases with age, it is more prevalent earlier in life (Chatterjee et al., 1982).



Figure 1-10: A mature cortical cataract (Jesse, 2014)

In Punjab, India, for example, the prevalence of cataracts amongst the 30-49 age group was 1%, with a significant increase in the 60-79 age group to reach 67% for those aged 70 years or older (World Health Organisation, 2010).

The global population is increasing exponentially, thus the expectation is that over the next 20 years, cataract diseases incidence will increase significantly, with developing areas being most affected (Brian and Taylor, 2001). In addition, people over 65 years of age will experience twice the number of cataract conditions in both developing and developed countries. In light of these facts, most studies and public health policies concentrate on preventing cataracts by delaying their progression, as well as by providing the facilities for much-needed cataract surgery (Brian & Taylor, 2001).

1.7.2 Presbyopia

Presbyopia is a common, irreversible, visual impairment, and the most common refractive impairment in later stages of life. Predictably, the refractive impairment is associated with a reduced accommodative amplitude and impaired near vision (Werner, et al., 2000). In 2005, it was estimated that up to 1.04 billion people in the world, mostly over the age of 35, are afflicted by presbyopia, and the number is expected to increase to 1.37 billion by the close of 2020. Of these people, 517 million either did not have spectacles, or had inadequate spectacles, and 410 million were functionally impaired in performing near tasks (Holden, et al., 2008).

The causes of the condition remain largely unclear but are closely tied to the understanding of the accommodation. Studies of changes in the amplitude of accommodation in relation to age have shown a linear decline in accommodation power with age (Lovicu & Robinson, 2004; Oveneri-Ogbomo & Oduntan, 2015). Some studies point to a loss of zonules and/or capsule elasticity with age, which means that when zonules are relaxed, the lens does not change shape (Ehrmann, et al., 2008). There is contradictory theoretical/empirical evidence as to whether ciliary muscle

atrophies with age. The continued deposition of lens fibres within the lens may cause it to become compact and stiffer, which in turn reduces the lens ability to respond to accommodation stimuli (Al-Ghoul, et al., 2001; Rosen, et al., 2006).

Without optical correction, the accommodation amplitude would be inadequate to meet the patient's near vision demands, which may lead to a significant functional disability (Strenk, et al., 2005; Oveneri-Ogbomo & Oduntan, 2015; Schachar, 2012). Multiple correctional treatments for presbyopia are available, but all are compensatory. Single vision spectacle lenses are typically used for patients with ametropia, those with low degree ametropia, as well as those with uncorrected myopia. Progressive addition lenses, bifocal lenses, and trifocal lenses can offer a clearer vision for a range of distances, especially when coupled with an equally diverse lens and frame materials (American Optometric Association, 2011). Contact lenses, both soft and rigid designs, may be used, on their own or together with spectacles, to correct for presbyopia, but just like spectacles, they require careful choices among mono-vision, bifocal, alternating vision bi-focal and simultaneous vision bifocal lenses (Werner, et al., 2000; Schachar, 2012). Refractive surgery may cause patients to become anisometric so as to achieve mono-vision, but this treatment is fraught with numerous serious side effects, including over-correction, ocular tenderness, and stromal haze (American Optometric Association, 2011).

1.8 Accommodation

Other than refractive surgery, the current treatments for presbyopia may not be fully satisfactory for some patients. The effective and efficient prevention and treatment of presbyopia demand a better understanding of the accommodation mechanism (Strenk, et al., 2005; Oveneri-Ogbomo & Oduntan, 2015; Schachar, 2012). The

accommodation plays an important role in vision, by focusing near and distant objects onto the retina. The lens has a remarkable ability to provide a clear view from infinity to a 10-centimetre distance within a few seconds. The accommodation has been a subject of extensive theoretical and empirical investigations since the 17th century, but significant advancements to its understanding date back to Helmholtz's work in 1855 (Helmholtz, 1855; Schachar, 2012).

Helmholtz showed that during accommodation, the lens posterior and anterior surfaces grow steep and the central thickness increases. According to Helmholtz (1855), the contraction of ciliary muscles minimises the zonular tension around the lens equator causing the lens to relax. The reduced zonular tension thickens the crystalline lens, steepens its curvature radius and decrease its diameter. When the ciliary muscles relax, on the other hand, they pull the lens radially and flatten it. Helmholtz's seminal theory is highly consistent with empirical data and remains important in understanding the accommodation (Schachar, 2012) (Figure1-10).

As shown in the Figure 1-11, the ciliary muscle's contraction causes the main muscle mass to move towards the eye axis (Croft, et al., 2001). The lens zonules, which are directly connected to the ciliary muscle, release the resting tension at the lens's elastic capsule, effectively reshaping the lens (Luedde, 1927; Fisher, 1968; Croft, et al., 2001). In the unaccommodated state, on the other hand, the ciliary muscle relaxes and the zonular fibres contract. Consequently, the axial thickness decreases and both the anterior and posterior lens surfaces' curvature reduce as the equatorial lens diameter increases (Croft, et al., 2001; Rosen, et al., 2006).

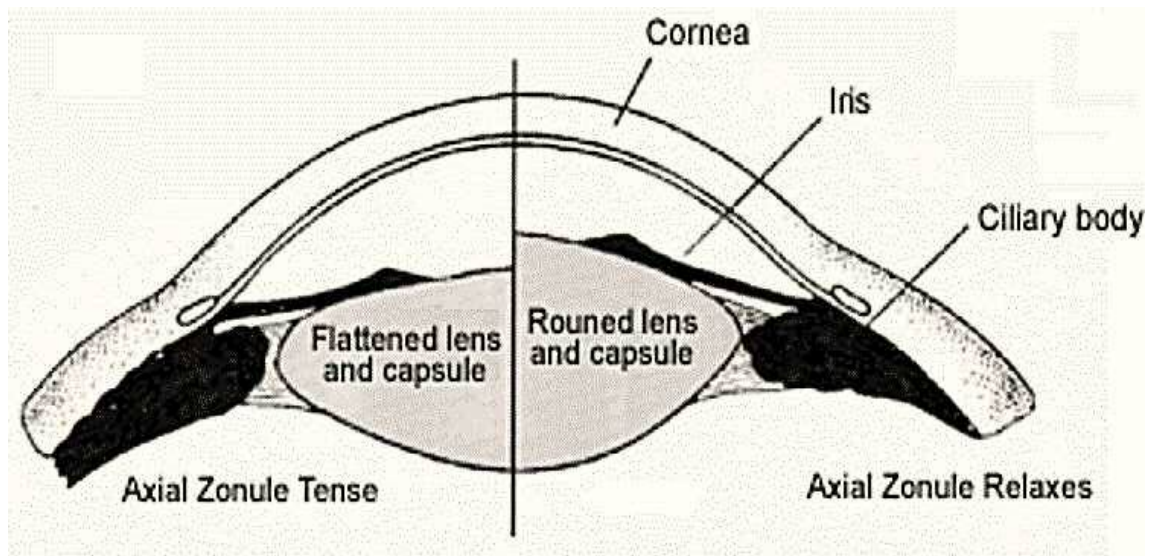


Figure 1-11: Lens behaviour in the accommodation and unaccommodation states. The right side of the drawing depicts an accommodated state as evidenced by the contracted ciliary muscle, as well as the thickened and steepened lens (Werner et al., 2000a)

As the shape of the lens changes during the accommodation process, the accommodative amplitude, which is measured in dioptres, also changes throughout the lens's life. The accommodative range reduces with age, from a maximum value of 15 dioptres in young people to 2-3 dioptres by the age of 40, and further to 1 dioptre by the age of 60 (Kuszak, 2006).

In cases of presbyopia, lens elasticity decreases, resulting in a reduction of deformability of the lens's nuclear tissue. In addition, the refractive index changes as the lens ages (Pierscionek, 1989). According to Helmholtz theory, therefore, during accommodation, there will be less steepening of the central anterior and posterior lens surfaces, flattening of the peripheral lens surface, and increased central thickness (Helmholtz, 1855; Schachar, 2012; Fincham, 1937; Norm & Jensen, 2004). Tscherning (1895)'s initial theory suggested that the contraction of the ciliary muscles increases zonular tension, but does not change the lens thickness. It was not until 1909

that Tscherning came round to the conclusion that the lens thickness increases (Norm & Jensen, 2004).

1.8.1 Internal lens changes during accommodation

The change in lens shape during accommodation also induces and/or is associated with the thickening of the cortex and nucleus (Daxecker, 1994; Dubbelman, et al., 2003). Multiple studies, including Patnaik (1967), Brown (1973), and Koretz et al. (1997), measured these changes, with the results suggesting that while the cortex's thickness remains the same, the accommodation-related increases in the sagittal lens thickness may be attributable to the increased thickness of the lens nucleus (Dubbelman, 2003). Patnaik (1967)'s slit-image photographic investigation of the lens internal structural changes during accommodation concluded that while there is an increase in the thickness in both the nucleus and the cortex, this was more emphasised in the nucleus relative to the cortex.

Other researchers, including Hockwin et al. (1982), Hockwin (1989), and Wegener (2001), recommended the use of the slit-lamp Scheimpflug imaging technique for investigating the lens changes and lens transparency under different conditions (Figure 1-12). According to Hockwin (1989), the cortical region shows an increase of ~ 0.004 mm/D in the anterior cortex and ~ 0.0006 mm/D in the posterior cortex. The Oxford system shows much smaller reductions in the cortex area (the anterior lens cortex and the posterior lens cortex reduced by ~ 0.001 mm/D and ~ 0.002 mm/D, respectively). There is, however, a consensus in respect to the changes in thickness in the nucleus region during accommodation (~ 0.040 mm/D and ~ 0.046 mm/D for the Hockwin system and Oxford system, respectively) (Dubbelman, et al., 2003).

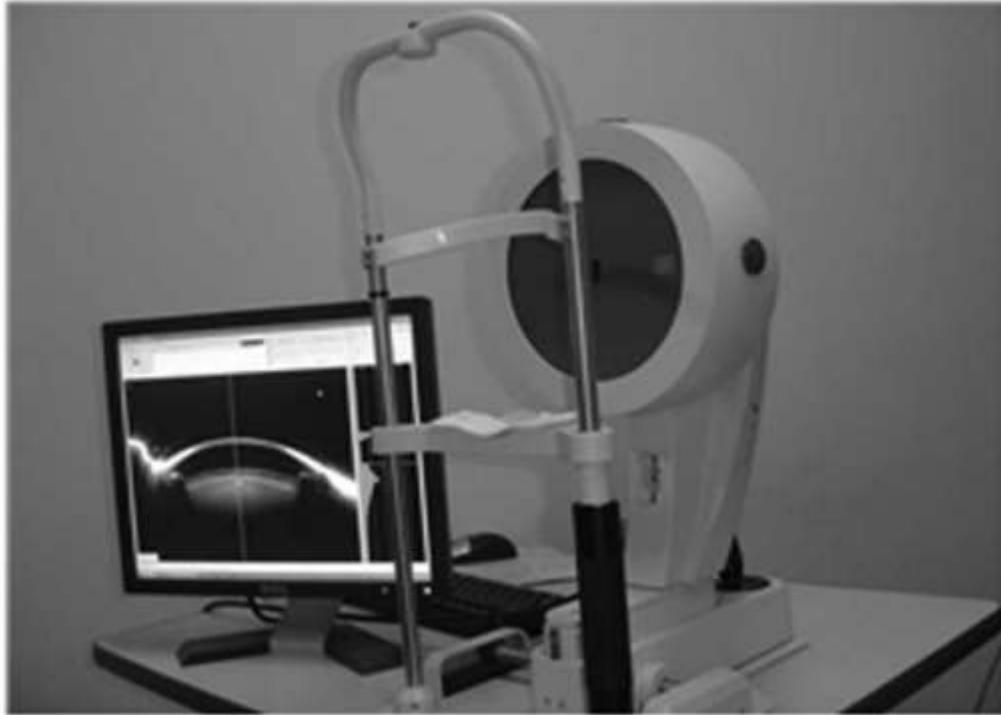


Figure 1-12: Slit-lamp Scheimpflug photography set-up (Xu & Hao, 2013)

1.9 Porcine lenses as a model of accommodation

Porcine lenses are used as a model for accommodation in humans largely because both human and porcine lenses have branched sutures from the combination of straight and S-shaped fibres. The suture shapes, however, are “star-shaped” for the human lenses and “Y-shaped” for the porcine lenses (Kuszak, 1995; Kuszak, 2004). Anatomically, pig lenses have a similar structure to human lenses, including capsule, epithelium and cortex layers (Simpanya, 2008). Geometrically, the linear relationship between optical and biometric properties in porcine lenses is similar to that in human lenses (Vilupuru, 2001). For example, the relationship between the focal length and the diameter, and between the lens thickness and the equatorial diameter are comparable in both the human and porcine lenses (Kammel, et al., 2012). In addition, age is considered as a function for some measurements, e.g. with age, the lens becomes thicker, the curvature

of the surface becomes flatter, and lastly, the lens diameter increases (Vilupuru, 2001). In terms of optical power, the paraxial refractive index in both human and porcine lenses is almost the same at 1.51 (Kreuzer, 1985; Vilupuru, 2001). Furthermore, Pierscionek, et. al. (1995) found that general protein distribution and metabolic activities within porcine lenses are also similar to human lenses (Jobling, 1995; Keenan, 2008).

The porcine lens is, therefore, anatomically, geometrically, and in terms of protein composition, similar to the human lens. However, physically, *in vivo*, the porcine lenses do not accommodate to any great extent within their environment (Walls, 1944; Kammel, 2012). Kammel et al. (2012) studied the changes in refractive power through young and old porcine lenses and found that older porcine lenses have reduced power. Porcine lenses can, therefore, be a suitable model for studying the presbyopic condition (Kammel, 2012).

On the other hand, there are many studies that have used young porcine lenses as a good model for understanding the accommodation condition (Trifonova, 2002; Roorda, 2004; Kammel, 2012; Matthew A. Reilly, 2009). This study uses young porcine lenses (6 months old) in the accommodated and unaccommodated states, in order to investigate the structure/ultrastructure of the lens before and after stretching. Ideally, the human lens would have been a better choice rather than porcine. However, the human research from Eye Banks are over two days old and have had the corneas removed before they are released for research. During this time, post-mortem effects such as degradation of the lens zonule and ciliary muscle will have taken place. Another complicating factor is that the majority of Eye Bank received donors eyes over 70 years of age, decades after the onset of presbyopia.

1.9.1 Lens stretching devices to imitate accommodation

Studying the accommodation mechanism or other aspects of lens biomechanics presents an inherent difficulty, as the mechanism only occurs *in vivo* (Fine, et al., 2005). While *in vivo* studies are possible with technologies such as magnetic resonance imaging and ultrasound imaging, they are unlikely to show the full picture without *ex vivo* studies. They are also likely to be of little use in animals that do not naturally accommodate. Over time, multiple devices have been produced to replicate accommodation *ex vivo*.

Initially, spinning disk devices mimicked the pull on the zonules by spinning isolated lenses (Fisher, 1971; Al-Ghoul et al., 2003). To achieve more accurate replication, lens stretching devices have been gradually adopted and innovated. A stretching device was first constructed in 1977 and used to measure changes in the amplitude of accommodation as human lenses aged. Since then, many research groups have designed lens stretchers to allow the measurement of multiple lens parameters during accommodation, including lens thickness, diameter, volume, curvature radius, and optical power (Marussich 2015; Kammel et al. 2012; Hahn et al. 2015).

The set-up requires that one attaches the lens ciliary muscle and sclera onto the device's attachment points using adhesives. To simulate the ciliary muscle's contraction and relaxation, the device stretches the tissues radially. More recent lens stretching experiments have sought to determine the potential of porcine lenses being used for, or offering insight necessary for, treating presbyopia and offering a better understanding the accommodation mechanism (Kammel et al. 2012; Hahn 2015).

Kammel et al. (2012), for example, compared the use of young porcine eyes to mature porcine eyes and found that the latter's lenses had similar optical properties to human lenses, including presbyopia and lower optical power. This information points to the potential of such research helping in understanding and treating similar disorders in humans (Glasser and Vilupuru 2001). Hahn (2015)'s study, on the other hand, used porcine lenses to investigate the potential of femtosecond-laser treatment, which by making laser incisions in the lens surface is used to enhance the lens flexibility, in treating presbyopia. The study showed that the lens parameters change at different levels of accommodation, before and after laser treatment. These results open up possibilities that may be further explored using methodologically robust clinical studies that may offer insight into the treatment of presbyopia (Carbine and Larson 2017). It is in this promising context that the present study is set.

1.10 Research problems, and objectives of the present study

In 1855, Helmholtz's accommodation theory postulated that the posterior and anterior surfaces of the lens do actually grow steep and the lens central thickness increases during accommodation (Schachar, 2012). Evidence from both the Oxford and Hockwin Systems indicate that the lens nucleus is the innermost part of the lens that is involved in the accommodation (Dubbelman, et al., 2003; Dubbelman, et al., 2005). It is, however, still unclear as to how exactly the lens anterior structure behaves during accommodation.

This is in a large part because of two practical difficulties, the first of which has been alluded to in a more helpful context in sub-section 1.8, namely that accommodation is exhibited by living humans/animals and therefore, it is difficult to study it in dead animals/humans (Fine, et al., 2005). As already pointed out, technological

improvements are, however, helping relieve this difficulty by offering means to replicate the eye/lens' natural behaviour during accommodation and allow for *ex vivo* research. Specifically, the lens stretcher has become a useful instrument in multiple studies into the overall lens shape, curvature, lens power, and volume, both in the accommodated and unaccommodated states (Schachar, 2012; Belin, et al., 2012). This present study primarily relies on the lens stretcher technique. The second practical difficulty facing research into the accommodation relates to the fact that while there have been substantial advancements in microscopic examinations of the eye's internal structure, it is still necessary for the whole organ to be dissected before any imaging may be undertaken. In the case of the eye lens, the interior structure must be preserved within a capsule that is critical in keeping the integral lens shape (Fine, et al., 2005; Schachar, 2012). This study attempts to keep the whole lens shape intact in both accommodated and unaccommodated conditions.

The rationale and hypotheses of this thesis are as follows:

1. It is accepted that the crystallin concentrations in different groups of animals are a consequence of their adaptations to their specific visual environments (Augusteyn, 2004). The changes in the crystallin densities between the lens cortex and nucleus, in both aquatic animal and terrestrial vertebrates/invertebrates, are, however, unclear. Hence, the hypothesis is that differences in lens crystallin proteins exist between groups of animals depending on their visual environmental demands.
2. Further, internal structural changes in the lens between the accommodated and unaccommodated states have not been fully addressed. This is particularly the case with respect to changes in lens crystallin protein packing and

concentration within the fibres between the lens cortex and nucleus with accommodation, which has never been measured experimentally. This study will seek to fill this gap and hypothesises that there is a difference in the spacing between crystallin proteins in unstretched and stretched porcine lenses, and that there are internal structural changes in both the cortex and nucleus during the accommodation process.

3. The lens curvature's behaviour during accommodation is related to internal structural changes. There is substantial research on the role of these curvature changes in lens functionality, but most of these studies limited themselves to ascertain the relative contribution of both anterior and posterior radius of lens curvatures to the lens's accommodative ability. This study sought to add to this area of research and hypothesises that the anterior and posterior lens radii of curvature change during the accommodation.
4. The lens suture ends are directly related to the tissue's optical quality (Kuszak et al., 1994, Sivak et al., 1994). The porcine lens contains Y-shaped sutures that create three angles. It is possible to evaluate the resultant suture angles in the anterior surface using light microscopy. This study aimed to measure the change in the lens suture angles between stretched and unstretched conditions, with the hypothesis that suture angles change during the accommodation.
5. The lens fibre width is depth-dependent (Al-Ghoul et al., 2003). In order to assess the effects of accommodation on the lens fibre widths at different lens depths, this study sought to measure the fibre widths in porcine lenses at different depths through the lens, from the anterior/posterior surface down to a depth of 300 μ m and through the whole lens. The aim was to measure changes

in lens fibre widths between stretched and unstretched lenses with the hypothesis that such changes have a role in the accommodation.

1.10.1 Aims and objectives

This study's overarching aim was to understand the lens structure and its ultrastructural behaviour in the accommodated and unaccommodated state. To this end, this study sought to meet the following objectives:

1. To investigate the ultrastructure and the density of the crystallin proteins in both the lens nucleus and cortex in the European squid, Atlantic salmon and porcine lenses.
2. To use synchrotron X-ray diffraction techniques, to investigate how the porcine lens protein ultrastructural changes during accommodation.
3. To optimise embedding and staining procedures for using electron microscopy to analyse the 3D ultrastructure of human lens tissue.
4. To analyse the changes in lens anterior and posterior radius curvature in the accommodated and in unaccommodated state.
5. To analyse the changes in lens anterior suture angles in the accommodated and unaccommodated states.
6. To analyse anterior and posterior shape of the lens sutures and lens suture confluence area.
7. To investigate the lens fibre widths a function of depth in the accommodated and unaccommodated lens.

Chapter Two

2 Ultrastructure of Atlantic Salmon, European squid, and porcine lenses

2.1 Introduction

The vertebrate eye's optical characteristics are mainly dependent on whether the eye is used in water or air (or both), and whether it is used under nocturnal or diurnal conditions (Sivak et al., 1999). Porcine, squid, and salmon eyes have the same basic anatomical structures, including the cornea, lens, iris, ciliary body, vitreous, retina, choroid and sclera, vasculature, and optic nerve (Soules and Link, 2005) (Figure 2-1). The cornea is a transparent structure comprising two curved and nearly parallel surfaces such that its refractive index is entirely dependent on the existence of a medium within it. The original aquatic environment constrained the original purpose of the cornea to a transparent window since there is a minimal difference in the density of the water and that of the aqueous humour (hence an equally minimal difference in refractive indices) (Sivak et al., 1994; Sivak et al., 1999). The vertebrate eye is characterised by a spherical (or near spherical) lens with a fairly high refractive index. Since the lens is a refractive structure, it is responsible for changes in the refractive power. The accommodative mechanism, therefore, must involve the lens movement, either by internal changes as is the case in vertebrates or by the whole lens moving forward/ backward as is the case in fish species (Sivak et al., 1994; Sivak et al., 1999; Cvekl & Ashery-Padan, 2014).

Terrestrial animals with highly oblate lenses accommodate by changing the lens shape and/or curvature. The lenses in teleost fish are almost entirely spherical. The barely ellipsoidal shape and high crystallin density reduce the lens pliability, which, in turn, means that such lenses need a different mechanism to achieve accommodation. In this case, the distance to the retina is altered through the axial movement of the lens, caused

by the retractor lentis muscle (Sivak, & Glenn, 1985). The squid lens is, on the other hand, structurally different from both the terrestrial animal lens and teleost fish lens.

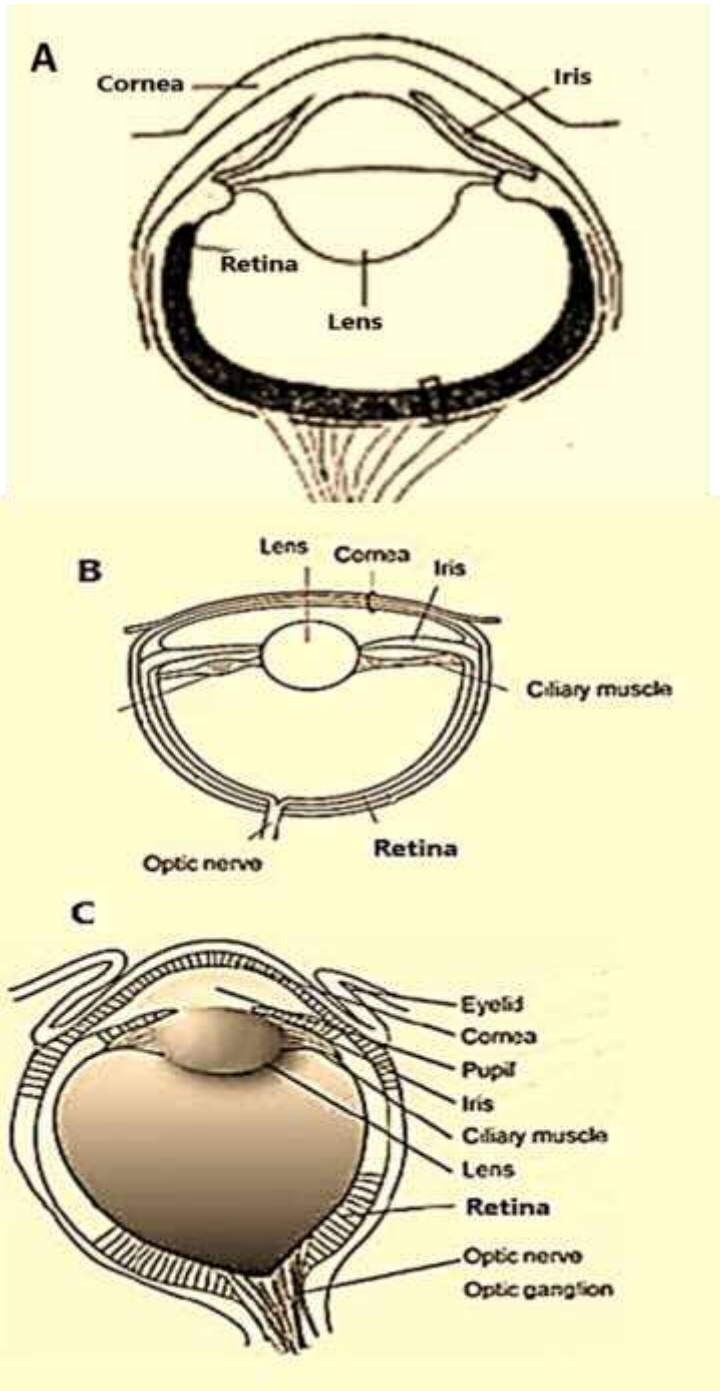


Figure 2-1: Anatomical structures of the A) cephalopoda B) fish, and C) human eyes. These generally include the cornea, lens, iris, ciliary body, vitreous, retina, choroid and sclera, vasculature and optic nerve as adapted from Archive-cephalopods (2012) and Noguera (2015).

It has an anterior plano-convex segment and a relatively larger posterior segment (with a larger diameter) linked by a septum with an associated ciliary body (Willekens, Vrensen, Jacob & Duncan, 1984) (See Figure 2-2). Unlike the case in most vertebrate lenses, it is likely that each structural element of the cephalopod lens develops from different ectodermal sources (Packard, 1972).



Figure 2-2: The eye of a Japanese flying squid (*Ommastrephes pacificus*). The anterior plano-convex hemi-spherical segment is on the right of the image, while the larger posterior sub-spherical segment is to the left.

Aquatic organism/creatures, that have camera-type eyes as a result of the similar refractive index between the cornea and water (about 1.3), need high lens power relative to those of terrestrial creatures (Land & Nilsson, 2002; Sweeney et al., 2007). The larger the optical power of a homogeneous refractive index lens, the greater the spherical aberration it generates, creating blurred images. To overcome this problem, aquatic organism/creatures have developed spherical, graded refractive index lenses that simultaneously achieve small eye sizes, fairly high sensitivity, and equally

excellent image quality. Due to the differential lens crystallin concentrations within lenses, research has shown a relatively higher refractive index at the centre compared to the lens cortex (Sweeney et al., 2007; Gordon, 2000). See Table 2-1.

| Lens within some groups of animals | Refractive Indices | |
|------------------------------------|--------------------|---------|
| | Cortex | Nucleus |
| Squid | 1.36 | 1.54 |
| Fish | 1.38 | 1.52 |
| Porcine | 1.39 | 1.47 |

Table 1-2: The refractive indices in the cortex and nucleus areas of squid, fish and porcine lenses (Sweeney Alison et al., 2007, Sanchez et al., 2011, Jagger, 1992).

The porcine lens was chosen as a representative of vertebrate lenses that have nearly similar internal structure. It is an entirely cellular structure situated within the lens capsule, behind the iris and the cornea, and supported by both the vitreous body and zonular muscles (Cvekl & Ashery-Padan, 2014). Many studies, including Davison (1990), Paterson et al. (1992), and Bloemendal et al. (2004), have found that the composition of the lens is unusual, in that approximately 35% of its weight comprises protein, while the remaining 65% is water. Water-soluble proteins—the crystallin protein family—comprising in excess of 90% of all the lens protein; the remainder being primarily membrane and cytoskeletal proteins (Bloemendal, 1977; Bloemendal et al., 2004).

The lens fibres contain three main crystallin types, α , β and γ , which give the lens transparency and refractive power (Bassnett et al., 2011; Roquemoire et al., 1992). The principal eye lens protein, α -crystallin, is a member of the small Heat Shock Protein family that is comprised of two closely related subunits, αA and αB -crystallin, each of which is ~20 kDa in mass. In the human lens, the two isoforms ($\alpha A:\alpha B$) are co-expressed in a ratio of 3:1 (Harding, 1991). The lens contains a very high concentration

of protein (up to 450 mg/ml in the nucleus or centre of the lens) contained in long fibre cells. Alpha-crystallin is the lens primary protein component and can approach 50 % of the lens total dry weight (De Jong, 1981). Alpha-crystallin has two important functions in the lens: structural and molecular chaperone function. In its structural role, it assists in the maintenance of short-range order in the lens cytoplasm, effectively ensuring proper refraction of light and lens transparency (Delaye, & Tardieu, 1983). As a molecular chaperone, alpha-crystallins maintain the solubility of the other classes of crystallin proteins, β and γ . There is no protein turnover in the centre of the lens, meaning that the crystallin proteins have to be very long-lived. Alpha-crystallins are also involved in minimising lens protein precipitation over decades, thereby, preventing lens opacification and cataract formation (Boyle & Takemoto, 1994).

Outside the lens, α B-crystallin is also expressed at significant levels (Bhat & Nagineni, 1989), where it has a key role as a molecular chaperone. In addition, to its role in the prevention of cataract formation, for example, α B-crystallin is of interest extralenticularly because its expression is associated with many other protein misfolding disorders. Thus, α B-crystallin is found in significant levels in the brains of patients with Alzheimer's disease (Renkawek, et al, 1994; Shinohara, et al 1993) and Parkinson's disease (Lowe 1992, Trojanowski et al, 1998), as well as in patients with multiple sclerosis (Van Noort et al, 1995) and ischaemic heart disease (Chiesi, et al, 1990). In vitro, α B-crystallin protects target proteins against heat-induced aggregation (Ecroyd, et al, 2005), enzyme inactivation (Ganea & Harding, 1995; Heath et al, 1996), and amyloid fibril formation (Ecroyd, et al, 2009).

The concentration and distribution of crystallins in the lens largely depends on the organism/creature (and its visual environment), and while the concentration of α - and

β -crystallins is highest in most vertebrate lens, γ -crystallin concentrations are higher in aquatic lenses. This is because their smaller size compared to α - and β -crystallins allows them to pack closer together, effectively increasing the lens refractive index (Delaye & Tardieu, 1983; Wistow, 1993; Wistow et al., 2005; Zhao, 2011). The transparency and refractive power of the lens are both associated with crystallin concentration. The lens transparency reduces gradually with age due to the increase of the insoluble fraction of proteins.

The squid lens is, however, an exception as it exhibits no opacity throughout its lifetime (Cai et al., 2017; Chang, 2017; Sweeney et al., 2007). Studies into the nature, concentration, and characteristics of crystallins in the squid lens have shown that the index gradient is achieved through a radial variation in the density of the lens-forming s-crystallin proteins, which are relatively denser at the centre than the periphery. The s-crystallins in squid lens are near variants to the glutathione s-transferase enzyme, but do not display any enzymatic activity (Cai et al., 2017; Chang, 2017; Sweeney et al., 2007). Fibre cells at varied radial positions in the lens generate different ratios for some 40 slightly different variants of s-crystallin. The mixtures form into a volume-spanning protein network of gels at different densities. The gelation inhibits protein aggregation and formation of opaque masses and minimises local density variations that may otherwise distort vision (Sweeney et al., 2007; Chang, 2017). Moreover, during the development of squid eyes, the lens cells expel both their nuclei and ribosomes, leaving s-crystallins, which comprise 95% of the residual non-water mass.

Unlike squid, cataracts occur very frequently in farmed salmon. Salmons are usually fed diets based on marine ingredients, whose availability, is limited. Non-marine feed substitutes have been shown to affect the lipid type as well as fatty acid composition in a number of salmon tissues (Tröbø et al., 2010). Recent studies, including Bell et al.

(1999), Torstensen et al. (2008), and Tröbe et al. (2010), have found a link between vegetable oils in feeds and severe outbreaks of cataracts in grown salmon. Plant proteins have low concentrations of the essential amino acid, histidine, relative to marine feed-based diets. The concentration of histidine positively prevents or slows the progression of cataract development in salmon (Tröbe et al., 2010).

The porcine lens crystallin is not dissimilar to other mammalian lenses in respect to its crystallin protein composition. The available evidence shows that the porcine and salmon lenses, have α , β , and γ crystallins, but α and β crystallins concentrations are predominant in porcine lenses (Bloemendal et al., 2004), while γ -crystallin concentration is relatively higher in squid and salmon lenses.

This study aims to provide further detail into the packing and ordering of the crystallin proteins in both the lens nucleus and cortex in the European squid, Atlantic salmon and pig lenses. Few small angle X-ray diffraction studies have been conducted on the lens, and of those, most have been conducted on mammalian lenses such as rabbit, bovine and porcine lenses (Delaye & Tardieu, 1983; Regini et al, 2004; Regini et al, 2009). In most of these previous studies, only a single X-ray pattern was taken of each individual sample, with the X-ray beam passing through the centre of the lens, more or less co-axial with its optical axis. The advent of computer-controlled moveable sample stages has allowed the use of small angle X-ray diffraction 2D grid scans, in which biological specimens are traversed in the X-ray beam and individual patterns are collected systematically, at precise points across the sample. Thus, changes in the X-ray patterns across the sample may be mapped. In a previous study, Regini et al. (2018) conducted the first investigation into the structure of squid lens (*Todarodes Pacificus*) using 2D grid scans at the SPring8 synchrotron in Japan. Unexpectedly, they found very intense anisotropic X-ray reflections which rotated at different points

in the scan (the possible origins of these reflections are discussed in section 2.4). The rationale for using European squid lens for this study was to see if the anisotropic X-ray reflections are specific to certain species (i.e. in those caught in Japanese or British waters). This investigation also sought to establish if the same anisotropic reflections occurred in lenses of other aquatic vertebrate groups, for which reason, the Atlantic salmon lens was chosen. Porcine lenses were also used as a terrestrial mammalian comparator.

It was hypothesised that the Bragg spacing, representing the average distance between the crystallin proteins, would decrease between the cortex and the nucleus, in pig, salmon, and squid, as the protein concentration increased. It was also hypothesised that the degree of crystallin ordering, as measured by the ratio of the height of the diffraction peak (H) to its full width at half maximum (FWHM), would increase towards the nucleus, indicating a higher degree of ordering.

2.2 Materials and methods

2.2.1 Tissue source and sample preparation

2.2.1.1 Porcine lens

All the studies were conducted in adherence with the ARVO Statement for the Use of Animals in Ophthalmic and Vision Research. This study used five fresh porcine eyes. All porcine eyes were obtained from a local abattoir, W. T. Maddock, Maddock Kemberly Meats, Maesteg, Wales, UK (by way of an agreement between the abattoir and Cardiff University) and are a by-product of meat production for the food chain. The fresh eyes were kept refrigerated (in an icebox) and subsequently transferred to the UK's national synchrotron facility, the Diamond Light Source, located at the Harwell Science and Innovation Campus, Oxfordshire. For each eye, the lenses were

dissected and placed in a lens stretcher, which was being used solely as a sample holder. All the porcine samples were placed in the X-ray beam in the unstretched position.

2.2.1.2 *A squid and European salmon lenses*

Fresh European squid (*Loligo vulgaris*) and Atlantic salmon (*Salmo salar*) eyes were obtained from a local fishmonger, Fishmongers LTD, Central Market, Cardiff (Wales). As the squid and salmon were sourced only from those freshly entering the food chain, no squids or Atlantic salmons were sacrificed/harmed for the sole purpose of this thesis. Four Atlantic salmon eyes and two European squid eyes were placed in an ice box before being transferred to the Diamond Light Source in Oxfordshire, UK, dissected and the lenses extracted for examination, on the very day that they were received.

2.2.2 Small angle X-ray scattering (SAXS)

Developed in the 1930s, SAXS is a powerful technique for analysing nanoscale density differentials, which means that it may be used to assess the size, mass, quantity, shape of molecules and molecular assemblies in partially ordered materials (Glatter & Kratky, 1982; Lipfert et al., 2007). High-intensity synchrotron-based third-generation SAXS facilities, which are needed for studies of weakly diffracting materials such as the lens, are however limited, due to cost. Only about five countries, including the UK, the US, Germany, Japan, and France, have such facilities (Kikhney and Svergun, 2015).

2.2.2.1 Synchrotron radiation

Experiments in this chapter and the next exclusively relied on synchrotron radiation techniques. A synchrotron refers to a particle–accelerator that generates radiation in a broad spectral range from hard X-rays to infrared (Helliwell, 2006). The electromagnetic radiations are emitted when electrons (or any other charged particles) moving at speeds close to the speed of light are forced by electric/magnetic fields to follow curved routes. Manmade sources of synchrotron radiation are high-energy, positron or electron circular accelerators, like storage rings. A typical synchrotron features an electron gun to generate electrons (labelled 1 in Figure 2-3), a linear accelerator (*Linac*) to accelerate the speed of electrons to relativistic levels (2), a booster ring to enhance electrons intensity, and an outer storage ring (4) (Diamond Light Source, 2018).

Essentially, the electron gun, Linac, booster ring, and external storage ring, are comprised of circular evacuated pipes in which electrons are forced to flow. The electrons only enter the storage ring after the linac accelerates them to reach several millions of electron volts before a booster ring boosts their energy to reach Giga electron volt levels. At this point, the electrons are transferred to the circular accelerator. The emitted photons are focused into a small, well-defined beam for experimental use in the beamlines. X-rays generated in this way are up to hundreds of times more intense than conventional X-rays, so the exposure time can be as low as a few seconds/minutes. Synchrotron radiation is very intense, and its wide spectral range makes it possible to obtain radiations of different wavelengths depending on the purpose (Diamond Light Source, 2018).

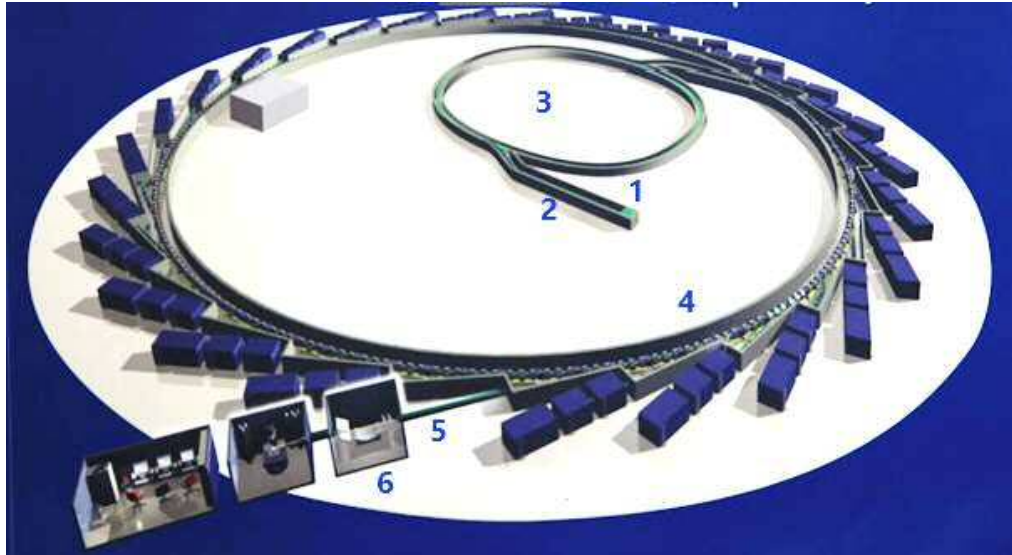


Figure 2-3: A schematic planar view of a synchrotron facility. The Electron gun, Linac, booster ring, and external storage ring are labelled 1, 2, 3, and 4, respectively. A Linac accelerates generated electrons to relativistic speeds before they are transferred to a booster ring and subsequently to the storage ring, from where they are moved into a nearly circular route. Emitted photons are then focused and transferred to beamlines (5), from where experiments are conducted (6) (Adapted from Image Of Diamond Imagenus.co, 2018).

Due to their high cost, there are only about 50 synchrotron facilities in the world today, even though the technology was developed in the 1940s. Some of the existing facilities, including the Diamond Light Source and the European Synchrotron Radiation Facility (ESRF), are third generation synchrotrons built using special sets of magnets known as insertion devices, which are installed in straight sections of the ring. The insertion devices make the electrons flow in a wiggling path, effectively producing an even more intense and tuneable light (Diamond Light Source, 2018).

2.2.2.2 General principles of X-ray diffraction

Perhaps one of the most fundamental principles underpinning the understanding of how waves reveal the specimen's ultrastructure is Bragg's law (see Figure 2-4) for a schematic representation of Bragg's law. According to this law, whenever a specimen

is, at certain incident angles, bombarded with X-rays of fixed wavelength similar to the spacing of an atomic-scale crystal lattice, intense reflected X-rays are generated when the scattered X-rays' wavefronts interfere constructively. Constructive interference occurs when the difference in the travel path is equal to the wavelength's integer multiples, such that:

$$n\lambda = 2d \sin \theta$$

Where:

n is an integer representing the order of reflection,

λ is the wavelength

d is the spacing of a lattice plane, and

θ is half the angle of diffraction (Hammond,1997).

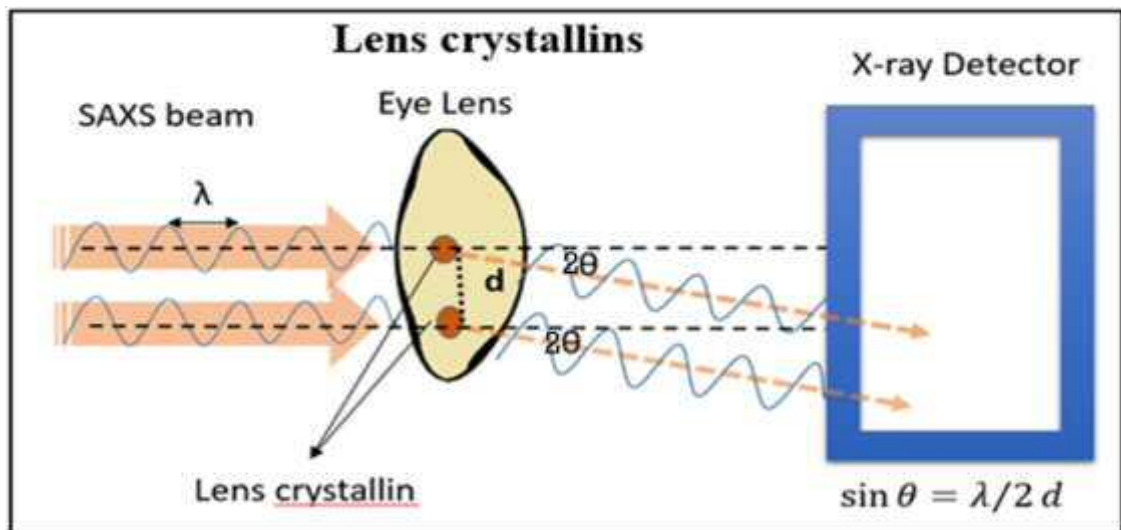


Figure 2-4: The x-rays are diffracted by two planes of crystalline lattice separated by a distance d . If the conditions of Bragg's law are satisfied, then constructive interference occurs.

2.2.2.3 Reciprocal space

The resultant X-ray scattering patterns often referred to as diffraction patterns, are recorded on a 2D detector in the form of separate data points or X-ray reflections. The spacing between these reflections is inversely proportional to the dimensions of the crystalline lattice. As such, the spacing in the diffracted pattern corresponds to the reciprocal of the crystal lattice's actual spacing (Hammond, 1997).

2.2.3 Mounting of samples for small angle X-ray scattering

2.2.3.1 Preparing fresh porcine samples

All the SAXS data were collected using the Diamond Light Source's small angle Beamline I22. Fresh lenses were wrapped in cling-film to minimise dehydration during X-ray exposure (Figure 2-5). Previous studies have shown that the use of cling film to envelop a biological sample in low angle X-ray studies does not give rise to any anomalous X-ray reflections or interfere with the X-ray pattern from the sample (Dr. Justyn Regini, private communication). Each of the fresh lenses was clamped on a motorised stage with the anterior lens surface facing the incident X-ray beam.

2.2.3.2 Preparing salmon and squid lens samples

Each lens was wrapped in cling film and placed into a sample holder with airtight Perspex chambers to keep the lens in its place. The sample holder was clamped on a motorised stage with the lens anterior surface facing the incident X-ray beam.

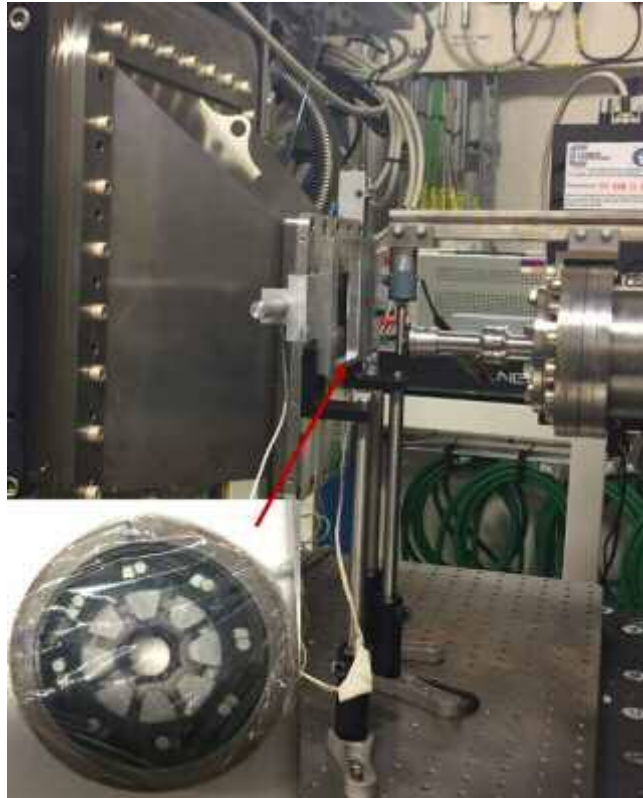


Figure 2-5: The process for preparing fresh lenses and clamping onto the front incident X-ray beam.

2.2.4 Small angle x-ray scattering

The X-ray scatter patterns were collected separately from each lens. Each lens was located 6.8 mm behind incident X-ray beam and the SAXS data were collected using a $150\mu\text{m} \times 300\mu\text{m}$ X-ray beam of wavelength 1\AA , directed perpendicularly to the whole lens for a 2D grid scan. The exposure time per data point was 0.1 seconds at 0.5 mm intervals along the lens horizontal and vertical meridians. Each 2D grid scan was 1 cm in length in both the x and y directions. This gave a 20×20 grid so each completed scan was composed of 400 individual X-ray patterns from one sample. In total, the five porcine lenses generated 2000 individual X-ray patterns, while the four Atlantic salmon lenses and two European squid lenses generated 1600 and 800 individual patterns, respectively. Figure 2-6 shows a typical small X-ray diffraction pattern from

a porcine lens. The pattern is dominated by a single X-ray reflection which is a broad diffuse ring. No other structural sampling is observed. The assumed interpretation of this reflection is that it is an interference function, and originates from the average nearest neighbour spacing between the crystallin proteins. The width or thickness of this reflection gives an indication of the ordering of the crystallin proteins within the lens fibres, with a narrower interference function indicating a high degree of ordering (Regini, 2009).

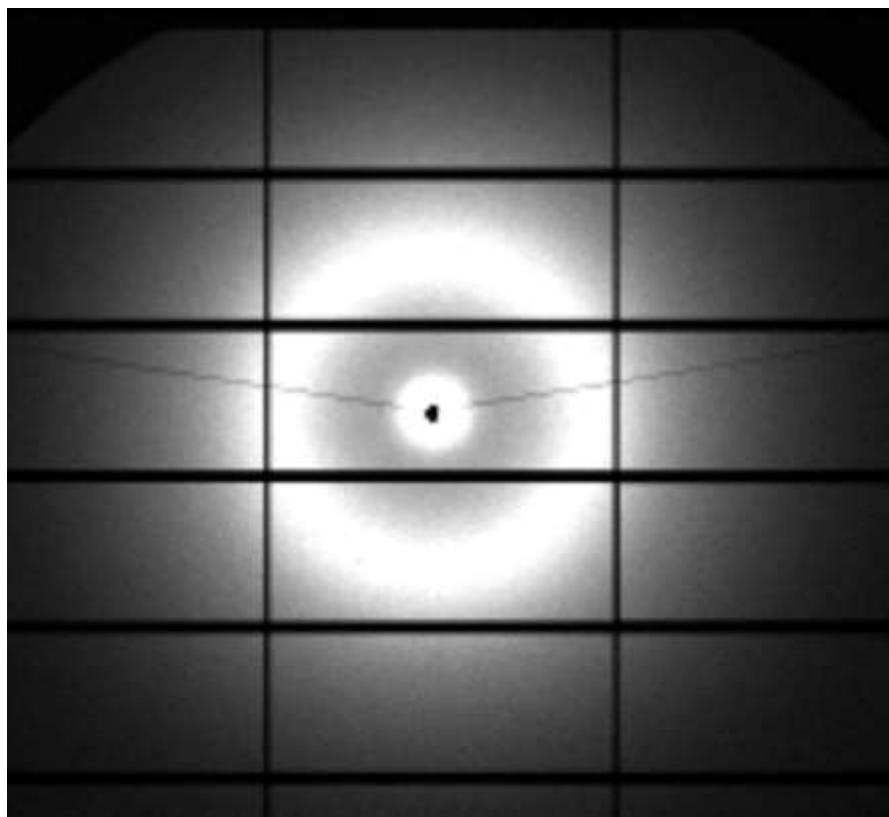


Figure 2-6: Small angle X-ray diffraction from a porcine lens.

2.2.5 Data analysis

The X-rays were scattered as they passed through the lens samples and were recorded by Pilatus 2P3M photodetector (Dectris, Switzerland). Since the lens crystallins have a short-range order (in order to ensure lens transparency), the resultant 2D scatter

patterns of the crystallins were easily detectable in European squid, Atlantic salmon, and porcine lenses.

The resultant 2D scatter patterns of the crystallins were converted into a 2D frame image with equivalent pixel intensities. In each frame, the SAXS pattern at each individual scan point was saved as a NEXUS (.nxs) file under the file scan number. All the raw NEXUS files were subsequently exported into the DIAMOND synchrotron in-house Data Analysis WorkbeNch 2.11.0 (DAWN) software for analysis (Basham et al., 2015, Filik et al., 2017), which included the determination of the ordering and nearest neighbour spacing between the crystallin proteins within the lens.

2.2.5.1 Data processing

All the data were imported into the DAWN 2.11.0 software and processed in order to extract the required data. The specific procedure is set out in the next section, immediately after a brief explanation of the role of silver behenate:

2.2.5.2 Calibration

Silver behenate (AgBeh) is a behenate acid salt, that is most often used as a standard for calibrating the medium to low angle X-ray diffraction q-range (i.e. the range of spacings being measured), both for lab instruments and at synchrotrons (Gilles, 1998). It was, therefore, used in this study to calibrate the SAXS scatter pattern positions. All the SAXS patterns in the original format were input into DAWN 2.11.0 software to subtract the background related to the Mylar and sample holder as well as to mask the grid due to the detector in order that the grid did not interfere with subsequent analysis.

2.2.5.3 Montage of Lenses

After the data were processed and the background subtracted from each individual X-ray pattern, a montage of all X-ray patterns for each lens was created separately using the DAWN 2.11.0 software. The individual X-ray diffraction patterns of fresh porcine lenses, European squid, and Atlantic salmon lenses are displayed as montages (the Figures 2-7 and 2-8). To determine the peak position within the meridians of interest, the SAXS pattern's locations were calculated for both vertical and horizontal meridians to include the mid meridian (through the lens nucleus) and the equatorial meridian (through lens cortex).

The area of interest in each montage was indicated, and both the peak position and the H/FWHM ratio were analysed in different vertical and horizontal planes of the 2D grid scan as indicated by orange and blue outlines respectively in Figure 2-9.

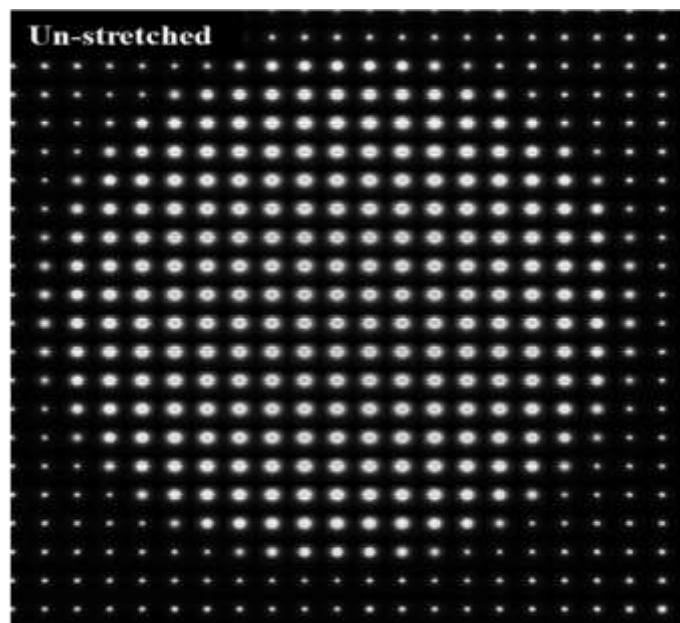


Figure 2-7: Montages of all X-ray patterns for a fresh porcine lens in an un-stretched position, with intervals at 0.5 mm along the lens horizontal and vertical meridians.

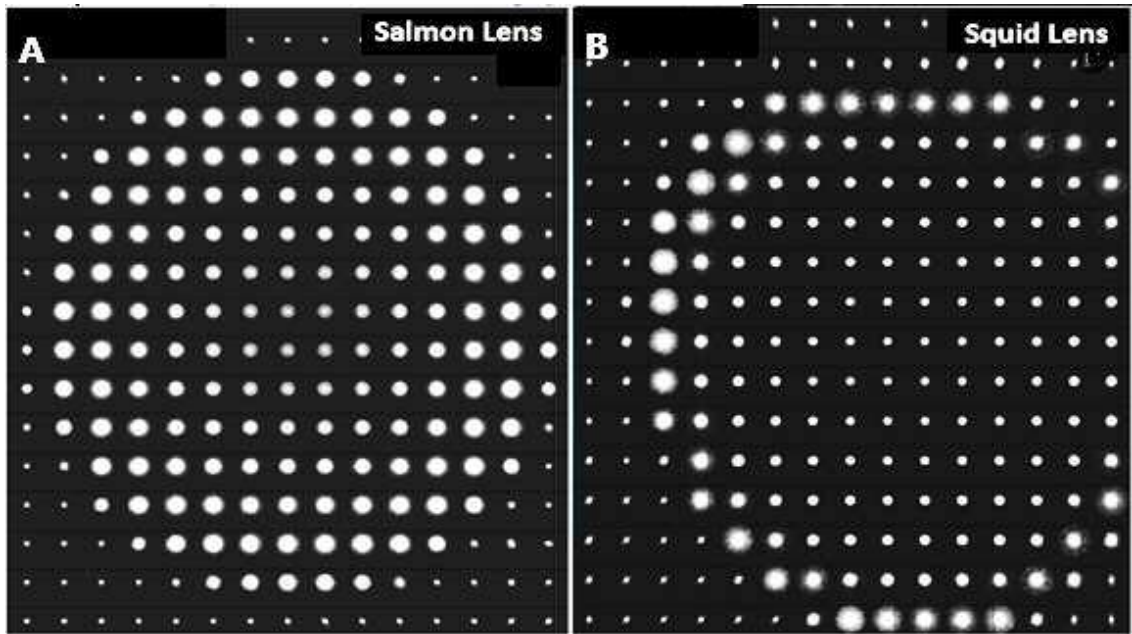


Figure 2-8: Montages of all X-ray patterns from Atlantic salmon (A) and European squid (B) lenses, with intervals at 0.5 mm along the lens horizontal and vertical meridians.

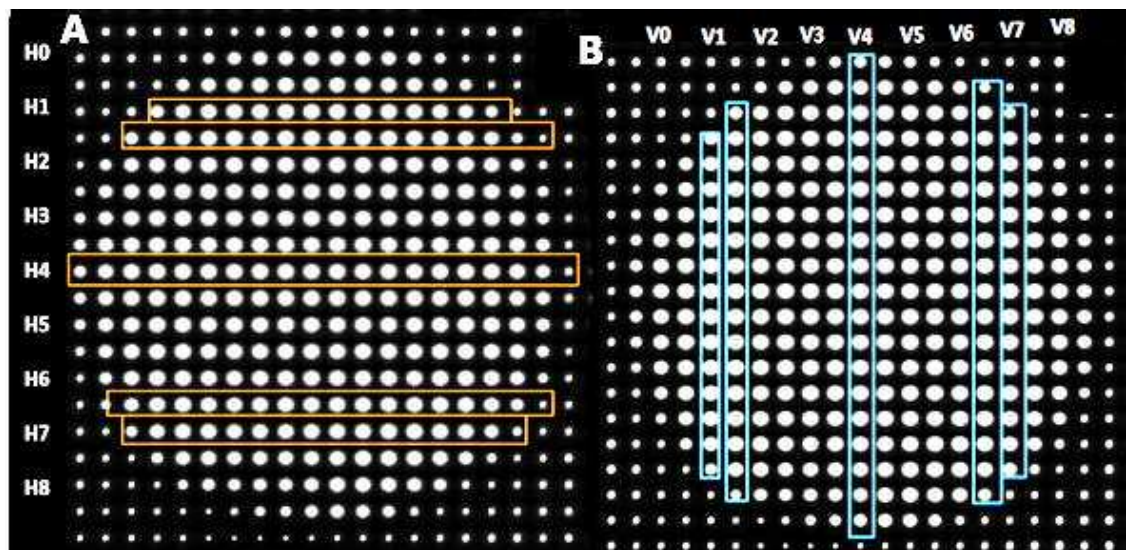


Figure 2-9: X-ray patterns from the porcine lens and the location of the horizontal and vertical meridian locations. The image (A) demonstrates the location of horizontal scatter patterns and their location (H mm). The image (B) demonstrates the location of vertical scatter patterns and their location (V mm).

2.2.6 Bragg spacing and H/FWHM ratio

After processing the original scan pattern for each lens, the peak position of either the interference function in the case of the porcine and Atlantic salmon lenses, and the anisotropic reflection from the European squid lenses, was processed in order to create the scattered intensity (y-axis) and reciprocal space q (x-axis) files using the “*Export to Text File*” menu option. This was done by performing a radial integration of the scattered intensity for each X-ray reflection being measured in each individual X-ray pattern. The peak fitting tool in “trace” perspective was then used to ascertain the position. To this end, the peak was identified on the graph.

The peak fitting tool was then used to find the peak position (corresponding to d , the average spacing between the crystallin proteins, Å), Full Width Half Maximum (to measure the width of a single broad reflection) for each pattern in fresh porcine, European squid, and Atlantic salmon lenses, and the height of each peak corresponding to the maximum X-ray intensity.

The peak positions, maximum intensity, and the FWHM were produced and the data were subsequently exported to Microsoft Excel® 2016 and MATLAB (Natick, Massachusetts: The MathWorks Inc., 2018) for further analysis. The Bragg spacing and H/FWHM ratio were determined to generate the following measurements:

2.2.6.1 Bragg spacing measurement

The average distance between the lens crystallins was measured from the peak’s position in the scatter pattern, i.e. I (the maximum scattered X-ray intensity) vs. q (reciprocal space), where each meridian was plotted across the lens from edge to edge

for fresh porcine, squid, and salmon mammal lenses. The distance between the two crystallins is $d = 2\pi/q$.

The Bragg equation is given as follows:

Equation 2.1

Where n is the order of diffraction, λ is the wavelength, d is the Bragg spacing and θ is half the diffraction angle. This equation allows d to be determined by measuring the scatter angle θ .

2.2.6.2 H/FWHM ratio measurement

The degree of order was measured in accordance with the measurements of the ratio of the high peak position and the FWHM of the lens crystallins within the equatorial meridians. The H/FWHM ratio of interference function spacing was obtained from the linear measurements of the SAXS data profile.

A high value of the ratio (such as would arise from a narrow peak with a high maximum intensity) indicates a higher level of ordering of the crystallin proteins at a particular point. NB: Due to the absence of an interference function in many of the individual patterns from both European squid lenses studied, it was decided to measure the Bragg spacing and H/FWHM of the intense anisotropic reflection.

2.2.7 Rotation of the anisotropic reflections

An attempt was made to measure the degree of rotation of the anisotropic reflections observed in the squid and salmon lenses. A new sub-routine of the DAWN 2.11.0 software was used to measure the predominant orientations within each SAXS pattern. The montage extracted from DAWN 2.11.0 depicted the X-ray reflection orientation's

real number from 0 to 180 degrees. The orientation's real numbers have been sorted into a grid according to the crystallin's actual geometric position within European squid and Atlantic salmon lenses. The data were then exported to Microsoft Excel application for further analysis according to the vertical meridians; at 0.5, 1.0, 3, 4.0, and 4.5 mm.

2.2.8 Statistical analysis

To investigate the ultrastructure of porcine, European squid, and Atlantic salmon lenses, the peak position and H/FWHM ratio were presented at different vertical and horizontal meridians to allow for the analysis of the differences between crystallin proteins in the cortex and nucleus areas. The data are presented as figures containing the average of the peak position and H/FWHM ratio in porcine, European squid, and Atlantic salmon lenses. All statistical analysis was completed using Microsoft Excel 2016 and Matlab 2017.

The study investigated changes in the Bragg spacing, if any, between the central nucleus and cortex areas along different lens meridians of the porcine, European squid, and Atlantic salmon lenses. All data were tested for normality using the Shapiro-Wilk test. While, normal data were tested using an unpaired *t*-test, Mann-Whitney U test was performed for non-normal data, at 5% significance level, along each vertical and horizontal meridians. All statistical analysis was completed using Microsoft Excel® 2016 and IBM SPSS 23 software packages.

2.3 Results

2.3.1 Individual X-ray scattering patterns and montages of patterns of the lens in pig, Atlantic salmon, and European squid

Figure 2-10 shows typical individual SAXS patterns from (A) European squid, (B) Atlantic salmon and (C) porcine lenses. The X-ray pattern from European squid lens (Figure 2-10 A) is characterised not only by an isotropic scattering of an interference function but also by intense anisotropic reflections. These intense anisotropic reflections were observed for the first time in a previous study by Regini, et. al. (2018). However, it was found that not all individual patterns displayed the interference function, this is discussed below.

Similarly, the Atlantic salmon lens (Figure 2-10 B) showed an interference function and intense anisotropic reflections. Compared to the European squid lenses, these reflections appeared narrower in width and closer to the backstop. An X-ray diffraction pattern from a porcine lens is shown in Figure 2-10 C. This is a typical pattern expected from a mammalian lens. The pattern is dominated by an interference function and showed no other structural sampling.

Figures 2-11 and 2-12 show a 2D Grid Scan montage from European squid lens with different expanded sections. Figures 2-13 and 2-14 show 2D Grid Scan montages with expanded views from an Atlantic salmon and porcine lens respectively. From the montages, it may be seen that a common feature among all three lens groups is that the intensities of individual X-ray patterns are greatest in the cortex area towards the periphery of the lenses. There is a decrease in the intensity toward the central nuclear area of the lenses. This change of intensity within different areas of the lens is more accentuated in European squid and Atlantic salmon lenses.

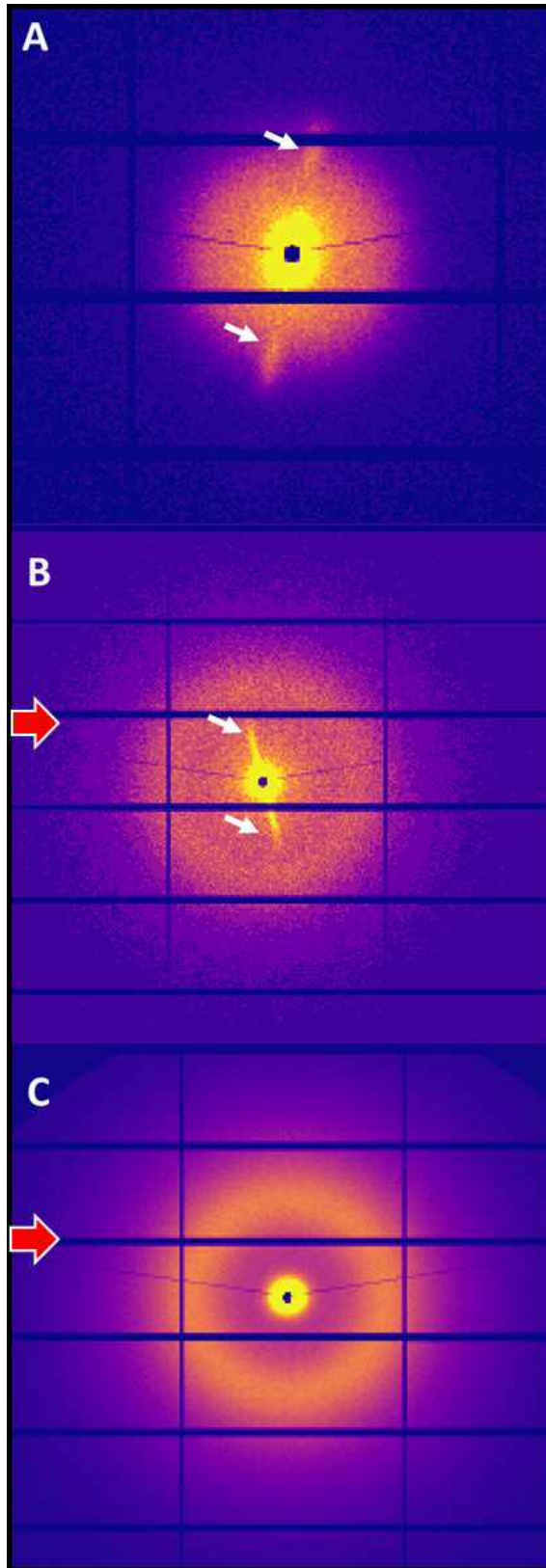


Figure 2-10: Typical SAXS patterns of (A) European squid, (B) Atlantic salmon, and (C) porcine lenses; white arrows indicate the anisotropic X-ray reflections and red arrows indicate the interference function.

The expanded section from the central area of the montage from the European squid lens (Figure 2-11) shows the striking feature that anisotropic reflections rotate around the centre of the pattern on either side of the vertical meridian of the lens. On the right-hand side of the meridian, the rotation is clockwise. Conversely, the rotation is anti-clockwise on the left-hand side of the vertical meridian of the lens. Figure 2-12 shows an expanded section of an outer cortex area of European squid lens. This demonstrates that the interference function was only detected in some individual patterns and not others. As can be seen, this reflection is much weaker than and those observed in the other groups. It may also be seen that it is a much larger ring occurring further away from the backstop than those found in Atlantic salmon or porcine lenses.

Figure 2-13 shows the expanded section from the central area of the montage from an Atlantic salmon lens. In a similar manner to that observed in European squid lens, the anisotropic reflections rotate around the centre of the pattern on either side of the vertical meridian of the lens. On the right-hand side of the meridian, the rotation is clockwise on the left-hand side of the vertical meridian of the lens.

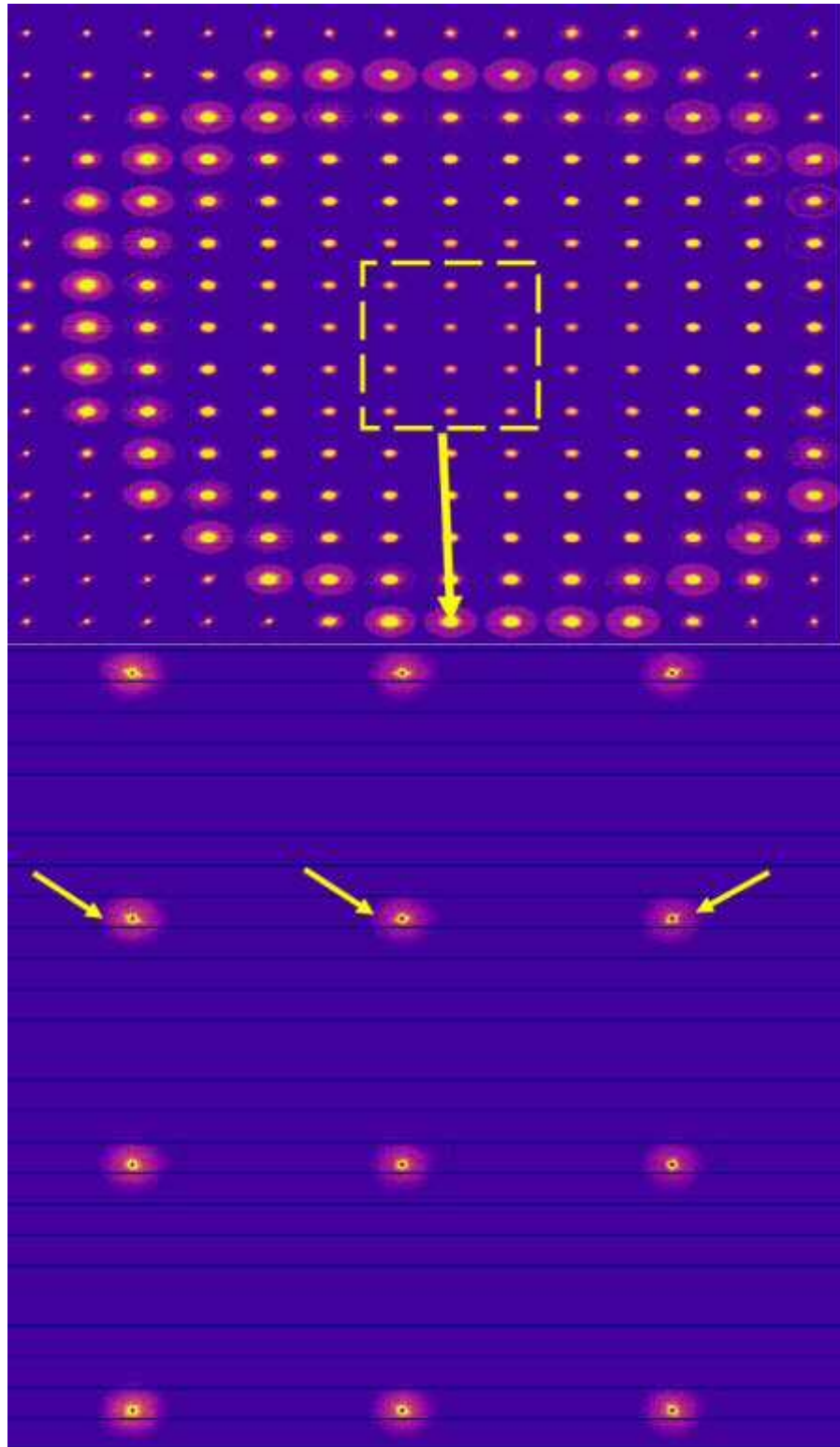


Figure 2-11: A 2D Grid scan montage of SAXS patterns at 0.5 mm intervals in horizontal and vertical meridians of an European squid lens with an expanded section showing the rotation of the anisotropic reflections (yellow arrows).

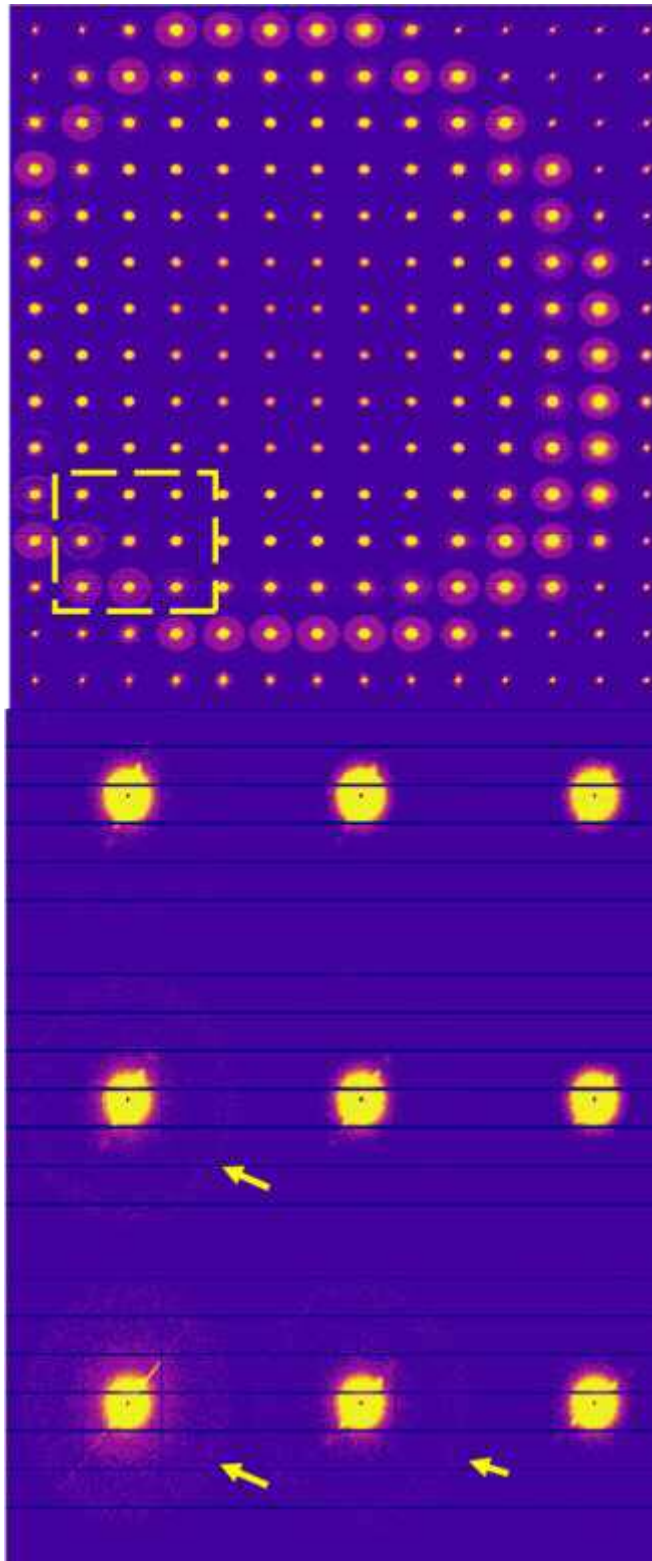


Figure: 2-12: A 2D Grid scan montage of SAXS patterns from European squid lens with an expanded section showing that it was only in some individual patterns that a faint interference function could be detected (yellow arrows), the patterns in the bottom left-hand corner in this case, with intervals at 0.5 mm along the lens horizontal and vertical meridians.

The montage of the porcine lens, Figure 2-13, displays the least variation of scattered X-ray intensity between the central nuclear and cortical peripheral areas. It was also found to have interference functions with the highest intensities relative to both European squid and Atlantic salmon lenses studied. The expanded view from the central region of the lens shows that there is no other structural sampling other than the interference function. This was found to be the case in all areas of the porcine lenses studied.

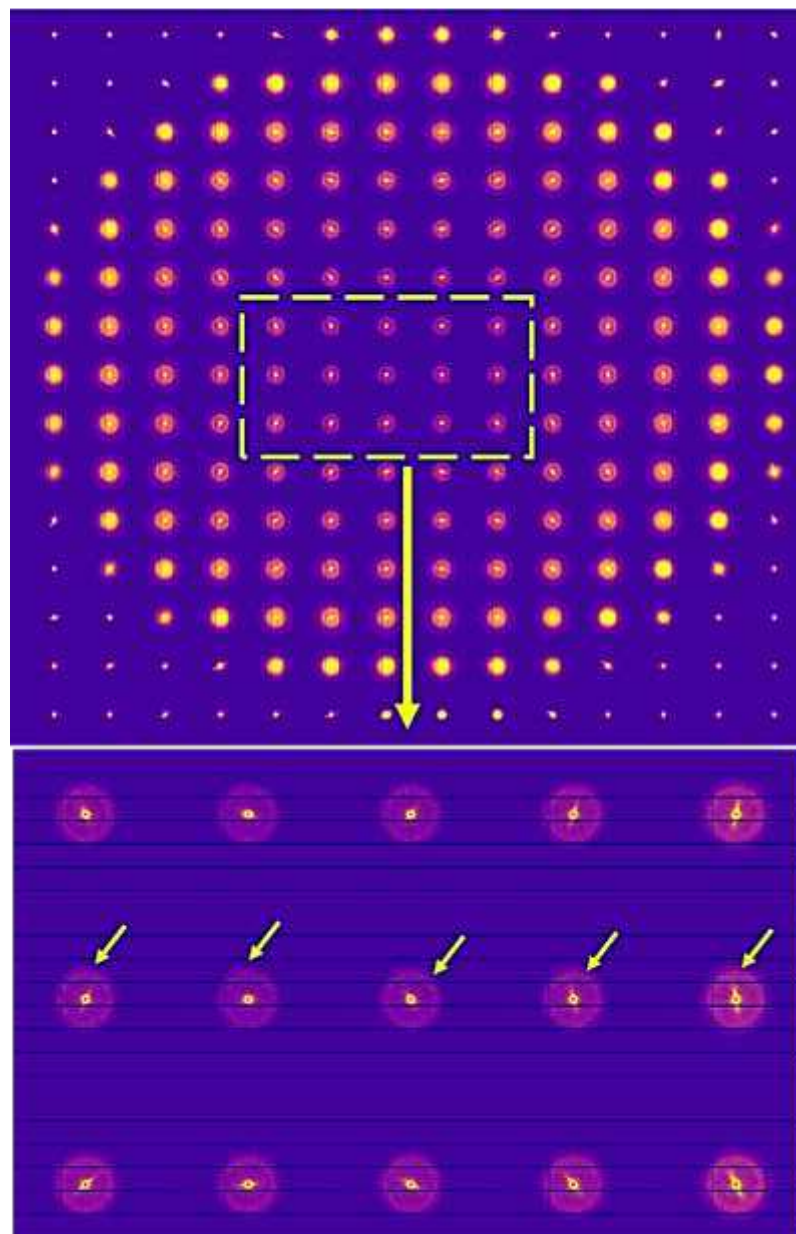


Figure 2-13: 2D Grid scan montage of SAXS patterns of an Atlantic salmon lens with an expanded section showing the rotation of the anisotropic reflections (yellow arrows).

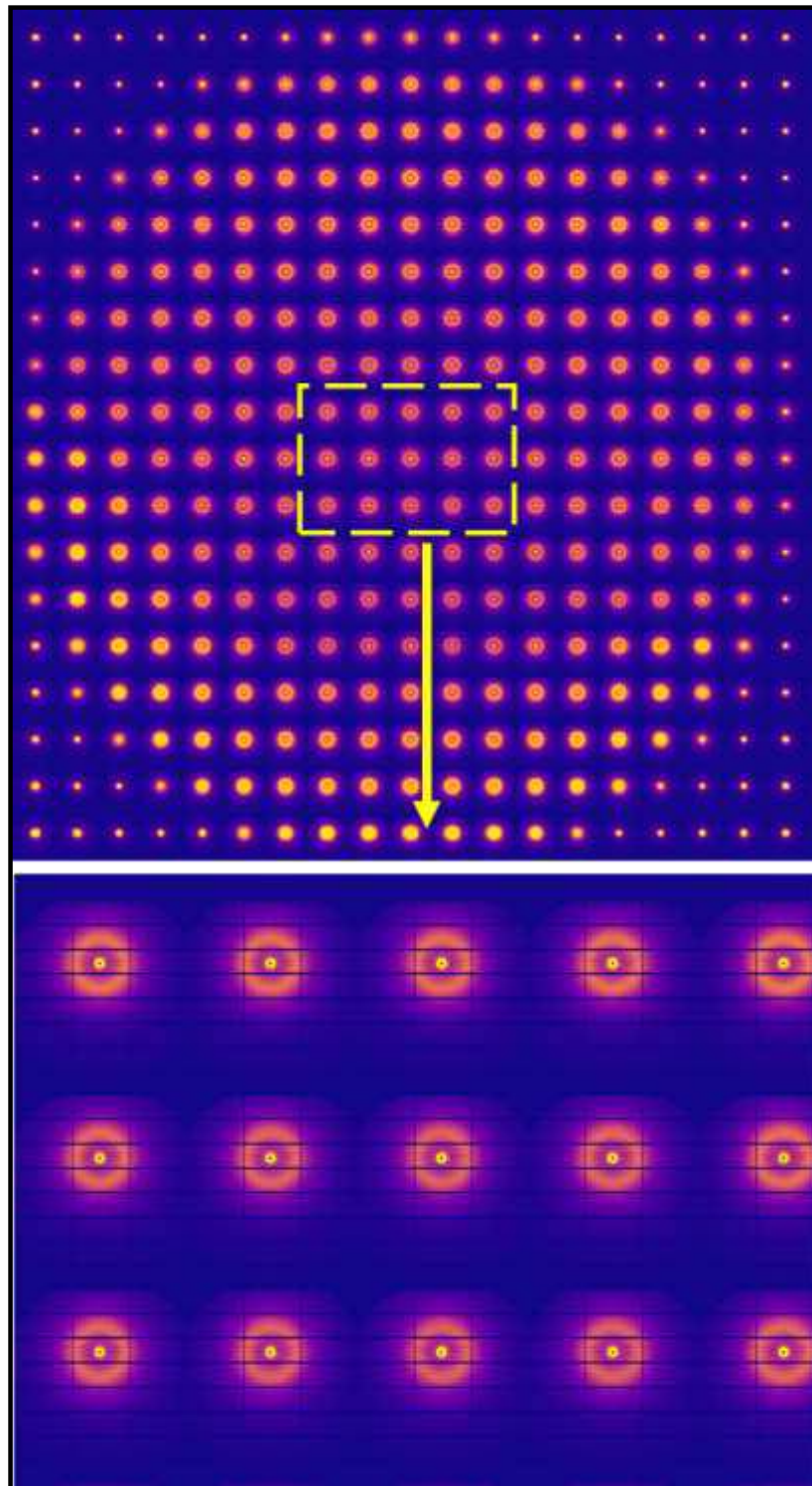


Figure 2-14: A 2D Grid scan montage of SAXS patterns from a porcine lens, with an expanded view of individual patterns.

2.3.2 The X-ray scattering intensity of the lens in pig, European squid, and Atlantic salmon

A difference in the total intensity of the scattered X-rays between the lens cortex region and the nucleus region occurred in European squid, Atlantic salmon, and porcine lenses. However, the scattered intensity profiles of European squid lens have been plotted from the anisotropic reflection. Changes in the scattered intensity as a function of the distance from scattering points, in pig, squid, and salmon are consistent with variations in protein concentration between the cortex and nucleus.

Figure 2-15 A showed a 3D plot of the intensity profiles from European squid lens plotted as a function of the lens diameter. These profiles were taken from a vertical section traversing down the central meridian of the lens. As can be seen, the scattered intensity peaks were highest and asymmetrical at the periphery of the lens at the outer edges of the cortex. The intensity of the peaks decreased and became more symmetrical towards the central nuclear region. Similarly, in Atlantic salmon lenses, the scatter intensity pattern in the centre of the lens was slightly less than at the lens edges (Figure 2-15 B). Figure 2-15 C showed typical intensity profiles from a porcine lens that similar to Atlantic salmon lens trends, except that the peaks remained more symmetrical towards the outer periphery.

In porcine case, the peak of the scattered intensity displayed the largest decrease moving away from the periphery towards the nucleus of the lens. The scattered intensity also maintains its symmetry toward the lens periphery (Figure 2-15 C). The interpretation of scattered intensity distributions from lenses is complicated as the total observed scattering involves contributions from a population of crystallins. The resultant pattern is, therefore, a function of different form and partial structure factors.

To analyse this complex signal, it was necessary to measure the total scattered intensity, then analyse data relating to both the average spacing between the crystallins and the order of the crystallins.

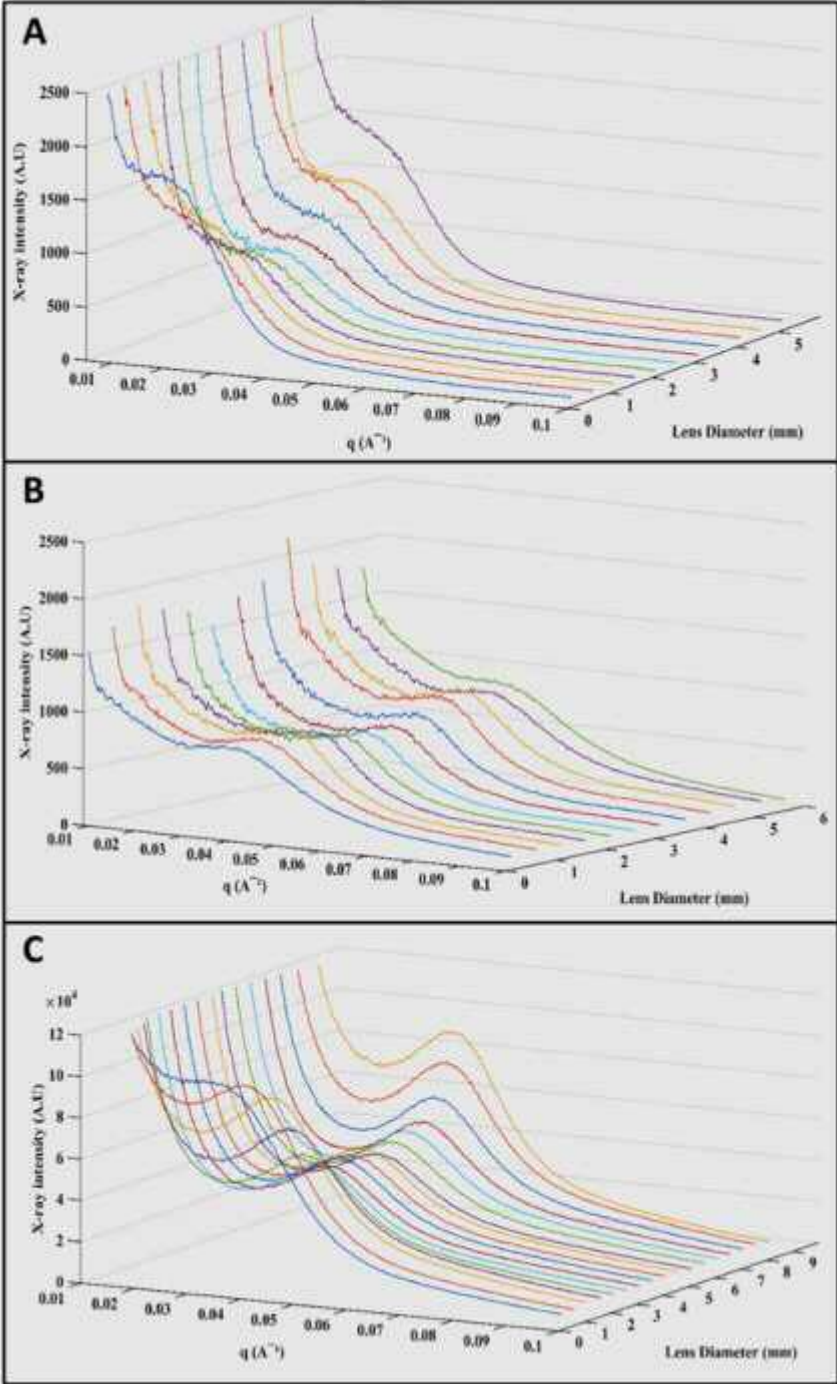


Figure 2-15: Intensity profile for the lens groups of animals through the middle meridian. The intensity profile for: European squid lens (A), Atlantic salmon lens (B) and porcine lens (C).

2.3.3 Bragg spacing and H/FWHM ratio for European squid, Atlantic salmon and porcine lenses

This study used SAXS to investigate the spatial distribution and ordering of crystallin proteins within different regions of European squid, Atlantic salmon, and porcine lenses. In order to investigate the change in the average distance between the crystallin proteins, X-ray scattering from the lenses of pig, squid, and salmon was measured at different vertical and horizontal meridians. The Bragg spacing of the anisotropic reflection in European squid lenses, the Bragg spacing of the interference function in Atlantic salmon and porcine lenses were measured. From the Atlantic salmon and European squid, at all meridians, the scattered X-ray intensity showed average a maximum peak at q , which corresponded to periodic density averages of for European squid and Atlantic salmon lenses, respectively.

Along the horizontal meridians within the cortex area, the anisotropic reflection's Bragg spacing in European squid lenses ranged from 37.4 to 38.2 nm. In Atlantic salmon lenses, the interference function's Bragg spacings were about half of those in the European squid lenses (Figure 2-16 A and B). In SAXS patterns along the vertical grid scan meridians within the cortex area, the Bragg spacings of the anisotropic reflections in European squid lenses were found to be about double those of the Atlantic salmon lenses (Figure 2-17 A and B) (see Table 2-2).

| Bragg spacing of horizontal meridians within lenses (Average \pm SD) (nm) | | | | | |
|---|----------------|----------------|----------------|----------------|----------------|
| | H 0.5 mm | H 1 mm | H 3 mm | H 4 mm | H 4.5 mm |
| European squid | 38.2 \pm 2.6 | 37.8 \pm 3.3 | 36.6 \pm 2.0 | 38.1 \pm 2.6 | 37.4 \pm 1.4 |
| | H 0.5 mm | H 1 mm | H 3 mm | H 4 mm | H 4.5 mm |
| Atlantic Salmon | 17.4 \pm 0.7 | 16.9 \pm 0.7 | 16.5 \pm 0.9 | 16.9 \pm 0.7 | 17.2 \pm 0.5 |
| | H 1mm | H 1.5 mm | H 4.5 mm | H 6.5 mm | H 7 mm |
| Porcine | 18.9 \pm 2.7 | 17.4 \pm 1.6 | 16.1 \pm 0.6 | 16.8 \pm 0.9 | 17.8 \pm 1.6 |
| Bragg spacing of vertical meridians within lenses (Average \pm SD) (nm) | | | | | |
| | V 0.5 mm | V 1 mm | V 3 mm | V 4 mm | V 4.5 mm |
| European squid | 38.0 \pm 1.7 | 36.6 \pm 1.9 | 36.3 \pm 1.6 | 37.4 \pm 2.1 | 36.4 \pm 2.0 |
| | V 0.5 mm | V 1 mm | V 3 mm | V 4 mm | V 4.5 mm |
| Atlantic Salmon | 17.5 \pm 1.1 | 16.9 \pm 0.7 | 16.4 \pm 0.6 | 16.9 \pm 0.4 | 17.3 \pm 1.1 |
| | V 1 mm | V 1.5 mm | V 4.5 mm | V 6.5 mm | V 7 mm |
| Porcine | 17.4 \pm 1.9 | 17.3 \pm 2.2 | 16.4 \pm 1.2 | 16.7 \pm 0.7 | 17.4 \pm 1.0 |

Table 2-2: Averages and standard deviations of the interference functions' Bragg spacing from meridians in the horizontal (H) and vertical (V) grids within the three animals, Bragg spacing of the anisotropic reflection in European squid lenses; Bragg spacing of the interference function in Atlantic salmon lenses; and Bragg spacing of the interference function in porcine lenses. The nucleus area is at H=3mm and V=3mm

For porcine lenses, the Bragg spacing for the interference function, from patterns along the horizontal grid scan direction ranged from 16.8 to 18.9 nm in the cortex area, and 16.1 nm in the nucleus area (Figure 2-16 C). The Bragg spacings along the vertical meridians of the porcine lens cortex as well as nucleus areas were found to be similar to those along the horizontal meridians (Figure 2-17 C) (see Table 2-2). Note that all the Bragg spacings provided are average values for the total number of lenses studied, from each of the creature/organism studied, at the same corresponding lens diameter along the horizontal and vertical meridians. Both vertical and horizontal meridians include the mid meridians (through the lens nucleus) and the equatorial meridians (through the lens cortex).

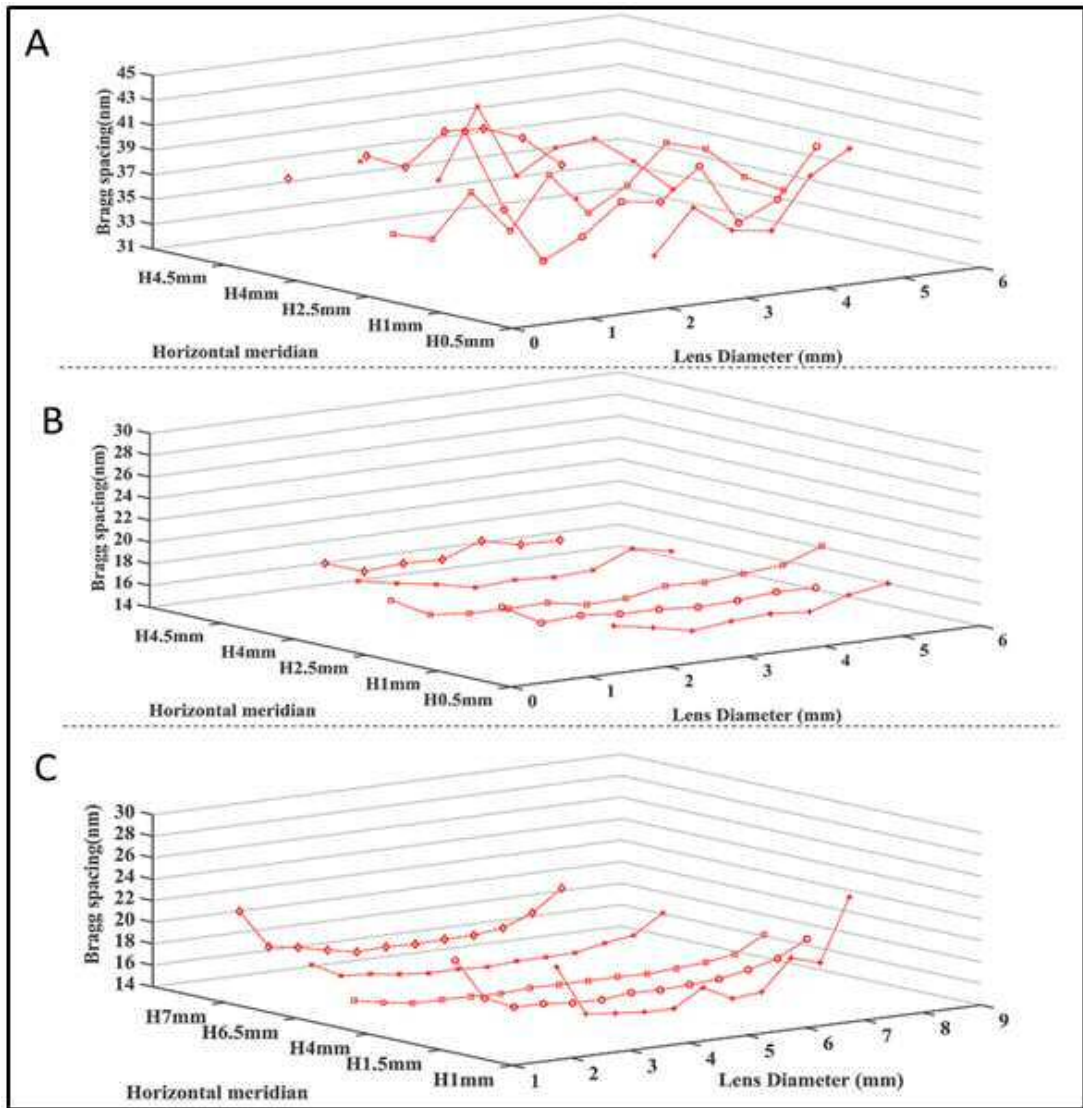


Figure 2-16: Average Bragg spacing in European squid, Atlantic salmon, and porcine lenses, derived from SAXS along the horizontal meridians in 2D scans. (A) Bragg spacing of the anisotropic reflection in European squid lenses; (B) Bragg spacing of the interference function in Atlantic salmon lenses, and (C) Bragg spacing of the interference function in porcine lenses.

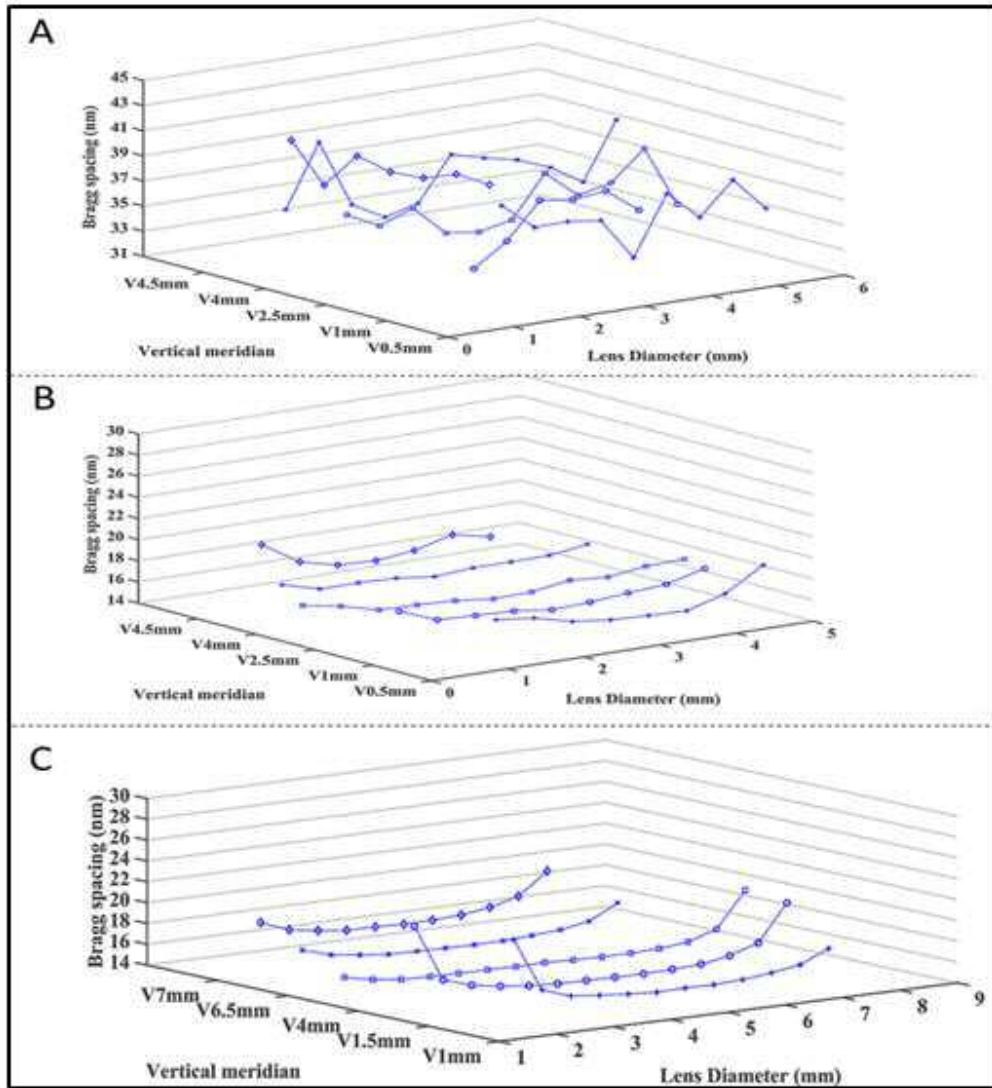


Figure 2-17: Average Bragg spacing derived from SAXS along the vertical meridians of a 2D scan. These charts show the average of Bragg spacing of the intense anisotropic reflection for European squid, Atlantic salmon, and porcine lenses: (A) Bragg spacing of the anisotropic reflection in European squid lenses; (B) Bragg spacing of the interference function in Atlantic salmon lenses; and (C) Bragg spacing of the interference function in porcine lenses.

The Bragg spacing in European squid lenses showed no significant difference between the central nuclear and cortex areas, along both the horizontal and vertical meridians. Further, while there was a significant reduction in the Bragg spacing in the Atlantic salmon lenses in the central nuclear area along the horizontal meridians at 0.5mm and at 4.5 mm ($p < 0.05$), there was no significant change at 1.0 and 4.0 mm. There was similarly no significant difference in the Bragg spacing between the central nuclear

and cortex areas in the Atlantic salmon lenses along all vertical meridians (Tables 2-2 and 2-3).

Lastly, in porcine lenses, there was a noticeable decrease ($p < 0.01$) in the Bragg spacing in the central nuclear area, both along the vertical and horizontal grid scan directions (Tables 2-2 and 2-3).

| The p-value of Bragg spacing difference between the central nuclear and cortex areas in horizontal meridians | | | | |
|---|------------|------------|-----------|------------|
| | H 0.5 mm | H 1 mm | H 4 mm | H 4.5 mm |
| European squid | p = 0.60 | p = 0.31 | p = 0.67 | p = 0.16 |
| | H 0.5 mm | H 1 mm | H 4 mm | H 4.5 mm |
| Atlantic Salmon | p = 0.01 | p = 0.07 | p = 0.31 | p = 0.03 |
| | H 1mm | H 1.5 mm | H 6.5 mm | H 7 mm |
| Porcine | p < 0.0001 | p < 0.0001 | p = 0.003 | p < 0.0001 |
| The p-value of Bragg spacing difference between the central nuclear and cortex areas in vertical meridians | | | | |
| | V 0.5 mm | V 1 mm | V 4 mm | V 4.5 mm |
| European squid | p = 0.92 | p = 0.63 | p = 0.37 | p = 0.73 |
| | V 0.5 mm | V 1 mm | V 4 mm | V 4.5 mm |
| Atlantic Salmon | p = 0.12 | p = 0.87 | p = 0.30 | p = 0.27 |
| | V 1 mm | V 1.5 mm | V 6.5 mm | V 7 mm |
| Porcine | p = 0.001 | p = 0.014 | p = 0.009 | p = 0.001 |

Table 2-3: The p-value of Bragg spacing difference between the central nuclear and cortex areas in the horizontal (H) and vertical (V) grids within European squid, Atlantic salmon and porcine lenses.

In order to investigate any change in the ordering of the crystallin proteins across the lens, the X-ray scattering from the porcine, European squid, and Atlantic salmon lenses were measured along different vertical and horizontal meridians and the H/FWHM ratios were calculated (where H is measured in arbitrary units of X-ray intensity and FWHM is measured in q units). Note that all the H/FWHM ratios given are average values for the typical lens studied from each of the organism/creature studied at the same corresponding lens diameter.

| H/FWHM ratio of horizontal meridians within lenses (Average± SD) | | | | | |
|---|----------|----------|----------|----------|----------|
| | H 0.5 mm | H 1 mm | H 3 mm | H 4 mm | H 4.5 mm |
| European squid ($\times 10^5$) | 1.1±0.3 | 1.1±0.7 | 0.7±0.4 | 0.9±0.4 | 1.3±0.6 |
| | H 0.5 mm | H 1 mm | H 3 mm | H 4 mm | H 4.5 mm |
| Atlantic salmon ($\times 10^4$) | 3.1±1.3 | 4.2±1.4 | 4.3±0.9 | 4.1±1.0 | 3.9±1.1 |
| | H 1 mm | H 1.5 mm | H 4.5 mm | H 6.5 mm | H 7 mm |
| Porcine ($\times 10^3$) | 3.7±0.4 | 3.6±0.5 | 3.7±0.6 | 4.1±0.6 | 3.9±0.5 |
| H/FWHM ratio of vertical meridians within lenses (Average± SD) | | | | | |
| | V 0.5 mm | V 1 mm | V 3 mm | V 4 mm | V 4.5 mm |
| European squid ($\times 10^5$) | 0.9±0.2 | 0.9±5.1 | 0.7±0.3 | 1.1±0.6 | 1.3±0.4 |
| | V 0.5 mm | V 1 mm | V 3 mm | V 4 mm | V 4.5 mm |
| Atlantic salmon ($\times 10^4$) | 3.2±0.4 | 4.4±1.0 | 4.1±0.9 | 4.4±1.3 | 3.9±1.1 |
| | V 1 mm | V 1.5 mm | V 4.5 mm | V 6.5 mm | V 7 mm |
| Porcine ($\times 10^3$) | 4.3±0.5 | 4.1±0.5 | 3.9±0.4 | 3.1±0.2 | 3.1±0.3 |

Table 2-4: The average and standard deviation of the H/FWHM ratio from patterns in the horizontal and vertical grids within the three groups of animals, H/FWHM ratio the anisotropic reflection in European squid lenses; H/FWHM ratio of the interference function in Atlantic salmon lenses; and H/FWHM ratio of the interference function in porcine lenses.

Along the horizontal and vertical meridians grid scans within the cortex area, the anisotropic reflection H/FWHM ratio in European squid lenses was $0.9 - 1.3 \times 10^5$, and the interference function's H/FWHM was $3.1 - 4.4 \times 10^4$ in the Atlantic salmon lenses (Figures 2-18 and 2-19 A and B) (Table 2-4).

In porcine lenses, along the horizontal and vertical grid scans within the cortex area, the interference function H/FWHM ratio was found to be between 3.1 and 4.3×10^3 (Figures 2-18 and 2-19 C). In the nucleus area, the interference function's H/FWHM ratio in the horizontal and vertical scans was 3.7×10^3 and 3.9×10^3 , respectively

(Figures 2-18 and 2-19 C). These data suggest that the H/FWHM ratio in the lens nucleus was relatively lower, when compared to the lens cortex in porcine, European squid and Atlantic salmon lenses (Table 2.4). (See Table 2-4). It should be noted that both the vertical and horizontal meridians include SAXS data derived from both the nucleus and cortex.

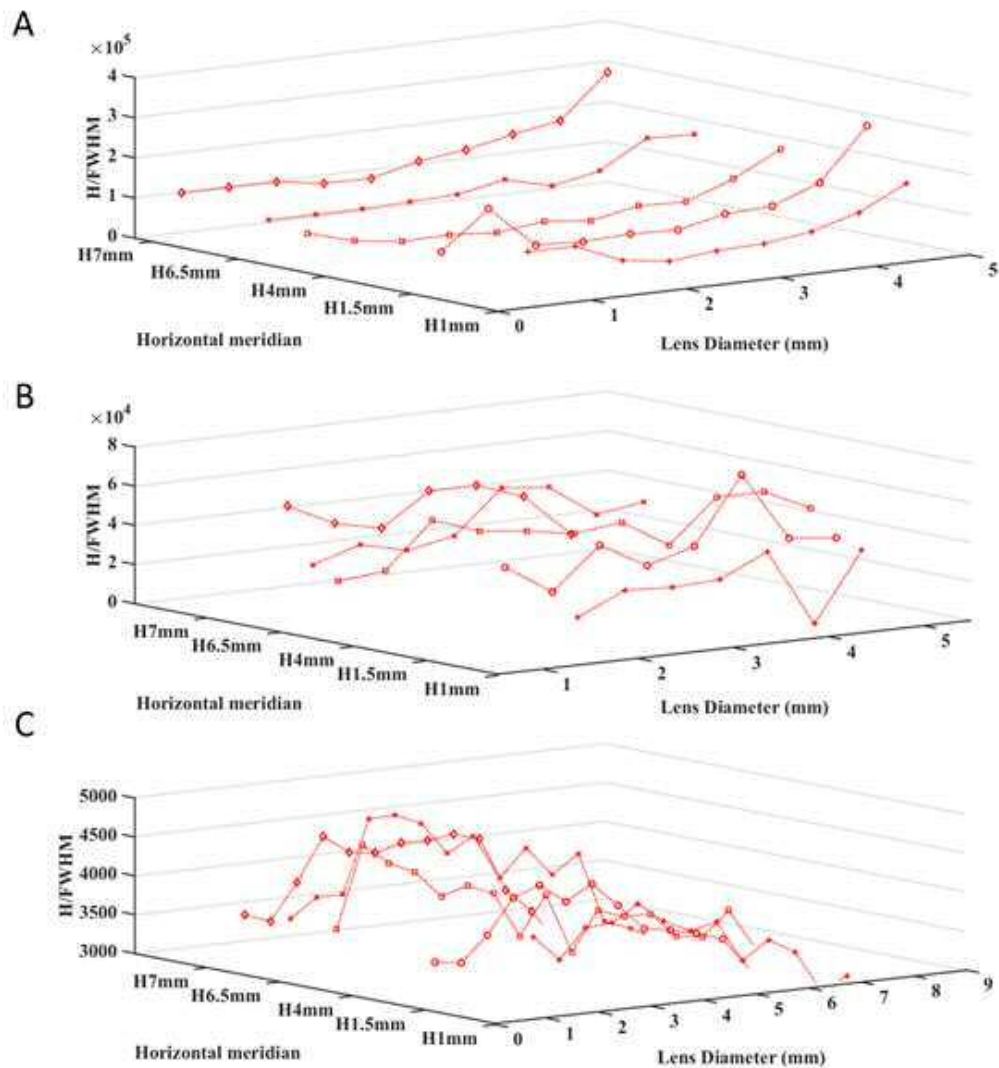


Figure 2-18: Average H/FWHM ratio derived from SAXS along the horizontal meridians of a 2D scan. These charts show the average of Bragg spacing for European squid, Atlantic salmon and porcine lenses: (A) H/FWHM ratio the anisotropic reflection in European squid lenses; (B) H/FWHM ratio of the interference function in Atlantic salmon lenses; and (C) H/FWHM ratio of the interference function in porcine lenses.

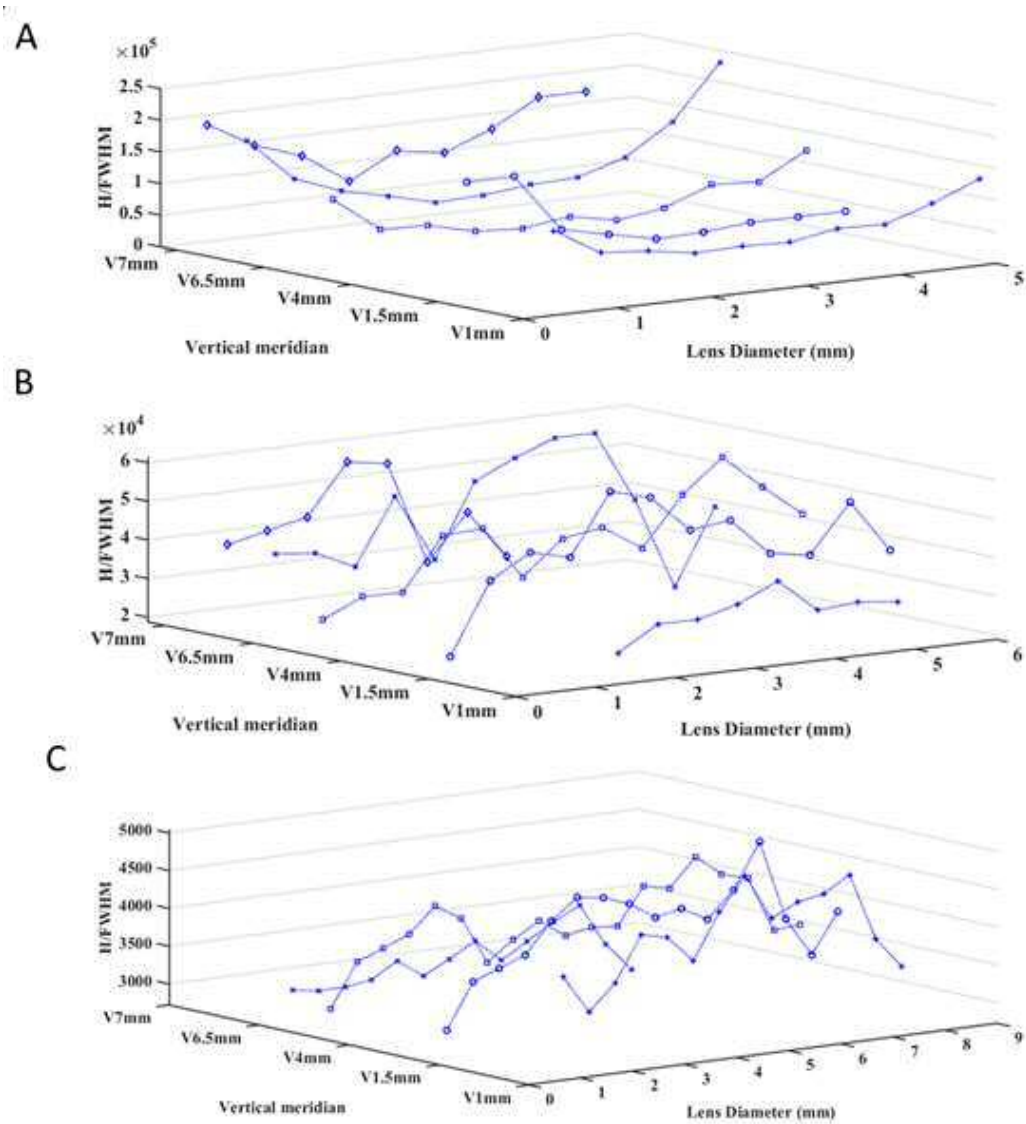


Figure 2-19: Average H/FWHM ratio derived from SAXS along the vertical meridians of a 2D scan. These charts show the average of Bragg spacing for European squid, Atlantic salmon and porcine lenses: (A) H/FWHM ratio the anisotropic reflection in European squid lenses; (B) H/FWHM ratio of the interference function in Atlantic salmon lenses; and (C) H/FWHM ratio of the interference function in porcine lenses.

2.4 Discussion

The vertebrate and mammalian lenses' ability to maintain their transparency in extremely cold/hot aquatic or terrestrial environments is indicative of the component structural protein's high stability (Wistow et al., 2005). The lens' ultrastructure is, in turn, a function of the evolutionary adaptations to the pig, squid, and salmon's respective visual environmental demands (Delaye & Tardieu, 1983; Wistow, 1993; Wistow et al., 2005). This study sought to both describe and better understand spacing and ordering of crystallin proteins or membrane structure in European squid, Atlantic salmon, and porcine lenses. To this end, SAXS was used to analyse the scattering elements in intact lenses within both the lens cortex and nucleus regions. This present study's data point to differences in the X-ray intensity profiles, Bragg spacing, and H/FWHM ratio between European squid, Atlantic salmon, and porcine lenses. This difference between pig, European salmon, and Atlantic squid may be a result of their respective visual environmental demands (Wistow, 1993).

2.4.1 The intensity profile of the lens in pig, European squid, and Atlantic salmon

The packing of the crystallin proteins and hence the protein concentration in the lens plays a significant role in the lens refractive index. The variations in density occur because these proteins form regions of lower and higher concentrations (Mirarefi et al., 2010). According to Delaye & Tardieu (1983), a high concentration of crystallins supports short-range interactions and reduces fluctuations in concentrations within lens cells, effectively minimising the optical medium's light scattering. This study established the existence of dissimilarities in the scattered intensity between the cortex and the nucleus regions in European squid, Atlantic salmon and porcine lenses.

From a functional perspective, the main optical difference between aquatic and terrestrial creatures is the cornea's negligible refractive (i.e. focusing) power in water. Out of water, the cornea is the eye's most powerful refractive interface. However, the lack of corneal focusing in aquatic environments means that the refractive power required of an eye lens in water is elevated to provide almost all of the focusing power, and as a result, such lenses tend to possess a pronounced spherical morphology compared with those of land or flying creatures/organisms (Sivak, 1983). From an optical perspective a high-powered spherical lens, if it were made of a material with a homogeneous refractive index, would lead to significant spherical aberration and distorted vision. To avoid this problem, many aquatic creatures/organisms have developed spherical lenses that have a graded refractive index profile (Pierscionek & Regini, 2012).

To achieve this, a radial gradient of lens protein concentration exists, higher in the centre of the lens. This results in a lens with a high refractive index at its centre and becomes lower towards the periphery. In the human lens, as in other mammalian lenses, the crystallin concentration is about 450 mg/ml in the central nucleus and 200 mg/ml in the outer layers of the cortex (Harding, 1991). By contrast, aquatic creatures/oragnisms have lenses with much higher protein content 900 mg/ml in teleost fish, for example (Mirarefi et al., 2010), and a steeper refractive index gradient. In a homogeneous refractive index lens, light is refracted at the lens surface and no further focusing occurs until the point at which the ray exits the lens. In a gradient index lens, however, light is continually focused as it passes through the lens. The contribution that the gradient index makes to the lens refractive power and, further, to the quality of the image that is subsequently produced at the retina, depends on the type of gradient, which varies across groups of creatures/organisms (Pierscionek & Regini,

2012). The gradient is, in turn, largely dependent on the nature of the lens crystallins composition and their concentrations. In many aquatic organisms/creatures, the steep refractive index gradient in the lenses allows for a small eye size, while at once ensuring extremely high sensitivity and excellent image quality.

As mentioned above, there is a marked decrease in the intensity between individual X-ray patterns towards the central nuclear area of the lenses. This trend occurred in pig, squid, and salmon, as can be seen in the 2D grid scan montages of Figure 2-14. The amount of scattered X-ray intensity is dependent on a number of factors, though here two main contributing factors have been considered. Firstly, despite all three of the different groups of lenses having different geometries, the thickness of the lenses increased markedly towards the central zone of each of the lenses. Such an increase in thickness in the sample will result in an attenuation of the X-ray beam entering the lens and the scattered X-rays leaving it. This would likely result in a decrease in the scattered intensity from the thicker areas of the lens, which was consistent with the observations in this study. Secondly, it was also mentioned above that the trend of the change in intensity within different areas of the lens was more accentuated in the aquatic lenses. This may be explained by the change in the protein density between the lens cortex and the nucleus. The amount of free bulk water in the lens will decrease with increasing protein concentration. This, in turn, will decrease the electron contrast between the amount of bulk water and the electrons in the sample. Due to the higher overall protein concentrations in the European squid and Atlantic salmon lenses, a greater change in scattered X-ray intensities would be expected between the cortex and the nucleus than that which occurs in porcine lenses.

The study's results suggest that there was higher crystallin density, reduced density fluctuations, and/or reduced changes in the orientation of optical material in the nucleus region, relative to the cortex region. The scattering intensity was generally lower in the nucleus region in in squid, salmon and porcine lenses.

The intensity profile in European squid lenses was clearly more asymmetric relative to the Atlantic salmon lenses. The profile from porcine lenses was even more symmetric relative to the Atlantic salmon lenses. This finding is indicative of differences in the crystallin shape (squid lens has separate back and front halves of different embryological origin), content and density in squid, salmon, as well as porcine lenses, and perhaps the possible role of the same in the respective lenses' suitability to the visual demands of their environments (Bloemendal, 1977; Cai et al., 2017; Delaye & Tardieu, 1983; West et al, 1995). The intensity profiles made it possible to measure the lens diameters. Accordingly, the diameters were 5.5 mm, 6.0 mm, and 9.0 mm for European squid, Atlantic salmon, and porcine lenses, respectively.

2.4.2 Bragg spacing and H/FWHM ratio for European squid, Atlantic salmon and porcine lenses

The vertical and horizontal meridians, both in the nucleus and cortex regions, are indicative of the crystallin composition and distribution of the intact lenses. The scatter patterns from both cortices and nuclei showed a characteristic scatter intensity that corresponded to a regular spacing between lens crystallins. This present study's results are consistent with past findings and the theoretical expectations, with respect to the

relatively lower scatter intensity in the cortex than the nucleus (Pierscionek & Regini, 2012).

The Bragg spacing of the anisotropic reflection from European squid lenses was much larger relative to both Atlantic salmon and porcine lenses. This will be discussed in the next section of this chapter. In Atlantic salmon and porcine lenses, the trend in the change in Bragg spacing of the interference function, across the diameter of the lenses, was seen to be almost the same in both the vertical and horizontal meridians. These spacings followed a symmetrical pattern in that they decreased towards the centre of the lens and then increased again to similar values and equal spacings along the second half of the meridian. These trends can be explained by a decrease in the nearest neighbour spacing between all the crystallin proteins in the lens with increasing protein concentration. The symmetrical trend may be explained by the symmetrical geometry of the lenses in a plane parallel to the optical axis, through which the X-ray beam passes.

The average values for the Bragg spacings from the interference functions from the Atlantic salmon and porcine lenses were very similar in both the vertical and horizontal meridians. At first, this seemed surprising, given the fact that European squid and Atlantic salmon lenses have much higher protein concentrations. However, one would expect the distances between the proteins to be smaller with higher concentrations. There are a number of factors which may influence the nearest neighbour spacing, including the age of the sample and the hydration of the sample. A comparison between Bragg spacings is only relevant if the lenses are age-matched, and of similar hydrations. In an intact mammalian lens, the reflection indexes to a spacing of about 16 nm, depending on the species, the age and hydration of the sample (Regini, 2009).

2.4.3 Rotation of the anisotropic reflection of the European squid and Atlantic salmon lenses

This study demonstrated, for the first time, the existence of an intense anisotropic reflection rotating around both meridians of a SAXS 2D grid scan from Atlantic salmon lenses. Similar reflections were observed from squid lenses in an earlier study by Regini, et al. (2018); however, this study did not measure the angle of orientation of the anisotropic reflection.

The most striking feature for the Atlantic salmon lens 2D grid scans was that the anisotropic reflections rotated around the centre of the pattern on either side of the meridian of the posterior segment of the lens. The anisotropic reflections appeared to rotate in a clockwise direction on the right of the vertical meridian of the lens, whereas they appear to rotate anti-clockwise on the left-hand side. It is clear that the Bragg spacing and H/HWFM of the isotropic reflections from the European squid lens did not follow the same trends as those taken from the porcine and Atlantic salmon lenses interference function. It is evident that some type structures with a high degree of ordering exist in Atlantic salmon lenses, but which either do not exist or are incapable of detection by this technique, in porcine lenses. This may be typical of European squid and Atlantic salmon lenses.

Regini et al. (2018)'s TEM investigation into similar structures in squid lenses, showed three distinct structures between each lamella of fibres. As shown in Figure 2-20, each lamella surface has a distinct thin band that is relatively darker than the interior, and there is another thin band of even darker contrast, signalled by red arrows, between adjacent structures. Regini et al. (2018) argue that these structures highly resemble the cell membrane complex (CMC), which is known to manifest in tissues (such as

hair/skin) as a pair of lipid layers separated by a channel of glycoproteins. In human lenses, the cell membrane contains inexplicably high cholesterol bilayers surrounded by liquid crystalline lipid membrane bilayers (Jacob, 2000). These membranes' organisation may contribute to the lens transparency and the gradual increase in membrane cholesterol towards the lens nucleus may be due to the need to maintain similar fluidity levels throughout the lens (Borchman et al., 1996). Worthington & Blaurock (1969) and Ohta et al. (2005) observed similarly strong diffracting anisotropic equatorial X-ray reflections in nerve and hair fibres, respectively. These were attributed to the lack of electron density in the CMC's central channel. The spherical curvature of the Atlantic salmon lens fibre cells' lamellae suggests that similar features may exist between them, accounting for the left- and right-handed rotation of the anisotropic reflection on either side of the meridian. Similar rotating low angle X-ray reflections have been observed in two-dimensional arrays of fibrillar systems, which are centrosymmetric in nature (Yagi et al., 2006). This study strongly suggests the presence of similarly highly ordered and regularly spaced structures in Atlantic salmon lenses, but future TEM studies will be needed to confirm them.

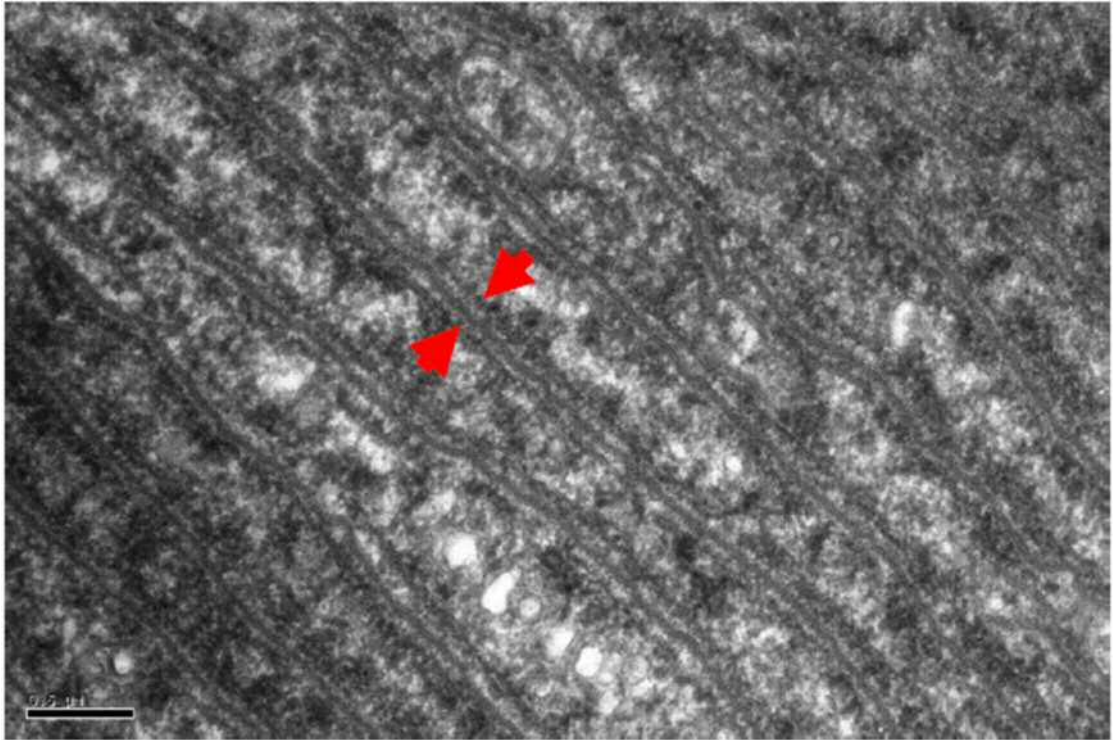


Figure 2-20: TEM image from the squid lens; (a section cut orthogonally to the direction of the fibres). Magnification 5000x (Regini et al., 2018).

2.5 Conclusion

This study sought to describe and understand the ultrastructure of the lens and the relationship of the crystallin proteins in different parts of the European squid, Atlantic salmon, and porcine lenses. To this end, X-ray scattering from intact lens cortex and nucleus, of a pig, European squid, and Atlantic salmon, were analysed. It is evident in this study's results that the lens crystallin profile is not identical in pig, squid, and salmon, which could be related to the respective species environments or their age. The scattered intensity was relatively lower in the lens nucleus than the cortex, in both terrestrial and aquatic species lens types.

Future work using lenses from donors at different ages and large samples are necessary in order to verify this study's results and/or clarify the actual nature of the relationship

between the lens ultrastructure and the lens' functional demands. The data also strongly indicated that Atlantic salmon lenses contain similar structures to the CMC identified previously by TEM in squid lens, which give rise to the rotating anisotropic reflections. Future work will need to include TEM studies to establish if CMCs are indeed present in the Atlantic salmon lens. It would also be of interest to conduct further small angle 2D grid SAXS scans and TEM studies on a range of lenses from different aquatic species to see if these structures are common to all or not.

Chapter Three

3 Measuring the crystallin proteins spacing and ordering between the in the accommodated and unaccommodated lens

The aim of this chapter is to determine if there is any change in the average distance between the crystallin proteins and their ordering in the accommodated and unaccommodated lens.

3.1 Introduction

The eye lens comprises concentric layers of fibre cells arranged in parallel to each other (Taylor et al., 1996; Pennisi, 2000; Kuszak et al., 2004; Andley, 2007; Tholozan and Quinlan, 2007; Cvekl and Ashery-Padan, 2014). Investigations into the lens molecular composition, which date back to the turn of the nineteenth century, mainly centre around finding the relationship between the lens optical features and its anatomy (Tardieu, 1988). These investigations established, among others, that the lens has a regular repetitive structure, its fibres are filled with protein, and this constituent protein comprises different types of crystallins. Undoubtedly, these progressions in research were largely possible because of the accompanying advancements in experimental technologies, including the development of Small Angle X-ray Scattering (*SAXS*).

The crystallins, which maintain the eye's transparency and give it its refractive power, comprise up to 90% of the eye's protein composition (Bloemendal, 1977; Tardieu, 1988; Slingsby et al., 1997; Bloemendal et al., 2004; Melinda et al., 2004; Andley, 2007; Yao & Xu, 2014). These proteins are both water-soluble (α -, β -, and γ -crystallin) and water-insoluble (lens cytoskeleton). The latter contains microtubules, microfilaments, and intermediate filaments, which maintain the lens shape and intracellular organisation (Quinlan & Prescott, 2004). Alpha-crystallins are molecular chaperones that prevent or slow down detrimental protein aggregation, effectively

maintaining lens transparency and refractive power (Ingolia and Craig, 1982; Piatigorsky, 1993; de Jong et al., 1993; Duncan et al., 2004; Andley, 2007). On the other hand, the β - and γ -crystallins, which belong to the same superfamily of proteins, may have a possible role in regeneration and repair of injured retinas (Fischer et al., 2008; Basha et al., 2012).

The accommodation draws on the lens' transparency and refractive power, as well as the activity of the ciliary muscle and the zonules, to focus far and near objects onto the retina (Schachar, 2006; Dubbelman et al., 2005; Santos-Neto and Alves, 2011; Schachar, 2012; Oveneri-Ogbomo and Oduntan, 2015). The lens provides a clear view from infinity (in the unaccommodated state) to less than 10 cm distance (in the accommodated state). The lens activity and molecular biology in accommodated and unaccommodated positions has been studied using the Scheimpflug imaging technique and many other techniques (Patnaik, 1967; Dickson and Crock, 1972; Brown, 1973; Dubbelman et al., 2005; Weeber and Van Der Heijde, 2008). SAXS has, for example, been used to characterise the structural organisation of the human lens fibre in both the nucleus and cortex regions (Robert et al., 2000). Similar studies into the lens structure in both the human and other animal groups (e.g. a frog, turtle, chick, pig, and bull) have also been undertaken (Krivandin et al., 1984; Krivandin and Feigin, 1990; Krivandin, 1997).

Studies into lens internal structural changes in the lens in the accommodated and unaccommodated states have, however, not been fully addressed by other researchers. This is in largely because the accommodation operates when living beings look at near (accommodated condition) and distant objects (unaccommodated condition). These types of experiments are, therefore, only achievable in *vivo*. However, the

investigation of the lens ultrastructure is nearly always conducted *ex vivo*, in which case, the lens can only be in an accommodated position (Croft et al., 2001).

This present study aims to use SAXS to investigate the lens crystallin spacing and ordering in both accommodated and unaccommodated positions. Specifically, the study used synchrotron X-ray scattering to determine the average distance between the spacing of lens crystallin proteins in accommodated and unaccommodated positions. The X-ray beam was passed through the lens crystallin proteins, following which it became scattered at a range of different angles. The X-ray detector then recorded the X-ray reflection's interference function, whose position is directly related to the average spacing between the lens crystallin proteins.

3.2 Materials and methods

3.2.1 Tissue sourcing

3.2.1.1 Porcine lens

Thirteen fresh and intact porcine eyes were obtained from a local abattoir, W. T. Maddock of Maesteg, Wales (UK). The porcine eyes were divided into two groups: fresh eyes ($n = 5$), and chemically fixed lenses ($n = 8$). The fresh eyes were kept refrigerated, then transported on ice in a cool box to the UK's national synchrotron facility, the Diamond Light Source, located at the Harwell Science and Innovation Campus, Oxfordshire. The lenses to be fixed were dissected and fixed on the same day of receipt.

3.2.2 Simulation of accommodation using a lens stretcher device

A lens stretching device can be used to simulate the accommodation. This study used two types of stretchers: the BIONIKO Manual Lens Stretcher (subsequently referred to herein as stretcher A) and the BIONIKO Manual Lens Stretcher V2 (stretcher B) both produced by BIONIKO Instruments, Arizona, USA. Although they are quite similar in design, the manufacturers state that stretcher B has an optimised geometry allowing 5.5 mm of stretch, compared to 4mm for stretcher A. Both stretchers employ the same radial stretching principal, and have eight stretcher arms which are attached to a ring that made it possible to radially stretch the lens by manually adjusting a central adjustment screw (Figures 3-1 A and 3-1 B).

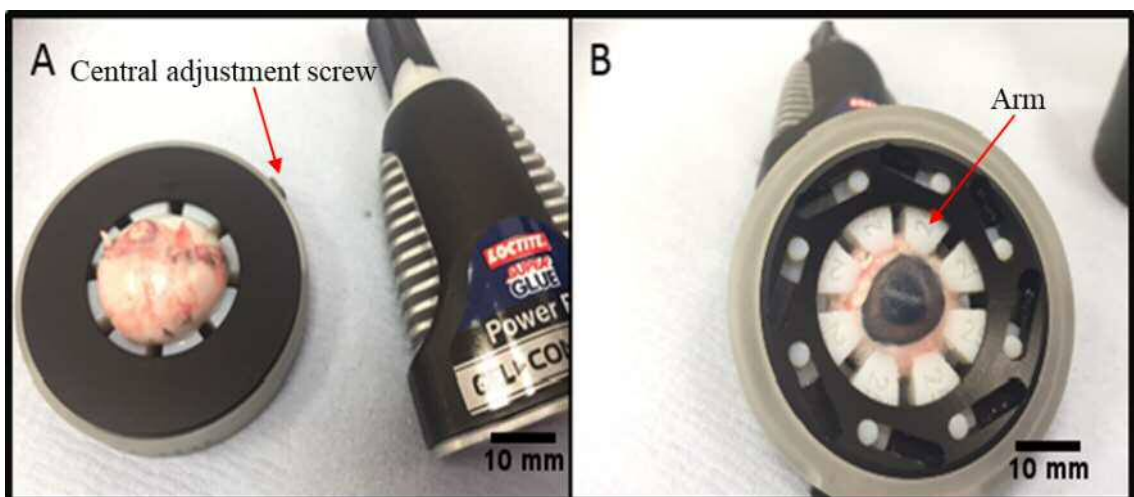


Figure 3-1: Correct positioning for attachment of the eyeball to the lens stretcher: (a) anterior and (b) posterior views.

3.2.2.1 Dissection of a porcine eye and positioning the lens in a stretcher

The dissection process for fixed lenses was undertaken within eight hours of the animal's death. The fresh lenses, on the other hand, were transferred to the Diamond Light Source laboratory and dissected within three days post-mortem.

In brief, the excess extra-ocular muscle and fat tissue surrounding the eye globe were removed. The scleral component of the eyeball, to which the device was to be attached, was dried by gently rolling it on a tissue paper, in order to ensure successful contact between the eye surface and the lens stretching device when the glue was applied. Loctite gel-based super glue (Henkel Limited, Winsford, UK) was applied to either the stretcher A or stretcher B in the un-stretched position and the eye globe was attached at the sclera and the lens stretching device (see Figures 3-1 A and B, showing the posterior and anterior views, respectively).

Firstly, the posterior eye tissues were removed (Figure 3-2 A). Using forceps, a scalpel, and a pair of scissors, the excess vitreous surrounding the lens was gently removed without disturbing the lens (see Figure 3-2 B).

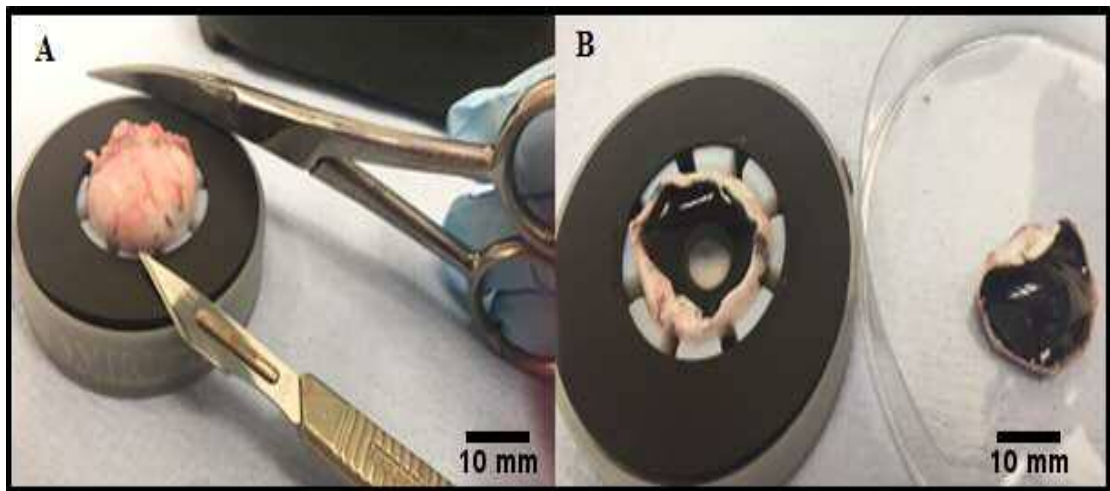


Figure 3-2: Posterior eye dissection: (A) point of a scalpel with Castroviejo scissor and (B) rest of sclera and vitreous.

The anterior chamber was dissected away from the adhered tissue in a three-step process. Firstly, the corneal button just inside the limbus was dissected away using forceps and a pair of corneal scissors. See Figure 3-3 A and 3-3B, which show the iris, visible after the cornea had been removed. Secondly, all the sclera that was not in

contact with the stretcher arms was carefully dissected away using a pair of thin sharp scissors. Lastly, the iris was removed and the lens was left suspended in the lens stretcher. Using the side lever on the lens stretcher device, the lens could remain unstretched (in the accommodated position) or stretched (in the unaccommodated position).

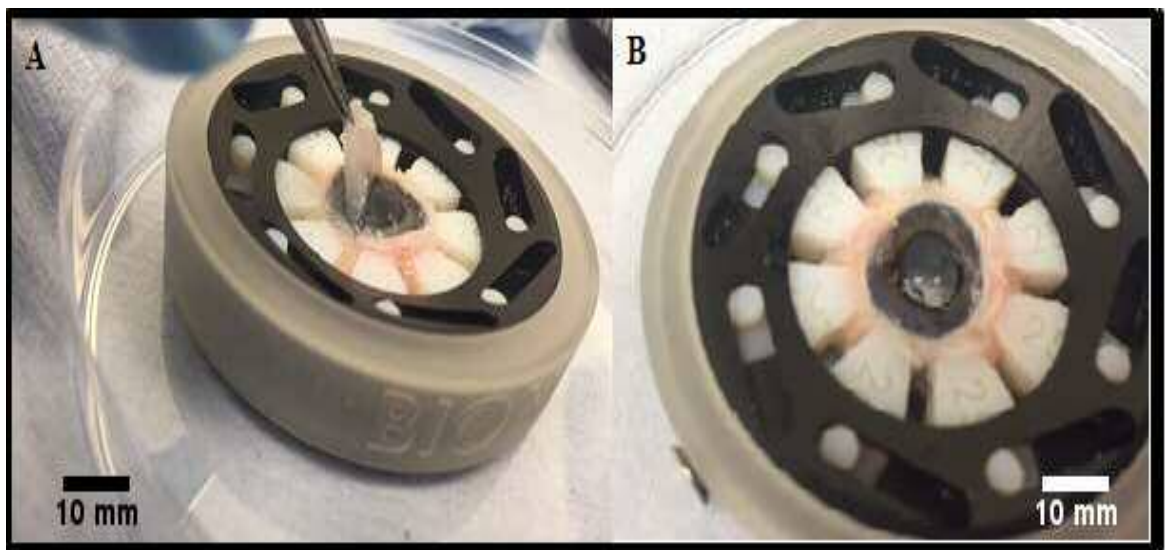


Figure 3-3: A) Corneal dissection and B) visible iris after cornea tissue removed.

3.2.3 Samples preparation

3.2.3.1 *Fresh porcine lenses*

For each fresh lens, the dissection process was undertaken within the stretcher device A, as set out in subsection 3.2.2.1. The process was undertaken at the Diamond Light Source laboratory within three days post-mortem.

3.2.3.2 Chemically fixed porcine lenses

The porcine lenses were divided into three groups: un-stretched lenses ($n = 3$), stretched lenses ($n=3$ using stretcher A), ($n=2$ using stretcher B). After dissection (following the same procedure as for fresh lenses stated above), all the lenses were, whilst still suspended in the stretching device, immersed in 4% paraformaldehyde in 0.2M phosphate buffer for seven days. They were then washed three times in 0.1M phosphate buffer pH 7.4. The lenses were removed from the stretcher device and immersed in a fresh gel of 1% Agarose. All lenses were then stored at 4°C for approximately two weeks before being transferred to the Diamond Light Source laboratory.

3.2.4 Mounting of samples for small angle X-ray scattering

3.2.4.1 Preparing fresh porcine samples

All the SAXS data were collected using the Diamond Light Source's *Beamline I22*. Fresh lenses, within the stretching device, were wrapped in cling-film to dehydration during exposure to X-rays. Each of the fresh lenses in lens stretcher A was clamped onto a controlled motorised stage with the anterior lens surface facing the incident X-ray beam. After collection of SAXS patterns from the unstretched lens, the device was altered to the stretched configuration, and the scan repeated.

3.2.4.2 Preparing fixed porcine samples

Each chemically fixed lens was wrapped in cling film and placed into a Perspex sample holder with mylar windows. As with the fresh lenses, the sample holder was clamped onto the motorised stage with the lens anterior surface facing the incident X-ray beam.

3.2.5 Small angle x-ray scattering

The X-ray scatter patterns were collected from each lens to acquire 20 x 20 2D grid scans, as described in Chapter 2; therefore, each sample generated 400 individual X-ray patterns.

3.2.5.1 Lenses Montage

After the data for each individual X-ray pattern were processed and the backgrounds subtracted, the montage of the SAXS patterns acquired from each lens was created using *DAWN*® software. A total of 4000 individual X-ray patterns were acquired for the fresh lenses and 3200 for the chemically-fixed lenses. The desired vertical and horizontal meridians in each montage were indicated as described before in subsection 2.2.6.2. The Bragg spacing and H/FWHM ratio were analysed as described previously in section 2.2.7.

3.2.6 Statistical analysis

To investigate the ultrastructure of both fresh and fixed porcine lenses, the Bragg spacing and H/FWHM ratio were determined at different vertical and horizontal meridians (through lens nucleus, lens cortex) to compare between crystallin proteins in the cortex and nucleus areas within fresh and fixed porcine lenses. The average Bragg spacing for both horizontal and vertical patterns were calculated and plotted separately. However, the typical H/FWHM ratio for both horizontal and vertical meridians were calculated and plotted separately. All statistical analysis was completed using Microsoft Excel® 2016 and MATLAB (Natick, Massachusetts: The *MathWorks* Inc., 2018).

The study investigated the ultrastructural changes, if any, between stretched and un-stretched positions, in the different meridians (through lens nucleus, lens cortex) of the fresh porcine lenses and the fixed porcine lenses. The study compared the Bragg spacing between un-stretched and stretched lenses at different lens meridians of the fresh porcine lenses and the fixed porcine lenses. All data were tested for normality using the Shapiro-Wilk test. While normal fresh lenses data were tested using a paired *t*-test, non-normal data were tested using a Wilcoxon test with a significance level of $p < 0.05$ for each vertical and horizontal meridians. For the fixed lenses, data were similarly tested for its normality using the Shapiro-Wilk test. Subsequently, normal data were tested using an unpaired *t*-test, while the Mann-Whitney U test was performed for non-normal data with a significance level of 5% in each vertical and horizontal pattern. The Bragg spacing was calculated to make comparisons between un-stretched and stretched lenses depending on the lens types (fresh and fixed lenses). All statistical analysis was completed using Microsoft Excel® 2016 and IBM SPSS 23 software packages.

3.2.7 Hypothesis

This study hypothesised that if there were any structural changes during the accommodation process at the molecular level, then these could be measured as changes in the Bragg spacing. Any changes occurring at the cellular/fibre level, on the other hand, could be identified by changes in the X-ray intensity profiles.

3.3 Results

3.3.1 Individual X-ray scattering patterns and montages of patterns of fresh and fixed lenses

Figure 3-4 shows typical individual SAXS patterns from (A) fresh porcine lens and (B) fixed porcine lens in un-stretched position. As described before for a porcine lens, the pattern is dominated by an interference function and show no other structural sampling. The obvious difference between the two patterns is that the interference function was much more diffuse, less intense and slightly larger in the X-ray pattern from the fixed porcine lens than the fresh lens.

Figure 3-5 (A) and (B) shows a 2D grid scan montage with expanded views from un-stretched fresh and fixed lenses respectively.

From the montages, it could be seen that a common feature in both fresh and fixed samples was that the intensities of individual X-ray patterns were at their most intense in the cortex area, towards the lens periphery (Figure 3-5). There was a marked decrease in the intensity toward the lens central nuclear area. This change in intensity within different areas of the lens was more accentuated in the fixed lens.

The montage of the fresh porcine lens, figure 3-5 (A), displays the different variations in the scattered X-ray intensity between the central nuclear and cortical peripheral areas. The expanded view from the central region of the lens shows that there is no other structural sampling other than the interference function. Similarly, the montage of the fixed porcine lens, figure 3-5 (B), shows the high variation of scattered X-ray intensity between the central nuclear and cortical peripheral areas. It was also found to have interference functions with fairly high intensity, though lower than that from the

fresh lenses. The magnified view from the central region of the lens shows that there was no other structural sampling other than the interference function. This was found to be the case in all areas of the fresh and fixed porcine lenses studied.

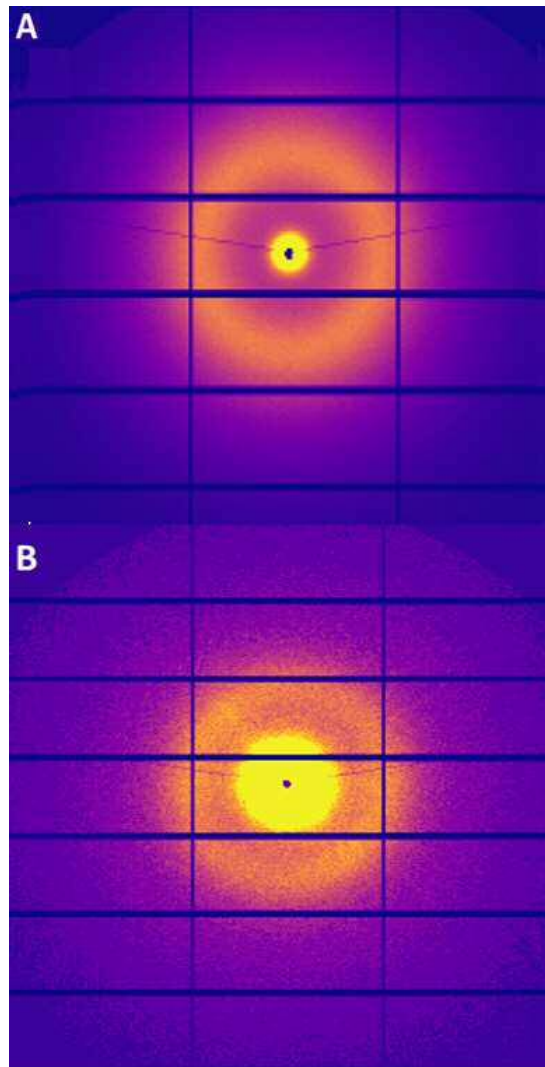


Figure 3-4: Typical individual SAXS patterns from (A) un-stretched fresh porcine lens and (B) un-stretched fixed porcine lens.

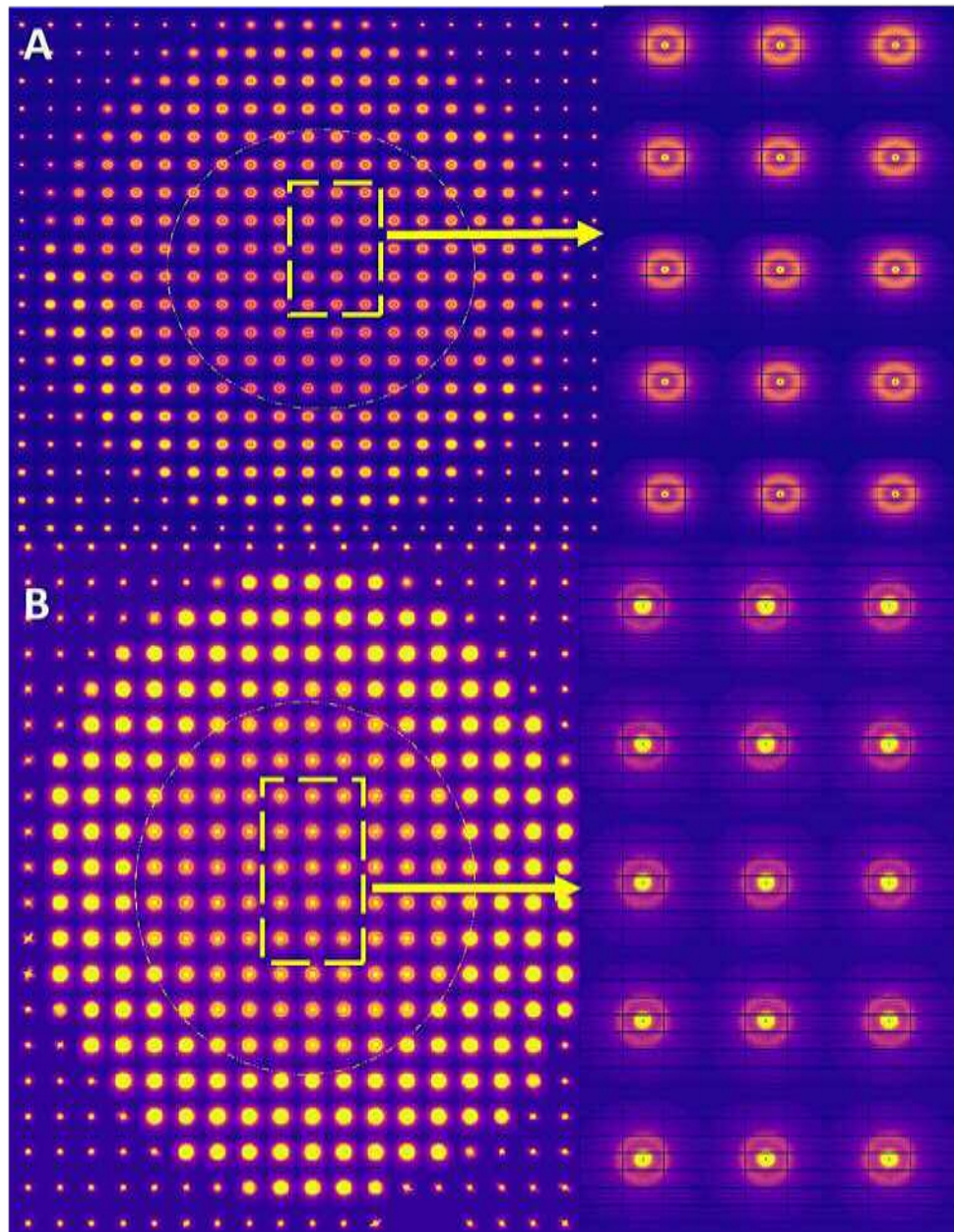


Figure 3-5: A 2D Grid scan montage of SAXS patterns with a magnified view of individual patterns from an un-stretched fresh porcine lens (A) and from an un-stretched fixed porcine lens. The nucleus areas in both images were marked within circular dotted lines in the scan montage for fresh/fixed lenses.

The X-ray scattering intensities of fresh and fixed lenses in both un-stretched and stretched positions were analysed. A difference in the total intensity of the scattered X-rays between the lens cortex region and the nucleus region occurred in fresh and fixed porcine lenses (Figure 3-6 and Figure 3-7). Changes in the scattering intensity as a function of the distance from scattering points, in fresh and fixed porcine lenses are consistent with variations in protein concentrations between the cortex and nucleus.

Figure 3-6 shows a 3D plot of typical intensity profiles from the fresh porcine lens in both the stretched and un-stretched positions. In both cases, the peak of the scattered intensity showed obvious increases in the intensity on each side of the lens, and then slightly diminished in a similarly symmetrical manner towards the lens centre. However, the relative difference in the peak heights from the periphery of the lens to the centre appeared greater in the un-stretched state than in the stretched state.

In fixed porcine lenses (Figure 3-7), the overall observed scattered intensity was much lower compared to the fresh lenses, even though both specimens showed symmetrical patterns in the scatter intensity from the periphery to the cortex. In both the stretched and un-stretched states the difference between the maximum peak heights and those at the centre was much greater than those seen in fresh samples. The maximum intensities occurred much closer to the periphery of the lens than in those from the fresh lens. However, in common with the fresh lens, the relative difference in the peak heights from the periphery of the lens to the centre appears to be greater in the un-stretched state.

The crystallin lens scatter intensity pattern is slightly complex to interpret because it depends on nature and number of component crystallins. The resulting pattern reflected the lens of different form and partial structural factors. Analysing this

complex signal required that the total scattering intensity was measured, followed by an analysis of data relating to both the spacing between the crystallins and the ordering of the crystallins

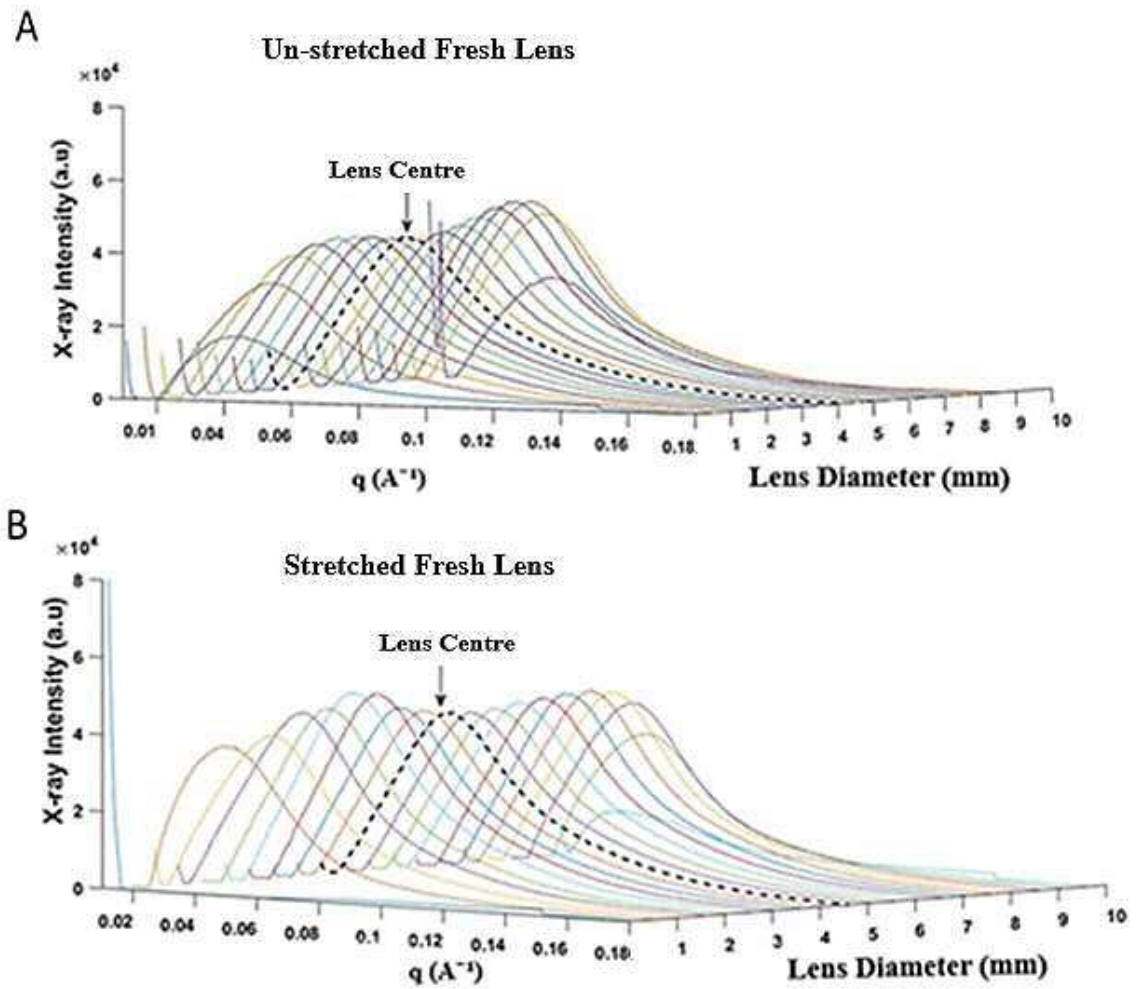


Figure 3-6: The middle meridian for the lens crystalline density plotted I versus q for the fresh lens: (A) un-stretched lens; (B) stretched lens.

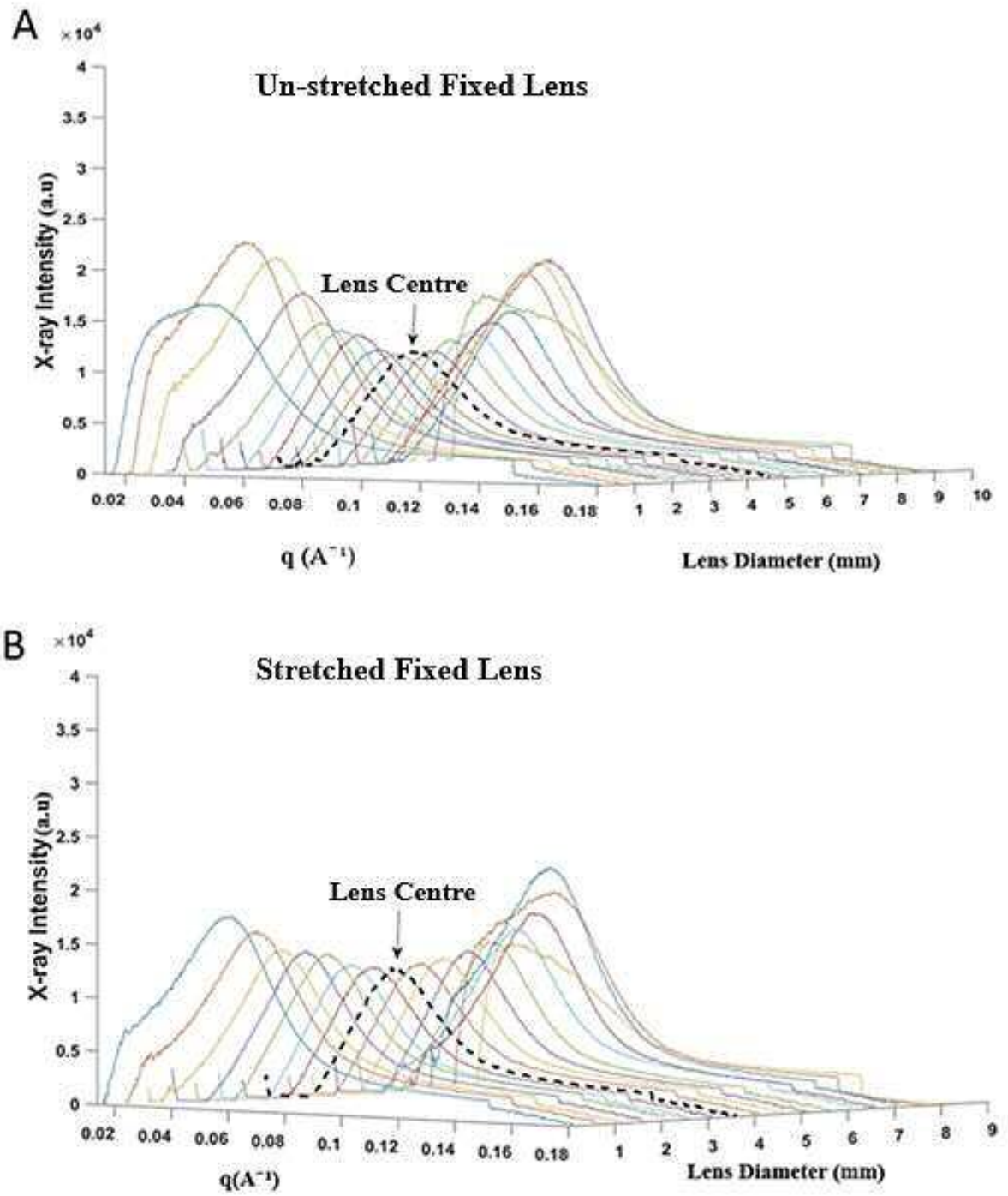


Figure 3-7: The middle meridian for the lens crystalline density plotted q vs I for fixed lens: (A) un-stretched; (B) stretched lens.

3.3.2 Bragg spacing and H/FWHM ratio for fresh and fixed lenses in both un-stretched and stretched positions

This study used SAXS to investigate the spatial distribution and ordering of crystallin proteins within different regions of fresh and fixed lenses in both un-stretched and stretched positions. In order to investigate the change in the average distance between the crystallin proteins, the X-ray scattering from the lenses from fresh in both positions (un-stretched and stretched) and fixed samples in both positions (un-stretched and stretched; stretcher A and B) were measured at different vertical and horizontal meridians across each lens. The Bragg spacing in all lenses was also measured (see Table 3-1).

| Horizontal meridians within fresh porcine lenses (Average \pm SD) (nm) | | | | | |
|--|----------------|-----------------|----------------|-----------------|----------------|
| | H 1 mm | H 1.5 mm | H 4 mm | H 6.5 mm | H 7 mm |
| Un-stretched | 18.1 \pm 0.9 | 18.5 \pm 3.0 | 16.3 \pm 0.8 | 17.1 \pm 1.3 | 17.8 \pm 1.8 |
| Stretched | 17.8 \pm 2.1 | 17.8 \pm 3.2 | 16.5 \pm 1.3 | 18.0 \pm 3.5 | 18.1 \pm 2.2 |
| Vertical meridians within fresh porcine lenses (Average \pm SD) (nm) | | | | | |
| | V 1 mm | V 1.5 mm | V 4 mm | V 6.5 mm | V 7 mm |
| Un-stretched | 18.9 \pm 2.7 | 17.4 \pm 1.6 | 16.1 \pm 0.6 | 16.8 \pm 0.9 | 17.8 \pm 1.6 |
| Stretched | 17.4 \pm 1.9 | 17.3 \pm 2.2 | 16.4 \pm 1.2 | 16.7 \pm 0.7 | 17.4 \pm 1.0 |

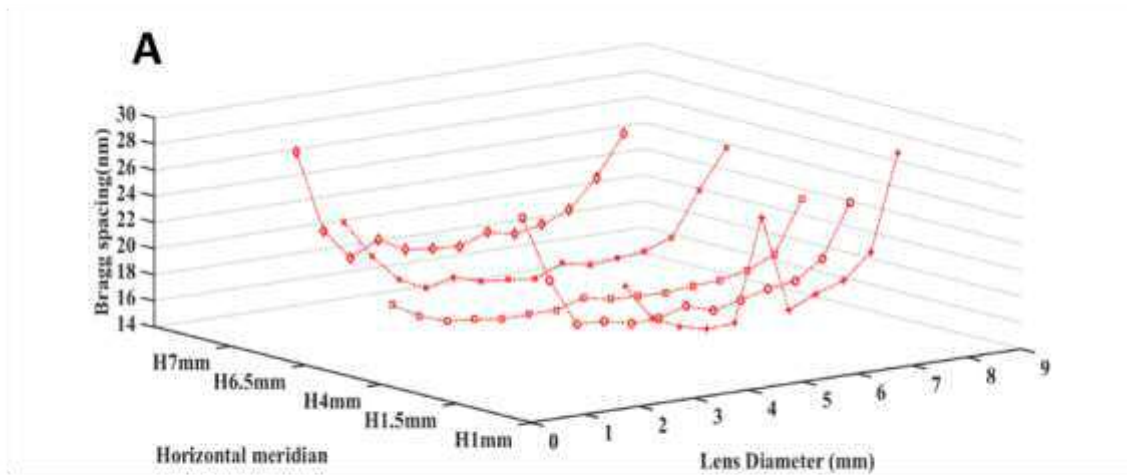
Table 3-1: Average and standard deviation of the interference functions Bragg spacing's from patterns in the horizontal (H) and vertical (V) grids within the fresh porcine lenses in both un-stretched and stretched positions.

The Bragg spacings for fresh lenses were plotted from a number of horizontal or vertical patterns every 0.5 mm across the 2D scan, presented as typical charts in stretched and un-stretched positions (Figure 3-8 and Figure 3-9 respectively). The Bragg spacing averages for the five fresh lenses were similarly depicted from both horizontal and vertical patterns, for both un-stretched and stretched lenses (Figures 3-10 and 3-11). Note that all the Bragg spacings given are average values for the total number of fresh lenses studied from both positions; un-stretched and stretched lenses at the same corresponding lens meridian in the horizontal and vertical directions.

The Bragg spacings in fresh, un-stretched and stretched lenses, measured from the horizontal and vertical patterns within the cortex area were plotted at 1, 1.5, 4, 6.5 and 7 mm (Figure 3-10 and 3-11[A] and [B]). In the central nuclear area (4mm), the Bragg spacings in the un-stretched and stretched lenses ranged from ~16.1-16.4 nm and ~16.3-16.5 nm, respectively.

The Bragg spacing in the central nuclear area, in all the fresh porcine lenses included in this study, from both vertical and horizontal grid scan directions, was found to be lower between lens meridians of 3 and 6 mm relative to the spacing in the cortex area. The 2D intensity profiles in unstretched and stretched fresh lenses indicate that there are clear changes between the average distance between crystallins across the lenses which are very similar in value in both the horizontal and vertical directions, However, there seems to be no significant change the overall values from the periphery to the nucleus between the stretched and un-stretched states.

Un-Stretched Lens



Stretched Lens

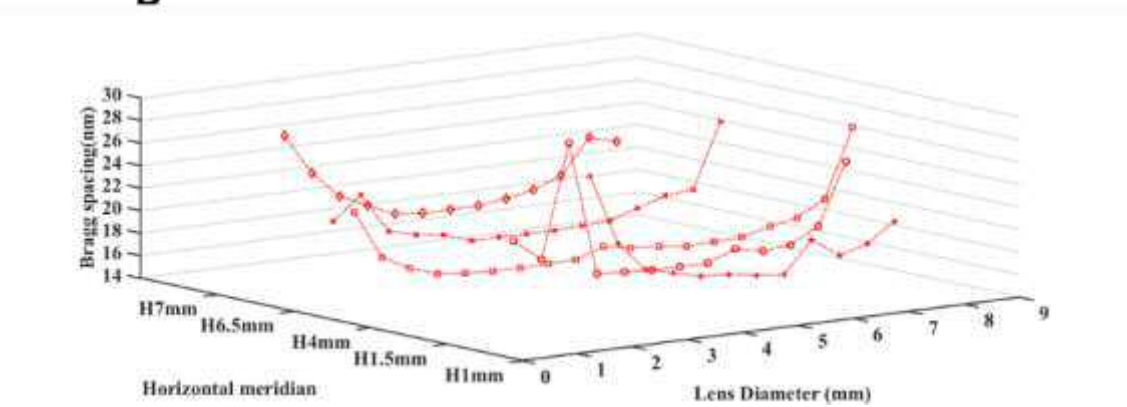


Figure 3-8: Typical Bragg spacing derived from SAXS patterns along the Horizontal meridians in a 2D scan. These charts show the typical Bragg spacing for un-stretched and stretched fresh porcine lenses. (A) Bragg spacing of the un-stretched fresh lens (B) Bragg spacing of the stretched lens.

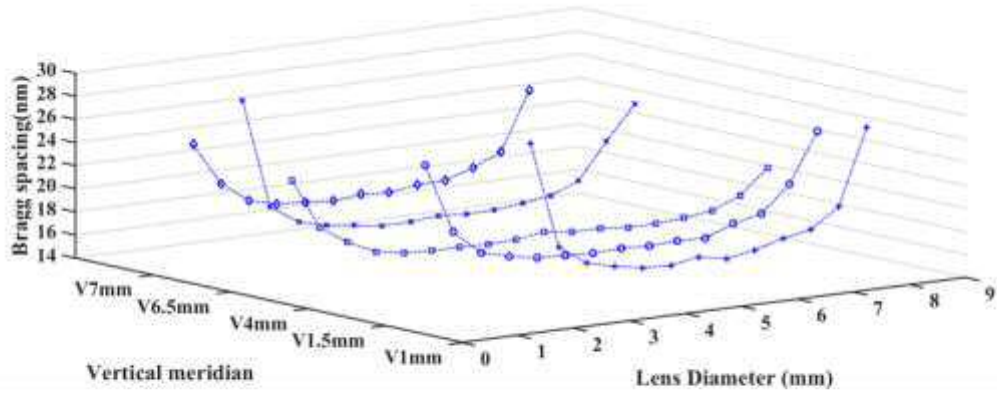
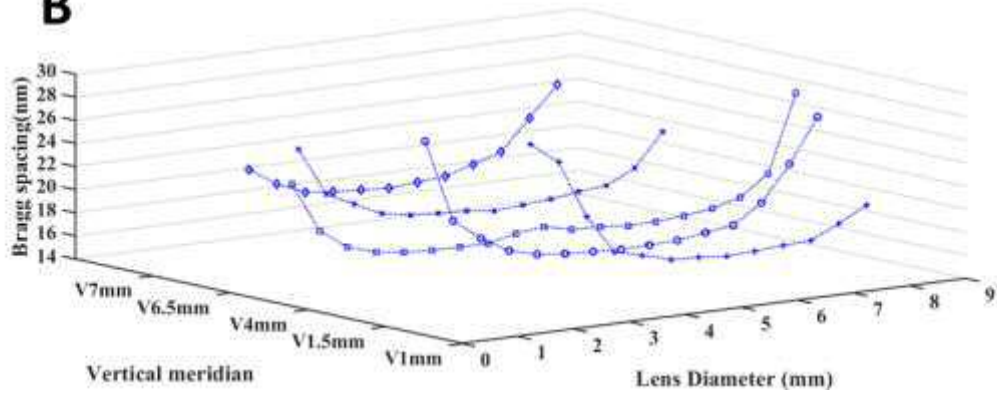
A**Un-Stretched Lens****Stretched Lens****B**

Figure 3-9: Typical Bragg spacing derived from SAXS patterns along the Vertical meridians in a 2D scan. These charts show the typical Bragg spacing for un-stretched and stretched fresh porcine lenses. (A) Bragg spacing of the un-stretched fresh lens (B) Bragg spacing of the stretched lens.

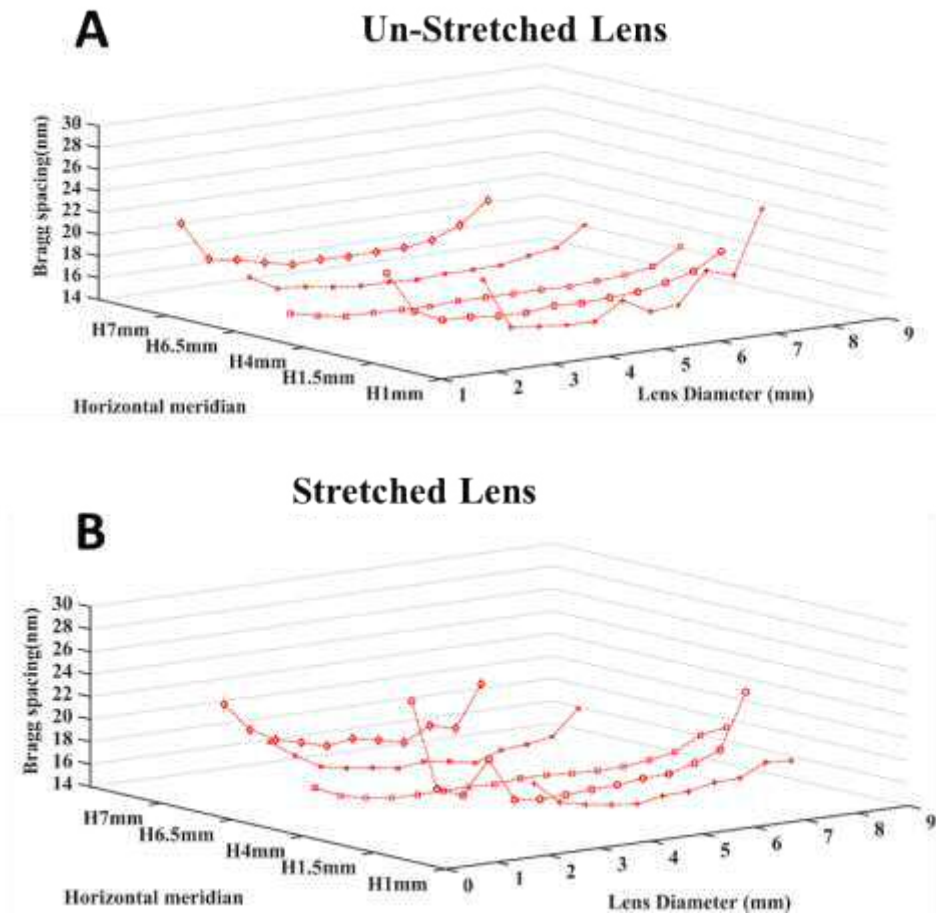


Figure 3-10: The average Bragg spacing derived from SAXS patterns along the Horizontal meridians in a 2D scan. These charts show the average Bragg spacing for un-stretched and stretched fresh porcine lenses. (A) Bragg spacing of the un-stretched fresh lens (B) Bragg spacing of the stretched lens.

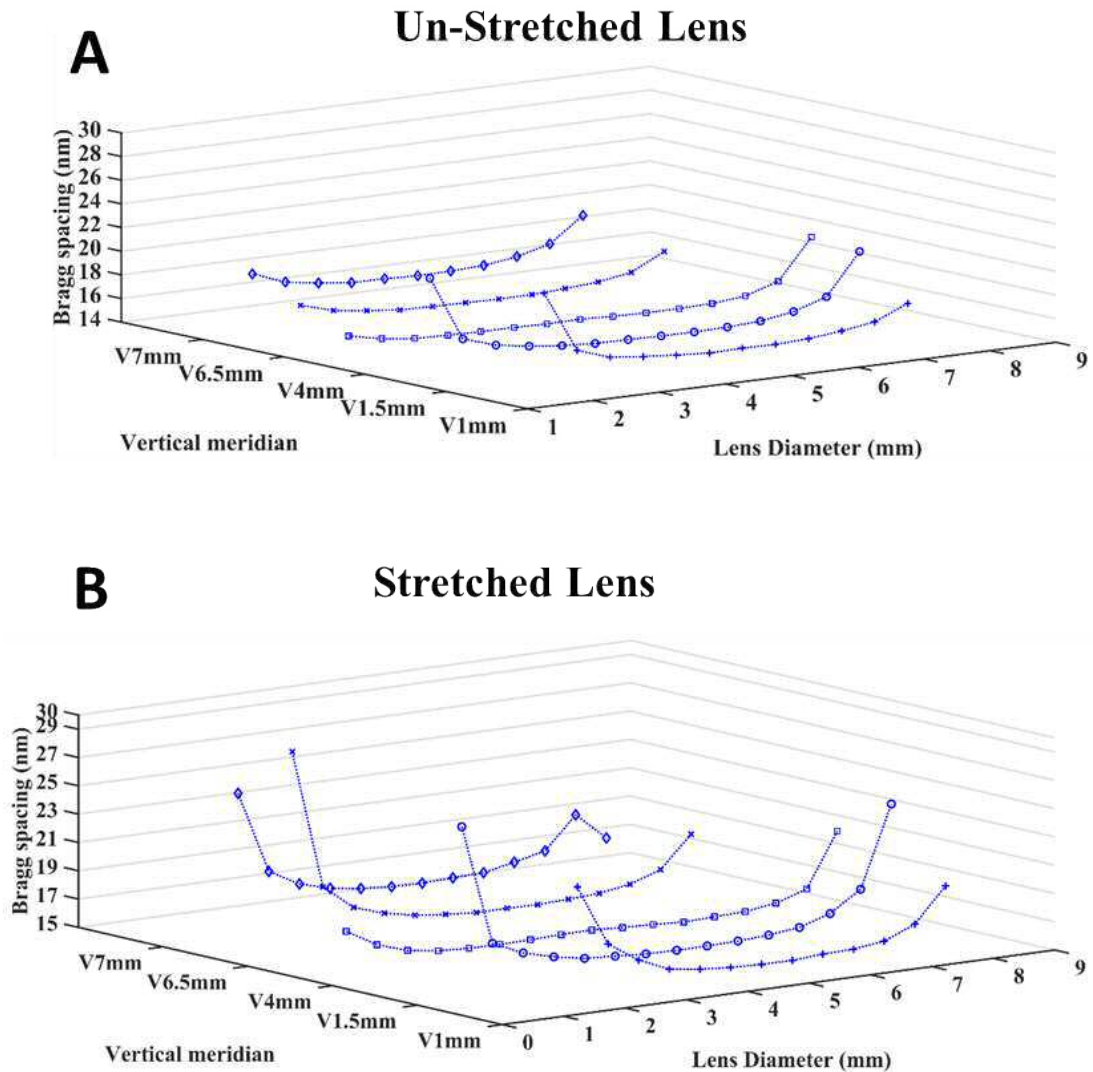


Figure 3-11: The average Bragg spacing derived from SAXS patterns along the Horizontal meridians in a 2D scan. These charts show the average Bragg spacing for un-stretched and stretched fresh porcine lenses. (A) Bragg spacing of the un-stretched fresh lens (B) Bragg spacing of the stretched lens.

The Bragg spacings for the fixed lenses were also plotted in a number of horizontal and vertical patterns every 0.5 mm across the 2D scan, presented as typical charts in un-stretched and stretched conditions (stretcher A and stretcher B) (Figure 3-12 and 3-13). The Bragg spacings averages for all fixed lenses (n = 9) were similarly depicted in both horizontal and vertical patterns, for both un-stretched and stretched lenses (Figures 3-14 and 3-15). Note that all the Bragg spacings given are average values for the total number of all fixed lenses studied from both positions; un-stretched

and stretched (stretcher A and stretcher B) lenses at the same corresponding lens meridian in the horizontal and vertical directions (see Table 3-2). However, as mentioned above, the scattered X-ray intensity from fixed lenses are altered by the fixation process due to dehydration.

When the lenses were fixed, in both unstretched or stretched states, in either of the two stretching devices, A and B, the Bragg spacings measured from the horizontal and vertical patterns within the cortex area were plotted at 1, 1.5, 4, 6.5 and 7 mm (Figure 3-14 and 3-15. A and B). In the central nuclear area within the horizontal pattern, the Bragg spacings were found to be ~16.3 nm in the unstretched lens and 18.6 and 17 nm following stretching within stretchers A and B, respectively. However, in the central nuclear area within vertical pattern, the Bragg spacing was found to be ~16.4 nm in unstretched lenses and 18.9 and 17.2 nm, in lenses stretched using Stretchers A and B respectively.

The Bragg spacing in the central nuclear area, un-stretched and stretched (stretcher A and stretcher B) of the fixed porcine lenses, both in vertical and horizontal grid scan directions, was found to be lower relative to the spacing in the cortex area. The 2D intensity profiles in unstretched and stretched fixed lenses indicate that there are clear changes between the average distance between crystallins across the lenses which are very similar in value in both the horizontal and vertical directions.

In order to investigate the change in the ordering of the crystallin proteins, the X-ray scattering intensity peaks from the interference functions from fresh and fixed lenses were measured at different vertical and horizontal meridians and the H/FWHM ratio (for each un-stretched and stretched) were calculated.

| Horizontal meridians within fixed porcine lenses (Average \pm SD) (nm) | | | | | |
|--|----------------|----------------|----------------|----------------|----------------|
| Meridians | H1 mm | H1.5 mm | H4 mm | H6.5 mm | H7 mm |
| Un-stretched | 16.7 \pm 1.1 | 16.7 \pm 1.6 | 16.3 \pm 0.7 | 16.5 \pm 1.0 | 16.8 \pm 1.2 |
| Stretched (stretcher A) | 21.1 \pm 2.5 | 19.7 \pm 2.2 | 18.6 \pm 1.7 | 19.6 \pm 2.4 | 20.6 \pm 3.7 |
| Stretched (stretcher B) | 18.6 \pm 2.5 | 17.1 \pm 1.3 | 17 \pm 1.4 | 16.8 \pm 0.9 | 17.3 \pm 1.3 |
| Vertical meridians within fixed porcine lenses (Average \pm SD) (nm) | | | | | |
| Meridians | V1 mm | V1.5 mm | V4 mm | V6.5 mm | V7 mm |
| Un-stretched | 16.5 \pm 0.6 | 16.1 \pm 0.5 | 16.4 \pm 0.8 | 17 \pm 1.4 | 17.2 \pm 1.5 |
| Stretched (stretcher A) | 21.3 \pm 2.7 | 20.6 \pm 3.9 | 18.9 \pm 2.4 | 19.3 \pm 2.4 | 19.9 \pm 2.6 |
| Stretched (stretcher B) | 17.9 \pm 1.5 | 17.5 \pm 1.8 | 17.2 \pm 1.3 | 16.7 \pm 0.2 | N/A |

Table 3-2: Average and standard deviation of the interference functions Bragg spacings from patterns in the horizontal (H) and vertical (V) grids within the fixed porcine lenses in un-stretched, and stretched sample using stretcher A and stretcher B.

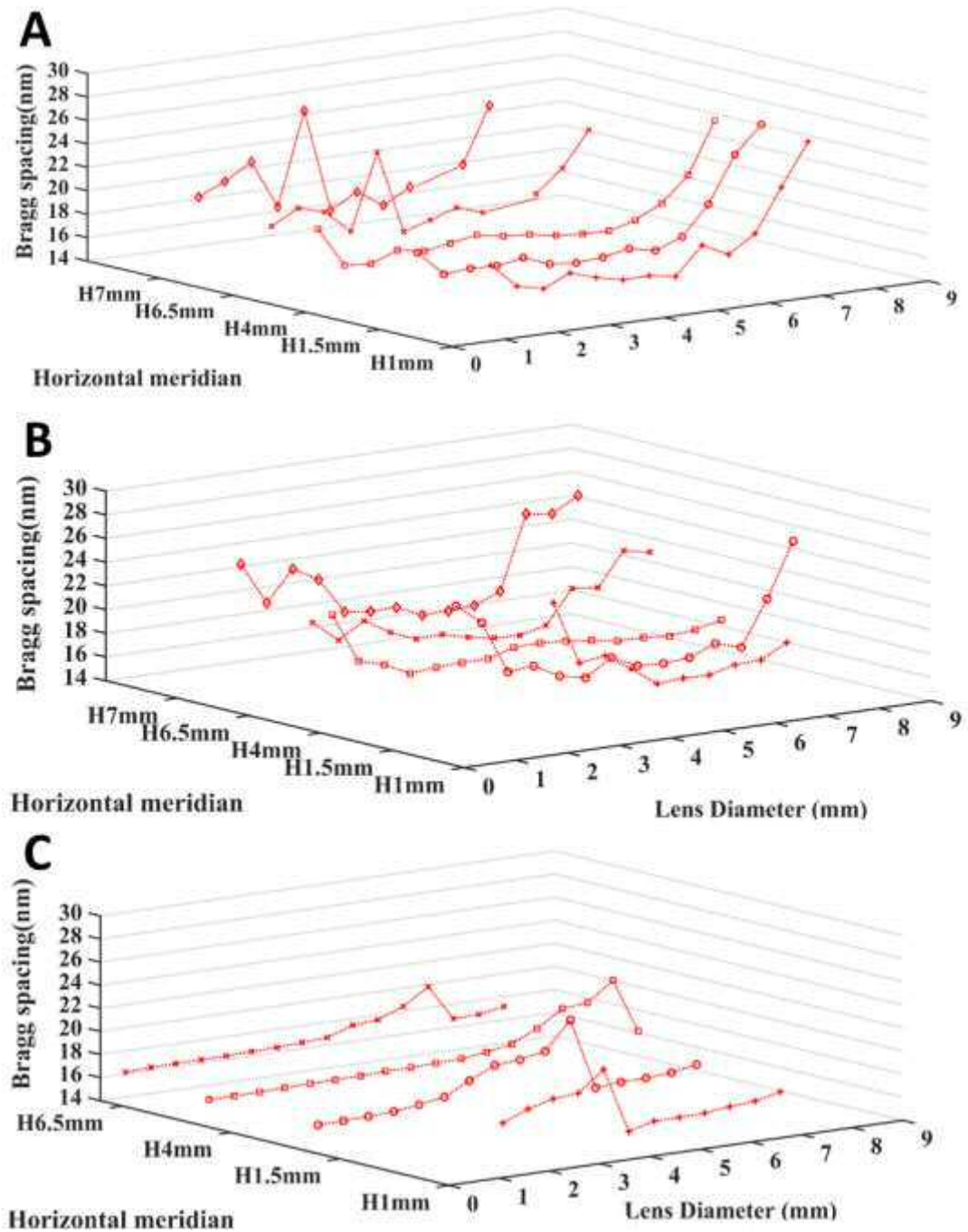


Figure 3-12: Typical Bragg spacing derived from SAXS patterns along the Horizontal meridians in a 2D scan. These charts show the typical Bragg spacing for un-stretched and stretched samples using stretcher A, and stretcher B of fixed porcine lenses. (A) Bragg spacing of the un-stretched fixed lens (B) Bragg spacing of the samples extended with stretcher A (C) Bragg spacing of the samples extended with stretcher B.

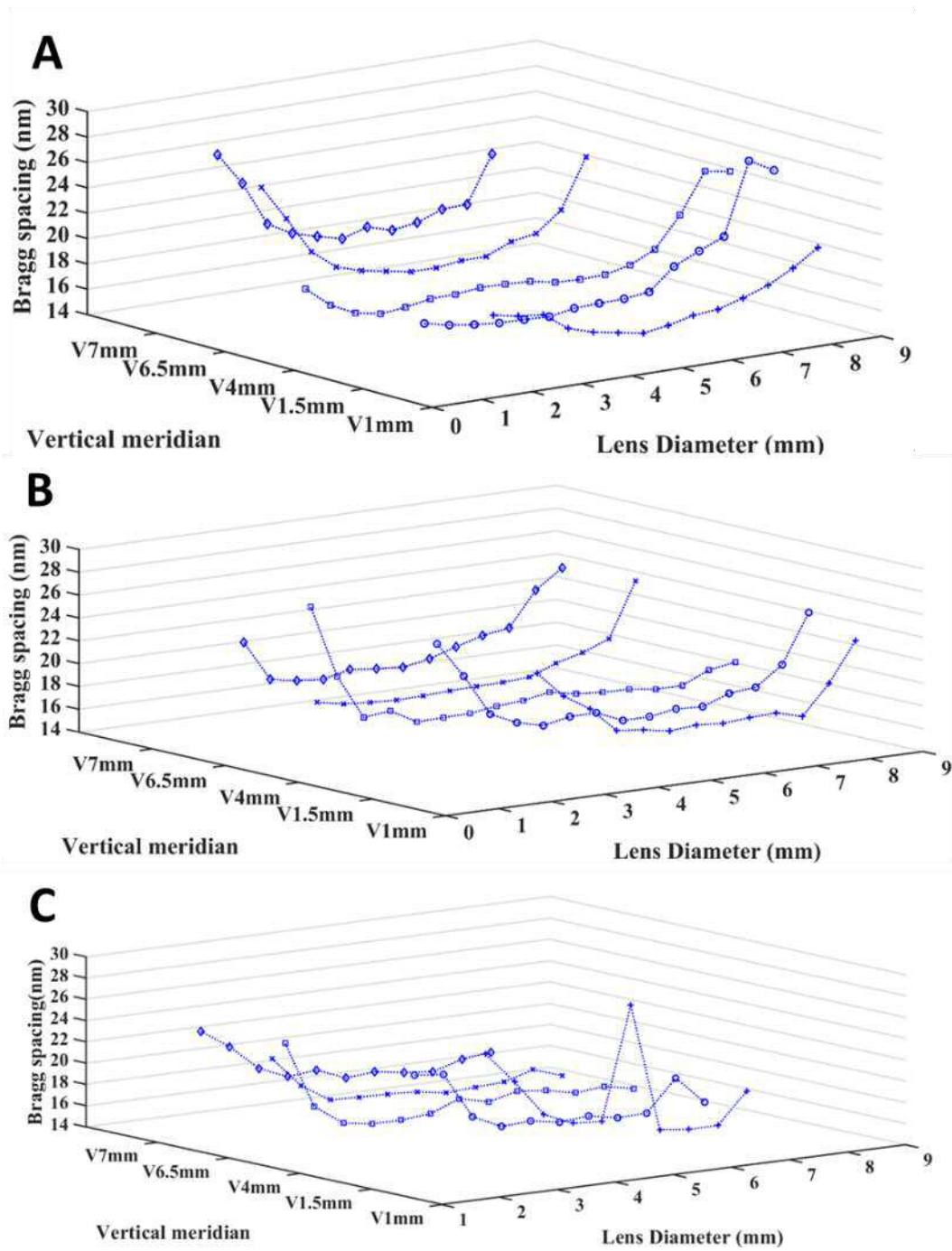


Figure 3-13: Typical Bragg spacing derived from SAXS patterns along the Vertical meridians in a 2D scan for a fixed lens. These charts show the typical Bragg spacing for un-stretched and stretched samples using stretcher A, and stretcher B. (A) Bragg spacing of the un-stretched fixed lens (B) Bragg spacing of the samples extended with stretcher A (C) Bragg spacing of the samples extended with stretcher B.

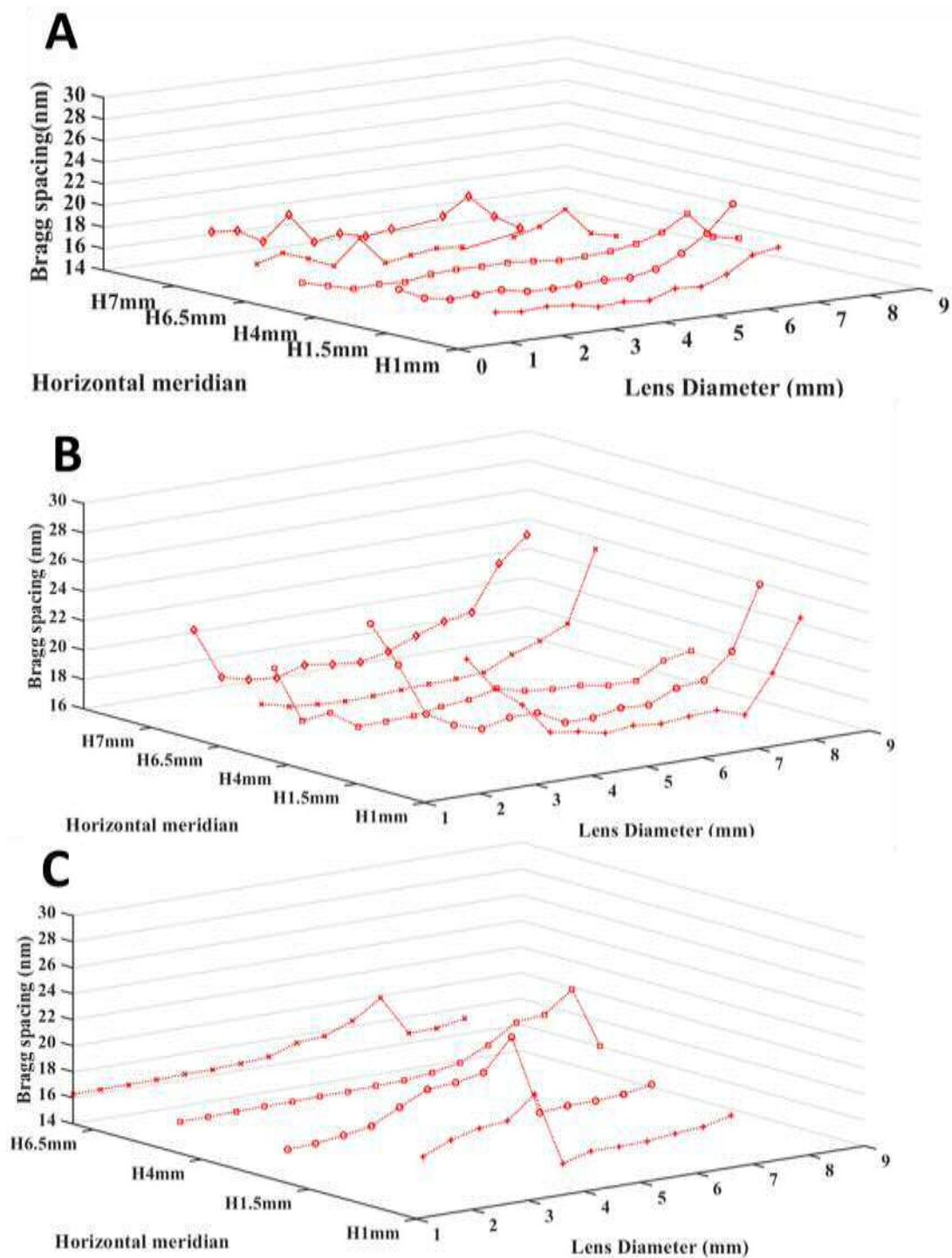


Figure 3-14: The average Bragg spacing derived from SAXS patterns along the Horizontal meridians in a 2D scan for fixed lenses. These charts show the typical Bragg spacing for un-stretched and stretched samples using stretcher A, and stretcher B. (A Bragg spacing of the un-stretched fixed lens (B) Bragg spacing of the samples extended with stretcher A (C) Bragg spacing of the samples extended with stretcher B.

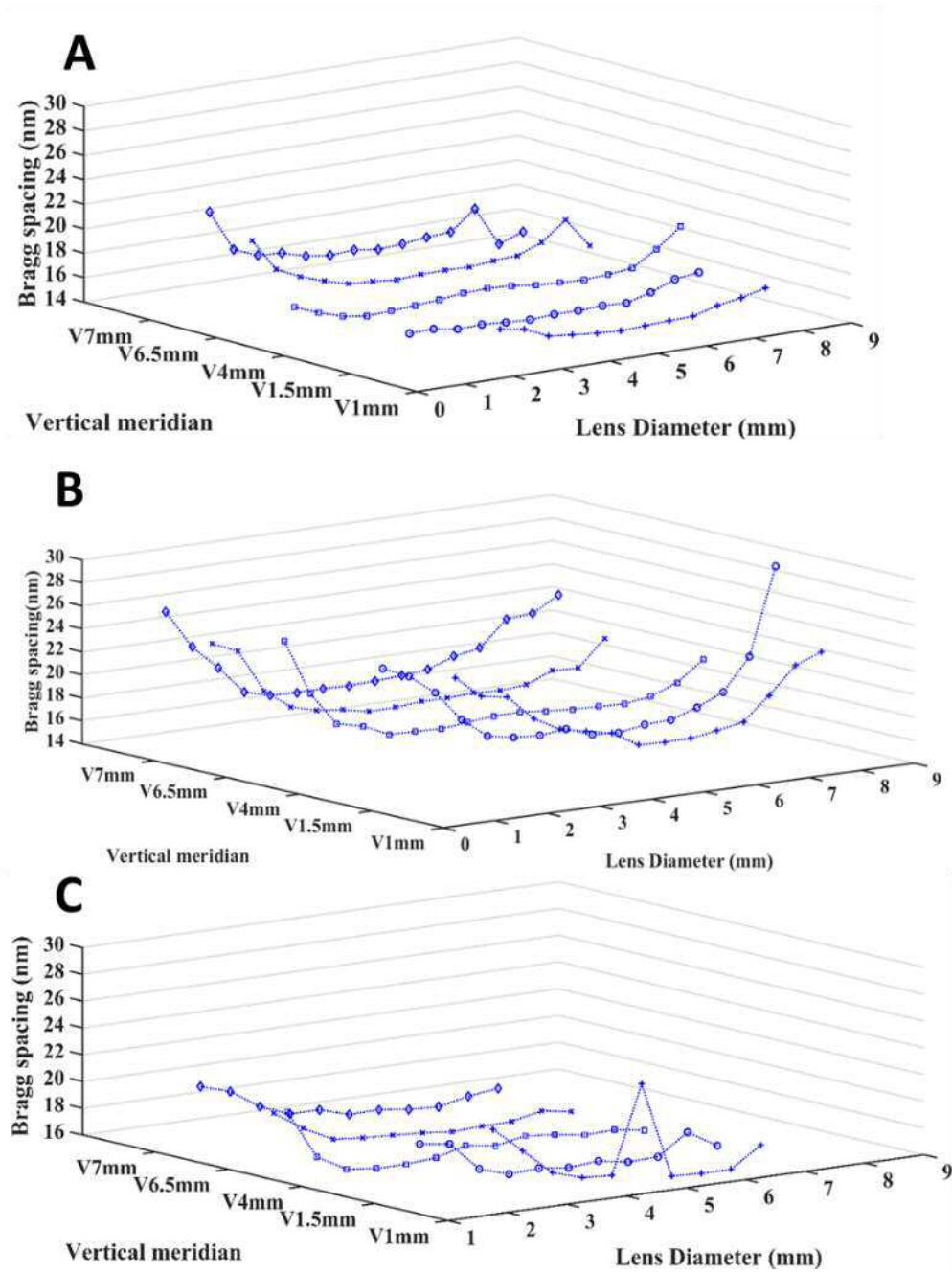


Figure 3-15: The average Bragg spacing derived from SAXS patterns along the Vertical meridians in a 2D scan for fixed lenses. These charts show the average Bragg spacing for un-stretched and stretched samples using stretcher A, and stretcher B. (A) Bragg spacing of the un-stretched fixed lens (B) Bragg spacing of the samples extended with stretcher A (C) Bragg spacing of the samples extended with stretcher B.

The H/FWHM ratios for fresh lenses were plotted from in a number of horizontal patterns, presented as typical charts in stretched and un-stretched conditions (Figure 3-16). The H/FWHM ratios for fresh lenses were also taken from a number of vertical patterns, presented as typical charts in stretched and un-stretched conditions (Figure 3-17). The H/FWHM ratio averages for a typical fresh lens were represented in both horizontal and vertical patterns, for both un-stretched and stretched lens. Note that all the H/FWHM ratio given values for a typical lens studied from fresh lenses at un-stretched/stretched positions at corresponding lens meridians (See Table 3-3).

| Horizontal meridians within fresh porcine lenses (Average \pm SD) | | | | | |
|---|---------------|-----------------|---------------|-----------------|---------------|
| | H 1 mm | H 1.5 mm | H 4 mm | H 6.5 mm | H 7 mm |
| Un-stretched ($\times 10^3$) | 3.7 \pm 0.4 | 3.6 \pm 0.5 | 3.7 \pm 0.6 | 4.1 \pm 0.6 | 3.9 \pm 0.5 |
| Stretched ($\times 10^3$) | 3.9 \pm 1.1 | 3.8 \pm 1.2 | 3.6 \pm 0.8 | 3.9 \pm 1.1 | 4.3 \pm 1.3 |
| Vertical meridians within fresh porcine lenses (Average \pm SD) | | | | | |
| | V 1 mm | V1.5 mm | V 4 mm | V 6.5 mm | V 7 mm |
| Un-stretched ($\times 10^3$) | 4.3 \pm 0.4 | 4.1 \pm 0.4 | 3.9 \pm 0.3 | 3.2 \pm 0.2 | 3.1 \pm 0.2 |
| Stretched ($\times 10^3$) | 5.1 \pm 0.5 | 4.8 \pm 0.7 | 3.7 \pm 0.7 | 3.4 \pm 0.7 | 2.9 \pm 0.5 |

Table 3-3: Average and standard deviation of the interference functions H/FWHM ratio from patterns in the horizontal (H) and vertical (V) grids within typical fresh porcine lens in both un-stretched and stretched positions.

The interference function's H/FWHM ratios in the cortex of un-stretched and stretched fresh lenses (measured from the horizontal and vertical meridian patterns), at 1, 1.5, 4, 6.5 and 7 mm are shown in Figures 3-16 and 3-17 [A] and [B]. In the central nuclear area within the horizontal pattern, the H/FWHM ratio was found to be \times in the unstretched lens and \times in stretched, fresh lenses. However, in the central nuclear area within vertical pattern, the H/FWHM ratio was \times before stretching and upon stretching, \times .

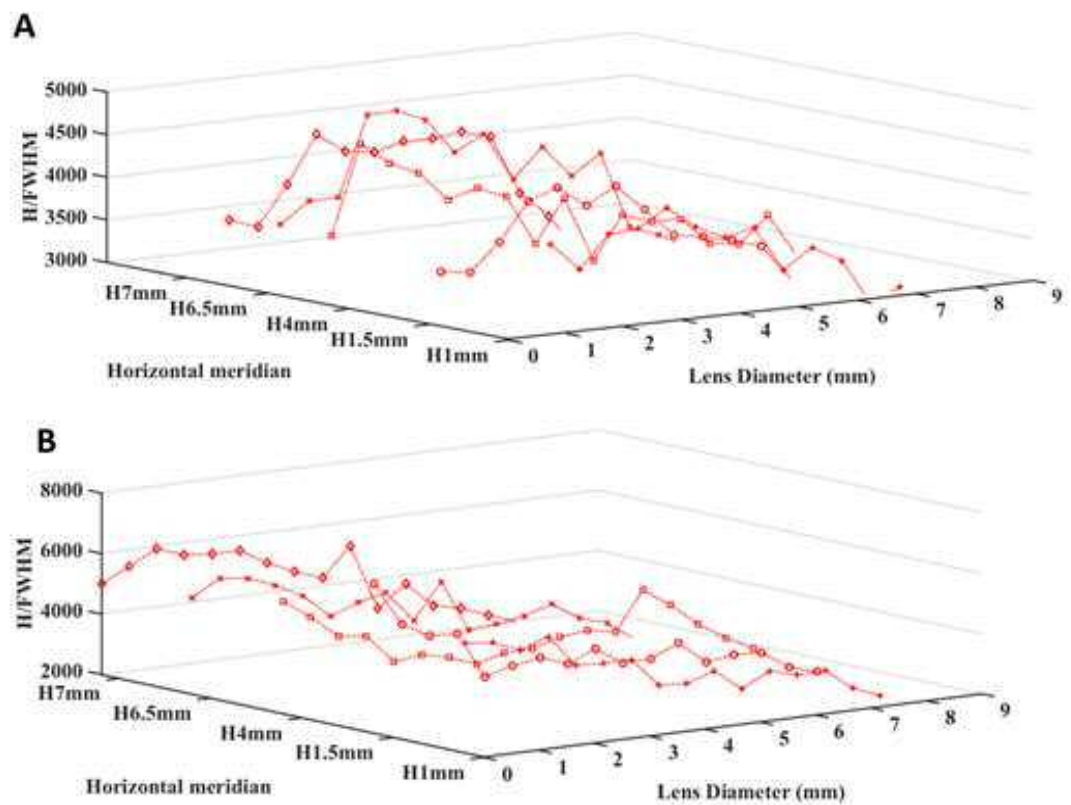


Figure 3-16: Typical H/FWHM ratio derived from SAXS patterns along the Horizontal meridians in a 2D scan. These charts show the typical H/FWHM ratio for un-stretched and stretched fresh porcine lens. (A) H/FWHM ratio of the un-stretched fresh lens (B) H/FWHM ratio of the stretched lens.

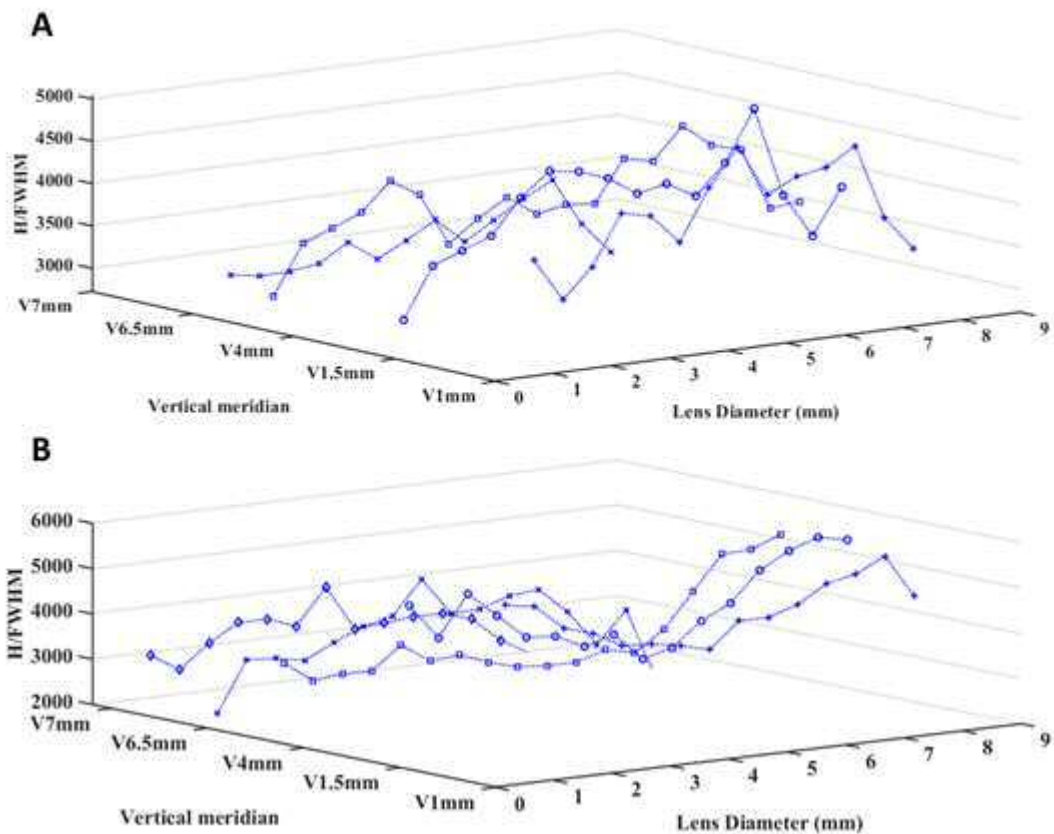


Figure 3-17: Typical H/FWHM ratio derived from SAXS patterns along the Vertical meridians in a 2D scan. These charts show the typical H/FWHM ratio for un-stretched and stretched fresh porcine lens. (A) H/FWHM ratio of the un-stretched fresh lens (B) H/FWHM ratio of the stretched lens.

However, as may be seen from Figures 3-16 and 3-17, the overall trends of the H/FWHM ratio are similar in both the vertical and horizontal directions in that in the un-stretched state the trend seems to have a maximum value around the centre of the lens diameter which then tails off towards the peripheries. In the stretched state the trends of the H/FWHM ratio appear more even than in the un-stretched state but also significantly higher towards one of the peripheries.

Similarly, the H/FWHM ratio for fixed lenses were plotted in a number of horizontal patterns, presented as typical charts in un-stretched and stretched conditions (stretcher A and stretcher B) (Figure 3-18). Also, the H/FWHM ratio for fixed lenses were

plotted in a number of vertical patterns, presented as typical charts in stretched and un-stretched conditions (Figure 3-19). The H/FWHM ratio averages for a typical fixed lens were represented in both horizontal and vertical patterns, both positions; un-stretched and stretched (stretcher A and stretcher B) lenses at the same corresponding lens meridian in the horizontal and vertical directions (See table 3-4).

The interference function's H/FWHM ratios in the cortex of un-stretched and stretched fixed lenses (measured from the horizontal and vertical meridian patterns), at 1, 1.5, 4, 6.5 and 7 mm are shown in Figures 3-18 and 3-19. A, B and C. At the horizontal patterns within the central nuclear area, the H/FWHM ratio was found to be \times in the unstretched lens and \times and \times in lenses stretched using stretchers A and B, respectively (Figure 3-18 A, B, and C). However, the patterns along the vertical grid within the central nuclear area, the H/FWHM ratio was found to be \times in the unstretched lens and about \times and \times in lenses stretched using Stretchers A and B respectively (Figure 3-19 A, B, and C).

Overall, the trend of the H/FWHM ratio in both the vertical and horizontal directions seemed much less marked than those from fresh porcine lenses. Generally however, there does seem to be slightly higher values in the centre of the lenses than at the edges in the un-stretched and those samples extended with stretcher A and stretcher B. The exception is from the vertical patterns from a lens extended with stretcher B whose values appear to be fairly constant.

| Horizontal meridians within fixed porcine lenses (Average \pm SD) | | | | | |
|---|---------------|----------------|---------------|----------------|----------------|
| Meridian | H1 mm | H1.5 mm | H4 mm | H6.5 mm | H7 mm |
| Un-stretched ($\times 10^5$) | 1.4 \pm 0.5 | 1.5 \pm 0.5 | 1.6 \pm 0.4 | 1.4 \pm 0.4 | 1.4 \pm 0.4 |
| Stretched (stretcher A) ($\times 10^5$) | 0.8 \pm 0.2 | 1.0 \pm 0.2 | 1.2 \pm 0.2 | 1.2 \pm 0.3 | 1.0 \pm 0.2 |
| Stretched (stretcher B) ($\times 10^7$) | 0.8 \pm 0.2 | 0.9 \pm 0.3 | 0.7 \pm 0.2 | 0.9 \pm 0.2 | 0.8 \pm 0.3 |
| Vertical meridians within fixed porcine lenses (Average \pm SD) | | | | | |
| Meridian | V1 mm | V1.5 mm | V4 mm | V6.5 mm | V7 mm |
| Un-stretched ($\times 10^5$) | 1.6 \pm 0.4 | 2.0 \pm 0.7 | 1.4 \pm 0.3 | 1.2 \pm 0.3 | 0.8 \pm 0.2 |
| Stretched (stretcher A) ($\times 10^5$) | 1.0 \pm 0.2 | 0.9 \pm 0.1 | 1.2 \pm 0.3 | 1.1 \pm 0.2 | 0.9 \pm 0.2 |
| Stretched (stretcher B) ($\times 10^7$) | 0.7 \pm 0.2 | 1.2 \pm 0.7 | 0.8 \pm 0.2 | 0.7 \pm 0.1 | 0.7 \pm 0.08 |

Table 3-4: Average and standard deviation of the interference functions of H/FWHM ratio from patterns in the horizontal (H) and vertical (V) grids within the typical fixed porcine lenses in un-stretched, stretched lens with stretcher A and stretched lens with stretcher B.

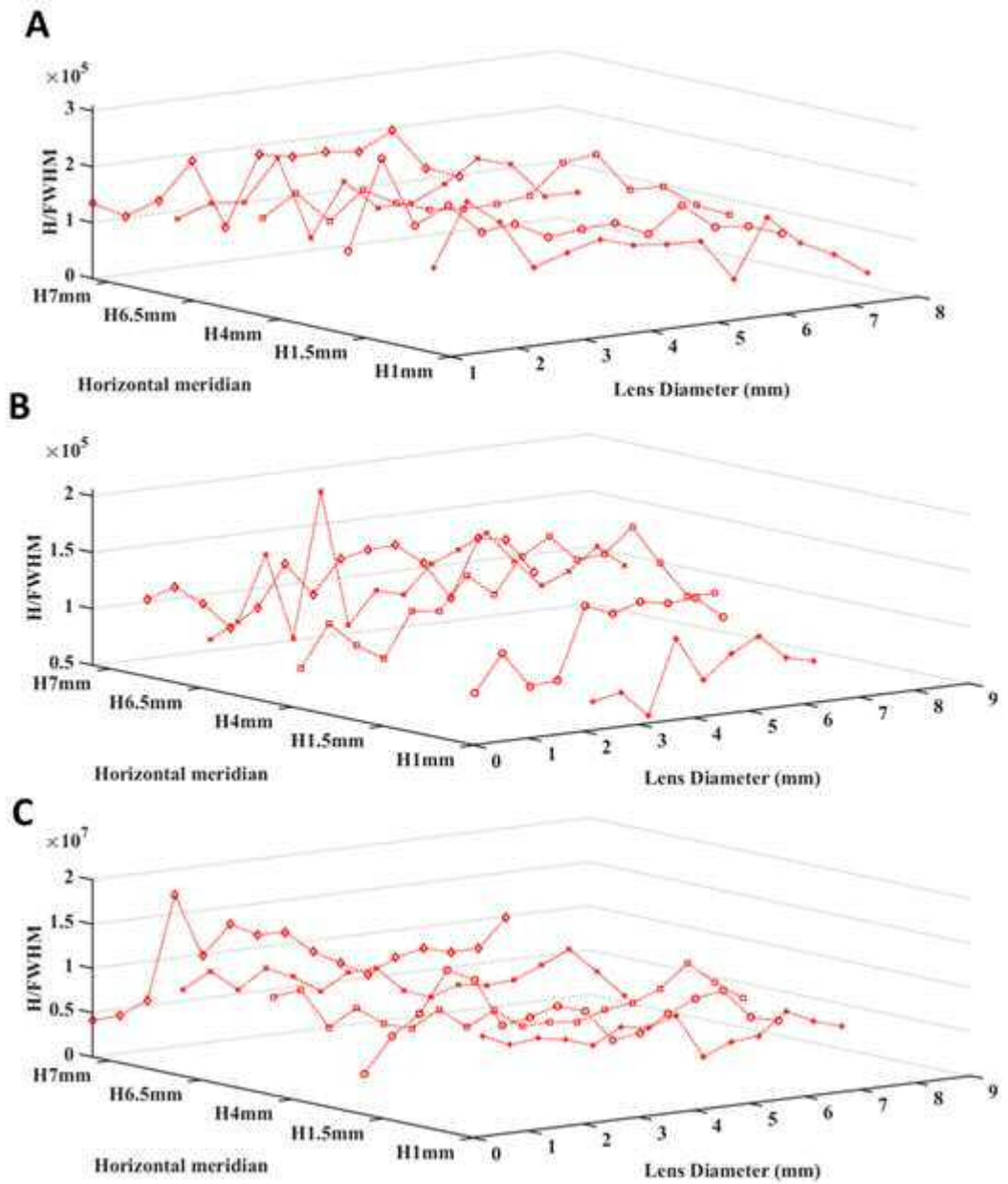


Figure 3-18: Typical H/FWHM ratio derived from SAXS patterns along the Horizontal meridians in a 2D scan for fixed lenses. These charts show the typical H/FWHM ratio for un-stretched, and stretched samples using stretcher A, and stretcher B. (A) H/FWHM ratio of the in un-stretched fixed lens (B) H/FWHM ratio of the samples extended with stretcher A (C) H/FWHM ratio of the samples extended with stretcher B.

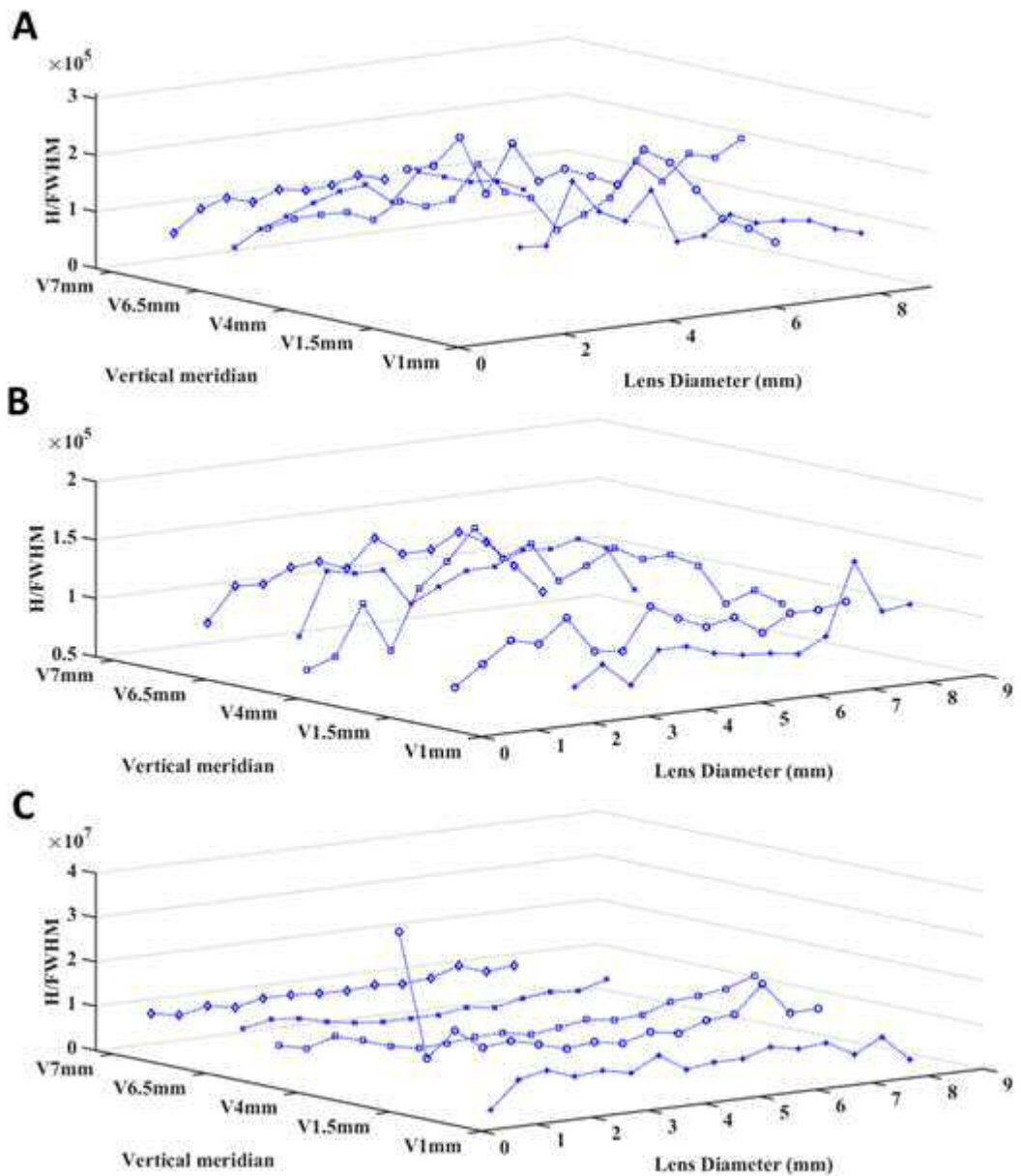


Figure 3-19: Typical H/FWHM ratio derived from SAXS patterns along the Vertical meridians in a 2D scan for fixed lenses. These charts show the typical H/FWHM ratio for un-stretched and stretched samples using stretcher A, and stretcher B. (A) H/FWHM ratio of the in un-stretched fixed lens (B) H/FWHM ratio of the samples extended with stretcher A (C) H/FWHM ratio of the samples extended with stretcher B.

3.3.3 Fresh and fixed lenses Bragg spacing in accommodated and unaccommodated states

In fresh lenses, the Bragg spacing showed no significant difference, at 5% significance level, between un-stretched and stretched states, along both the horizontal and vertical meridians. As this experiment was conducted using two different stretching devices, there was a clearly noticeable difference in the Bragg spacing along both the horizontal and vertical meridians ($p < 0.0001$), between fixed un-stretched and fixed stretched lenses that had been stretched using stretcher A; at 1 mm (16.5 ± 0.8 nm versus 21.1 ± 2.5 nm), 1.5 mm (16.1 ± 0.5 nm versus 19.7 ± 2.3 nm), 4 mm (16.1 ± 0.3 nm versus 18.8 ± 1.92 nm), 6.5 mm (16.5 ± 0.8 nm versus 19.4 ± 2.6 nm) and 7 mm (16.9 ± 1.1 nm versus 20.0 ± 3.7 nm) (Table 3-5). Furthermore, there was a significant difference in Bragg spacing in vertical meridians between fixed un-stretched and fixed stretched lenses that had been stretched using stretcher A; at 1mm (16.6 ± 0.6 nm versus 20.9 ± 2.8 nm), 1.5 mm (15.9 ± 0.4 nm versus 19.8 ± 3.0 nm), 4mm (16.2 ± 0.5 nm versus 19.1 ± 2.8 nm), 6.5 mm (16.9 ± 1.5 nm versus 19.3 ± 2.7 nm) and 7 mm (17.4 ± 1.5 nm versus 19.4 ± 2.7 nm) (Table 3-5).

Notably, while, there was no significant difference in Bragg spacing between fixed un-stretched and fixed stretched lenses using the second stretching device (Stretcher B), in horizontal meridians at both 1mm, 6.5 mm and, horizontal Bragg spacing showed significant at 1.5 mm (16.2 ± 0.6 nm versus 17.7 ± 1.8 nm) and 4mm (16.1 ± 0.3 nm versus 16.6 ± 0.2 nm). Lastly, while in vertical Bragg spacing between fixed un-stretched and fixed stretched lenses, using the second stretching device (Stretcher B), showed significant difference at 1 mm (16.4 ± 0.6 nm versus 18.6 ± 2.5 nm), 1.5mm (15.8 ± 0.2 nm versus 17.2 ± 1.3 nm) and 4mm (16.3 ± 0.5 nm versus 17.2 ± 1.5 nm),

there was no significant difference between vertical Bragg spacing between fixed un-stretched and fixed stretched lenses at 6.5mm and 7 mm (Table 3-5). Notably, however, there was a significant difference in Bragg spacing between fixed un-stretched and fixed stretched lenses using the first stretching device (Stretcher A), in both horizontal and vertical meridians compared with fresh lenses in the same meridians.

| The p-value of Bragg spacing difference between un-stretched and stretched fresh lenses. | | | | | |
|---|------------|------------|------------|------------|------------|
| | H 1mm | H 1.5 mm | H 4 mm | H 6.5 mm | H 7 mm |
| Horizontal meridians | p = 0.532 | p = 0.321 | p = 0.490 | p = 0.087 | p = 0.722 |
| | V 1mm | V 1.5 mm | V 4 mm | V 6.5 mm | V 7 mm |
| Vertical meridians | p = 0.481 | p = 0.220 | p = 0.462 | p = 0.310 | p = 0.932 |
| The p-value of Bragg spacing difference between un-stretched and stretched (stretcher A) fixed lenses. | | | | | |
| | H 1mm | H 1.5 mm | H 4 mm | H 6.5 mm | H 7 mm |
| Horizontal meridians | p < 0.0001 | p < 0.0001 | p < 0.0001 | p < 0.0001 | p < 0.0001 |
| | V 1 mm | V 1.5 mm | V 4 mm | V 6.5 mm | V 7 mm |
| Vertical meridians | p < 0.0001 | p < 0.0001 | p < 0.0001 | p < 0.0001 | p < 0.0001 |
| The p-value of Bragg spacing difference between un-stretched and stretched (stretcher B) fixed lenses. | | | | | |
| | H 1mm | H 1.5 mm | H 4 mm | H 6.5 mm | H 7 mm |
| Horizontal meridians | p = 0.252 | p = 0.009 | p = 0.011 | p = 0.143 | p = 0.73 |
| | V 1 mm | V 1.5 mm | V 4 mm | V 6.5 mm | V 7 mm |
| Vertical meridians | p = 0.006 | p = 0.002 | p = 0.015 | p = 0.683 | p = 0.979 |

Table 3-5: The p-value of Bragg spacing difference in the horizontal (H) and vertical (V) grids between fresh un-stretched and stretched lenses, and fixed un-stretched and stretched (stretcher A and stretcher B) lenses.

3.4 Discussion

The lens crystallin's X-ray scattering intensity was examined for whole porcine lenses in fresh and fixed conditions in both un-stretched and stretched states. This study examined the peak positions and the H/FWHM ratio from the interference function in the lens cortex and nucleus regions using 2D grid scans, with a view of determining whether the stretching (unaccommodated lens) has an effect on the average spacing between the crystallin proteins or their ordering.

3.4.1 The intensity profile of the lens in fresh and fixed lenses

The crystallin proteins' concentration and packing in the lens plays a significant role in determining the lens refractive index (Mirarefi et al., 2010). A high crystallin concentration, according to Delaye & Tardieu (1983), supports short-range interactions and reduces fluctuations in concentrations within the lens cells, effectively minimising the optical medium's light scattering. This study established the existence of dissimilarities in the scattered intensity between the cortex and the nucleus regions in both fresh and fixed lenses.

There is a marked decrease in the scatter intensity between individual X-ray patterns toward the lens central nuclear area. This trend occurs in both fresh and fixed porcine lenses, as can be seen in the 2D grid scan montages in Figures 3-4 and 3-5. Generally, the amount of scattered X-ray intensity is dependent on a number of factors such as the lens thickness and the species, and the crystallin concentrations. In spite of the fact that both fresh and fixed lenses have the same geometries, however, both lenses were prepared differently for the experiment i.e. one group was kept fresh and other was fixed. The SAXS patterns from whole fixed lenses may, therefore, have been altered

by the fixation process. It is well known from EM and SAXS studies that fixation with paraformaldehyde causes dehydration and shrinking of biological samples (Jongebloed et al., 1998; Huang & Yeung, 2015). The loss of water from the fixed samples leads to a lack of electron contrast resulting in lower scattered X-ray intensity. Unlike the case with the fresh porcine lens, therefore, the total observed scatter intensity was low potentially due to the dehydration during the fixation process.

The results of fresh lenses show that the scattered X-ray intensity reduces towards the lens nucleus region, but it increases in the cortex and the X-ray intensity is highest towards the lens edges (See Figure 3-6 and Figure 3-7). In fixed lenses, however, the X-ray intensity variations develop due to the fixation-related dehydration of the tissue. In spite of the fixation effects, this study's results show that the intensity sharply decreases toward the lens centre and increases towards the lens edges. This can be explained by the differential concentration of crystallins within the lens.

3.4.2 Bragg spacing and H/FWHM ratio for fresh and fixed lenses

Delays & Tardieu (1983) argue that short-range spatial ordering of the lens crystallins is very important in determining the lens transparency throughout life. The arrangement of the crystallins between the lens cortex and the nucleus is, however, not identical. The present study used SAXS to measure the scattering intensity of whole intact porcine lenses through different meridians. The vertical and horizontal meridians, both in the nucleus and cortex regions, are indicative of the intact lenses crystallin composition and distribution. The scatter patterns from both the cortex and nucleus show a characteristic scatter intensity that corresponds to a regular spacing between lens crystallins. This present study's results are consistent with past findings

and the theoretical expectations, with respect to the relative lower scatter intensity in the cortex than the nucleus.

The Bragg spacings of the interference reflection obtained from fresh and fixed porcine lenses show that the changes across the lenses were nearly similar in both vertical and horizontal meridians. Towards the lens centre, the Bragg spacing reduces in a symmetrical fashion, then increases to reach similar and equidistant spacing toward the outer end of the second half of the meridian. The reduction in spacing towards the centre may be explained by the diminishing spacing between the crystallin proteins with increasing protein concentration towards the centre. The symmetrical trend, on the other hand, may be explained by the symmetrical geometry of the lenses in a plane parallel to the optical axis, through which the X-ray beam passes.

The average Bragg spacing values from the fresh and fixed porcine lenses interference functions are nearly similar in both the vertical and horizontal meridians. According to Mirarefi et al. (2010), examining the spatial distribution of the crystallins within whole intact lens fibre cells allows for the exploration of the crystallins in situ spatial arrangement in their natural environment, thereby excluding the complications related to the disruption of the lens (including oxidation and aggregation).

3.4.3 Scattering of the fresh and fixed lenses in accommodated and unaccommodated states

Using the porcine lenses in this experiment as a model for the accommodation is justified for two reasons (1) the crystallin concentration and distribution within porcine lenses is similar to human lens, and (2) many studies in this area have similarly used porcine lens as a proxy for different features of the lens during the accommodation,

including the lens curvature, thickness, power, and capsule (Bloemendal et al., 2004; Trifonova et al., 2002; Roorda, & Glasser, 2004; Kammel et al., 2012).

The main difference between the accommodated and unaccommodated states in fresh lenses can be seen in the intensity profiles. The relative difference in the peak heights from the periphery of the lens to the centre appears to be greater in the un-stretched state and lower in the stretched state. This indicates that there has been an obvious change in the thickness of the lens and also indicates a change in the position of electron density i.e. mass within the lens when extended. This observation taken with the finding that there is no significant difference in the distance between the proteins (Bragg spacing) upon stretching, suggests that the accommodation process is at the cellular level and involves the re-organisation of the lens fibres themselves, and not at the molecular level of the crystallin proteins.

For fixed lenses stretched using “Stretcher A”, there are clearly noticeable differences between Bragg spacing in accommodated and unaccommodated conditions in fixed lenses compared with fresh lenses. This may be a result of experimental variations, not least because the fresh lenses used in this study were stretched after three days post-mortem, at which time the ciliary muscles attached to the lenses were expectedly not as strong to stretch the lenses. It also indicated that chemical fixation used in this study can be a solution for better preservation of the lens features for more accurate and realistic experiments to further our understanding of the accommodation mechanism.

Further, the lenses stretched using the second stretching device “Stretcher B”, however, exhibited no such differences as seen in lenses stretched using “Stretcher A”, which can be explained as a result of unequal strain that is artificially induced by

stretching devices and/or possibly ruptured/over-extended zonules as a result of stretching. It is arguable that no two mechanical stretchers are exactly similar to each other. The measurement of Bragg spacing offers valuable information about the protein distribution within the lens in accommodated and unaccommodated conditions.

3.5 Conclusion

The scatter intensity patterns from both the cortices and nuclei show a characteristic scatter intensity that corresponds to a regular spacing between lens crystallins. The Bragg spacing of the interference reflections obtained from fresh and fixed porcine lenses show that the changes across the lenses meridian were nearly similar in both vertical and horizontal meridians. Towards the lens centre, the Bragg spacing reduces in a symmetrical fashion, then increases to reach similar and equidistant spacing toward the outer end of the second half of the meridian.

Finally, for the lenses stretched using “Stretcher A”, there are clearly noticeable differences between accommodated and unaccommodated conditions in fixed lenses compared to fresh lenses. However, the lenses stretched using the second stretching device, exhibited no such differences. The measurement of Bragg spacing may, therefore, point to the general information about the protein distribution within the lens in accommodated and unaccommodated conditions, in fixed and fresh porcine lenses.

This is the first study of its kind and clearly needs to be repeated and improved by increasing and diversifying the lens samples. Some of the anomalous results such as the large increase in the H/FWHM ratios at just one peripheral edge in stretched fresh

lens (Figures 3-16 and 3-17) may, in part, be due to an inconsistent radial tension from the lens stretchers themselves. The lens stretching devices used in this study are simple mechanical devices. Ideally, future studies would require a computer controlled lens stretching device in which the rate and amount of tension applied to the tissue could be controlled and measured more accurately.

Chapter Four

4 The lens curvature and microstructural changes between the accommodated and unaccommodated state

4.1 Introduction

During accommodation, the lens focuses objects at different distances onto the retina, so that they can be clearly seen (Helmholtz, 1855; Schachar, 2012; Oveneri-Ogbomo & Oduntan, 2015). Helmholtz's theory postulates that the ciliary muscle contracts to release the radial tension on the zonular fibres. As a result, the lens surface curvature steepens anteriorly more than posteriorly, with consequent thickening of the lens axial diameter (Brown, 1973). The lens equatorial diameter decreases and so increases its dioptric power (Brown, 1973). The relaxation of the ciliary muscle increases zonular tension, thereby flattening the lens, and reducing dioptric power (Helmholtz, 1855; Fisher, 1988; Burd et al., 1999; Schachar, 2012).

It is possible that both primate and non-primate lens suture patterns affect the lens optical quality (Kuszak & Brown, 1994), even though their exact role in the accommodation remains unclear (Zoltoski et al., 2012). Several researchers (Sivak et al., 1994, Kuszak et al., 1991) argue that there is a relationship between the suture branch type and optical power in both primate and non-primate lenses. These studies suggest that an association exists between suture types (and the suture end) and the level of accommodation amongst different groups of animals.

Moreover, *in vivo* experiment show evidence of internal lens changes during accommodation (Dubbelman et al., 2003). An *in vivo* study by Dubbelman et al. (2003) suggested that most of the internal changes that occur during accommodation are within the nucleus, along with the lens visual axis. Zoltoski et al. (2012) found that the

accommodation response *in vivo* increased lens thickness by 0.13 ± 0.05 mm/D, and further that the lens' unique structural features allowed an end-to-end arrangement of lens fibres to interface within sutures, leading to a change in lens curvature for near vision. In an *ex vivo* study, Kuszak et al. (2006), however, found no difference in lens fibre measurements between the accommodated and unaccommodated state, except for those caused by the tape and flare of lens fibres' ends at the suture junction. Furthermore, the accommodation involved simultaneous increases in the lens surface curvature and thickness because of the overlaps at the end of the lens fibres within the suture area (Kuszak et al., 2006).

Since it is difficult to simulate the *in vivo* accommodation in an *ex vivo* experiment, it is impossible to determine the precise changes in lens fibres. However, a lens stretcher can be used to provide an acceptable and good model of the accommodation and has been widely used in several studies (Dubbelman et al., 2003; Hermans et al., 2008; Cortés et al., 2015). The changes in the lens internal structure during accommodation have been measured in many empirical studies, including Patnaik (1967), Brown (1973), and Koretz et al. (1997), which demonstrated an increase in sagittal lens thickness during accommodation.

To further our understanding, in this study, the hypothesis that internal lens structural differences occur between the accommodated and unaccommodated state was not fully addressed. Therefore, the aims of this study were to determine the accommodative changes in the:

- (i) Anterior and posterior radius of lens curvature,
- (ii) Fibre widths as a function of lens depth, and

- (iii) Anterior and posterior suture angles and intersection shape and size.

4.2 Materials and methods

Preliminary experiments were performed to optimise embedding and staining procedures for lens tissues and identify lens features, as observed in past studies, as a prelude to novel three-dimensional serial block-face scanning electron microscopy (SBF SEM) studies. The usual ultrastructural features (lens fibres) were clearly visible. However, subsequent experiments carried out by an expert microscopist (RY), using different fixation/staining techniques, failed to provide tissue samples suitable for SBF SEM. These steps have been outlined in Appendix 1. As the stains used did not penetrate the lens sample tissues, it was not possible to progress these experiments to SBF SEM of the lens. To further the investigation into the lens structural changes as a function of accommodation, the experiments in this chapter were carried out to analyse lens microstructural features.

4.2.1 Source of tissues

Twenty-two porcine eyes, without pathology, from freshly slaughtered pigs (6 months old; therefore, suitable for use in an accommodation model, according to Kammel, 2012), were obtained within six hours after sacrifice from a local abattoir (Maddock Kembery Meats, Maesteg, Wales).

Six lenses were used for analyses of lens curvature in the accommodated and unaccommodated lens, following optical coherence tomography. Five lenses were used to measure superficial lens fibre widths in the accommodated and unaccommodated lens following light microscopy. An additional five were used to

measure anterior and posterior surface lens fibre widths up to a depth of 300 μm , whilst in a simulated aqueous humour buffer, images of the accommodated and unaccommodated lens were acquired using confocal laser scanning microscopy. The final six lenses, in the accommodated and unaccommodated lens, were cryo-embedded (see below), serial sectioned and labelled with wheat germ agglutinin (WGA) to analyse lens fibre widths throughout the lens depths.

4.2.1.1 Simulation of accommodation using a lens stretcher

Lenses were prepared and mounted into two lens stretcher devices to simulate the effects of accommodation on the lenses, as previously described in section 3.2.2.

4.2.1.2 Optical Coherence Tomography: measurement of the lens surface curvature

To examine the changes in anterior and posterior radius of lens curvature as a function of simulated accommodation, four lenses were inserted into a BIONIKO manual lens stretcher (Stretcher A), and two lenses were placed in a BIONIKO Manual Lens Stretcher V2 (Stretcher B). Next, 3D volumetric image datasets of the anterior and posterior surfaces of each lens, in the unstretched (accommodated) and stretched (unaccommodated) state, were acquired using a custom built research optical coherence tomography (OCT) scanner, with a microscope module attached (within the Viva Scientia Bioimaging Laboratories at Cardiff School of Optometry and Vision Sciences).

The first step was to connect the microscope module to the OCT scanner. The system was then turned on for 15 minutes to warm up, before adjusting the microscope head to achieve a significant clearance between the objective lens and the slide holder.

In brief, the lens stretcher that contained the porcine lens was mounted onto the OCT microscope stage. The microscope head was adjusted until the signal intensity, attributed to the sample, was optimal on the live B scan view, and the reference arm was adjusted until the image appeared in the top third of the screen. The raw spectral data (i.e. the data acquired by the OCT as it scans through the sample, but before it is converted to an image format) represents the interferometric data acquired as a result of the combination of reflected light from the sample arm and the reference light from the reference arm. The data was saved in FDI format from the anterior lens surface, and the lens stretcher was turned over, to obtain scans of the posterior lens surface. The lens stretcher device was then stretched, and scans were similarly acquired.

4.2.1.3 Determination of anterior and posterior lens curvature radii

The spectral data acquired was converted from FDI format into digital TIFF image files using custom-written MATLAB (*MathWorks, Inc*) software (OCT FDI data processing v2). The acquired data in FDI file format was then converted to a TIFF image.

The dispersion (implying that the wavelengths are not focussed at the same depth) was computed by selecting a box window around the image of the porcine lens radius of curvature. The processed TIFF image appeared in the 'Processed' folder, where the original folder containing FDI files was situated. Lastly, image contrast and brightness were adjusted to achieve clearer visualisation, and image calibration parameters (see below) were inserted to convert pixels into micrometres.

A scaling factor of $6.62\mu\text{m}/\text{pixel}$ was used for the pixel-to-micrometer conversion and the scan's angle as taken during the calibration was 12 degrees.

For each image, a region of interest box was produced to contain the maximum width and top half of the image. The top half of the image was used because the further away from the apex of the lens you are, the flatter the lens shall be and hence the greater the radius of curvature. To compute the anterior and posterior radii of the lens' curvature in the unstretched and stretched lenses, the box width and height measurements were input into an open-sourced online circular arc calculator, www.Handymath.com (Handymath, 2017). Measurements were performed in triplicate to generate a mean for subsequent statistical analysis.

4.2.2 Measurement of superficial lens fibre widths and suture angle using light microscopy

In an attempt to determine superficial lens fibre widths and suture angles in the accommodated and unaccommodated lens, five porcine lenses were mounted into a BIONIKO manual lens stretcher (Stretcher A), previously described. Images of each porcine lens in the unstretched and stretched positions were captured using a light microscope (*DMRB Microscope, Leica Microsystems Ltd.UK*), with an attached *LEICA MC170 HD* camera (*Microsystems Ltd., UK*) and LAS EZ image analysis software. Images (at a magnification of 10X) from five regions of interest (ROI), namely the suture junction, superior, inferior, temporal, and nasal regions of each lens were acquired.

4.2.2.1 Measurement of lens fibre widths

To determine the width of lens fibres within the five regions of interest, a Java-based image processing program, *ImageJ* software version 1.5 1n (National Institute of Health, Bethesda, Maryland, USA) was used. To begin with, image pixels were converted to micrometres (μm) (each one micron equal 2.59 pixel) in the acquired Tagged Image File Format (TIFF) images. Lens fibre widths were measured in a group of 10 lens fibres, in six different areas per region of interest, using *Image J's* Straight Line tool. Measurements of the 10 widths were taken perpendicular to the lens fibres' axis direction (Figure 4-1).

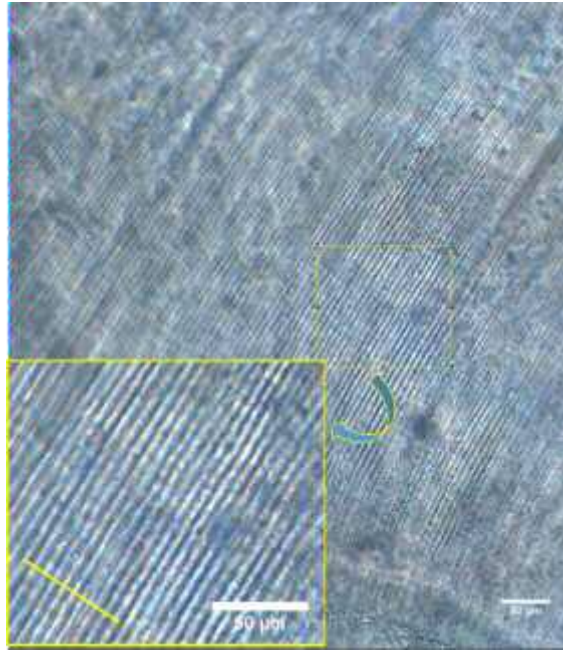


Figure 4-1: Lens fibers within the suture junction region of an unstretched lens (ie. accommodated lens). The image was enlarged (yellow below left box) and the width of 10 lens fibre was measured. For each ROI, six measurements were acquired. Scale bar represents 50 μ m.

The average lens fibre width was computed for each of the five lens regions of interest, before and after stretching, using Statistical Package for the Social Sciences (SPSS).

4.2.2.2 Quantification of suture angles

It was necessary for the lens area being investigated to be clearly visible in order to measure the suture angles. The suture meeting points in the central lens were clearly observable in the tiff images acquired from the centre ROI of four of the five lenses, before and after stretching. The lens suture in the porcine lens is Y-shaped (See Figure 4-2). The angles made by this Y-shape were labelled as A, B, and C before stretch, and A', B', and C' after stretch (Figure 4-2). Using the *ImageJ* 'angle' tool the three angles (A-C) were measured in triplicate, in the unstretched and stretched lenses. The average and the significant difference between unstretched and stretched positions of all angles

were then calculated using circular data statistics software, Oriana (RockWare Inc, U.S.A).

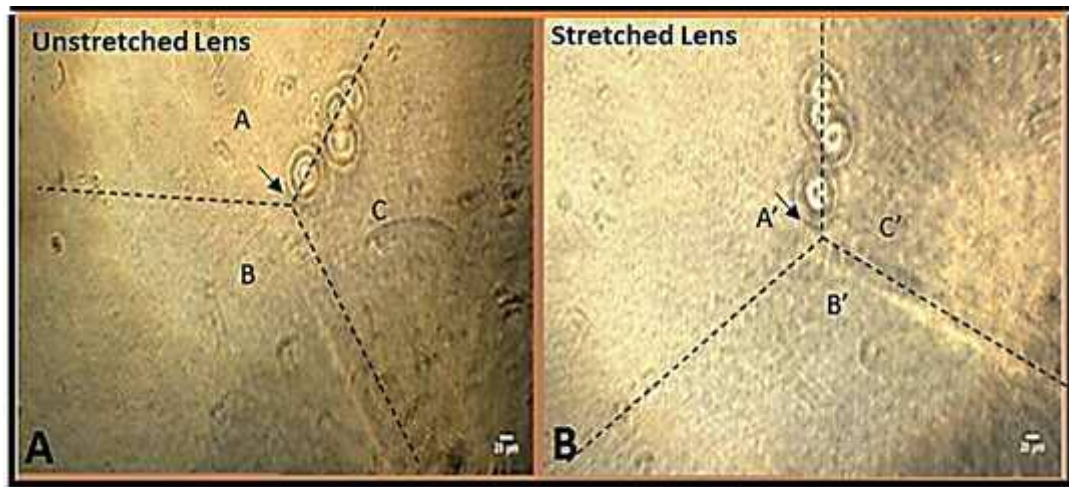


Figure 4-2: Suture angles within the centre ROI in the A) unstretched (A, B, C) and B) stretched (A', B', C') porcine lens. The arrow points to the suture junctions of the Y-shaped suture. Scale bar 25 μm .

4.2.3 Measurement of lens fibre widths and suture intersection area within the anterior and posterior lens using confocal laser scanning microscopy

Since in the earlier experiments and in those of other researchers using light microscopy, lens fibres could only be visualised in the superficial lens, this next experiment sought to investigate changes in lens fibre widths and suture intersection area parameters at increased lens depth using confocal laser scanning microscopy. Additionally, in order to quantify lens fibre widths, in as close to *in vivo* state as possible, the unstretched and stretched lenses were imaged whilst submerged in a simulated aqueous humour.

4.2.3.1 Sample preparation

Five porcine eyes were acquired, dissected and mounted into a BIONIKO manual lens stretcher (Stretcher A), as described earlier in section 3.3.2. The stretcher device with

the attached lens was immersed into an artificial aqueous humour solution (consisting of 125 mM sodium chloride (NaCl), 0.5 mM magnesium chloride (MgCl₂), 4.5 mM potassium chloride (KCl), 10 mM sodium bicarbonate (NaHCO₃), 2 mM calcium chloride (CaCl₂), 5 mM glucose, 20 mM sucrose, and 10 mM HEPES (pH 7.2–7.4) (Lim et al., 2009) in a petri dish (Appendix 3). This aimed to prevent dehydration of the lens during the imaging process, in order to maintain lens transparency.

4.2.3.2 Confocal imaging

The lenses were imaged using the Laser Scanning Microscope LSM880 (Carl Zeiss Ltd, Cambridge, UK) with a W Plan-Apochromat 10× 0.5 numerical aperture water dipping objective lens. 3D confocal image z-stacks (image resolution: 512 x 512 x 8 pixels) at 3µm depth intervals were acquired from each lens using ZEN v2 software, with an incident wavelength of 633-750 nm, depending on the lens depth. Each 3D image z-stack was acquired for approximately 200 to 400 µm depths, from either the anterior or posterior lens surface for each unstretched and stretched lens (Figure 4-3).

4.2.3.3 Measurement of the suture confluence area

3D confocal image z-stack profiles were adjusted using the image Z profile tool in Image J to identify the image depth for each lens in both the unstretched and stretched conditions. Therefore, image z-stack profiles up to 300 µm depths were generated in both the unstretched and stretched lenses (Figure 4-4).

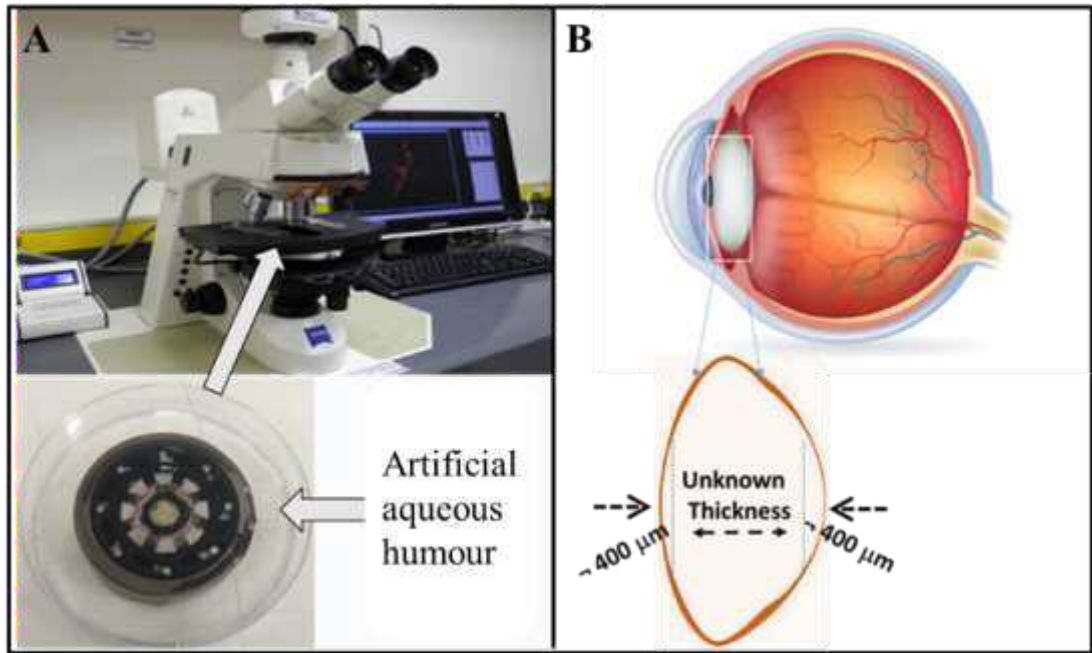


Figure 4-3: Confocal imaging of the porcine lens. A) The lens within a lens stretcher (inset) is submerged in artificial aqueous humour in a petri dish, which is placed onto the microscope sample stage. B) Schematic image of the eye and the lens (copied from Anatomy Organ, 2017), up to 400 μm in depth from the anterior or posterior lens surfaces, where images were collected.

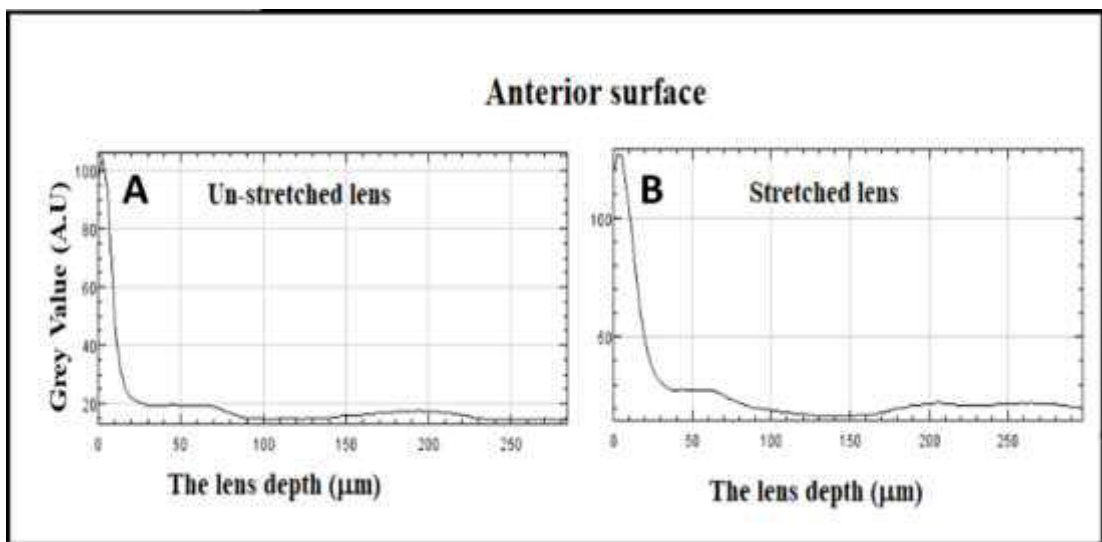


Figure 4-4: The z-profile of the anterior lens up to 300 μm depth for the unstretched (A) and stretched lens (B). The z-stacks of both stretched and unstretched lenses were modified to start from the optical slice that included the first image of the anterior-lens surface, zero μm to up to 300 μm .

The suture confluence area (i.e. the gap between sutures at the lens centre) was determined in each unstretched and stretched lens, at depths of 30, 60, 90, 120, 150, 180, 210, 240, 270, and 300 μm from each of the lens' anterior or posterior surfaces. The depth increments were defined as positive for the anterior lens (e.g. 30 μm) and negative for posterior lens (e.g. -30 μm).

The suture confluence area was quantified as a measure of the 'mass area' using the region of interest (ROI) manager tool in *ImageJ* software (NIH, Bethesda, Maryland, USA). The measurement was repeated three times at each depth for greater precision. At some depths, the suture confluence area was not visible, so areas were recorded using the smallest amount in ROI manager tool which is 0.69 μm^2 . Mean measurements and their standard deviations were calculated at each different depth.

4.2.3.4 Measurement of lens fibre widths

Lens fibre widths of lenses, before and after stretching, were measured at depths of 120, 150, 180, 210, 240, 270, and 300 μm from the posterior surfaces, while at the anterior surface, lens fibre borders could only be clearly visualised to a depth of 120 μm . At each depth, the width of 10 lens fibres was measured using the *ImageJ* 'Line' tool in ten different areas (avoiding the lens suture area). Each fibre width measurement was taken perpendicular (90°) to the lens fibre axis direction. The mean and standard deviations of the lens fibre widths were calculated in four of the five lenses, as the lens fibres of the fifth lens were not visible.

4.2.3.5 Statistical analyses

All statistical analyses were completed using IBM SPSS 23 and Microsoft Excel 2016. All data (at each depth) were tested for normality using the Shapiro-Wilk test. Normally distributed data were then compared using a paired *t-test*, while non-normally distributed data were compared using the Wilcoxon test.

For the suture confluence area, the data were analysed at 30, 60, 90, 120, 150, 180, 210, 240, 270, and 300 μm depths from both the anterior and posterior surfaces, in order to determine differences between unstretched and stretched lenses at each depth. Lens fibre width data were analysed at 120, 150, 180, 210, 240 μm for the anterior surface and at 120, 150, 180, 210, 270, and 300 μm from the posterior surface.

4.2.4 Determination of lens fibre widths throughout the full depth of unstretched and stretched porcine lenses

Since the full thickness of the lens could not be visualised using confocal microscopy, next an investigation into lens fibre widths at different depths in five ROIs, namely the suture junction area, superior, inferior, nasal, and temporal, in accommodated and the unaccommodated lens was performed.

4.2.4.1 Sample preparation

Six porcine lenses were isolated and dissected as described in subsection 3.2.2, and mounted, with a known orientation, onto a BIONIKO manual lens stretcher (Stretcher A) to simulate accommodation. Three of the lenses were stretched and three lenses remained unstretched. All lenses, whilst still attached to the stretcher device, were

immersed in 4% paraformaldehyde in 0.2 M phosphate buffer for seven days to preserve lens structure in their respective states. Then the lenses were washed three times in 0.1 M phosphate buffer pH 7.4, removed from the stretcher device and immersed in 10% sucrose (in order to avoid crystal formation in frozen tissues) for one hour, 20% sucrose for one hour, and finally, in 30% sucrose solution for 24 hours.

4.2.4.2 Cryoembedding and sectioning

The lenses were snap frozen in liquid nitrogen-cooled isopentane (Thermo Scientific, UK) and embedded in OCT mounting media (Thermo Scientific, Leicestershire, UK) in foil moulds, such that the lens anterior surface was positioned downwards, on the cutting side of the mould.

A marker was placed on superior ROI in order to keep precise regional location (see sub-section 4.2.4.1). Serial 25µm thick lens cryosections were cut using a cryostat (Leica CM3050 S, Leica Microsystems, UK), and transferred with a fine paint brush onto Superfrost® Plus slides (Thermo Scientific, Leicestershire, UK).

4.2.4.3 Wheat germ agglutinin labelling to visualise lens fibre membranes

The cryosections from both the unstretched and stretched lenses were washed in phosphate buffered saline (PBS) three times for five minutes each, then incubated in 5µg/ml fluorescein-conjugated wheat germ agglutinin, WGA, (diluted from a 1mg/ml stock solution, Life Technologies Corporation, Oregon, USA) in PBS for 20 hours. Then sections were washed three times in PBS for five minutes, before 5µg/ml Hoechst 33342 (Life Technologies Corporation, Oregon, USA) was applied for 10 minutes. The sections were washed again with PBS, then mounted in *ProLong Gold Antifade*, (Life Technologies Corporation, Oregon, USA).

4.2.4.4 Determination of lens diameter and lens fibre widths throughout lens depth

Sections were selected at 1mm depths through the lens, up to 7mm. The lens sections were observed under a DM6000B microscope (Leica Microsystems, Milton Keynes, UK) using a TRITC (LP)/N21 filter Ex/Em wavelengths of 552nm/578nm for visualisation of WGA labelling, and a DAPI (BP)/A4 filter (Ex/Em wavelengths of 359nm/461nm) for visualisation of Hoechst labelled nuclei.

Images of each lens section were captured using a LEICA DFC 350 FX camera (Microsystems, Milton Keynes, UK), and Leica LASX image software (Microsystems, Milton Keynes, UK), and the image location within each ROI, namely suture junction area, superior, inferior, nasal and temporal was noted (Figure 4-5). An overview of the regions within the lens from which the images were captured is shown in Figure 4-5.

Finally, vertical (superior to inferior) and horizontal (nasal to temporal) lens diameters were also measured in the fluorescent images. The measurements were performed three times in each section, and at each depth for all “unstretched” and “stretched” lenses.

4.2.4.5 Statistical analysis

All statistical analyses were completed using IBM SPSS 23 and Microsoft Excel 2016. Similarly, for the previous experiment (4.2.3.5), the data for each depth (1, 2, 3, 4, 5, 6, 7 mm) and each ROI were tested for normality using the Shapiro-Wilk test. Normally distributed data were then compared using an unpaired *t*-test, while non-normally distributed data were compared using the Mann-Whitney U test. The lens fibre widths data were categorised into two types: (i) the lens fibre widths in each ROI and depth and(ii) the lens fibre widths according to the lens nucleus and

anterior/equatorial/posterior lens cortex, which allowed comparisons to be made between unstretched and stretched lenses at each depth.

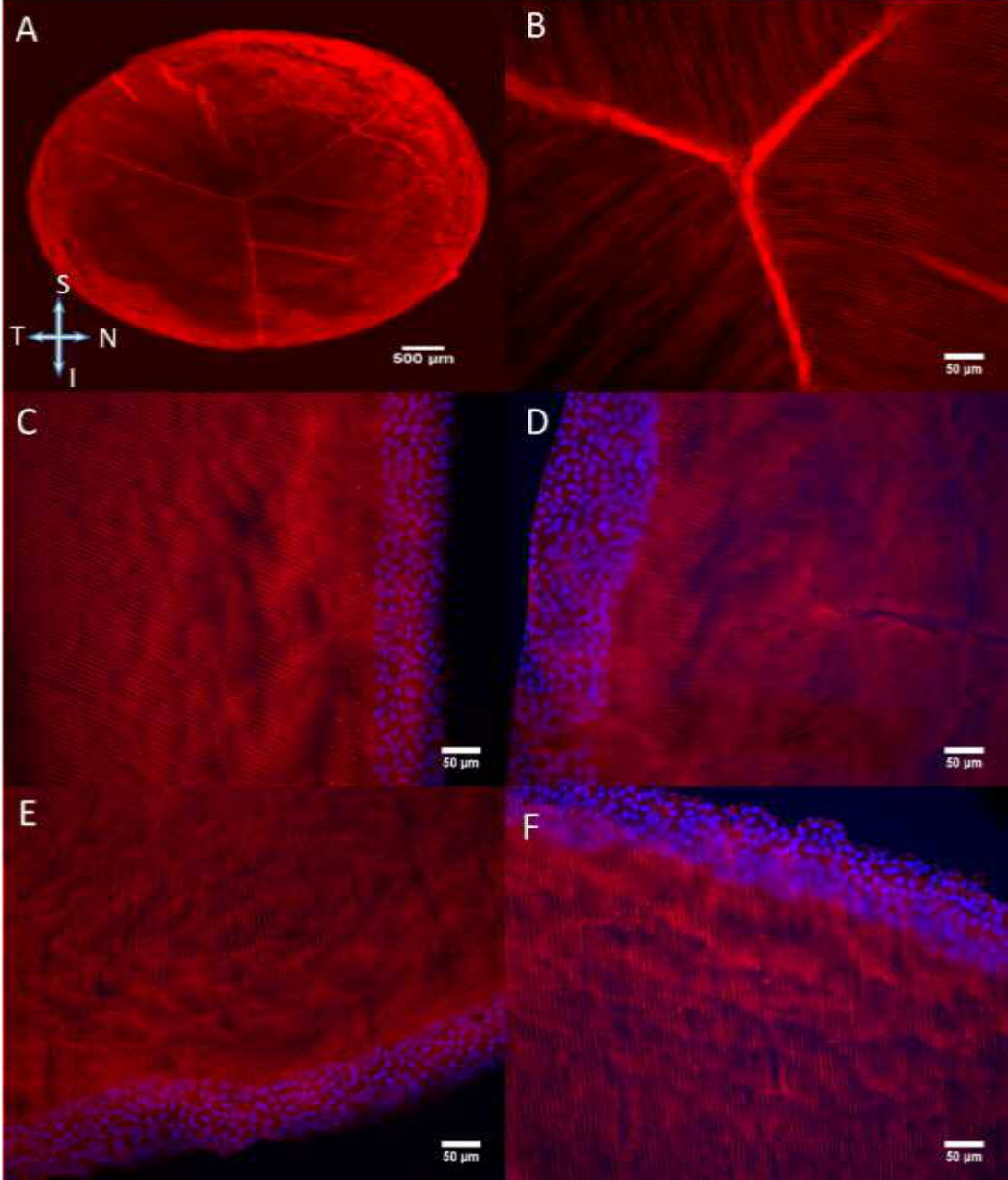


Figure 4-5: WGA labelled lens fibres in lens cryosection (A), and ROIs showing the suture confluence area (B), superior (C), inferior (D), nasal (E), and temporal (F) regions. The red pseudo colour illustrates the lens fibre membranes that were stained with wheat germ agglutinin. Blue colour illustrates the epithelial cell nuclei labelled with Hoechst. The scale bar: 500µm for image A, and 50µm for images B, C, D, E, and F.

4.3 Results

4.3.1 The radius of curvature of the lens surface in simulations of the accommodated and unaccommodated state

The anterior and posterior lens radii of curvature, in unstretched and stretched states (using two different stretching devices: A and B) are presented in Figure 4-6. Using Stretcher A, significant increases were observed in both the anterior lens radius of curvature (from 7.42 ± 0.02 mm to 7.73 ± 0.05 mm ($p=0.005$)) and in the posterior lens radius of curvature (from 5.31 ± 0.04 mm to 5.66 ± 0.05 mm ($p=0.004$)) (Figure 4-6). However, no statistically significant changes in either the anterior or posterior radii of curvature were observed using Stretcher B.

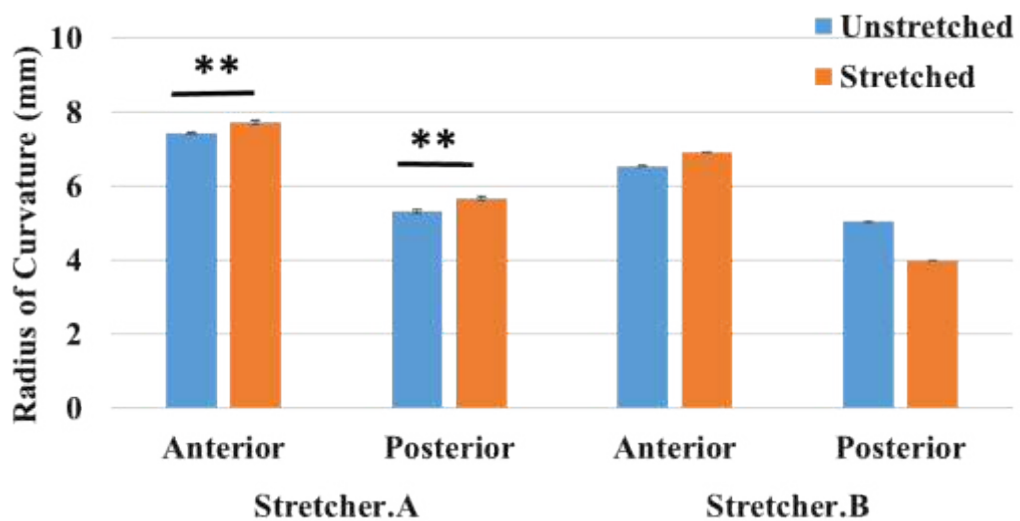


Figure 4-6: Anterior and posterior average lens radii of curvature before and after induced stretching using two different stretching devices A ($n = 4$ lenses) and B ($n = 2$ lenses). Error bars represent standard deviations of the mean and ** denotes $p < 0.01$.

4.3.2 Lens Fibre widths and suture angle in the superficial lens

4.3.2.1 Superficial lens fibre widths in the accommodated and unaccommodated state

No statistically significant difference was observed in average superficial lens fibre widths (see Appendix 3) between stretched and unstretched lenses (Figure 4-7).’’

When considered within regions, no difference was evident in the suture junction lens fibre widths between unstretched and stretched conditions ($p > 0.050$) (Figure 4-7. A).

However, in inferior lens fibre widths, significant differences were observed between stretched and unstretched states in two of the five lenses. These data were inconsistent as an increase in stretched lens fibre widths occurred in one ($p = 0.038$) lens and a decrease in the other ($p = 0.001$). See Figure 4-7. B.

The superior lens fibre widths altered following stretching in only 1 of the 5 lenses ($p = 0.037$) (see Figure 4-7. C). Inconsistent findings were also observed in the temporal region, with a significant increase in the stretched lens’ fibre widths ($p = 0.015$), but a reduction in fibre widths in two other stretched lenses’ ($p = 0.040$ and $p = 0.002$) (Figure 4-8. D). A reduction in the nasal lens fibre widths was observed in two of the five stretched lenses ($p = 0.019$ and $p = 0.003$) (Figure 4-7. E).

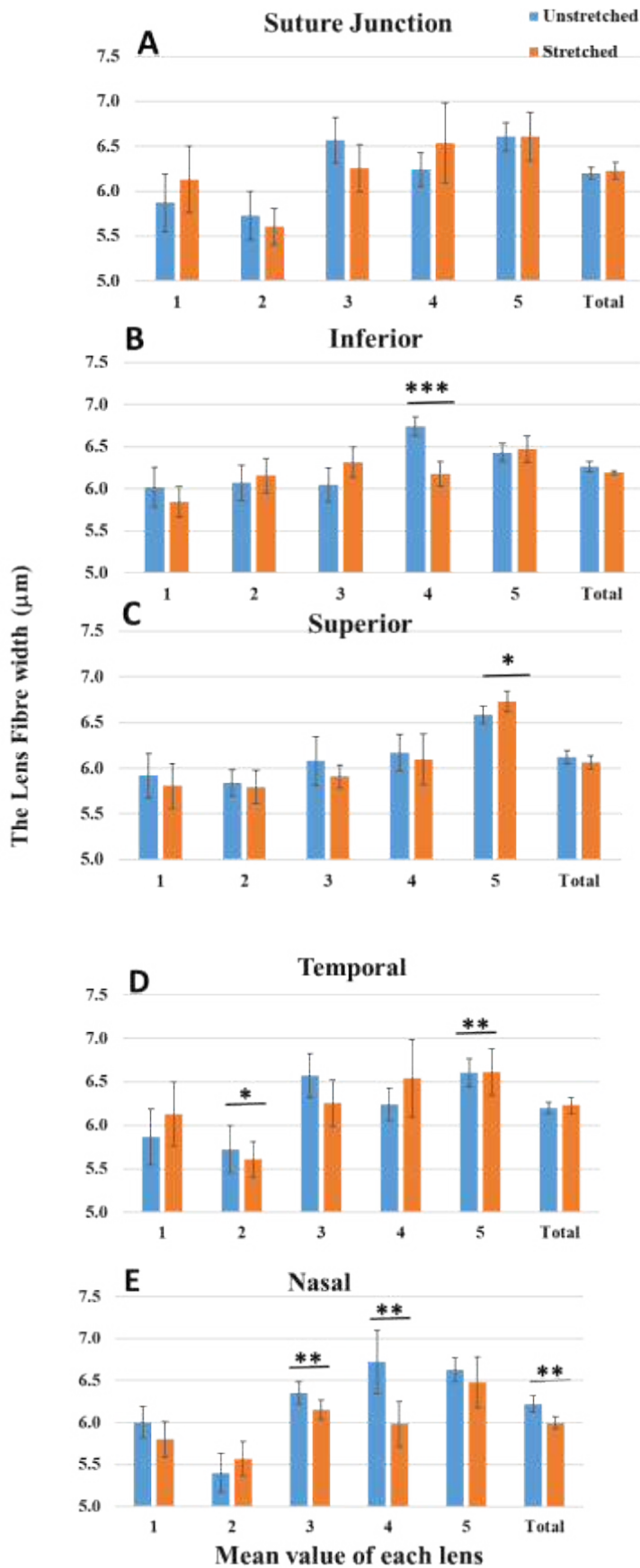


Figure 4-7: Regional mean lens fibre widths in stretched and un-stretched states. The mean fibre widths of five lenses in the stretched and unstretched configurations were analysed within the superficial anterior lens in five areas: suture junction (A), superior (B), inferior (C), nasal (D), and temporal (E). In all these areas, the lens fibre widths were between 5.5 µm to 7.5 µm. * denotes $p < 0.05$, ** denotes $p < 0.01$, *** denotes $p < 0.001$. Error bars represent standard deviation.

4.3.2.2 Suture angles in anterior porcine lens visualised using light microscopy

The angles, formed by the Y-shaped porcine lens sutures in the unstretched lenses, showed no significant changes upon stretching ($p > 0.050$). See Table 4-1.

| Angle | A | B | C |
|-------------|---------------------------------|---------------------------------|---------------------------------|
| Unstretched | $120.3^{\circ} \pm 5.1^{\circ}$ | $119.9^{\circ} \pm 3.8^{\circ}$ | $119.7^{\circ} \pm 3.7^{\circ}$ |
| Stretched | $121.8^{\circ} \pm 2.2^{\circ}$ | $119.6^{\circ} \pm 3.4^{\circ}$ | $120.1^{\circ} \pm 3.8$ |
| P values | P = 0.600 | P = 0.808 | P = 0.821 |

Table 4-1. Average, standard deviations and P value for the anterior superficial angle.

4.3.3 Lens fibre widths and suture intersection area within the anterior and posterior lens using confocal laser scanning microscopy

4.3.3.1 The anterior and posterior lens fibre widths and suture confluence area size (Up to $300\mu\text{m}$ from Surface) within stretched and unstretched lenses in simulated aqueous humour

Lens fibre widths were recorded in the anterior and posterior lens. In the anterior lens, the average lens fibre width in unstretched lenses ($n = 4$ lenses) was $5.1 \pm 0.6 \mu\text{m}$ and for stretched lenses ($n = 4$ lenses) was $5.6 \pm 0.3 \mu\text{m}$. In the posterior lens, the average of lens fibre width in unstretched and stretched lenses was $5.5 \pm 0.1 \mu\text{m}$ ($n = 4$), and was $5.7 \pm 0.2 \mu\text{m}$ ($n = 4$), respectively.

There were significant increases in the stretched lens anterior fibre widths at depths of 120 μm through to 240 μm ($p < 0.050$), except at 210 μm (Figure 4-8). Increases were similarly observed in the stretched lens posterior fibre widths, but only at depths of 150 μm and 180 μm ($p < 0.001$).

The suture confluence area (the gap between sutures at the lens pole, Figure 4-9) appeared to increase gradually with depth from both the anterior and posterior surfaces, in both stretched and unstretched lenses. Upon stretching, the suture confluence area decreased in the anterior of the lens, at depths of 30 μm ($p = 0.003$), 60 μm ($p = 0.013$) and 180 μm ($p = 0.012$). Conversely, stretching saw an increase in the posterior area, at depths of -30 μm ($p = 0.027$) and -240 μm ($p = 0.000$), coupled with a decrease at -210 μm ($p = 0.006$) (Table 4-2).

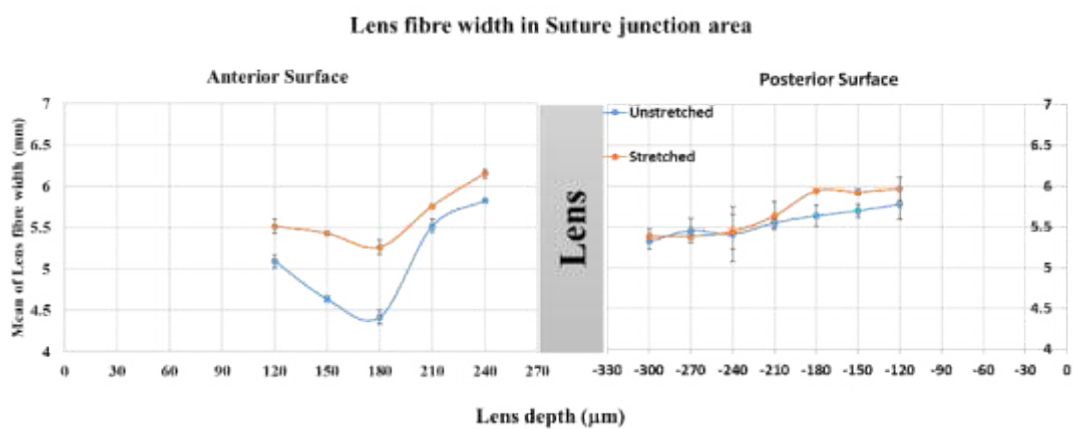


Figure 4-8: The lens fibre widths in both anterior and posterior surfaces. In the anterior lens surface, the average lens fibre width in unstretched lenses was $5.1 \pm 0.6 \mu\text{m}$ ($n = 4$) and for stretched lenses was $5.6 \pm 0.3 \mu\text{m}$ ($n = 4$). In the posterior lens, the average of lens fibre width in unstretched and stretched lenses ($n = 4$) was $5.5 \pm 0.1 \mu\text{m}$, and ($n = 4$) was $5.7 \pm 0.3 \mu\text{m}$, respectively.

Confluence Area

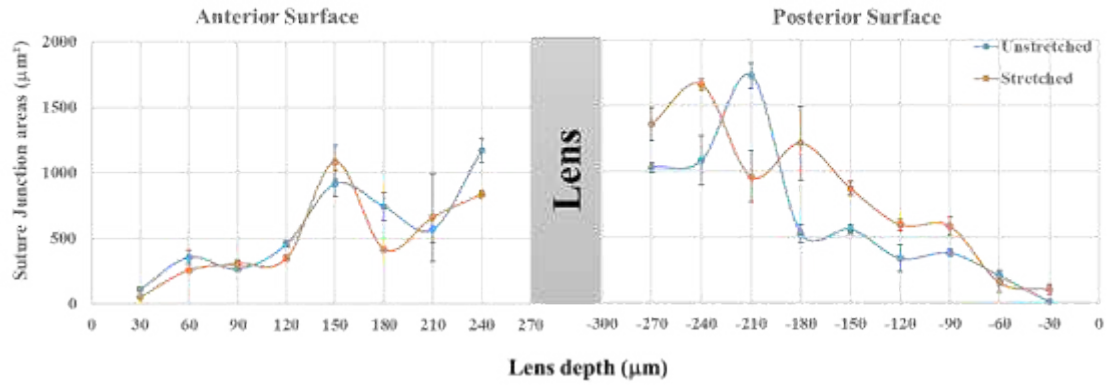


Figure 4-9: The suture confluence area in both the anterior and posterior surfaces: in the anterior lens, the mean of confluence area in unstretched lenses (n = 4) was $574.1 \pm 64.7 \mu\text{m}^2$ and for stretched lenses (n = 4) was $494.7 \pm 72.9 \mu\text{m}^2$. However, in the posterior lens surface, the average confluence area in unstretched lenses (n = 4) was $652.5 \pm 67.7 \mu\text{m}^2$ and for stretched lenses (n= 4) was $833.4 \pm 102.9 \mu\text{m}^2$.

| Anterior lens (mean \pm sd, μm^2) | | | Posterior lens(mean \pm sd, μm^2) | | |
|---|---------------|----------------|---|----------------|----------------|
| Depth (μm) | Unstretched | Stretched | Depth (μm) | Unstretched | Stretched |
| 30 | 113 \pm 19 | 53 \pm 4 | -30 | 10 \pm 5 | 101 \pm 40 |
| 60 | 356 \pm 51 | 258 \pm 315 | -60 | 204 \pm 46 | 152 \pm 73 |
| 90 | 266 \pm 20 | 305 \pm 28 | -90 | 381 \pm 26 | 587 \pm 69 |
| 120 | 457 \pm 27 | 348 \pm 22 | -120 | 339 \pm 103 | 594 \pm 43 |
| 150 | 919 \pm 102 | 1081 \pm 131 | -150 | 561 \pm 34 | 871 \pm 55 |
| 180 | 742 \pm 107 | 415 \pm 18 | -180 | 529 \pm 69 | 1217 \pm 280 |
| 210 | 569 \pm 98 | 659 \pm 337 | -210 | 1730 \pm 98 | 958 \pm 194 |
| 240 | 1169 \pm 93 | 836 \pm 26 | -240 | 1084 \pm 188 | 1663 \pm 40 |
| 270 | N/A | N/A | -270 | 1032 \pm 38 | 1359 \pm 129 |

Table 4-2: Anterior and posterior suture confluence area (mean \pm standard deviation) as a function of lens depth.

4.3.3.2 Lens suture shape within the anterior and posterior lens

In the anterior confocal image of the lens suture area, the shape of the suture end, at the suture confluence area (lens pole) appeared change as a function of depth (Figure 4-10). At the 30 μm depth, the Y suture shape appeared to converge with a very tiny gap in the suture confluence area, then increased again at 150 μm (Figure 4-10 (E)). The images in Figure 4-10 showed the non-regularity at the suture end shape and the gap in the suture itself at different depths.

The visual appearance of the shape and gap between lens sutures at the anterior surface did not appear different between unstretched and stretched lenses (Figure 4-10. unstretched and stretched lenses). In three of the five lenses, at the 150 μm depth, there was a slight decrease in the gap when the lenses were stretched. However, the posterior view of the suture junction was different relative to the anterior (see Figure 4-11. unstretched and stretched lenses). One of the three angles in the posterior Y suture was narrower than the other two angle sutures (about 70°) (Figures 4-11. A and A's dash arrow) in four of the five lenses. This narrow-angle disappeared at the 90 μm depth, to create appropriate Y suture angles (Figures 4-11 (C) and 4-11 (C)'s dash arrow). Further, the suture confluence area increased with depth, and at 210 μm , the area was narrower in stretched lenses compared to unstretched lenses. These observations were present in three of the five lenses (Figures 4-11 (G) and 4-11 (G)'s dash arrow).

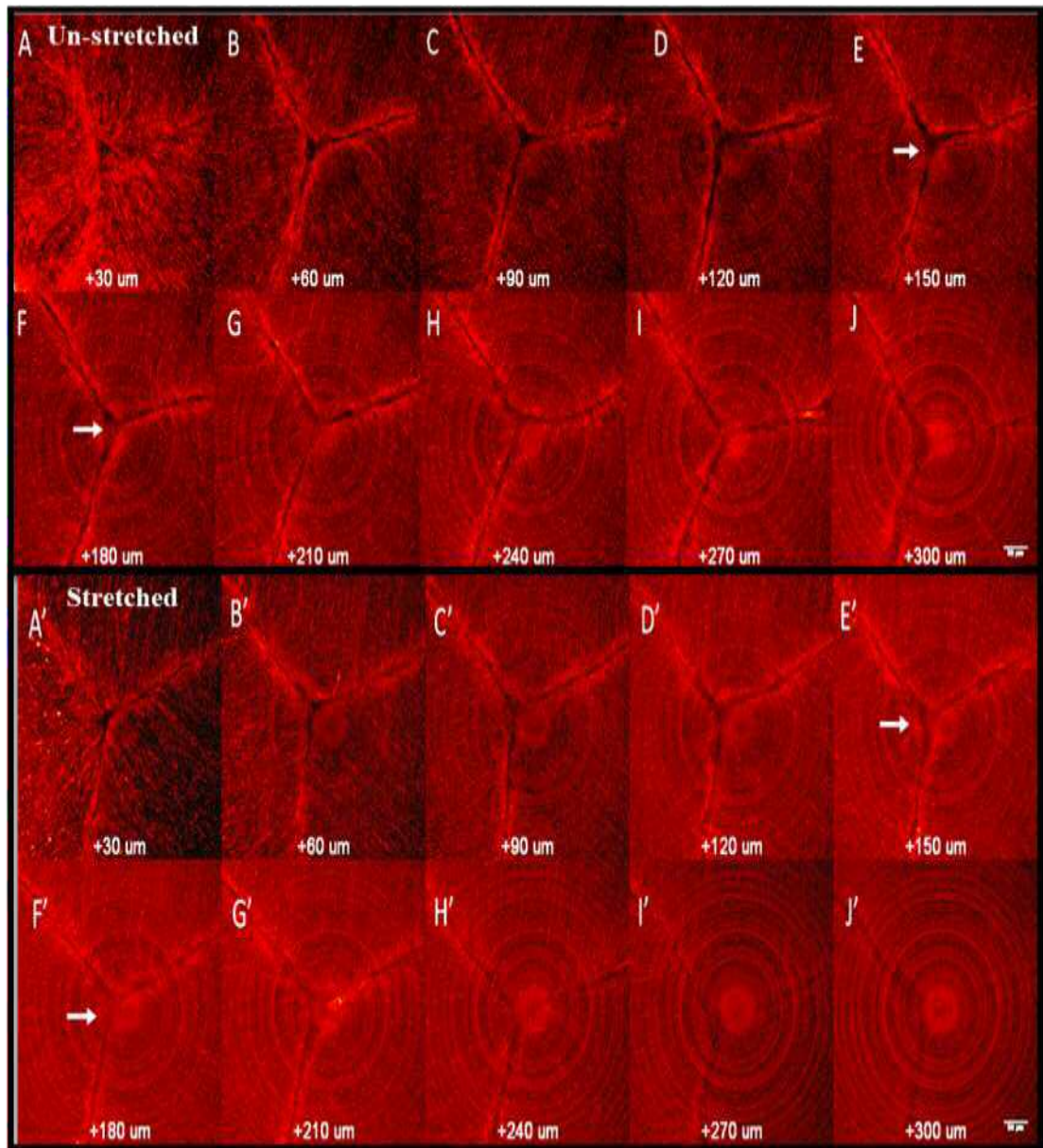


Figure 4-10: The anterior lens suture at different depths in the un-stretched and stretched conditions. The white arrow points to the suture end at the lens pole. In both un-stretched and stretched conditions, at depth 30 μm , the suture ends are tight to each other. At 300 μm , the suture ends become separated from each other compared with first photo 30 μm . The patterns of concentric circles seen in these images are an optical artefact. Scale bar 50 μm .

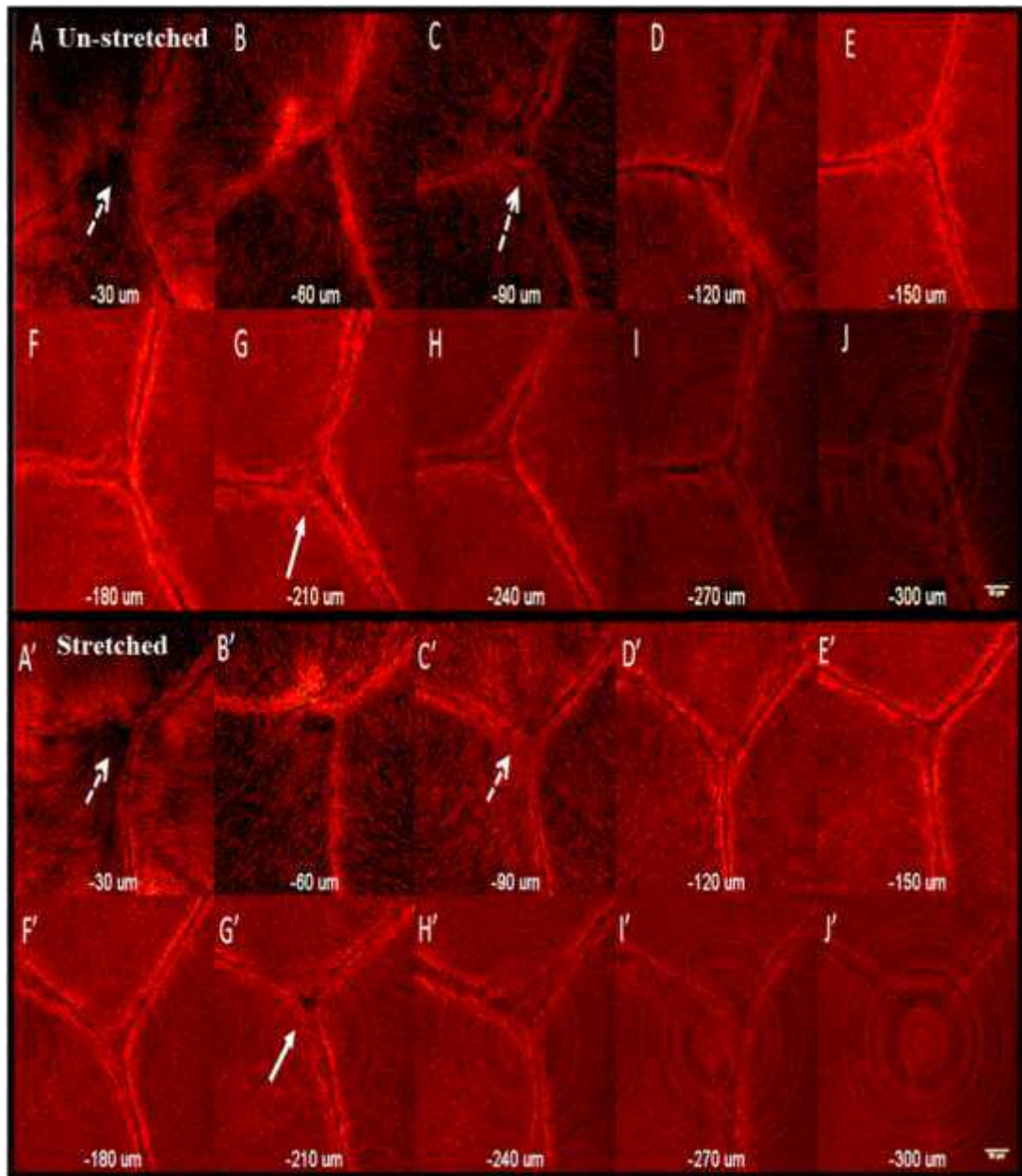


Figure 4-11: The posterior lens suture at different depths in the unstretched and stretched conditions. The white dash arrow points to the narrow suture branch (70° angle) that is clear in the $-30\ \mu\text{m}$ image but disappears at about $-90\ \mu\text{m}$. At about the depths of $-210\ \mu\text{m}$, the suture ends start to drift apart relative to images A and A' in the montage. The patterns of concentric circles seen in these images are an optical artefact. Scale bar $50\ \mu\text{m}$.

The suture's pattern appears to alter with depth. At the 300 μm depth, the suture pattern in the posterior surface is more undulated relative to the anterior lens surface at a similar depth (Figure 4-12).

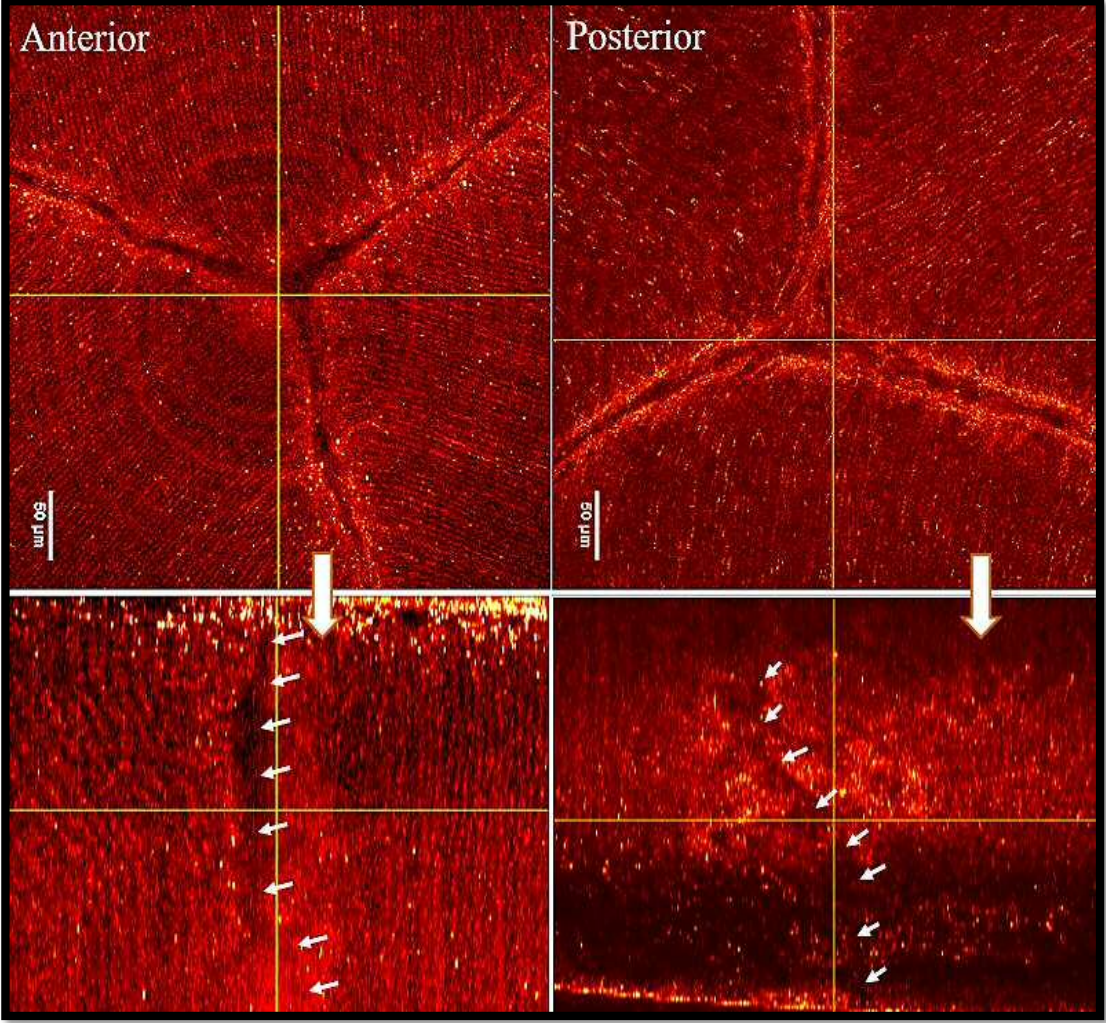


Figure 4-12: Orthogonal of the suture pattern at a depth of 300 μm in the anterior and posterior lens surfaces. The white arrow shows the suture line's undulation as a function of depth. The posterior surface shows more curvature than the anterior surface. Scale bar 50 μm .

4.3.4 Lens Fibre Widths throughout the full depth of the porcine lens

Since it was not possible to observe and measure the fibre widths throughout the whole lens, serial cryosections of 3 stretched and 3 unstretched lenses were cut. Then, regional (suture junction, superior, inferior, nasal, and temporal) lens fibre width measurements were performed at one-millimetre depth intervals, ranging from 1 mm to 7 mm for unstretched lenses and 1 mm to about 6.6 mm for stretched lenses. Lens fibre widths as a function of depth and stretch are presented in Table 4-3 and Figure 4-13.

| Lens Fibre Widths (mean+/-standard deviation) (µm) | | | | | | | | |
|--|--------------------|----------|----------------|-----------|-----------|----------|----------|----------|
| | Depths | 1 mm | 2 mm | 3 mm | 4 mm | 5 mm | 6 mm | 7 mm |
| Suture Junction | <i>Unstretched</i> | 5.3±0.07 | 4.0±0.0.0 3 | 3.7±0.04 | 3.5±N/A | 4.3±0.15 | 4.4±0.30 | 4.2±0.14 |
| | <i>Stretched</i> | 5.2±0.15 | 4.5±0.07 | 4.9±0.18 | 5.2±0.57 | 4.2±0.10 | 5.1±0.15 | 5.4±0.10 |
| Superior | <i>Unstretched</i> | 5.8±0.14 | 6.9±0.05 | 8.1±0.10 | 9.8±0.09 | 8.7±0.06 | 5.9±0.14 | 7.6±0.14 |
| | <i>Stretched</i> | 5.9±0.05 | 9.2±0.07 | 10.4±0.07 | 10.3±0.13 | 8.6±0.17 | 7.5±0.08 | 5.6±0.06 |
| Inferior | <i>Unstretched</i> | 6.1±0.02 | 7.2±0.16 | 9.4±0.17 | 9.9±0.02 | 8.8±0.07 | 7.4±0.11 | 7.0±0.11 |
| | <i>Stretched</i> | 5.9±0.05 | 8.2±0.07 | 9.8±0.07 | 10.1±0.13 | 9.2±0.17 | 5.8±0.08 | 5.7±0.06 |
| Nasal | <i>Unstretched</i> | 5.6±0.02 | 8.4±0.05 | 9.2±0.08 | 9.1±0.11 | 8.0±0.16 | 6.0±0.33 | 7.2±0.04 |
| | <i>Stretched</i> | 5.9±0.15 | 8.8±0.23 | 9.3±0.08 | 9.4±0.16 | 9.5±0.05 | 5.6±0.18 | 6.1±0.14 |
| Tempora | <i>Unstretched</i> | 5.7±0.09 | 8.2±0.09 | 9.2±0.16 | 9.9±0.09 | 8.5±0.08 | 6.3±0.29 | 7.4±0.10 |
| | <i>Stretched</i> | 6.4±0.19 | 8.6±0.07 | 10.5±0.05 | 10.4±0.09 | 8.2±0.07 | 5.9±0.12 | 5.5±0.10 |

Table 4-3: Mean and standard deviations of lens fibre widths in five areas: suture junction, superior, inferior, nasal, and temporal, as well as different depths 1-, 2-, 3-, 4-, 5-, 6-, and 7-mm.

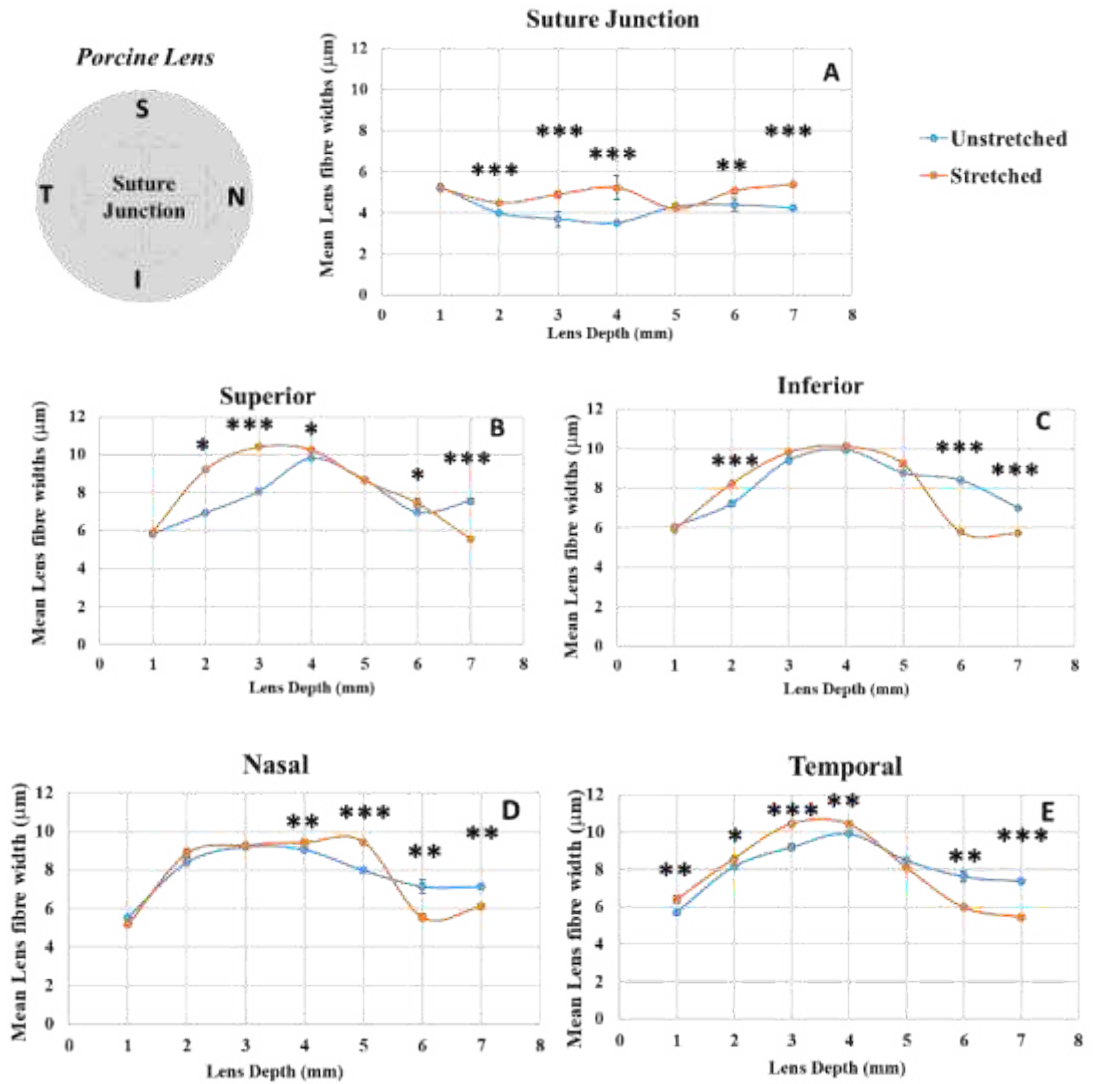


Figure 4-13: Lens fibre widths measured in 25µm tissue sections at 1mm depth intervals in five areas: the suture junction area (A), superior area (B), inferior area (C), nasal area (D), and temporal area (E). The top left inset in this figure demonstrates the location of B, C, D, and E areas relative to the suture junction area. In all these areas, the lens fibre widths clearly increased towards the lens centre and then decreased towards the posterior, with the exception of the suture junction area.

All the lens fibre widths increased as a function of depth when stretched ($p < 0.05$) at the depths of 2 mm ($6.9 \pm 2.2 \mu\text{m}$ versus $7.9 \pm 2 \mu\text{m}$), 3 mm ($8.2 \pm 2.1 \mu\text{m}$ versus $9.3 \pm 2.0 \mu\text{m}$), and 4 mm ($9.0 \pm 1.9 \mu\text{m}$ versus $9.4 \pm 1.9 \mu\text{m}$). A decrease in the posterior cortical lens fibre widths was observed upon stretching at depths of 6 mm ($7.1 \pm 2.1 \mu\text{m}$ versus $6.0 \pm 1.1 \mu\text{m}$), and at 7 mm ($6.7 \pm 1.7 \mu\text{m}$ versus $5.7 \pm 0.8 \mu\text{m}$) ($p < 0.001$). Stretching also decreased the lens fibre widths in the superior, inferior, nasal and temporal regions at 6 ($p < 0.05$) and 7 mm ($p < 0.01$) depths (Figures 4-13A-E). At more anterior depths of stretched lenses, the results were inconsistent. Stretching increased the fibre widths at depths of 2 to 4, 6, and 7 within the suture junction area; and at 2 to 4 in the superior area; 2 mm in the inferior area; 4 and 5mm in the nasal region; and 1-4 mm in the temporal area ($p < 0.05$). No difference in inferior lens fibre widths between stretched and unstretched lenses was observed at depths of 1 mm as well as between depths of 3 mm and 5 mm ($p > 0.05$) (Figure 4-13.C).

Additional analysis to compare lens fibre widths as a function of lens anatomical regions (i.e. nucleus versus anterior, posterior, and equatorial cortices) identified a significant increase in lens fibres widths in stretched lenses within the nucleus ($43.3 \pm 4.49 \mu\text{m}$ versus $45.35 \pm 3.6 \mu\text{m}$, $p = 0.002$); the anterior cortex ($67.3 \pm 3.56 \mu\text{m}$ versus $72.9 \pm 2.82 \mu\text{m}$, $p = 0.001$) and the equatorial cortex ($90.5 \pm 1.39 \mu\text{m}$ versus $96.5 \pm 1.88 \mu\text{m}$, $p = 0.000$). Interestingly, a significant decrease in the posterior cortical lens

fibre widths ($71.2 \pm 2.7 \mu\text{m}$ versus $59.6 \pm 1.38 \mu\text{m}$, $p = 0.000$) was observed upon stretching (Figure 4-14).

4.3.5 General observations of the porcine lens throughout the full depth

The lens diameters were measured from the superior to the inferior (vertical) and from the nasal to the temporal (horizontal) regions. The average and standard deviations were presented in Figure 4-15.

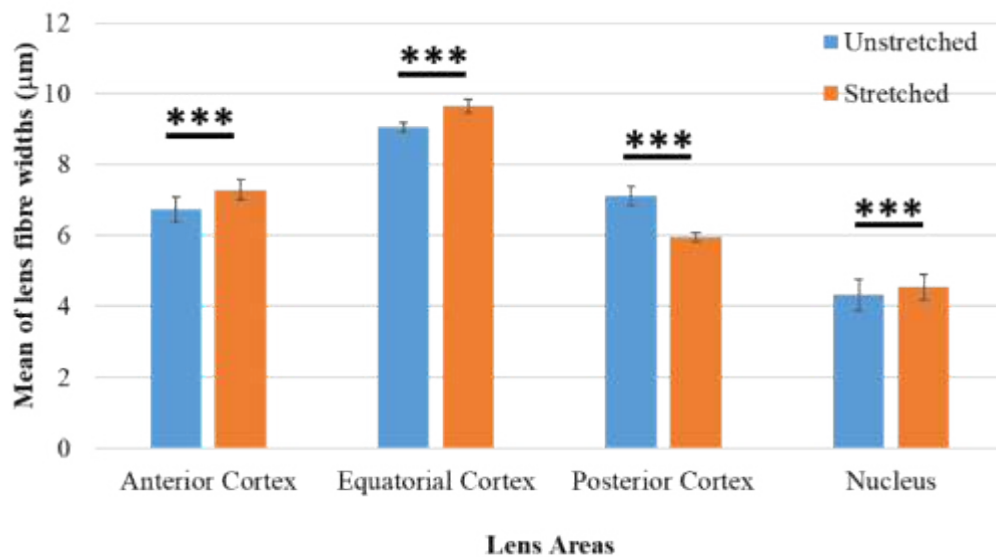


Figure 4-14: Lens fibre widths in nuclear and cortical areas in unstretched ($n = 3$) and stretched ($n = 3$). The lens fibre widths measured in lens tissue sections; anterior cortex (included the lens fibre widths in superior, inferior, lateral and nasal areas at 1 and 2 mm depths), equatorial cortex (included the lens fibre widths in superior, inferior, lateral and nasal areas at 3, 4 and 5 mm depths), posterior cortex (included the lens fibre widths in superior, inferior, lateral and nasal areas at 6 and 7mm depths) and nucleus (included the lens fibre widths in suture area at 3, 4 and 5 mm depths).

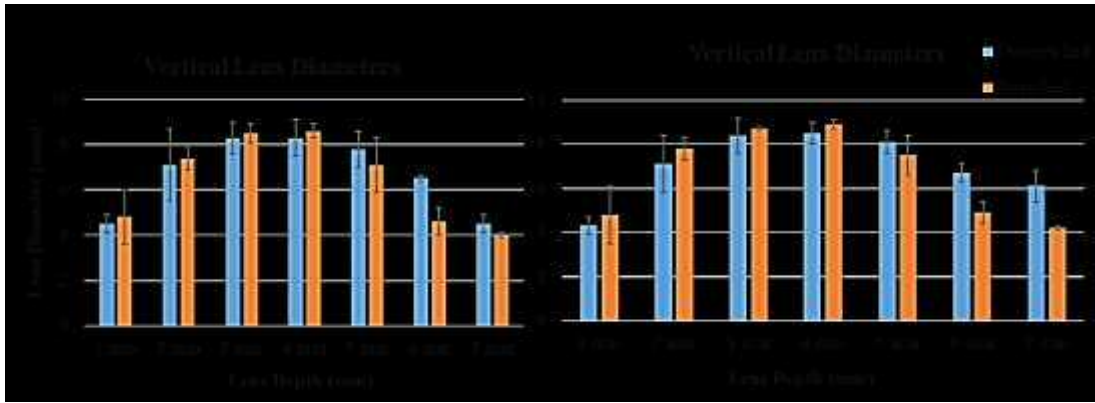


Figure 4-15: Vertical and horizontal measurements diameters as a function of lens depths in un-stretched (n=1) and stretched (n=1) lens.

4.4 Discussion

While human eyes are the most appropriate species for studying the accommodation, the availability of young lenses (i.e. under 40 years, as the eye lens loses its flexibility to accommodate with age) in a fresh condition is very low. Even though porcine lenses are thought not to accommodate (Barrett, 1938), porcine lenses have been used in many studies as a model for accommodation and presbyopia studies (Hahn et al., 2015; Sueiras et al., 2015). In 2012, Kammel et al. specified the age range of porcine lenses that can be usefully applied to accommodation and presbyopia studies. Young porcine lenses change in optical power upon stretching; to a greater extent (approximately 5 times greater than in adult porcine lenses) (Kammel et al., 2012). The lenses used in this study were aged 6 months, and all were received in fresh condition (within 6 hours of sacrifice).

4.4.1 The behaviour of the lens curvature radii during the accommodated and unaccommodated states as seen under optical coherence tomography

Helmholtz's theory postulates that the ciliary muscle contracts to release the radial tension on the zonular fibres. As a result, the lens surface curvature steepens anteriorly more than posteriorly, with consequent thickening of the lens axial diameter (Brown, 1973). The accommodative changes in the anterior and posterior lens surfaces have been shown in multiple empirical works, both in monkeys and humans (Rosales et al., 2008; Ostrin et al., 2006; Rosales et al., 2008).

It is unsurprising, therefore, that the results of the present study showed that the accommodation in porcine lens resulted in changes in the anterior and posterior lens radii curvature. The anterior and posterior radii of curvature increased in the unaccommodated lens, which was consistent with Rosales et al. (2008), but also inconsistent with a number of existing works. For example, Hahn et al. (2015), found that on stretching (unaccommodated), the lens thickness, diameter, and anterior radius of curvature increased by 140%, 54%, and 57%, respectively, while the posterior radius of curvature showed no appreciable change.

4.4.2 Individual lens fibre widths

This study found that the mean of superficial lens fibre widths was $6.1 \pm 0.2 \mu\text{m}$ in the accommodated state. This is significantly higher than the width found by existing studies. Hoyer (1982), for example, determined that the porcine lens fibre was much smaller than was measured in the present study. Hoyer (1982)'s scanning electron microscopy investigation of the superficial (porcine) lens fibre established that the maximum lens fibre width was $4.5 \mu\text{m}$. The difference in the fibre width values between the present study and Hoyer (1982) likely stems from the fact that the SEM specimen preparation protocol relied upon chemical agents that cause dehydration and shrinkage of the lens cells.

4.4.3 The lens fibre width as a function of depth and areas

This study also investigated the lens fibre width at different depths within the five different areas. The results were consistent with past studies on the Y-shaped suture as there was a gradual reduction in the lens fibre width, at the rate of 2:1, from the equator towards the suture ends (Kuszak et al., 1984; Kuszak, 1995a). While the equatorial region cuts across four lens areas (inferior, nasal, superior, and temporal), the lens fibre width measurements at the suture junction area were only taken in areas close to, but not in, the suture ends. The average fibre width in equatorial regions decreased towards the suture junction area. In addition, since the lens fibre measurements were

taken from strained sections of whole lenses, it was clear that, at the suture junction area, the average fibre width decreased as a function of increasing depth from the anterior surface towards the centre of the lens. The width then began to increase again towards posterior pole. However, the opposite trend manifests within the equatorial areas, gradually increasing from the anterior surface up to the lens centre. The width then decreases towards the posterior surface.

4.4.4 Lens fibre widths in accommodated and unaccommodated states

4.4.4.1 Lens fibre widths at the lens surface using upright microscopy in accommodated and unaccommodated states

The current study showed the trend of changes in the lens fibre widths between accommodated and unaccommodated whole lenses, starting from the anterior cortex, through the nucleus, to the posterior cortex. The structure of the lens fibre changes considerably with both senescence and maturation, in large part because of the limited space and necessity for a higher refractive index (Lovicu & Robinson, 2004; Costello et al., 2013a). In a healthy lens, the cortical lens fibres are more regularly packed compared to the nuclear fibres (Al-Ghoul & Costello, 1997). This is particularly relevant in respect to cataracts and age-related sight problems (Al-Ghoul et al., 2001; Costello et al., 2013a; Al-Khudari et al., 2007). In nuclear cataracts, for example, the nuclear fibres exhibit higher compaction relative to healthy lens fibres in the same region at the same age (Al-Ghoul et al., 2001). With aging, however, the lens epithelial

layer differentiates to form new lens fibre shells within the lens cortex. As a result, the nuclear lens fibres exhibit higher compaction relative to the cortical lens fibres (Brown et al., 1988; Al-khudari et al., 2007).

There is a theoretical and empirical literature consensus that the whole lens thickness changes during accommodation, i.e. the thickness increases and reduces during accommodation and unaccommodation, respectively (Lovicu & Robinson, 2004; Kuszak, 1995b). At the superficial lens fibre level, the present study found no statistically significant differences in the fibre widths of any of the five areas in the superficial lens fibre widths between the unaccommodated and accommodated conditions. As this study was mainly focused on the superficial lens fibre widths, these results were consistent with the existing *ex vivo* study into the fibre cells behaviour within the anterior area during accommodation in both humans and monkeys which relied on a dissecting microscope (Kuszak & Zoltoski, 2005). Kuszak & Zoltoski (2005) found no significant difference in the lens fibre morphology or dimensions between the accommodated and unaccommodated conditions, which keeps the lens transparent.

4.4.4.2 Lens fibre widths at the anterior and posterior lens surfaces in accommodated and unaccommodated states

This study made three important observations related to changes in the lens fibre width between accommodated (unstretched) and unaccommodated (stretched) lenses, as a

function of depth within five lens areas. Firstly, the lens fibre width exhibited resistance to change in most areas at 1 mm and 5 mm. Secondly, most of the increases in the lens fibre widths across most lens areas, when stretched, occurred at the depths of 2 mm, 3 mm, and 4 mm. Thirdly, there was a decrease in the lens fibre width when stretched within the lens posterior region (except at the suture junction at the 7 mm depth). These results, however, do little to clarify the ambiguity in the existing literature (Kuszak et al., 2006; Kuszak et al., 2004; Parreno et al., 2018).

Parreno et al. (2018), for example, found that a 6% equatorial strain in mouse lens increased the fibre width by $11.7 \pm 0.2 \mu\text{m}$ and a 9% strain increased the fibre width by $11.8 \pm 0.1 \mu\text{m}$, effectively, the average lens fibre width increased by 5.8% and 9.0%, respectively. While there was a general increase in the lens fibre width with any equatorial strain, strains of under 2% produced no statistically significant change in the fibre widths ($p > 0.99$). The fibre widths returned to their original sizes once the strain had been withdrawn.

This present study uses a lens stretching device that mimics the *in vivo* lens stretching more accurately, and showed an increase in lens fibre widths across most lens areas at the depths of 2 mm, 3 mm, and 4 mm, when stretched. The present study also showed that the lens fibre width did not alter at 1 mm and 5 mm, which is consistent with Kuszak and Zoltoski (2005). The divergence between the rest of the study's findings (the increase in the lens fibre widths at depths of 2 mm, 3 mm, and 4 mm, and the

decrease in the lens fibre within the lens posterior region) and Kuszak and Zoltoski (2005) may be accounted for by differences in the experimental methods and/or the depths/areas from which the measurement were performed. In this study, all samples used to simulate the accommodated and unaccommodated state were chemically fixed before dissection, and measurements were taken after the staining process. In Kuszak and Zoltoski (2005), on the other hand, the lenses were fixed (using an unclear fixation protocol) and the measurements were taken using a stereo surgical dissecting microscope. Further, while the lens fibre widths in the present study were from defined depths in the superior, nasal, temporal, inferior, and centre regions of the lens, Kuszak, and Zoltoski (2005) measured the lens fibre width at unspecified depths in the anterior, middle or equatorial and posterior regions. Lastly, and perhaps most importantly, while Kuszak and Zoltoski (2005) used primate lenses (with a more complex star-shaped suture), this present study used porcine lenses.

This study also took measurements of the lens fibre widths obtained from both the nucleus and the cortex (anterior, posterior, and equatorial cortex). With the exception of the posterior cortex, the results showed that in the unaccommodated lens, there was a significant increase in the lens fibre widths in both the nucleus and the cortex. To understand why this is so, it is helpful, once again, to remember the functions of, and the manner in which the zonules attach to the lens capsule. The anterior zonular fibres insert nearer to the anterior visual axis, compared to the posterior zonular fibres (Figure 4-16) (Helmholtz, 1855; Schachar, 2012). The anterior surface is relatively more

responsive to accommodative strain, compared to the posterior lens surface (Rosales & Marcos, 2006; Lovicu & Robinson, 2004). Further, Goldberg's investigation of the zonules' function using a 3D animated model of the lens in both accommodated and unaccommodated conditions, concluded that when the lens is accommodated by ciliary body contraction, the anterior zonules lose tension while the posterior zonules stretch and apply force on the posterior lens capsule playing a role in shaping the posterior lens thickness and curvature (Goldberg, 2011). During unaccommodated conditions when the ciliary body relaxes, the posterior zonules lose tension as the lens flattens and are pulled back by the increasing strain of the anterior zonules (Goldberg, 2011).

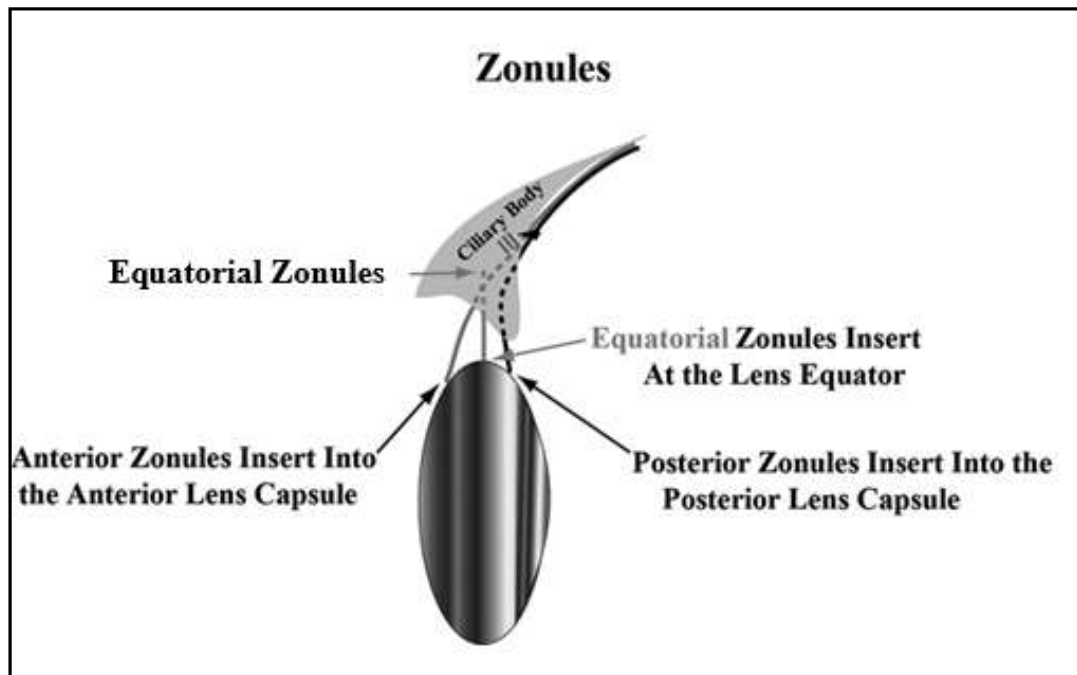


Figure 4-16: Diagrammatic representation of the origin and insertion of the zonules with lens capsule. adapted from (Schachar, 2012).

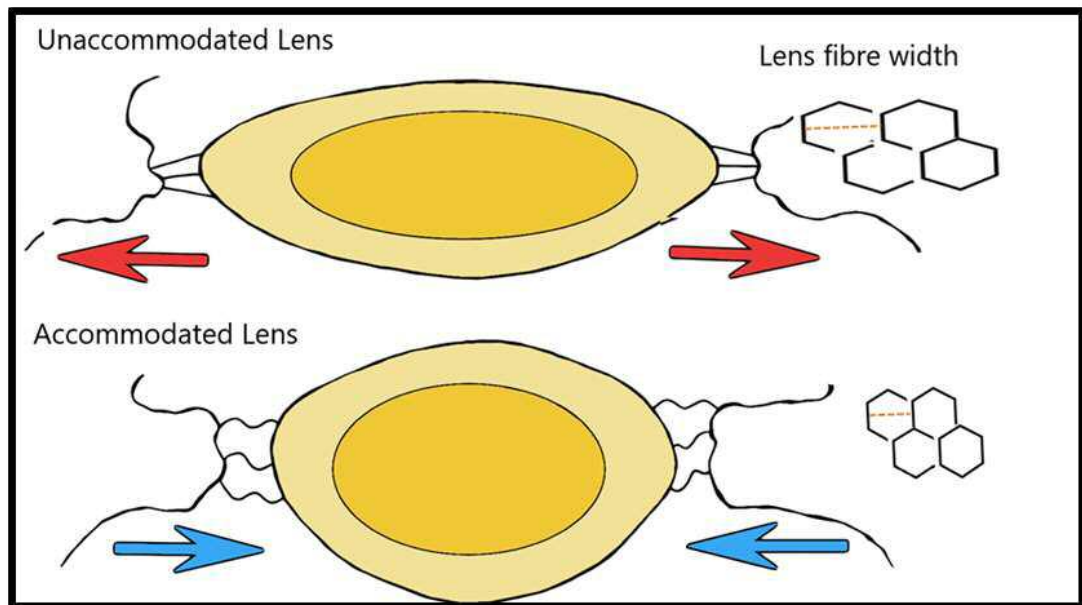


Figure 4-17: The axial thickness decreases in the unaccommodated states, while the axial thickness increases in the accommodated states. The diagram also shows an expectation of how the lens fibre width increases in an unaccommodated lens and the lens fibre width decreases in an accommodated lens.

Figure 4-17 proposes what may happen with respect to the lens fibre widths during the unaccommodated and accommodated states, stretching on the anterior zonular fibres at the lens equatorial/anterior area occurs, allowing the axial lens thickness to decrease as a result of increasing the main unit of the lens (lens fibre widths) in the anterior and equatorial lens area (Figure 4-17). The opposite occurs during the loss of the tension on the posterior zonular fibres at the posterior lens, the axial lens thickness increases as a result of decreasing the main unit of the lens (lens fibre widths) (Figure 4-17).

Therefore, the current results found that the lens fibre increased in the nucleus, anterior and equatorial cortex (in an unaccommodated lens), which is consistent with the findings of Patnaik (1967) and Dubbelman et al. (2003) regarding changes during the

accommodation. These are similarly supported by both Hockwin and Oxford systems. According to the Hockwin and Oxford systems, the nucleus region thickness showed increases of ~ 0.040 mm/D, while the Hockwin system showed that the anterior cortical region expresses a slight increase (~ 0.004 mm/D) (Hockwin, 1989, Hockwin et al., 1982).

Counter-intuitively, the present study found that the lens fibre widths in the posterior cortex decreased in the unaccommodated state. Consistent with the Oxford system, the current result showed that without accommodation, there is an appreciable decrease in the lens fibre width in the posterior cortex, compared to that in the anterior/equatorial lens cortex. The Oxford system estimated that the change in the posterior lens surface during accommodation was ~ -0.002 mm/D (Dubbelman et al., 2003).

This study's findings in this respect are contradictory to Kuzak et al. (2005). While Kuzak et al. (2005) concluded that there was no appreciable difference in lens fibre widths between accommodated and unaccommodated states, except for those caused by the tape and flare of lens fibres' ends at the suture junction, this study's findings, backed up, by the Oxford/ Hockwin systems, showed that the accommodation involved and/or resulted in changes in the lens fibre widths. It is, however, necessary to put the observations in this study in their proper context. This is in part because the stretching device used in this study applied force equatorially through the zonules (to simulate the unaccommodated states). The strain was artificially induced, and the lenses used were obtained from species that do not naturally accommodate. The

measured fibre widths can establish a wide spectrum of information, provided that these variations are biological and not experimentally induced artefacts. However, the measured fibre widths are also likely to be affected by not only the magnitude of the strain applied by the stretching device, but also by the conditions under which the measurements are taken.

4.4.5 Lens suture angles

4.4.5.1 The Y-shaped suture angle in anterior and posterior surfaces

The lens suture morphology varies between species, between line-, umbilical-, Y-, and star-shaped (Kuszak and Costello, 2004). The present study's results were consistent with Kuszak, & Costello (2004), which found that the porcine lens has an anterior Y-shaped suture, each of whose planes creates a 120° angle. The anterior lens suture angles that observed under a light microscope in this study, on the other hand, showed no significant change during the accommodation.

However, the confocal microscopy results suggested that the Y-shaped suture angles in the posterior and anterior were not identical and clearly not 120°, especially in the posterior lens. In four of the five lenses studied, very narrow suture angles (~70°) were observed in the posterior surface. With increasing depth, these angles gradually increased to become the same as the other suture angles. Al-Ghoul et al. (2003) argued that the fibre ends in the lateral-posterior region are packed into short irregular rows with variable orientation in relation to the posterior pole. The rest of the fibre ends are arranged fairly randomly. Towards the suture branches within the peri-sutural region,

the fibre ends are arranged in short rows oriented at angles to the posterior pole (Al-Ghoul et al., 2003). Furthermore, this suggests that anterior and posterior fibre ends are exposed to various signals, which influence the direction of the growth of the fibres, thereby affecting the overall structural organisation of the fibres (Kuszak et al., 2006, McAvoy et al., 1999). This causes unequal suture ends at the posterior and anterior surfaces.

Further, this study indicated that the suture lines grow increasingly undulated as a function of depth in the lens equatorial plane. As there may be no previous optical experimental structural studies that have investigated the porcine lens sutures at different depths, these structures have not been observed before and their precise function is not known. Kuszak et al (2005) suggested that there is a unique circulatory system within the confluence of suture branches (at the poles) to supply a fluid and nutrients into lens, and then to the fibres via aquaporin water channels, being transported along the length of fibres, and subsequently between fibres toward the equator via gap junctions. It may be that the changes to the undulating suture line are indicative of a change in the circulatory system with depth and a concomitant increase in the crystallin protein concentration and refractive index within the lens fibres. The lens suture helps achieve alterations in the shape of the lens during accommodation, as well as playing important physiological functions such as allowing fluid to flow through the lens (Kuszak et al., 2006; Vaghefi et al., 2012).

4.4.5.2 General observations on the Y-suture confluence area

This study also illustrated a simple protocol for measuring the area within the suture confluence at different depths in fresh lenses, both in the posterior and anterior surfaces. The suture confluence area (at pole) was clearly unequal at different depths in the anterior and posterior surfaces. Stretching was mildly significant in the suture confluence at the anterior surface and strongly significant at the posterior surface. This was consistent with Parreno et al. (2018), whose investigation of the suture gap area in mice lens, before and after the application of strain, showed that a 10% axial strain induced a significant increase in the suture gap area. The suture gap area returned to its original size when the axial strain was withdrawn (Parreno et al., 2018).

Furthermore, the change of suture confluence area can partly explain, anatomically, how the secondary fibre shells are constructed through lens life. It may be that new fibre shells are arranged with the ends of the fibres tightly packed in the confluence areas of the posterior and anterior lens poles compared with older, deeper fibre shells. Kuszak (2005) used computer modeling to understand the secondary fibre development, which suggested that the posterior fibres' ends are closer to the posterior pole than that in the anterior pole. The current study showed that within 60 μm depth, the suture confluence area is more tightly packed at posterior surface, than the anterior. However, at a depth of 90 μm , the confluence suture area's trends were dissimilar in both anterior and posterior surfaces as a function of depth. The confluence of all three suture lines was slightly off-centre. The structural changes with depth is controversial

to the concept that suture branches originate peripherally and continue to develop to confluence at the lens poles (Kuszak et al., 2006, Kuszak and Zoltoski, 2005).

4.5 Conclusion

Studying biometric changes of/in the lens during accommodation is important in our understanding of both the accommodation and age-related changes resulting in disorders such as presbyopia (Rosales et al., 2008). This study's results showed that the accommodation involved changes in the lens fibre width. Particularly, the results found that the lens fibre width increased in the nucleus, anterior and equatorial cortex (in the unaccommodated lens), which is consistent with Patnaik (1967) and Dubbelman et al. (2003)'s findings of changes during accommodation. These are similarly supported by both Hockwin and Oxford systems (Hockwin, 1989, Hockwin et al., 1982). This study also found that the lens fibre widths in the posterior cortex decreased in the unaccommodated state, which is consistent with the Oxford system, which showed that the change in the posterior lens surface during accommodation is negative (~ -0.002 mm/D) (Dubbelman et al., 2003).

Further, this study's findings indicate that the anterior lens suture angle showed an appreciable change as a function of the anterior/posterior lens depth. In this respect, this study offers possible solutions for enhancing the experimental protocols by putting forward enhanced chemical fixation to better preserve the lens features for more

accurate and realistic experiments. Maintaining the integrity of the lens in both accommodated and unaccommodated conditions should be instrumental in contributing towards understanding the accommodative activity of the lens sutures, fibres, and other related parts.

Chapter Five

5 General discussion

Normal vision mainly depends on both the ocular lens maintaining its transparency and the accommodation mechanism (Trokel, 1962; Harding, 1991). Nearly all people living beyond middle age may suffer from presbyopia. An estimated 10.8 million people in the world are blind and a further 35.1 million people are visually impaired due to cataracts (World Health Organisation, 2010). On the other hand, up to 108 million and 517 million people across the world are afflicted by impaired distant vision and near vision, respectively.

Advancing the understanding of the accommodation is, therefore, extremely important. The Helmholtz theory is an important starting point. It postulates that during accommodation or near vision, the ciliary muscles contract to ease tension on the zonules. As a result, the lens surface curvature steepens relatively more anteriorly than posteriorly, simultaneously causing an increase in the lens axial diameter and a reduction in the equatorial diameter. In spite of the Helmholtz theory's popularity and broad empirical support (Schachar, 2006), experimental research has been slow in understanding the internal structural changes causing and/or caused by accommodation, in a large part, because of the difficulty of simulating the unaccommodated state *ex vivo*. Even with the advances in stretching device technology, it is still necessary to keep the lens intact in order to maintain the integrity of the internal structures. Research into the behaviour of the lens internal structures

during accommodation does, however, hold good potential for understanding and treating disorders such as presbyopia.

This present study's results may be categorised into four distinct groups: i) lens crystallin proteins and their ordering in different groups of animals, ii) crystallin proteins in the accommodation, iii) the change of other lens features (mainly suture/ lens widths) as a function of the lens depth, and iv) the change of lens fibre widths in nuclear and cortical areas during accommodation.

5.1 Crystallin proteins and their ordering in different groups of animals

The underpinning aim of this study was to understand the structural and ultrastructural composition of the lenses of mammalian and aquatic species. In the case of the terrestrial mammals, which accommodate by deformation, a further aim was to investigate any structural and ultrastructural changes in the accommodated and unaccommodated states. All samples were chosen on the basis of availability. Atlantic salmon was chosen as a representative of Teleost fish, the European squid as a representative of cephalopods, and porcine as a mammalian representative. The detailed X-ray scattering from intact lens cortex and lens nucleus of a terrestrial animal and two aquatic animals showed that the lens crystallin profiles were different. This is expected, since the type and distribution of component structural proteins in vertebrate lenses depends on the animals and their evolutionary demands (Delaye & Tardieu, 1983; Wistow, 1993; Wistow et al., 2005).

The lens refractive index and transparency are, in turn, dependent on the crystallin types and their concentrations, the visual environment, and age (Cai et al., 2017; Chang, 2017; Sweeney et al., 2007). This study's findings confirmed that the crystallin concentration, particularly in porcine lenses, is relatively higher in the nucleus than in the cortex. Pierscionek, et. al. (1995) found that the general protein distribution and metabolic activities within porcine lenses were similar to human lenses (Jobling, 1995; Keenan, 2008), and therefore, the porcine lenses were used as the model for accommodation in the SAXS experiment.

Further, this study has demonstrated, for the first time, the existence of an intense anisotropic reflection rotating around both meridians of a SAXS 2D grid scan derived from Atlantic salmon lenses. Similar reflections have been observed to occur from squid lenses in an earlier study by Regini et al. (2018). However, this study did not measure the angle of orientation of the anisotropic reflections.

5.2 Crystallin proteins in accommodated and unaccommodated states

There was a marked decrease in the intensity between individual X-ray patterns towards the central nuclear area, in both unstretched fresh and fixed porcine lenses. Generally, the amount of scattered X-ray intensity is dependent on factors such as the lens thickness, age, hydration, species, and the crystallin concentrations (Cai et al., 2017; Chang, 2017; Sweeney et al., 2007). The total observed scattered X-ray intensity

in fixed lenses was relatively lower compared with fresh lenses. As such, in spite of the fact that fresh and fixed lenses had the same geometries, as well as crystallin type and concentrations, their differential experimental treatment may have altered the fixed lenses (perhaps due to dehydration) resulting in different SAXS scatter patterns.

Part of this study's primary objective was to compare scatter patterns in the accommodated and unaccommodated states. Fixed lenses stretched using "Stretcher A", clearly showed noticeable increases in Bragg spacing between stretched and unstretched states, in all horizontal and vertical meridians. The Bragg spacing in the horizontal meridian (at 1 mm), for example, increased in fixed lenses, stretched using stretcher A, from 16.5 ± 0.8 nm to 21.1 ± 2.5 nm. In the vertical meridian, at 1mm, the Bragg spacing in fixed stretched lenses increased from 16.6 ± 0.6 nm to 20.9 ± 2.8 nm.

The fresh lenses, on the other hand, showed no significant difference between unstretched and stretched positions in all horizontal and vertical meridians. This may be a consequence of experimental variations, not least because the fresh lenses used in this study were stretched after three days post-mortem, at which time the ciliary muscles attached to the lenses were likely not as strong, which would affect the stretching of the lenses.

The chemical fixation protocol relied upon in this study may actually provide better preservation of the lens structural integrity. It is important that fresh lenses be used for such experiments as soon as possible after animal sacrifice.

Finally, the fixed lenses, stretched using the second stretching device, “Stretcher B”, generally exhibited no noticeable increase in Bragg spacing in the unaccommodated states in all horizontal and vertical meridians. This may be due to the unequal strain induced by stretching devices. It is possible that the zonules could have been ruptured or overextended as a result of the stretching process, as the manufacturers state that stretcher B has an optimised geometry allowing 5.5 mm of stretch, compared to 4mm for stretcher A.

Bragg spacing measurements offer valuable general information about the constituent protein distribution within the lens in the accommodated and unaccommodated states. To the researcher’s knowledge, this study is the first of its kind to compare the Bragg spacing in lenses between accommodated and unaccommodated states.

5.3 The change of other lens features as a function of the lens depths

Predictably, it was necessary to select and/or adapt the existing specimen preparation protocols to ensure that the integrity of the internal lens structure was maintained, and just as importantly, to ensure these structures could be visualised using the available imaging methods. The first step, therefore, was to develop an embedding and staining protocol to visualise the lens fibres at the highest possible resolution in three dimensions, for the first time, using SBF SEM. Unfortunately, the embedding tissue processing protocols failed to yield adequately embedded blocks to permit satisfactory ultrathin sectioning or SBF SEM examination, so lower resolution methods were used.

This study's estimation of the average lens fibre width, at $6.14 \pm 0.15 \mu\text{m}$, is consistent with Hoyer (1982)'s finding of the same at $4.5 \mu\text{m}$. Hoyer (1982)'s SEM estimate of the average fibre width is slightly smaller, possibly because of the shrinkage resulting from the SEM specimen preparation protocol used. Further, this present study investigated the lens fibre width as a function of both the depth and region (equatorial/suture junction). The results were consistent with previous studies with respect to the Y-shaped suture. There is a gradual reduction in the lens fibre width from the equator towards the suture endings (Kuszak et al., 1984; Kuszak, 1995a). While the fibre widths at the suture junction area reduced with depth from the lens anterior towards the centre, it increased towards the posterior pole. In contrast, the equatorial regions showed an opposite trend, in that fibre widths increased with depth from the anterior towards the centre, and decreased towards the posterior.

The current study also indicated that the lens suture lines grow increasingly undulated with depth in the lens equatorial plane. Past optically-based structural studies have investigated the lens width at different depths, but these structures have not been observed before, and their particular function is still not known (Kuszak et al., 2004b; Kuszak et al., 2006). Kuszak et al (2004a) suggested that there is a unique circulatory system within the confluence of suture branches supplying a fluid and nutrients to the lens and then to the fibres. It may be that the change in the undulating suture line may be indicative of a change in the circulatory system as a function of the lens depth (Kuszak et al., 2006). Table 5-1 shows the change in crystallin protein concentrations

in the cortex and nucleus, as well as the lens ultrastructural features as a function of the lens depths (mainly lens suture/fibres) from the present study compared to findings by past studies in respect to the same lens features.

5.4 The change of lens fibre widths during accommodation

This study also investigated the changes in the lens fibre width during accommodation. This study did not only take advantage of the technological improvements (including the lens stretcher and advanced imaging technologies), it also used fixation protocols that preserve the lens interior structure within the capsule to maintain its shape in order to mimic the lens in its natural condition.

These innovations should help to further our understanding of the structural and ultrastructural changes during the accommodation, in the hope of advancing knowledge of cataracts, presbyopia, and other disorders (Walls, 1944; Kammel et al., 2012).

This study indicated that, while the lens fibre widths in the internal region increased during accommodation, the anterior lens surface exhibited a resistance to accommodative stretching. Past studies either found no structural changes in the lens fibre, or that there was an increase in the lens fibre width due to the effect of straining (Kuszak et al., 2006; Kuszak et al., 2004; Parreno et al., 2018). Methodological differences, including the fact that the depths within the lens from where the samples were drawn and the use of porcine/primate lenses, may account for the divergences

between this study's findings and past studies (Kuszak et al., 2006; Kuszak et al., 2004; Parreno et al., 2018).

| Lens Features | Current Study's Results | Other Studies' Results and/or Conclusions |
|--|---|---|
| <i>Crystallin Concentration (SAXS Method)</i> | Shown a marked decrease in the intensity between individual X-ray patterns toward the centre of the nucleus of the European squid, Atlantic salmon, and porcine lenses. | Mirarefi et al. (2010)'s results were consistent with the present study. Crystallin density variations occur due to particles randomly and spontaneously forming regions of lower and higher concentrations. |
| <i>Bragg Spacing (SAXS Method)</i> | In porcine lenses, the Bragg spacing is appreciably reduced in the central nuclear area compared to the cortex area. | A high concentration of crystallins supports short-range interactions and reduces fluctuations in concentrations within lens cells (Delaye & Tardieu, 1983) |
| <i>Anisotropic Reflection (SAXS Method)</i> | Shown, for the first time, the existence of an intense anisotropic reflection rotating around both meridians of a SAXS 2D grid scan from Atlantic salmon lenses. | Regini et al. (2018) observed similar reflections in squid lenses. |
| <i>Individual Lens Fibre Widths</i> | Superficial porcine lens fibre widths for fresh lens were found to be $6.14 \pm 0.15 \mu\text{m}$ in the accommodated state. | Hoyer (1982)'s SEM study of porcine lens estimated the average fibre width to be $4.5 \mu\text{m}$. The shorter width may be due to shrinkage/dehydration caused by reagents used to prepare specimens in Hoyer (1982) |
| <i>The Lens Fibre Width as Function of Depth</i> | The average fibre width in the equatorial region reduced toward the suture junction area. | Kuszak et al. (1984) and Kuszak (1995a) found a gradual, but steady reduction in the lens fibre width, in the ratio of 2:1, from the equator towards the suture ends |
| <i>Anterior Lens Suture Angles</i> | The suture planes create a 120° angle. | The result was consistent with Kuszak, & Costello (2004). |
| <i>The suture lines as a function of depth</i> | The suture lines were increasingly undulated as a function of depth in the lens equatorial plane. | Kuszak et al (2005) suggested that there is a unique circulatory system within the confluence of suture branches. |

Table 5-1: Summary of results of crystallin proteins, and the change of other lens feature as a function of the lens depths.

Equally notable, this study measured the lens fibre widths for fibres obtained from both the nucleus and (the anterior, posterior and equatorial regions of) the cortex. The results showed a significant increase in the unaccommodated lens fibre widths in both the nucleus and the cortex (with the exception of the posterior cortex). As proposed in Chapter four, this may be caused by the manner in which zonules attach to the lens capsule. The anterior zonular fibres insert nearer to the anterior visual axis compared to the posterior zonular fibres (Helmholtz, 1855; Schachar, 2012), such that the anterior surface is relatively more responsive to the accommodative strain (Rosales & Marcos, 2006; Lovicu & Robinson, 2004). Secondly, Goldberg (2011) showed that when the lens is accommodated, the ciliary body contracts to relax anterior zonules (as posterior zonules contract). This exerts force on the posterior lens capsule. The opposite occurs when the lens is in the unaccommodated condition. It therefore follows that in unaccommodated state, the anterior zonular fibres stretch at the lens equatorial/anterior area, causing the axial lens thickness to decrease as a result of increasing the main unit of the lens (lens fibre widths) in both the anterior and equatorial lens area (Goldberg, 2011).

This present study's findings of increases lens fibre widths in the nucleus, anterior and equatorial cortex (in an unaccommodated lens) is not only consistent with Patnaik (1967) and Dubbelman et al. (2003), but is also backed by both the Hockwin and Oxford systems. Both Oxford and Hockwin systems estimate that the nucleus region thickness increases by ~ 0.040 mm/D and the Hockwin system suggests that the

anterior cortical region increases by ~ 0.004 mm/D (Hockwin, 1989, Hockwin et al., 1982). Further, this study found an appreciable decrease, during accommodation, in the posterior lens cortex relative the anterior/equatorial lens cortex. The Oxford system estimates this reduction in the posterior lens surface at ~ -0.002 mm/D (Dubbelman et al., 2003).

These findings are summarised in Table 5-2. This table shows each of the key variables of interest in this study in respect to the lens ultrastructural changes in accommodated and unaccommodated conditions, compared with the findings by past studies in respect to the same variable/findings.

5.5 Conclusion

In conclusion, this research advanced the understanding of the nature of the lens structure and accommodation. The lens crystallins vary in concentration across different groups of animals and regions within the lens. This thesis offers information about suture line shape, at different depths, in the anterior and posterior lens. This is important because it fosters the understanding of abnormal changes within the lens that affect the lens shape. Importantly, this thesis concludes that the accommodation mechanism involves and/or results in changes in lens fibre widths. This thesis also puts forward enhanced experimental procedures (including chemical fixation that preserves the lens morphology), that can be used to better understand lens fibre behaviour within accommodated and unaccommodated lenses. The accurate simulation of *in vivo* conditions, during the accommodative mechanism, holds the promise of revealing

even more novel information, or at the very least, furthering the understanding of how lens sutures, lens fibres, and other lens parts, contribute to the accommodation.

| Lens Features | Current Study | Other studies |
|--|--|---|
| <i>Anterior and posterior radius of curvatures</i> | The anterior and posterior curvature radii increased in unaccommodated lenses. | The magnitude and direction of change in both anterior and posterior curvatures are consistent with Kammel et al. (2012), but inconsistent with Hahn et al. (2015) and Rosales et al. (2006). |
| <i>lens fibre at 1 and 5mm</i> | There was no significant difference in the fibre widths at 1mm and 5mm depths in accommodation conditions. | Kuszak and Zoltoski (2005) found no significant difference in the lens fibre morphology or dimensions within anterior/posterior lens in accommodation conditions. |
| <i>lens fibre at the rest of depths</i> | There was an increase in the lens fibre widths at 2, 3, 4, 7 mm depths. | Parreno et al. (2018) found that a 6% equatorial strain in mouse lens increased the fibre width by $11.7 \pm 0.2 \mu\text{m}$ and a 9% strain increased the fibre width by $11.8 \pm 0.1 \mu\text{m}$. |
| <i>Through whole fixed lenses</i> | The lens fibre widths increased, in the unaccommodated lens, in the nucleus, anterior and equatorial cortex. | The anterior cortex region exhibited a slight increase, while the nucleus region thickness increased by $\sim 0.040 \text{ mm/D}$ (Hockwin, 1989, Hockwin et al., 1982). |
| | The lens fibre widths in posterior cortex decreased in unaccommodated state | The Oxford system provides that the change in the posterior lens surface during accommodation is negative ($\sim -0.002 \text{ mm/D}$) (Dubbelman et al., 2003) |

Table 5-2: Summary of results of curvature and lens fibre widths during the accommodation.

5.5.1 The study limitations

This study had a number of weaknesses, key among which included:

- The relatively small sample sizes. Increasing sample sizes would have been beneficial to reduce the effect of any experimental errors.
- SAXS presented numerous challenges to gathering near-perfect scattering patterns and analysing data. The problem primarily rests in the ambiguity of data, due to limited information in the scattering intensity profile. The proteins' shape cannot, for example, be recovered without complementary microscopy information.
- Further, the most accurate age for modelling accommodation in healthy human lenses is under 40 years (Al-Ghoul et al., 2001; Costello et al., 2013a; Al-Khudari et al., 2007). The availability of fresh human lenses in this age range, or indeed any other age, is predictably limited.

5.5.2 Future work

Naturally, this study's shortcomings offer a fertile ground for further work to be done in the same, or related area. More specifically:

- With respect to SAXS experiments, there is a need to need to examine more lenses, in order to clarify the nature of the relationship between the lens ultrastructure and its functional demands.

- Further, while there are understandable challenges in obtaining samples, the need for more studies using human lenses at different ages (including 40 years and below) cannot be over-emphasised, in order to better understand crystallin proteins and the role of lens fibre widths in the accommodation.
- Future work will also need to include TEM studies, besides SAXS, in order to establish if the cell membrane complexes (CMCs) are indeed present in Atlantic salmon lenses.
- There are also immense prospects for further optimisation of SBFSEM embedding protocols.
- Lastly, the lens stretching devices used in this thesis are simple manual devices. For greater accuracy and consistency in simulating the accommodation, future studies require computer-controlled lens stretching devices, in which the rate and amount of strain applied to the tissue could be closely controlled and measured.

6 References

- AL-GHOUL, K. J. & COSTELLO, M. J. 1997. Light microscopic variation of fiber cell size, shape and ordering in the equatorial plane of bovine and human lenses. *Mol Vis*, 3, 2.
- AL-GHOUL, K. J., KIRK, T., KUSZAK, A. J., ZOLTOSKI, R. K., SHIELS, A. & KUSZAK, J. R. 2003a. Lens structure in MIP-deficient mice. *Anat Rec A Discov Mol Cell Evol Biol*, 273, 714.
- AL-GHOUL, K. J., KUSZAK, J. R., LU, J. Y. & OWENS, M. J. 2003b. Morphology and organization of posterior fiber ends during migration. *Mol Vis*, 9, 119.
- AL-GHOUL, K. J., NORDGREN, R. K., KUSZAK, A. J., FREEL, C. D., COSTELLO, M. J. & KUSZAK, J. R. 2001. Structural evidence of human nuclear fiber compaction as a function of ageing and cataractogenesis. *Exp. Eye Res.*, 72, 199.
- AL-KHUDARI, S., DONOHUE, S. T., AL-GHOUL, W. M. & AL-GHOUL, K. J. 2007. Age-related compaction of lens fibers affects the structure and optical properties of rabbit lenses. *BMC Ophthalmology*, 7, 19.
- ANDLEY, U. P. 2008. The lens epithelium: Focus on the expression and function of the α -crystallin chaperones. *Int. J. Biochem. Cell Biol.*, 40, 317.
- ASSOCIATION, A. O. 2011. OPTOMETRIC CLINICAL PRACTICE GUIDELINE CARE OF THE PATIENT WITH PRESBYOPIA *American Optometric Association* [Online].
- AUGUSTEYN, R. C. 2004. alpha-crystallin: a review of its structure and function. *Clin Exp Optom*, 87, 356.
- AUGUSTEYN, R. C. 2007. Growth of the human eye lens. *Mol Vis*, 13, 252.
- AUGUSTEYN, R. C. 2008. Growth of the lens: in vitro observations. *Clin Exp Optom*, 91, 226.
- AUGUSTEYN, R. C. 2010. On the growth and internal structure of the human lens. *Exp Eye Res*, 90, 643.
- BARRETT, J. 1938. ACCOMMODATION IN THE EYES OF MAMMALS. *The British Journal of Ophthalmology*, 22, 148.
- BASHA, E., O'NEILL, H. & VIERLING, E. 2012. Small heat shock proteins and α -crystallins: dynamic proteins with flexible functions. *Trends in Biochemical Sciences*, 37, 106.
- BASSNETT, S., SHI, Y. & VRENSEN, G. F. J. M. 2011. Biological glass: structural determinants of eye lens transparency. *Philosophical transactions of the Royal Society of London. Series B, Biological sciences*, 366, 1250.
- BELIN, M., BELIN, M. W., KHACHIKIAN, S. S. & AMBROSIO, R. 2012. *Elevation Based Corneal Tomography*, Jaypee Brothers, Medical Publishers Pvt. Limited.
- BELL, J. G., MCVICAR, A. H., PARK, M. T. & SARGENT, J. R. 1991. High Dietary Linoleic Acid Affects the Fatty Acid Compositions of Individual Phospholipids from

- Tissues of Atlantic Salmon (*Salmo salar*): Association with Stress Susceptibility and Cardiac Lesion. *The Journal of Nutrition*, 121, 1163.
- BHAT, S. P. & NAGINENI, C. N. 1989. α B subunit of lens-specific protein α -crystallin is present in other ocular and non-ocular tissues. *Biochemical and Biophysical Research Communications*, 158, 319.
- BLAUROCK, A. E. & WORTHINGTON, C. R. 1966. Treatment of low angle x-ray data from planar and concentric multilayered structures. *Biophysical journal*, 6, 305.
- BLOEMENDAL, H. 1981. *Molecular and cellular biology of the eye lens*, New York, Wiley.
- BLOEMENDAL, H., DE JONG, W., JAENICKE, R., LUBSEN, N. H., SLINGSBY, C. & TARDIEU, A. 2004. Ageing and vision: structure, stability and function of lens crystallins. *Progress in Biophysics and Molecular Biology*, 86, 407.
- BORCHMAN, D., CENEDELLA, R. J. & LAMBA, O. P. 1996. Role of Cholesterol in the Structural Order of Lens Membrane Lipids. *Experimental Eye Research*, 62, 191.
- BOSCIA, F., GRATTAGLIANO, I., VENDEMIALE, G., MICELLI-FERRARI, T. & ALTOMARE, E. 2000. Protein Oxidation and Lens Opacity in Humans. *Investigative Ophthalmology & Visual Science*, 41, 2461.
- BOYLE, D. & TAKEMOTO, L. 1994. *Characterization of the α - γ and α - β Complex: Evidence for an In Vivo Functional Role of α -Crystallin as a Molecular Chaperone.*
- BRIAN, G. & TAYLOR, H. 2001. Cataract blindness: challenges for the 21st century. *Bulletin of the World Health Organization*, 79, 249.
- BROWN, N. 1973. The change in shape and internal form of the lens of the eye on accommodation. *Experimental Eye Research*, 15, 441.
- BROWN, N. 1976. Dating the onset of cataract. *Trans Ophthalmol Soc U K*, 96, 18-23.
- BURD, H. J., JUDGE, S. J. & FLAVELL, M. J. 1999. Mechanics of accommodation of the human eye. *Vision Research*, 39, 1591.
- CAI, J., TOWNSEND, J. P., DODSON, T. C., HEINEY, P. A. & SWEENEY, A. M. 2017. Eye patches: Protein assembly of index-gradient squid lenses. *Science*, 357, 564.
- CHANG, S. 2017. *How squid build their graded-index spherical lenses.*
- CHATTERJEE, A., MILTON, R. C. & THYLE, S. 1982. Prevalence and aetiology of cataract in Punjab. *The British Journal of Ophthalmology*, 66, 35.
- CHIESI, M., LONGONI, S. & LIMBRUNO, U. 1990. *Cardiac alpha-crystallin. III. Involvement during heart ischemia.*
- CHOW, R. L. & LANG, R. A. 2001. Early eye development in vertebrates. *Annual review of cell and developmental biology*, 17, 255.
- CHUN-HONG XIA, X. G., BRUCE BEUTLER 2011. Normal development of the mammalian lens.

- COHEN, A. I. 1965. The Electron Microscopy of the Normal Human Lens. *Investigative Ophthalmology & Visual Science*, 4, 433.
- COLLIN, R., GRIFFITH, W. P., PHILLIPS, F. L. & SKAPSKI, A. C. 1974. Staining and fixation of unsaturated membrane lipids by osmium tetroxide: Crystal structure of a model osmium(VI) di-ester. *Biochimica et Biophysica Acta (BBA) - General Subjects*, 354, 152.
- COOK, C. A., KORETZ, J. F., PFAHNL, A., HYUN, J. & KAUFMAN, P. L. 1994. Aging of the human crystalline lens and anterior segment. *Vision Research*, 34, 2945.
- CORTÉS, L. P., BURD, H. J., MONTENEGRO, G. A., D'ANTIN, J. C., MIKIELEWICZ, M., BARRAQUER, R. I. & MICHAEL, R. 2015. Experimental protocols for Ex vivo lens stretching tests to investigate the biomechanics of the human accommodation apparatus. *Investigative Ophthalmology and Visual Science*, 56, 2926.
- COSTELLO, M. J., BRENNAN, L. A., BASU, S., CHAUSS, D., MOHAMED, A., GILLILAND, K. O., JOHNSEN, S., MENKO, A. S. & KANTOROW, M. 2013a. Autophagy and mitophagy participate in ocular lens organelle degradation. *Experimental Eye Research*, 116, 141.
- COSTELLO, M. J., MOHAMED, A., GILLILAND, K. O., FOWLER, W. C. & JOHNSEN, S. 2013b. Ultrastructural Analysis of the Human Lens Fiber Cell Remodeling Zone and the Initiation of Cellular Compaction. *Experimental eye research*, 116, 10.1016/j.exer.2013.10.015.
- CROFT, M. A., GLASSER, A. & KAUFMAN, P. L. 2001. Accommodation and presbyopia. *Int Ophthalmol Clin*, 41, 33.
- CVEKL, A. & ASHERY-PADAN, R. 2014. The cellular and molecular mechanisms of vertebrate lens development. *Development*, 141, 4432.
- DAXECKER, F. 1994. Further studies by Christoph Scheiner concerning the optics of the eye. In: HENKES, H. E. (ed.) *History of Ophthalmology: Sub auspiciis Academiae Ophthalmologicae Internationalis*. Dordrecht: Springer Netherlands.
- DE JONG, W. W., LEUNISSEN, J. A. & VOORTER, C. E. 1993. Evolution of the alpha-crystallin/small heat-shock protein family. *Molecular Biology and Evolution*, 10, 103.
- DELAYE, M. & TARDIEU, A. 1983. Short-range order of crystallin proteins accounts for eye lens transparency. *Nature*, 302, 415.
- DICKSON, D. H. & CROCK, G. W. 1972. Interlocking patterns on primate lens fibers. *Invest Ophthalmol*, 11, 809.
- DRIESSEN, H. 1996. β,γ -Crystallins. In: ZAIDI, Z. H. & SMITH, D. L. (eds.) *Protein Structure — Function Relationship*. Boston, MA: Springer US.

- DUBBELMAN, M. & VAN DER HEIJDE, G. L. 2001. The shape of the aging human lens: curvature, equivalent refractive index and the lens paradox. *Vision Research*, 41, 1867.
- DUBBELMAN, M., VAN DER HEIJDE, G. L. & WEEBER, H. A. 2005. Change in shape of the aging human crystalline lens with accommodation. *Vision Res*, 45, 117.
- DUBBELMAN, M., VAN DER HEIJDE, G. L., WEEBER, H. A. & VRENSEN, G. F. J. M. 2003. Changes in the internal structure of the human crystalline lens with age and accommodation. *Vision Research*, 43, 2363.
- DUNCAN, G., WORMSTONE, I. M. & DAVIES, P. D. 1997. The aging human lens: structure, growth, and physiological behaviour. *British Journal of Ophthalmology*, 81, 818.
- ECROYD, H. & CARVER, J. A. 2008. Crystallin proteins and amyloid fibrils. *Cellular and Molecular Life Sciences*, 66, 62.
- ECROYD, H., MEEHAN, S., HORWITZ, J., AQUILINA, J. A., BENESCH, J. L. P., ROBINSON, C. V., MACPHEE, C. E. & CARVER, J. A. 2007. Mimicking phosphorylation of alphaB-crystallin affects its chaperone activity. *The Biochemical journal*, 401, 129.
- EHRMANN, K., HO, A. & PAREL, J.-M. 2008. Biomechanical analysis of the accommodative apparatus in primates. *Clinical & experimental optometry*, 91, 302.
- FINE, I. H., PACKER, M. & HOFFMAN, R. S. 2005. Refractive lens surgery.
- FISCHER, D., HAUKE, T. G., MÜLLER, A. & THANOS, S. 2008. Crystallins of the β/γ -superfamily mimic the effects of lens injury and promote axon regeneration. *Molecular and Cellular Neuroscience*, 37, 471.
- FISHER, R. F. 1969. The significance of the shape of the lens and capsular energy changes in accommodation. *The Journal of Physiology*, 201, 21.
- FISHER, R. F. 1971. Elastic properties of the human lens. *Exp Eye Res*, 11.
- FISHER, R. F. 1973. Presbyopia and the changes with age in the human crystalline lens. *J Physiol*, 228, 765.
- FISHER, R. F. 1988. The mechanics of accommodation in relation to presbyopia. *Eye (Lond)*, 2 (Pt 6), 646.
- FUHRMANN, S. 2010. Chapter Three - Eye Morphogenesis and Patterning of the Optic Vesicle. In: CAGAN, R. L. & REH, T. A. (eds.) *Current Topics in Developmental Biology*. Academic Press.
- GANEVA, E. & HARDING, J. J. 1995. Molecular Chaperones Protect Against Glycation-Induced Inactivation of Glucose-6-Phosphate Dehydrogenase. *European Journal of Biochemistry*, 231, 181.
- GARLAND, D. L., DUGLAS-TABOR, Y., JIMENEZ-ASENSIO, J., DATILES, M. B. & MAGNO, B. 1996. The Nucleus of the Human Lens: Demonstration of a Highly Characteristic Protein Pattern by Two-Dimensional Electrophoresis and

- Introduction of a New Method of Lens Dissection. *Experimental Eye Research*, 62, 285.
- GILLES, R., KEIDERLING, U. & WIEDENMANN, A. 1998. Silver behenate powder as a possible low-angle calibration standard for small-angle neutron scattering. *Journal of Applied Crystallography*, 31, 957.
- GILLILAND, K. O., METLAPALLY, S. & COSTELLO, M. J. 2009. Morphological Analysis of Extensive Fiber Cell Compaction in the Adult Nucleus of Aged Human Transparent Lenses. *Investigative Ophthalmology & Visual Science*, 50, 4388.
- GLATTER, O. & KRATKY, O. 1982. *Small angle x-ray scattering*, London; New York, Academic Press.
- GLUENZ, E., WHEELER, R. J., HUGHES, L. & VAUGHAN, S. 2015. Chapter 24 - Scanning and three-dimensional electron microscopy methods for the study of Trypanosoma brucei and Leishmania mexicana flagella. In: BASTO, R. & MARSHALL, W. F. (eds.) *Methods in Cell Biology*. Academic Press.
- GOLDBERG, D. B. 2011. Computer-animated model of accommodation and theory of reciprocal zonular action. *Clinical ophthalmology (Auckland, N.Z.)*, 5, 1559.
- GREILING, T. M. S. & CLARK, J. I. 2012. Chapter one - New Insights into the Mechanism of Lens Development Using Zebra Fish. In: JEON, K. W. (ed.) *International Review of Cell and Molecular Biology*. Academic Press.
- HAHN, J., FROMM, M., HALABI, F. A., BESDO, S., LUBATSCHOWSKI, H., RIPKEN, T. & KRÜGER, A. 2015. Measurement of ex vivo porcine lens shape during simulated accommodation, before and after fs-laser treatment. *Investigative Ophthalmology and Visual Science*, 56, 5332.
- HAMMOND, C. 1997. *The basics of crystallography and diffraction*, Oxford; New York, International Union of Crystallography : Oxford University Press.
- HARDING, J. 1991. *Cataract Biochemistry, Epidemiology and Pharmacology*, UK, British Library Cataloguing in Publication Data.
- HEATH, M. M., RIXON, K. C. & HARDING, J. J. 1996. Glycation-induced inactivation of malate dehydrogenase protection by aspirin and a lens molecular chaperone, α -crystallin. *Biochimica et Biophysica Acta (BBA) - Molecular Basis of Disease*, 1315, 176.
- HELLIWELL, J. R. 2004. Single-crystal X-ray techniques. In: PRINCE, E. (ed.) *International Tables for Crystallography Volume C: Mathematical, physical and chemical tables*. Dordrecht: Springer Netherlands.
- HELMHOLTZ, H. 1855. Ueber die Accommodation des Auges. *Archiv für Ophthalmologie*, 1, 1.
- HERMANS, E. A., DUBBELMAN, M., VAN DER HEIJDE, G. L. & HEETHAAR, R. M. 2008. Change in the accommodative force on the lens of the human eye with age. *Vision Research*, 48, 119.

- HOCKWIN, O. 1989. [Scheimpflug photography of the lens]. *Fortschr Ophthalmol*, 86, 304.
- HOCKWIN, O., DRAGOMIRESCU, V. & LASER, H. 1982. Measurements of lens transparency or its disturbances by densitometric image analysis of scheimpflug photographs. *Graefe's Archive for Clinical and Experimental Ophthalmology*, 219, 255.
- HOLDEN, B. A., FRICKE, T. R., HO, S. M., WONG, R., SCHLENTHER, G., CRONJÉ, S., BURNETT, A., PAPAS, E., NAIDOO, K. S. & FRICK, K. D. 2008. Global vision impairment due to uncorrected presbyopia. *Archives of Ophthalmology*, 126, 1731.
- HORWITZ, J. 1992. Alpha-crystallin can function as a molecular chaperone. *Proceedings of the National Academy of Sciences*, 89, 10449.
- HORWITZ, J. 2003. Alpha-crystallin. *Experimental Eye Research*, 76, 145.
- HOYER, H. E. 1982. Scanning electron-microscopic study of lens fibers of the pig. *Cell Tissue Res*, 224, 225.
- INGOLIA, T. D. & CRAIG, E. A. 1982. Four small Drosophila heat shock proteins are related to each other and to mammalian alpha-crystallin. *Proceedings of the National Academy of Sciences*, 79, 2360.
- INOUE, R., TAKATA, T., FUJII, N., ISHII, K., UCHIYAMA, S., SATO, N., OBA, Y., WOOD, K., KATO, K., FUJII, N. & SUGIYAMA, M. 2016. New insight into the dynamical system of α B-crystallin oligomers. *Scientific Reports*, 6, 29208.
- JAGGER, W. S. 1992. The optics of the spherical fish lens. *Vision Research*, 32, 1271.
- JOBLING, A., STEVENS, A. & AUGUSTEYN, R. C. 1995. Distribution of proteins across the porcine lens. *Clinical and Experimental Optometry*, 78, 87.
- JONGEBLOED, W. L., VAN DER WANT, J.J.L., WORST, J.G.F. & KALICHARAN, D. 1998. Stereoscopic Images of Human Cataractous Lens Fibers Obtained with Field Emission Scanning Electron Microscopy. *Scanning Microscopy*, 12, 653.
- KAMMEL, R., ACKERMANN, R., MAI, T., DAMM, C. & NOLTE, S. 2012. Pig Lenses in a Lens Stretcher: Implications for Presbyopia Treatment. *Optometry and Vision Science*, 89, 908.
- KASHIMA, K., TRUS, B. L., UNSER, M., EDWARDS, P. A. & DATILES, M. B. 1993. Aging studies on normal lens using the Scheimpflug slit-lamp camera. *Investigative Ophthalmology & Visual Science*, 34, 263.
- KEENAN, J., F ORR, D. & PIERSCIONEK, B. 2008. *Patterns of crystallin distribution in porcine eye lenses*.
- KHURANA 2009. *Theory and Practice of Optics and refraction*, India, Elsevier.
- KORETZ, J. F., COOK, C. A. & KAUFMAN, P. L. 1997. Accommodation and presbyopia in the human eye. Changes in the anterior segment and crystalline lens with focus. *Investigative Ophthalmology & Visual Science*, 38, 569.

- KREUZER, R. O. & SIVAK, J. G. 1985. Chromatic aberration of the vertebrate lens. *Ophthalmic Physiol Opt*, 5, 33.
- KRIVANDIN, A. V. 1997. [On the supramolecular structure of eye lens crystalline. A study by small-angle x-ray scattering]. *Biofizika*, 42, 1274.
- KRIVANDIN, A. V. & FEIGIN, L. A. 1990. [Absence of small-angle maximums on the x-ray images of ocular lens tissue]. *Biofizika*, 35, 461.
- KRIVANDIN, A. V., L'VOV I U, M., OSTROVSKII, M. A., FEDOROVICH, I. B. & FEIGIN, L. A. 1984. [X-ray diffraction in the intact isolated frog ocular lens]. *Biofizika*, 29, 873.
- KUSZAK, J. R. 1995a. The development of lens sutures. *Progress in Retinal and Eye Research*, 14, 567.
- KUSZAK, J. R. 1995b. The Ultrastructure of Epithelial and Fiber Cells in the Crystalline Lens. In: KWANG, W. J. & JONATHAN, J. (eds.) *International Review of Cytology*. Academic Press.
- KUSZAK, J. R., BERTRAM, B. A., MACSAI, M. S. & RAE, J. L. 1984. Sutures of the crystalline lens: a review. *Scan Electron Microsc*, 1369.
- KUSZAK, J. R. & BROWN, H. G. 1994. Embryology and anatomy of the crystalline lens. In: DOWLING, J. E. & RAVIOLA, E. (eds.) *Basic Sciences*. W.B. Saunders Company: Philadelphia.
- KUSZAK, J. R., MAZURKIEWICZ, M., JISON, L., MADURSKI, A., NGANDO, A. & ZOLTOSKI, R. K. 2006. Quantitative analysis of animal model lens anatomy: accommodative range is related to fiber structure and organization. *Vet Ophthalmol*, 9, 266.
- KUSZAK, J. R., SIVAK, J. G. & WEERHEIM, J. A. 1991. Lens optical quality is a direct function of lens sutural architecture. *Invest Ophthalmol Vis Sci*, 32, 2119.
- KUSZAK, J. R. & ZOLTOSKI, R. K. 2005. The Mechanism of Primate Accommodation at the Lens Fiber Level Revealed by Correlative Microscopic and Computer Generated Animations. *Investigative Ophthalmology & Visual Science*, 46, 731.
- KUSZAK, J. R., ZOLTOSKI, R. K. & SIVERTSON, C. 2004a. Fibre cell organization in crystalline lenses. *Exp. Eye Res.*, 78, 673.
- KUSZAK, J. R., ZOLTOSKI, R. K. & TIEDEMANN, C. E. 2004b. Development of lens sutures. *Int J Dev Biol*, 48, 889.
- LAND, M. F. N., D.E 2002. Animal Eyes.
- LARSON, M. J. & CARBINE, K. A. 2017. Sample size calculations in human electrophysiology (EEG and ERP) studies: A systematic review and recommendations for increased rigor. *International Journal of Psychophysiology*, 111, 33.
- LAPATTO, R., NALINI, V., BAX, B., DRIESSEN, H., LINDLEY, P.F., BLUNDELL, T.L. AND SLINGSBY, C., 1991. High resolution structure of an oligomeric eye lens β -

- crystallin: loops, arches, linkers and interfaces in β B2 dimer compared to a monomeric γ -crystallin. *Journal of molecular biology*, 222, 1067
- LIM, J. C., WALKER, K. L., SHERWIN, T., SCHEY, K. L. & DONALDSON, P. J. 2009. Confocal microscopy reveals zones of membrane remodeling in the outer cortex of the human lens. *Invest Ophthalmol Vis Sci*, 50, 4304.
- LIPFERT, J., COLUMBUS, L., CHU, V. B., LESLEY, S. A. & DONIACH, S. 2007. Size and Shape of Detergent Micelles Determined by Small-Angle X-ray Scattering. *The Journal of Physical Chemistry B*, 111, 12427.
- LOCKE, M. 1994. Preservation and contrast without osmication or section staining. *Microscopy Research and Technique*, 29, 1.
- LOVICU, F. J. & ROBINSON, M. L. 2004. Development of the Ocular Lens.
- LOWE, J., MCDERMOTT, H., PIKE, I., SPENDLOVE, I., LANDON, M. & MAYER, R. 1992. *alpha B crystallin expression in non-lenticular tissues and selective presence in ubiquitinated inclusion bodies in human disease.*
- LUEDDE, W. H. 1927. Mechanism of Accommodation. *American Journal of Ophthalmology*, 10, 15.
- LUFT, J. H. 1961. Improvements in epoxy resin embedding methods. *J Biophys Biochem Cytol*, 9, 409.
- LYNN. WALLS, G. 1944. *The Vertebrate Eye and Its Adaptive Radiation.*
- M. GORDON, J. 2000. *Spherical Gradient-Index Lenses as Perfect Imaging and Maximum Power Transfer Devices.*
- MARUSSICH, L., MANNIS, F., NANKIVIL, D., MACEO HEILMAN, B., YAO, Y., ARRIETA-QUINTERO, E., HO, A., AUGUSTEYN, R. & PAREL, J. M. 2015. Measurement of Crystalline Lens Volume During Accommodation in a Lens Stretcher. *Invest Ophthalmol Vis Sci*, 56, 4239.
- MCAVOY, J. W., CHAMBERLAIN, C. G., DE LONGH, R. U., HALES, A. M. & LOVICU, F. J. 1999. Lens development. *Eye*, 13, 425.
- MELINDA K. DUNCAN, A. C., MARC KANTOROW, PIATIGORSKY, J., DUNCAN, M. K., . & ET AL. 2004. *Lens Crystallins Development of the Ocular Lens*, Cambridge University Press.
- MIRAREFI, A. Y., BOUTET, S., RAMAKRISHNAN, S., KISS, A. J., CHENG, C. H. C., DEVRIES, A. L., ROBINSON, I. K. & ZUKOSKI, C. F. 2010. Small-angle X-ray scattering studies of the intact eye lens: Effect of crystallin composition and concentration on microstructure. *Biochimica et Biophysica Acta - General Subjects*, 1800, 556.
- MOHAMED, A., GILLILAND, K. O., METLAPALLY, S., JOHNSEN, S. & COSTELLO, M. J. 2013. Simple fixation and storage protocol for preserving the internal structure of intact human donor lenses and extracted human nuclear cataract specimens. *Mol. Vision*, 19, 2352.

- MOREAU, K. L. & KING, J. A. 2012. Protein misfolding and aggregation in cataract disease and prospects for prevention. *Trends in molecular medicine*, 18, 273.
- MORI, B. & TANI, G. 1988. *Soft Dehydration in the Embedding Method for Transmission Electron Microscopy*.
- NORN, M. & A JENSEN, O. 2004. *Marius Tscherning (1854-1939): His life and work in optical physiology*.
- OHTA, N., OKA, T., INOUE, K., YAGI, N., KATO, S. & HATTA, I. 2005. Structural analysis of cell membrane complex of a hair fibre by micro-beam X-ray diffraction. *Journal of Applied Crystallography*, 38, 274.
- OSTRIN, L., KASTHURIRANGAN, S., WIN-HALL, D. & GLASSER, A. 2006. *Simultaneous Measurements of Refraction and A-Scan Biometry During Accommodation in Humans*.
- OVENSERI-OGBOMO, G. & A. ODUNTAN, O. 2015. *Mechanism of accommodation: A review of theoretical propositions*.
- PARRENO, J., CHENG, C., NOWAK, R. B. & FOWLER, V. M. 2018. The effects of mechanical strain on mouse eye lens capsule and cellular microstructure. *Molecular biology of the cell*, 29, 1963.
- PATNAIK, B. 1967. A photographic study of accommodative mechanisms: Changes in the lens nucleus during accommodation. *Investigative Ophthalmology & Visual Science*, 6, 601.
- PEDDIE, C. J. & COLLINSON, L. M. 2014. Exploring the third dimension: Volume electron microscopy comes of age. *Micron*, 61, 9.
- PENNISI, E. 2000. Developmental biology: Embryonic lens prompts eye development. *Science (Washington, D. C.)*, 289, 522.
- PIATIGORSKY, J. 1993. Puzzle of crystallin diversity in eye lenses. *Developmental Dynamics*, 196, 267.
- PIERSCIONEK, B. K. & REGINI, J. W. 2012. The gradient index lens of the eye: An opto-biological synchrony. *Progress in Retinal and Eye Research*, 31, 332.
- PIERSCIONEK, B. K. & WEALE, R. A. 1995. The optics of the eye-lens and lenticular senescence. A review. *Doc Ophthalmol*, 89, 321.
- PIERSCIONEK, B. K. P. D. & CHAN, D. Y. C. P. D. 1989. Refractive Index Gradient of Human Lenses. *Optometry & Vision Science*, 66, 822.
- Q TROJANOWSKI, J., GOEDERT, M., IWATSUBO, T. & M-Y LEE, V. 1998. *Fatal attractions: abnormal protein aggregation and neuron death in Parkinson's disease and Lewy body dementia*.
- QUAN HUANG, B. & YEUNG, E. 2015. Chemical and Physical Fixation of Cells and Tissues: An Overview.
- QUINLAN, R., PRESCOTT, A., QUINLAN, R. & PRESCOTT., A. 2004. *Lens Cell Cytoskeleton*
- Development of the Ocular Lens*, Cambridge University Press.

- REGINI, J. W., ELLIOTT, G. F. & HODSON, S. A. 2004a. The Ordering of Corneal Collagen Fibrils with Increasing Ionic Strength. *J. Mol. Biol.*, 336, 179.
- REGINI, J. W., GROSSMANN, J. G., BURGIO, M. R., MALIK, N. S., KORETZ, J. F., HODSON, S. A. & ELLIOTT, G. F. 2004b. Structural Changes in α -Crystallin and Whole Eye Lens During Heating, Observed by Low-angle X-ray Diffraction. *J. Mol. Biol.*, 336, 1185.
- REGINI, J. W. & MEEK, K. M. 2009. Changes in the X-ray diffraction pattern from lens during a solid-to-liquid phase transition. *Curr Eye Res*, 34, 492.
- REGINI, J. W., NAOTO YAGI ROBERT D. YOUNG, A HIDETOSHI TANIOKA, C SHIGERU KINOSHITA, C MASATO HOSHINO, B KENTARO UESUGI, B KEITH M. MEEK, A CARLO KNUPP, A BARBARA K. PIERSCIONEK, D ANDREW J. QUANTOCK, A, AND GERALD F. ELLIOTT 2018. Membrane structures and functional correlates in the bi-segmented eye lens of the cephalopod.
- REILLY, M. A., HAMILTON, P. D., PERRY, G. & RAVI, N. 2009. Comparison of the behavior of natural and refilled porcine lenses in a robotic lens stretcher. *Experimental Eye Research*, 88, 483.
- RENKAWEK, K., VOORTER, C. E., BOSMAN, G. J., VAN WORKUM, F. P. & DE JONG, W. W. 1994. Expression of alpha B-crystallin in Alzheimer's disease. *Acta neuropathologica*, 87, 155.
- REYNOLDS, E. S. 1963. The use of lead citrate at high pH as an electron-opaque stain in electron microscopy. *The Journal of cell biology*, 17, 208.
- ROBERT, F., JACOB, R.J.C. & MASON, P.R., 2000. Determination of human eye lens membrane structure by x-ray diffraction analysis. *the Rigaku Journal*, 17, 5.
- ROORDA, A. & GLASSER, A. 2004. Wave aberrations of the isolated crystalline lens. *Journal of Vision*, 4, 1.
- ROQUEMORE, E. P., DELL, A., MORRIS, H. R., PANICO, M., REASON, A. J., SAVOY, L. A., WISTOW, G. J., ZIGLER, J. S., JR., EARLES, B. J. & HART, G. W. 1992. Vertebrate lens alpha-crystallins are modified by O-linked N-acetylglucosamine. *J Biol Chem*, 267, 555.
- ROSALES, P., DUBBELMAN, M., MARCOS, S. & VAN DER HEIJDE, R. 2006. Crystalline lens radii of curvature from Purkinje and Scheimpflug imaging. *Journal of Vision*, 6, 5.
- ROSALES, P., WENDT, M., MARCOS, S. & GLASSER, A. 2008. Changes in crystalline lens radii of curvature and lens tilt and decentration during dynamic accommodation in rhesus monkeys. *Journal of Vision*, 8, 18.
- ROSEN, A. M., DENHAM, D. B., FERNANDEZ, V., BORJA, D., HO, A., MANNS, F., PAREL, J.-M. & AUGUSTEYN, R. C. 2006. In vitro dimensions and curvatures of human lenses. *Vision Research*, 46, 1002.
- SAINTE-MARIE, G. U. Y. 1962. *A Paraffin-Embedding Technique for Studies Employing Immunofluorescence*.

- SANCHEZ, I., MARTIN, R., USSA, F. & FERNANDEZ-BUENO, I. 2011. The parameters of the porcine eyeball. *Graefe's Archive for Clinical and Experimental Ophthalmology*, 249, 475.
- SANTOS-NETO, DOS, E., ALVES & RUIZ, M. 2011. New concepts in accommodation and presbyopia. *Revista Brasileira de Oftalmologia*.
- SCHACHAR, R. A. 2006. The Mechanism of Accommodation and Presbyopia. *International Ophthalmology Clinics*, 46, 39.
- SCHACHAR, R. A. 2012. *The mechanism of accommodation and presbyopia*, Amsterdam, Kugler Publications.
- SHARMA, K. K. & SANTHOSHKUMAR, P. 2009. Lens aging: effects of crystallins. *Biochimica et biophysica acta*, 1790, 1095.
- SHI, Y., BARTON, K., DE MARIA, A., PETRASH, J. M., SHIELS, A. & BASSNETT, S. 2009. The stratified syncytium of the vertebrate lens. *Journal of Cell Science*, 122, 1607.
- SHIBATA, T., HOCKWIN, O., WEIGELIN, E., KLEIFELD, O. & DRAGOMIRESCU, V. 1984. *Biometrie der Linse in Abhängigkeit vom Lebensalter und von der Kataraktmorphologie. Auswertung von Scheimpflug-Photos des vorderen Augenabschnittes*.
- SHINOHARA, H., INAGUMA, Y., GOTO, S., INAGAKI, T. & KATO, K. 1993. *Alpha B crystallin and HSP28 are enhanced in the cerebral cortex of patients with Alzheimer's disease*.
- SIVAK, J. G., ANDISON, M. E. & PARDUE, M. T. 1999. Vertebrate optical structure. In: ARCHER, S. N., DJAMGOZ, M. B. A., LOEW, E. R., PARTRIDGE, J. C. & VALLERGA, S. (eds.) *Adaptive Mechanisms in the Ecology of Vision*. Dordrecht: Springer Netherlands.
- SIVAK, J. G., HERBERT, K. L., PETERSON, K. L. & KUSZAK, J. R. 1994. The interrelationship of lens anatomy and optical quality i. non-primate lenses. *Experimental Eye Research*, 59, 505.
- SLINGSBY, C., NORLEDGE, B., SIMPSON, A., BATEMAN, O. A., WRIGHT, G., DRIESSEN, H. P. C., LINDLEY, P. F., MOSS, D. S. & BAX, B. 1997. X-ray diffraction and structure of crystallins. *Progress in Retinal and Eye Research*, 16, 3.
- SOULES, K. A. & LINK, B. A. 2005. Morphogenesis of the anterior segment in the zebrafish eye. *BMC Developmental Biology*, 5, 12.
- SPARROW, J., BRON, A., BROWN, N., AYLIFFE, W. & HILL, A. 1987. *The Oxford Clinical Cataract Classification and Grading System*.
- STEVENSON, J. 1839. Cataract; its Natural, Symptoms and Cure.
- STRENK, S. A., STRENK, L. M. & KORETZ, J. F. 2005. The mechanism of presbyopia. *Progress in Retinal and Eye Research*, 24, 379.
- SUEIRAS, V. M., MOY, V. T. & ZIEBARTH, N. M. 2015. Lens capsule structure assessed with atomic force microscopy. *Molecular Vision*, 21, 316.

- SWEENEY ALISON, M., DES MARAIS DAVID, L., ANDREW BAN, Y.-E. & JOHNSEN, S. 2007. Evolution of graded refractive index in squid lenses. *Journal of The Royal Society Interface*, 4, 685.
- TARDIEU, A. 1988. Eye lens proteins and transparency: from light transmission theory to solution X-ray structural analysis. *Annu Rev Biophys Biophys Chem*, 17, 47-70.
- TAYLOR, V. L., AL-GHOUL, K. J., LANE, C. W., DAVIS, V. A., KUSZAK, J. R. & COSTELLO, M. J. 1996. Morphology of the normal human lens. *Invest Ophthalmol Vis Sci*, 37, 1396.
- THOLOZAN, F. M. D. & QUINLAN, R. A. 2007. Lens cells: More than meets the eye. *The International Journal of Biochemistry & Cell Biology*, 39, 1754.
- THYLEFORS, B., CHYLACK JR., L. T., KONYAMA, K., SASAKI, K., SPERDUTO, R., TAYLOR, H. R. & WEST4, S. 2002. A simplified cataract grading system The WHO Cataract Grading Group. *Ophthalmic Epidemiology*, 9, 83.
- TOOSI FARAHBAKHS, Z., L HUANG, Q., L DING, L., ALTENBACH, C., STEINHOFF, H.-J., HORWITZ, J. & L. HUBBELL, W. 1995. *Interaction of .alpha.-crystallin with Spin-Labeled Peptides*.
- TORSTENSEN, B. E., ESPE, M., SANDEN, M., STUBHAUG, I., WAAGBØ, R., HEMRE, G. I., FONTANILLAS, R., NORDGARDEN, U., HEVRØY, E. M., OLSVIK, P. & BERNTSEN, M. H. G. 2008. Novel production of Atlantic salmon (*Salmo salar*) protein based on combined replacement of fish meal and fish oil with plant meal and vegetable oil blends. *Aquaculture*, 285, 193.
- TOYAMA, B. H. & HETZER, M. W. 2013. Protein homeostasis: live long, won't prosper. *Nature reviews. Molecular cell biology*, 14, 55.
- TRIFONOVA, N., KALAYDJIEV, S., STAMENOVA, M., TRIFONOVA, R. & BREIPOHL, W. 2002. Porcine eye lens crystallins: antigenic similarity with human crystallins and tool for the detection of anti-crystallin antibodies. *Graefe's Archive for Clinical and Experimental Ophthalmology*, 240, 777.
- TROKEL, S. 1962. The Physical Basis for Transparency of the Crystalline Lens. *Investigative Ophthalmology & Visual Science*, 1, 493.
- TRÖBE, C., RHODES, J. D., SANDERSON, J., BRECK, O. & WAAGBØ, R. 2010. Effect of plant-based feed ingredients on osmoregulation in the Atlantic salmon lens. *Comparative Biochemistry and Physiology Part B: Biochemistry and Molecular Biology*, 155, 354.
- VAGHEFI, E., WALKER, K., PONTRE, B. P., JACOBS, M. D. & DONALDSON, P. J. 2012. Magnetic resonance and confocal imaging of solute penetration into the lens reveals a zone of restricted extracellular space diffusion. *American Journal of Physiology-Regulatory, Integrative and Comparative Physiology*, 302, R1250.
- VAN MONTFORT, R. L. M., BATEMAN, O. A., LUBSEN, N. H. & SLINGSBY, C. 2003. Crystal structure of truncated human β B1-crystallin. *Protein Science*, 12, 2606.

- VAN NOORT, J. M., VAN SEHEL, A. C., BAJRAMOVIC, J. J., OUAGMIRI, M. E. I., POLMAN, C. H., LASSMANN, H. & RAVID, R. 1995. The small heat-shock protein α B-crystallin as candidate autoantigen in multiple sclerosis. *Nature*, 375, 798.
- VIHINEN, H., BELEVICH, I. & JOKITALO, E. 2013. *Three dimensional electron microscopy of cellular organelles by serial block face SEM and ET*.
- VILUPURU, A. S. & GLASSER, A. 2001. Optical and biometric relationships of the isolated pig crystalline lens. *Ophthalmic and Physiological Optics*, 21, 296.
- VOORTER, C. E., LEUNISSEN, J. A. & DE JONG, W. W. 1993. Evolution of the alpha-crystallin/small heat-shock protein family. *Molecular Biology and Evolution*, 10, 103.
- WANG, X., GARCIA, C. M., SHUI, Y.-B. & BEEBE, D. C. 2004. Expression and Regulation of α -, β -, and γ -Crystallins in Mammalian Lens Epithelial Cells. *Investigative Ophthalmology & Visual Science*, 45, 3608.
- WEEBER, H. A. & VAN DER HEIJDE, R. G. L. 2008. Internal deformation of the human crystalline lens during accommodation. *Acta Ophthalmologica*, 86, 642.
- WEGENER, A. & LASER, H. 2001. *[Image analysis and Sheimpflug photography of anterior segment of the eye--a review]*.
- WERNER, L., TRINDADE, F., PEREIRA, F. & WERNER, L. 2000. Physiology of accommodation and presbyopia. *Arquivos Brasileiros de Oftalmologia*, 63, 503-509+487.
- WEST-MAYS, J. A., PINO, G. & LOVICU, F. J. 2010. Development and use of the lens epithelial explant system to study lens differentiation and cataractogenesis. *Progress in Retinal and Eye Research*, 29, 135.
- West, J. A., Sivak, J.G. & Doughty, M. J. 1995. Microscopical evaluation of the crystalline lens of the squid (*Loligo opalescens*) during embryonic development. *Exp. Eye Res.* 60, 19-35.
- WISTOW, G. 1993. Lens crystallins: gene recruitment and evolutionary dynamism. *Trends in Biochemical Sciences*, 18, 301.
- WISTOW, G., WYATT, K., DAVID, L., GAO, C., BATEMAN, O., BERNSTEIN, S., TOMAREV, S., SEGOVIA, L., SLINGSBY, C. & VIHTELIC, T. 2005. γ N-crystallin and the evolution of the $\beta\gamma$ -crystallin superfamily in vertebrates. *FEBS Journal*, 272, 2276.
- WORTHINGTON, C. R. 1969. Structural parameters of nerve myelin. *Proc Natl Acad Sci U S A*, 63, 604.
- XU, K. & HAO, Y. 2013. Determination of the density of human nuclear cataract lenses. *Molecular medicine reports*, 8, 1300.
- YAGI, T., KUNO, Y., KOGA, K. & MUKAI, T. Drifting and Blinking Compensation in Electro-oculography (EOG) Eye-gaze Interface. 2006 IEEE International Conference on Systems, Man and Cybernetics, 8-11 Oct. 2006 2006. 3222.

- YAO, Y. & XU, G. X. 2014. Advances of crystallins and age-related cataract. *International Eye Science*, 14, 255.
- ZHAO, H., BROWN, P. H., MAGONE, M. T. & SCHUCK, P. 2011. The molecular refractive function of lens γ -Crystallins. *Journal of molecular biology*, 411, 680.
- ZOLTOSKI, R. K., WYLES, E., HARTHAN, J. S. & KUSZAK, J. R. 2012. Effect Of Accommodation On The Lens Ultrastructure As Measured Using Slit Lamp Photos And Wave Front Analysis. *Investigative Ophthalmology & Visual Science*, 53, 1343.

Online:

- ARCHIVES.EVERGREEN.EDU, 2019. ARCHIVE - Cephalopods - Comparative Physiology of Vision. [online] Available at: <http://archives.evergreen.edu/webpages/curricular/2011-2012/m2o1112/web/cephalopods.html> [Accessed 27 Jun. 2019].
- ANATOMY ORGAN, 2017. The Eye Diagram. [Online] Available at: <http://anatomyorgan.com/the-eye-diagram/> . [Accessed in 26 Feb 2019].
- ANDLEY, U.P., 2007. Crystallins in the eye: Function and pathology. *Progress in Retinal and Eye Research*, 26, pp.78-98.
- DIAMOND LIGHT SOURCE, 2018. How do synchrotrons work?. [Online] Available at: HYPERLINK "<https://www.diamond.ac.uk/industry/Synchrotron-Oxford/What-is-Synchrotron/How-do-synchrotrons-work.html>" <https://www.diamond.ac.uk/industry/Synchrotron-Oxford/What-is-a-Synchrotron/How-do-synchrotrons-work.html> [Accessed 20 Jan 2019].
- HANDYMATH, 2017. Solutions for Technicians. [Online] Available at: HYPERLINK "<http://www.handymath.com/>" <http://www.handymath.com/> [Accessed 13 Feb 2018].
- IMAGE OF DIAMOND IMAGENUS.CO, 2018. 99000+ New Image Of Diamond 2018,. [Online] Available at: HYPERLINK "<http://www.imagenus.co/%20>" <http://www.imagenus.co/> [Accessed 20 Jan 2018].
- JESSE M. VISLISEL, 2014. Mature cortical cataract ", EyeRounds.org, The University of Iowa, <http://webeye.ophth.uiowa.edu/eyeforum/atlas/pages/mature-cortical-cataract.htm>. [Accessed 2 Feb 2018].
- NOGUERA, P.U.C., BRUNO, D. & SEMENAS, L., 2015. 'The Fish Necropsy Manual. [Online] Available at: HYPERLINK "<http://www.necropsymanual.net/en/>" <http://www.necropsymanual.net/en/> [Accessed 17 Jan 2019].
- WORLD HEALTH ORGANISATION, 2010. Global data on visual impairment 2010. [Online] Available at: HYPERLINK "<http://www.who.int/blindness/publications/globaldata/en/>"

<http://www.who.int/blindness/publications/globaldata/en/>. [Accessed 15 Feb 2018].

7 Appendixes

7.1 Appendix 1: Preparation of pig lenses for serial block face scanning electron microscopy (SBFSEM)

7.1.1 Primary fixation

Two fixation methods were attempted by Dr R. Young in a bid to ensure adequate preservation throughout the crystalline lens' thickness. In some cases, eosin dye was mixed with the fixative (to about 1%) so as to visualise the depth of the fixative's penetration when the lens was cleaved into suitably sized pieces for further analysis. The lenses, which were acquired from a local abattoir within six hours of the animal's death, were immersed in freshly prepared 4% paraformaldehyde in either 0.1M sodium cacodylate or 0.1M Sorensen phosphate buffer, pH 7.2. The timings ranged between four and eight hours at room temperature and up to three days at 4°C, on a rotator.

Slices of ~100µm were obtained from different section planes using either a vibratome or a scalpel. Lens slices, as well as smaller segments, were subsequently transferred to 2.5% glutaraldehyde/2% paraformaldehyde fixative in buffer at room temperature for up to four hours. In some cases, lenses were fixed whilst clamped in a lens-stretcher device, with the entire assembly immersed into the fixative.

7.1.2 Embedding techniques

Fixed lens specimens were processed through a sequence of heavy metal solutions (passed through a 2µm Millipore syringe filter before use), to enhance the backscatter electron signal for serial block-face scanning electron microscopy. To achieve this end, the lenses were fixed in 1.1% osmium tetroxide/1.5% potassium ferricyanide in 0.1M sodium cacodylate buffer for one hour and rinsed three times at ten-minute intervals. To accelerate fixation, the lenses were stored in 1% tannic acid in buffer for two hours

with a single change of reagent. Each was then rinsed thrice using distilled water for ten minutes. The samples were then immersed in 1% aqueous uranyl acetate for one hour, following which each was again rinsed thrice using distilled water at ten-minute intervals. Each specimen was subsequently dehydrated with ethanol and propylene oxide adjusted to the type and size of the tissue (i.e. in graded series of ETOH 70%, 90%, 2x 100% ETOH for 15 minutes and twice in Propylene Oxide for 15 minutes).

They were infiltrated and embedded in Araldite CY212 epoxy resin, by firstly adding a volume of embedding mixture to equal the remaining volume (without the accelerator), and mixed well. Afterward, the resin was changed twice between hourly intervals to reduce any traces of propylene. The vials were then left in the rotator overnight. In the next morning, 100% resin mixture was changed out four times within 150 minutes, and then three times more over the subsequent five hours, before being left again overnight with the lids removed from the tubes to facilitate the evaporation of residual propylene oxide. In the following morning, the resin was changed three times at three-hour intervals. Polyethylene capsules were then stationed in a holder and numbered strips of paper inserted into the cavities. A drop of fresh resin was placed in the capsules before the specimen was transferred to the appropriate capsule. The blocks were then cured for 24 hours in a 60 °C oven in order to polymerise the resin.

All the foregoing procedures were carried out in a fume hood on account of the hazardous nature of the majority of the reagents. Unfortunately, however, these processes failed to yield adequately embedded blocks to permit satisfactory ultrathin sectioning or serial block face SEM examination.

7.1.3 Microwave Tissue Processing

As an alternative, a microwave-assisted fixation and resin embedment of fresh pig lens specimen was attempted using *Pelco EM Pro Microwave*, available on demonstration from Agar Scientific 09.2017. The detailed description of the protocol employed is included in Appendix 6, with the exception that Araldite CY212 resin and ethanol dehydration were used in place of the resin Durcupan and acetone, respectively. The blocks prepared by this system appeared well-embedded even though the resultant tissue specimens were prone to shattering on impact with the ultramicrotome knife, and therefore making sectioning difficult. The resultant blocks were unsuitable for serial block face SEM on account of the disintegration of the tissue specimen on the knife's contact. It is arguable, therefore, that while the resin infiltration and polymerisation was acceptably successful, the heavy metal reagents had either penetrated incompletely or had rendered the tissue too brittle for smooth interaction with the knife. The optimisation of the lens preparation schedule is, therefore, still required.

7.1.4 Serial block face protocol attempted

| Serial BlockFace | Step No. | Hours | Minutes | Seconds | Watts | Temperature Limit | Vacuum | User Prompt |
|--|----------|-------|---------|---------|-------|-------------------|--------|-------------|
| Glutaraldehyde fixation ON - Vacuum ON | 1 | 0 | 2 | 0 | 100 | 50 | ON | OFF |
| Glutaraldehyde fixation OFF - Vacuum ON | 2 | 0 | 2 | 0 | 0 | 50 | ON | OFF |
| Glutaraldehyde fixation ON - Vacuum ON | 3 | 0 | 2 | 0 | 100 | 50 | ON | OFF |
| Glutaraldehyde fixation OFF - Vacuum ON | 4 | 0 | 2 | 0 | 0 | 50 | ON | OFF |
| Glutaraldehyde fixation ON - Vacuum ON | 5 | 0 | 2 | 0 | 100 | 50 | ON | OFF |
| Glutaraldehyde fixation OFF - Vacuum ON | 6 | 0 | 2 | 0 | 0 | 50 | ON | OFF |
| Glutaraldehyde fixation ON - Vacuum ON | 7 | 0 | 2 | 0 | 100 | 50 | ON | OFF |
| Glutaraldehyde fixation OFF - Vacuum ON | 8 | 0 | 2 | 0 | 0 | 50 | ON | ON |
| Buffer Wash 1 | 9 | 0 | 0 | 40 | 100 | 50 | ON | ON |
| Buffer Wash 2 | 10 | 0 | 0 | 40 | 100 | 50 | ON | ON |
| Buffer Wash 3 | 11 | 0 | 0 | 40 | 100 | 50 | ON | ON |
| 2% osmium tetroxide 1.5% potassium ferricyanide ON - Vacuum ON | 12 | 0 | 2 | 0 | 100 | 50 | ON | OFF |

| | | | | | | | | |
|---|----|---|---|----|-----|----|----|-----|
| 2% osmium tetroxide 1.5% potassium ferricyanide OFF - Vacuum ON | 13 | 0 | 2 | 0 | 0 | 50 | ON | OFF |
| 2% osmium tetroxide 1.5% potassium ferricyanide ON - Vacuum ON | 14 | 0 | 2 | 0 | 100 | 50 | ON | ON |
| 2% osmium tetroxide 1.5% potassium ferricyanide ON - Vacuum ON | 15 | 0 | 2 | 0 | 100 | 50 | ON | OFF |
| 2% osmium tetroxide 1.5% potassium ferricyanide OFF - Vacuum ON | 16 | 0 | 2 | 0 | 0 | 50 | ON | OFF |
| 2% osmium tetroxide 1.5% potassium ferricyanide ON - Vacuum ON | 17 | 0 | 2 | 0 | 100 | 50 | ON | ON |
| UHQ Water Wash 1 | 18 | 0 | 0 | 40 | 100 | 50 | ON | ON |
| UHQ Water Wash 2 | 19 | 0 | 0 | 40 | 100 | 50 | ON | ON |
| UHQ Water Wash 3 | 20 | 0 | 0 | 40 | 100 | 50 | ON | ON |
| 1% Thiocarbohydrazide ON - Vacuum ON | 21 | 0 | 2 | 0 | 100 | 50 | ON | OFF |
| 1% Thiocarbohydrazide OFF - Vacuum ON | 22 | 0 | 2 | 0 | 0 | 50 | ON | ON |
| 1% Thiocarbohydrazide ON - Vacuum ON | 23 | 0 | 2 | 0 | 100 | 50 | ON | OFF |
| 1% Thiocarbohydrazide OFF - Vacuum ON | 24 | 0 | 2 | 0 | 0 | 50 | ON | ON |
| 1% Thiocarbohydrazide ON - Vacuum ON | 25 | 0 | 2 | 0 | 100 | 50 | ON | OFF |
| 1% Thiocarbohydrazide OFF - Vacuum ON | 26 | 0 | 2 | 0 | 0 | 50 | ON | ON |
| 1% Thiocarbohydrazide ON - Vacuum ON | 27 | 0 | 2 | 0 | 100 | 50 | ON | OFF |

| | | | | | | | | |
|--|----|---|---|----|-----|----|----|-----|
| 1% Thiocarbohydrazide OFF - Vacuum ON | 28 | 0 | 2 | 0 | 0 | 50 | ON | ON |
| UHQ Water Wash 1 | 29 | 0 | 0 | 40 | 100 | 50 | ON | ON |
| UHQ Water Wash 2 | 30 | 0 | 0 | 40 | 100 | 50 | ON | ON |
| UHQ Water Wash 3 | 31 | 0 | 0 | 40 | 100 | 50 | ON | ON |
| 2% osmium tetroxide ON - Vacuum ON | 32 | 0 | 2 | 0 | 100 | 50 | ON | OFF |
| 2% osmium tetroxide OFF - Vacuum ON | 33 | 0 | 2 | 0 | 0 | 50 | ON | OFF |
| 2% osmium tetroxide ON - Vacuum ON | 34 | 0 | 2 | 0 | 100 | 50 | ON | OFF |
| 2% osmium tetroxide OFF - Vacuum ON | 35 | 0 | 2 | 0 | 0 | 50 | ON | OFF |
| 2% osmium tetroxide ON - Vacuum ON | 36 | 0 | 2 | 0 | 100 | 50 | ON | OFF |
| 2% osmium tetroxide OFF - Vacuum ON | 37 | 0 | 2 | 0 | 0 | 50 | ON | OFF |
| 2% osmium tetroxide ON - Vacuum ON | 38 | 0 | 2 | 0 | 100 | 50 | ON | OFF |
| 2% osmium tetroxide OFF - Vacuum ON | 39 | 0 | 2 | 0 | 0 | 50 | ON | ON |
| UHQ Water Wash 1 | 40 | 0 | 0 | 40 | 100 | 50 | ON | ON |
| UHQ Water Wash 2 | 41 | 0 | 0 | 40 | 100 | 50 | ON | ON |
| UHQ Water Wash 3 | 42 | 0 | 0 | 40 | 100 | 50 | ON | ON |
| 1% uranyl acetate ON - Vacuum ON | 43 | 0 | 2 | 0 | 100 | 50 | ON | OFF |
| 1% uranyl acetate OFF - Vacuum ON | 44 | 0 | 2 | 0 | 0 | 50 | ON | ON |
| 1% uranyl acetate ON - Vacuum ON | 45 | 0 | 2 | 0 | 100 | 50 | ON | OFF |

| | | | | | | | | |
|--|----|---|---|----|-----|----|----|-----|
| 1% uranyl acetate OFF - Vacuum ON | 46 | 0 | 2 | 0 | 0 | 50 | ON | ON |
| 1% uranyl acetate ON - Vacuum ON | 47 | 0 | 2 | 0 | 100 | 50 | ON | OFF |
| 1% uranyl acetate OFF - Vacuum ON | 48 | 0 | 2 | 0 | 0 | 50 | ON | ON |
| 1% uranyl acetate ON - Vacuum ON | 49 | 0 | 2 | 0 | 100 | 50 | ON | OFF |
| 1% uranyl acetate OFF - Vacuum ON | 50 | 0 | 2 | 0 | 0 | 50 | ON | ON |
| UHQ Water Wash 1 | 51 | 0 | 0 | 40 | 100 | 50 | ON | ON |
| UHQ Water Wash 2 | 52 | 0 | 0 | 40 | 100 | 50 | ON | ON |
| UHQ Water Wash 3 | 53 | 0 | 0 | 40 | 100 | 50 | ON | ON |
| Lead aspartate at 45oC ON - Vacuum ON | 54 | 0 | 2 | 0 | 100 | 45 | ON | OFF |
| Lead aspartate at 45oC OFF - Vacuum ON | 55 | 0 | 2 | 0 | 0 | 45 | ON | ON |
| Lead aspartate at 45oC ON - Vacuum ON | 56 | 0 | 2 | 0 | 100 | 45 | ON | OFF |
| Lead aspartate at 45oC OFF - Vacuum ON | 57 | 0 | 2 | 0 | 0 | 45 | ON | ON |
| Lead aspartate at 45oC ON - Vacuum ON | 58 | 0 | 2 | 0 | 100 | 45 | ON | OFF |
| Lead aspartate at 45oC OFF - Vacuum ON | 59 | 0 | 2 | 0 | 0 | 45 | ON | ON |
| Lead aspartate at 45oC ON - Vacuum ON | 60 | 0 | 2 | 0 | 100 | 45 | ON | OFF |
| Lead aspartate at 45oC OFF - Vacuum ON | 61 | 0 | 2 | 0 | 0 | 45 | ON | ON |
| UHQ Water Wash 1 | 62 | 0 | 0 | 40 | 100 | 50 | ON | ON |

| | | | | | | | | |
|---|----|---|---|----|-----|----|----|-----|
| UHQ Water Wash 2 | 63 | 0 | 0 | 40 | 100 | 50 | ON | ON |
| UHQ Water Wash 3 | 64 | 0 | 0 | 40 | 100 | 50 | ON | ON |
| Dehydration 30% Acetone ON - Vacuum ON | 65 | 0 | 1 | 0 | 150 | 50 | ON | OFF |
| Dehydration 30% Acetone OFF - Vacuum ON | 66 | 0 | 1 | 0 | 0 | 50 | ON | OFF |
| Dehydration 30% Acetone ON - Vacuum ON | 67 | 0 | 1 | 0 | 150 | 50 | ON | ON |
| Dehydration 50% Acetone ON - Vacuum ON | 68 | 0 | 1 | 0 | 150 | 50 | ON | OFF |
| Dehydration 50% Acetone OFF - Vacuum ON | 69 | 0 | 1 | 0 | 0 | 50 | ON | OFF |
| Dehydration 50% Acetone ON - Vacuum ON | 70 | 0 | 1 | 0 | 150 | 50 | ON | ON |
| Dehydration 70% Acetone ON - Vacuum ON | 71 | 0 | 1 | 0 | 150 | 50 | ON | OFF |
| Dehydration 70% Acetone OFF - Vacuum ON | 72 | 0 | 1 | 0 | 0 | 50 | ON | OFF |
| Dehydration 70% Acetone ON - Vacuum ON | 73 | 0 | 1 | 0 | 150 | 50 | ON | ON |
| Dehydration 90% Acetone ON - Vacuum ON | 74 | 0 | 1 | 0 | 150 | 50 | ON | OFF |
| Dehydration 90% Acetone OFF - Vacuum ON | 75 | 0 | 1 | 0 | 0 | 50 | ON | OFF |
| Dehydration 90% Acetone ON - Vacuum ON | 76 | 0 | 1 | 0 | 150 | 50 | ON | ON |
| Dehydration 100% Acetone ON - Vacuum ON | 77 | 0 | 1 | 0 | 150 | 50 | ON | OFF |
| Dehydration 100% Acetone OFF - Vacuum ON | 78 | 0 | 1 | 0 | 0 | 50 | ON | OFF |

| | | | | | | | | |
|---|----|---|----|---|-----|----|-----|-----|
| Dehydration 100% Acetone ON - Vacuum ON | 79 | 0 | 1 | 0 | 150 | 50 | ON | ON |
| Dehydration 100% Acetone ON - Vacuum ON | 80 | 0 | 1 | 0 | 150 | 50 | ON | OFF |
| Dehydration 100% Acetone OFF - Vacuum ON | 81 | 0 | 1 | 0 | 0 | 50 | ON | OFF |
| Dehydration 100% Acetone ON - Vacuum ON | 82 | 0 | 1 | 0 | 150 | 50 | ON | ON |
| Dehydration 100% Acetone ON - Vacuum ON | 83 | 0 | 1 | 0 | 150 | 50 | ON | OFF |
| Dehydration 100% Acetone OFF - Vacuum ON | 84 | 0 | 1 | 0 | 0 | 50 | ON | OFF |
| Dehydration 100% Acetone ON - Vacuum ON | 85 | 0 | 1 | 0 | 150 | 50 | ON | ON |
| Durcupan Infiltration | 86 | 0 | 3 | 0 | 150 | 50 | ON | OFF |
| Durcupan Infiltration | 87 | 0 | 3 | 0 | 150 | 50 | ON | ON |
| Durcupan Infiltration | 88 | 0 | 3 | 0 | 150 | 50 | ON | ON |
| Durcupan Infiltration | 89 | 0 | 3 | 0 | 150 | 50 | ON | ON |
| Durcupan Infiltration | 90 | 0 | 3 | 0 | 150 | 50 | ON | ON |
| Durcupan Infiltration | 91 | 0 | 3 | 0 | 150 | 50 | ON | ON |
| Durcupan Infiltration | 92 | 0 | 3 | 0 | 150 | 50 | ON | ON |
| Durcupan Infiltration | 93 | 0 | 3 | 0 | 150 | 50 | ON | ON |
| Polymerisation | 94 | 1 | 30 | 0 | 650 | 90 | OFF | ON |

7.2 Appendix 2: Protocol for preparation of artificial aqueous humor

Material: 125 mM NaCl, 0.5 mM MgCl₂, 4.5 mM KCl, 10 mM NaHCO₃, 2 mM CaCl₂, 5 mM glucose, 20 mM sucrose, 10 mM HEPES, pH 7.2–7.4, 300 ± 5 mOsm, balance and spatula.

1. Wearing a lab coat and gloves
2. All chemical substance should be in hand and in order.
3. All the works carry on the fume hood.
4. Transfer open pan balance to fume hood and weigh 3.6525g powder of NaCl. Clear up any spillage of powder immediately with damp tissue.
5. Add NaCl powder to 250 ml distilled water.
6. Repeat steps (4 and5) with following subunits: Mgcl₂ 23.8028mg, 167.75mg KCl, 420mg NaHCO₃, 111mg CaCl₂, 450.5mg glucose, 3.425g sucrose and 5 ml HEPES.
7. Transfer to pH meter and correct pH to 7.2–7.4, 300 ± 5 mOsm with 1M HCl
8. Make up to 500 with distilled water. Keep in fridge and can be used within two weeks.

7.3 Appendix 3: Average and standard deviations lens widths for the various lenses/areas

| Regions | Lens Condition | | Lens(1) | Lens(2) | Lens(3) | Lens(4) | Lens(5) | All Lenses |
|-----------------|--------------------|---------|---------|---------|---------|---------|---------|------------|
| Suture Junction | <i>Unstretched</i> | Mean/SD | 5.9±0.3 | 5.7±0.3 | 6.6±0.3 | 6.2±0.2 | 6.6±0.2 | 6.2±0.1 |
| | <i>Stretched</i> | Mean/SD | 6.1±0.4 | 5.6±0.2 | 6.3±0.3 | 6.5±0.4 | 6.6±0.3 | 6.2±0.1 |
| Inferior | <i>Unstretched</i> | Mean/SD | 6.0±0.2 | 6.1±0.2 | 6.0±0.2 | 6.7±0.1 | 6.4±0.1 | 6.3±0.1 |
| | <i>Stretched</i> | Mean/SD | 5.8±0.2 | 6.2±0.2 | 6.3±0.2 | 6.2±0.1 | 6.5±0.2 | 6.2±0.1 |
| Temporal | <i>Unstretched</i> | Mean/SD | 5.9±0.3 | 5.7±0.2 | 6.2±0.2 | 6.3±0.2 | 6.6±0.2 | 6.1±0.1 |
| | <i>Stretched</i> | Mean/SD | 5.9±0.4 | 5.6±0.2 | 6.2±0.3 | 6.1±0.4 | 6.9±0.2 | 6.5±0.1 |
| Nasal | <i>Unstretched</i> | Mean/SD | 6.0±0.2 | 5.4±0.2 | 6.4±0.1 | 6.7±0.4 | 6.6±0.1 | 6.2±0.1 |
| | <i>Stretched</i> | Mean/SD | 5.8±0.2 | 5.6±0.2 | 6.2±0.1 | 6.0±0.3 | 6.5±0.3 | 6.0±0.1 |
| Superior | <i>Unstretched</i> | Mean/SD | 5.9±0.2 | 5.8±0.1 | 6.1±0.3 | 6.2±0.2 | 6.6±0.1 | 6.1±0.1 |
| | <i>Stretched</i> | Mean/SD | 5.8±0.2 | 5.8±0.2 | 6.1±0.1 | 6.1±0.3 | 6.7±0.1 | 6.1±0.1 |

8 Submitted abstracts and Future publications

8.1 Abstracts (1): Changes in the X-ray diffraction pattern of porcine lens before and after simulated accommodation

S. Al-Atawi, J. Albon, K. Meek, S. Hayes, J. Bell, J. Regini

First published: 07 September 2017 <https://doi.org/10.1111/j.1755-3768.2017.0S074>

The European Association for Vision and Eye Research (EVER) 2017 Congress, took place 9 September, 2017 in Nice, France.

Purpose: During the accommodation process, the morphology of the lens changes. The crystallin proteins within the lens fibres are the primary structural unit of organisation at the cellular level, and play a major role in maintaining transparency and refractive power. All the structural information about the lens from X-ray scattering techniques have so far been performed on samples in the relaxed accommodated state. It is thought that largest structural changes occur in the lens nucleus during accommodation.

Aims: To measure any changes in the average distance between the crystallin proteins, and their ordering within the lens fibres before and after stretching using small angle x-ray scattering.

Methods: Fresh porcine lenses were mounted into a commercially available lens stretching device (Bioniko, Florida, USA). Samples were placed in the X-ray beam at

the Diamond synchrotron and 2D grid scans performed. Scans were taken in the same lens in both the accommodated and unaccommodated states, before and after a stretching.

Results: All patterns show a reduction in both the X-ray intensity and in the average spacing between the crystallin proteins, in the centre of the lens compared with the periphery. This is consistent with the increase of protein concentration from the lens cortex to the nucleus. No significant changes in the average spacing between the crystallin proteins was observed upon stretching. Substantial changes in both the X-ray intensity, and in the ordering of the proteins were recorded at the peripheral margins of lenses in the stretched state.

Conclusions: The changes in the X-ray intensity, and in the ordering of the crystallin proteins at the peripheral margins of the lens are somewhat in contrast to the notion that the nucleus undergoes the largest structural changes.

8.1.1 Abstract (2): Internal lens structure changes during simulated accommodation

S. Al-Atawi¹, N. White¹, K.M. Meek¹, Young R¹, J.W. Regini¹ and J. Albon¹.

¹Structural Biophysics Research Group, School of Optometry and Vision Sciences, Cardiff University, Maindy road, CF24 4HQ.

First presented at 3rd International Conference and Expo on Optometry & Vision Science - October 08-09, 2018 - Edinburgh, Scotland

Aim: Since the internal structural changes that occur during the lens accommodation process are not fully understood, in this study we aimed to analyse lens fibre widths during simulated accommodation.

Methods: Porcine eyes (n=11) were dissected and attached to a lens stretcher. 3D image stacks (between 120µm to 240/270 µm depth) of the anterior and posterior surfaces of five lenses, whilst immersed in artificial aqueous humour solution, were acquired using confocal microscopy in the un-stretched configuration and then the stretched configuration. Three lenses remained in the un-stretched configuration and 3 lenses were subjected to stretching. All 6 lenses were fixed with 4% paraformaldehyde, snap frozen and then serially cut into cryosections 25µm in thickness. 1mm interval sections were incubated in PBS- wheat germ agglutinin- Hoechst 33342 solution. Lens

fibre widths were measured following acquisition of fluorescent images of each lens at different depths.

Result: From the confocal images, analysis of lens fibre widths in anterior and posterior lens demonstrated a significant difference between unstretched and stretched configurations in both anterior (mean lens fibre width: $5.1 \pm 0.589 \mu\text{m}$ versus $5.625 \pm 0.345 \mu\text{m}$, $p < 0.0001$) and posterior surfaces ($5.55 \pm 0.16 \mu\text{m}$ versus $5.67 \pm 0.25 \mu\text{m}$, $p < 0.0001$). In fluorescent images, lens fibre widths were unchanged between unstretched and stretched configurations at depths of 1mm (mean lens fibre width: $5.7 \pm 0.29 \mu\text{m}$, versus $5.7 \pm 0.52 \mu\text{m}$, $p = 0.411$), and at 5mm ($7.7 \pm 1.89 \mu\text{m}$, versus $7.9 \pm 2.14 \mu\text{m}$, $p = 0.2309$ and at 6mm ($6 \pm 1.08 \mu\text{m}$, versus $5.97 \pm 0.89 \mu\text{m}$, $p = 0.814$). An increase in mean lens fibre widths was observed in stretched lenses at depths 2mm ($6.9 \pm 1.76 \mu\text{m}$, versus $7.9 \pm 1.9 \mu\text{m}$, $p < 0.0001$), at 3mm ($8.9 \pm 2.42 \mu\text{m}$, versus $8.98 \pm 2.326 \mu\text{m}$, $p = 0.0002$), and at 4mm ($8.45 \pm 2.8 \mu\text{m}$ versus $9.1 \pm 2.2 \mu\text{m}$, $p = 0.033$). A decrease in cortical lens fibre widths occurred ($6.67 \pm 1.37 \mu\text{m}$ versus $5.65 \pm 0.29 \mu\text{m}$, $p < 0.0001$) at 7mm.

Conclusion: Controversy exists as to whether nuclear lens fibres are altered during accommodation. This study shows lens fibre width alters at some depths, but not in others during accommodation.

8.1.2 Ultrastructure of aquatic mammal and porcine lenses

S. Al-Atawi, J. Albon, K. Meek, B. Pierscionek, J. Regini

8.1.3 Changes in the X-ray diffraction pattern of porcine lens before and after simulated accommodation


S. Al-Atawi, J. Albon, K. Meek, B. Pierscionek S. Hayes, J. Bell, J. Regini

8.1.4 Internal lens structure changes during simulated accommodation

S. Al-Atawi, N. White, K.M. Meek, Young R, J.W. Regini and J. Albon.

9 Figure Permissions

Figure 1-1: Vertebrate eye and lens.



Welcome, **Saleha**
Not you?

[Log out](#) | [Cart \(0\)](#) | [Manage Account](#) | [Feedback](#) | [Help](#) | [Live Help](#)

Get Permission / Find Title
Publication Title or ISBN/ISSN [Go](#)
[Advanced Search Options](#)

Note: Copyright.com supplies permissions but not the copyrighted content itself.

1 PAYMENT — 2 REVIEW — 3 **CONFIRMATION**

Step 3: Order Confirmation

[Start new search >](#) [View your Order History >](#)

[Print order information:](#) includes order confirmation, terms and conditions, and citation information ([What's this?](#))

Thank you for your order! A confirmation for your order will be sent to your account email address. If you have questions about your order, you can call us 24 hrs/day, M-F at +1.855.239.3415 Toll Free, or write to us at info@copyright.com. This is not an invoice.

Confirmation Number: 11780196
Order Date: 01/08/2019


If you paid by credit card, your order will be finalized and your card will be charged within 24 hours. If you choose to be invoiced, you can change or cancel your order until the invoice is generated.

Payment Information

Saleha Al-atawi
Cardiff university
al-atawisk@cardiff.ac.uk
[+44 7440604554](tel:+447440604554)
Payment Method: n/a

Order Details

Journal of cell science


| | |
|--|--|
| Order detail ID: 71756540 | Permission Status:  Granted |
| Order License Id: 4504260905310 | Permission type: Republish or display content |
| ISSN: 1477-9137 | Type of use: Republish in a thesis/dissertation |
| Publication Type: e-Journal | View details |
| Volume: | |
| Issue: | |
| Start page: | |
| Publisher: COMPANY OF BIOLOGISTS LTD. | |
| Author/Editor: Company of Biologists | |




Note: This item will be invoiced or charged separately through CCC's **RightsLink** service. [More info](#) \$ 0.00

Total order items: 1 **This is not an invoice.** **Order Total: 0.00 USD**

Figure 1-2:

[IMAIOS] Re: Need a permission to use image in phd thesis

 IMAIOS Support team <contact@imaios.com>
Wed 19/12/2018, 08:46
Saleha Al-Atawi

  Reply all | 

Inbox

You replied on 19/12/2018 09:56.

In replies all text above this line is added to the ticket

Your request ([#78895](#)) has been deemed solved.

Barbara (IMAIOS)
19 déc. 09:46 CET

Dear Saleha,

We grant you the permission to use some images from e-Anatomy for your thesis, provided it is for educational, offline and non-profit purposes, and source is cited as "e-Anatomy, Micheau A, Hoa D, www.imaios.com".

Feel free to contact me if you have any question.

Sincerely,
Barbara

IMAIOS SAS

=====

Follow us:
LinkedIn <http://www.linkedin.com/company/imaios-sas>
Facebook <https://www.facebook.com/pages/Imaios/201783243198187>
Twitter <https://twitter.com/IMAIOS>

=====

Figure 1-3:

**SPRINGER NATURE LICENSE
TERMS AND CONDITIONS**

Feb 22, 2019

This Agreement between Cardiff university -- Saleha Al-atawi ("You") and Springer Nature ("Springer Nature") consists of your license details and the terms and conditions provided by Springer Nature and Copyright Clearance Center.


| | |
|--|---|
| License Number | 4534140257100 |
| License date | Feb 22, 2019 |
| Licensed Content Publisher | Springer Nature |
| Licensed Content Publication | Nature Reviews Molecular Cell Biology |
| Licensed Content Title | Protein homeostasis: live long, won't prosper |
| Licensed Content Author | Brandon H. Toyama, Martin W. Hetzer |
| Licensed Content Date | Dec 21, 2012 |
| Licensed Content Volume | 14 |
| Licensed Content Issue | 1 |
| Type of Use | Thesis/Dissertation |
| Requestor type | academic/university or research institute |
| Format | print and electronic |
| Portion | figures/tables/illustrations |
| Number of figures/tables/illustrations | 1 |
| High-res required | no |
| Will you be translating? | no |
| Circulation/distribution | <501 |
| Author of this Springer Nature content | no |

| | |
|----------------------------|--|
| Title | Structural changes in the lens during accommodation |
| Institution name | Cardiff University |
| Expected presentation date | Mar 2019 |
| Portions | Crystallin is a long-lived lens protein important for eye function. Figure 2 |
| Requestor Location | Cardiff university cardiff cardiff, wales CF24 4HQ United Kingdom Attn: Cardiff university |
| Billing Type | Invoice |
| Billing Address | Cardiff university cardiff cardiff, United Kingdom CF24 4HQ Attn: Cardiff university |
| Total | 0.00 USD |
| Terms and Conditions | |

Figure 1-4:

each this p: DEV The cellular and m Diamond Light So DEV The cellular and m Rightslink® by Co Copyright Cle

eration=confirmPurchase



Welcome, Saleha
Not you?

Log out | Cart (0) | [Manage Account](#) | [Feedback](#) | [Help](#) | [Live Help](#)

Get Permission / Find Title

 [Go](#)
[Advanced Search Options](#)

Note: Copyright.com supplies permissions but not the copyrighted content itself.

1 PAYMENT — 2 REVIEW — **3 CONFIRMATION**

Step 3: Order Confirmation

[Start new search >](#) | [View your Order History >](#)

Print order information:
includes order confirmation, terms and conditions, and citation information
[\(What's this?\)](#)

Thank you for your order! A confirmation for your order will be sent to your account email address. If you have questions about your order, you can call us 24 hrs/day, M-F at +1.855.239.3415 Toll Free, or write to us at info@copyright.com. This is not an invoice.

Confirmation Number: 11793065
Order Date: 02/22/2019

If you paid by credit card, your order will be finalized and your card will be charged within 24 hours. If you choose to be invoiced, you can change or cancel your order until the invoice is generated.

Payment Information

Saleha Al-atawi
Cardiff university
al-atawisk@cardiff.ac.uk
[+44 7440604554](tel:+447440604554)
Payment Method: n/a

Order Details

Development

| | |
|---|--|
| <p>Order detail ID: 71820051 Order License Id: 4534150346957 ISSN: 1477-9129 Publication Type: e-Journal Volume: Issue: Start page: Publisher: COMPANY OF BIOLOGISTS, Author/Editor: Company of Biologists</p> | <p>Permission Status: ✔ Granted Permission type: Republish or display content Type of use: Republish in a thesis/dissertation View details</p> |
|---|--|

Note: This item will be invoiced or charged separately through CCC's RightsLink service. [More info](#) \$ 0.00

Total order items: 1

This is not an invoice.

Order Total: 0.00 USD

Figure 1-5:

Order Completed

Thank you for your order.

This Agreement between Cardiff university -- Saleha Al-atawi ("You") and Elsevier ("Elsevier") consists of your license details and the terms and conditions provided by Elsevier and Copyright Clearance Center.

Your confirmation email will contain your order number for future reference.

[printable details](#)

| | |
|--|--|
| License Number | 4534150867556 |
| License date | Feb 22, 2019 |
| Licensed Content Publisher | Elsevier |
| Licensed Content Publication | Progress in Retinal and Eye Research |
| Licensed Content Title | The development of lens sutures |
| Licensed Content Author | J.R. Kuszak |
| Licensed Content Date | Jan 1, 1995 |
| Licensed Content Volume | 14 |
| Licensed Content Issue | 2 |
| Licensed Content Pages | 25 |
| Type of Use | reuse in a thesis/dissertation |
| Portion | figures/tables/illustrations |
| Number of figures/tables/illustrations | 1 |
| Format | both print and electronic |
| Are you the author of this Elsevier article? | No |
| Will you be translating? | No |
| Original figure numbers | Schematic diagram depicting the life-long growth scheme of the lens. Fig 5 |
| Title of your thesis/dissertation | Structural changes in the lens during accommodation |
| Publisher of new work | Cardiff University |
| Expected completion date | Mar 2019 |
| Estimated size (number of pages) | 1 |
| Requestor Location | Cardiff university cardiff |
| | cardiff, wales CF24 4HQ United Kingdom Attn: Cardiff university |
| Publisher Tax ID | GB 494 6272 12 |
| Total | 0.00 USD |

[ORDER MORE](#) [CLOSE WINDOW](#)

Figure 1-8 (A)

Copyright Clearance Center RightsLink®

Home Account Info Help



Title: Protein misfolding and aggregation in cataract disease and prospects for prevention
Author: Kate L. Moreau,Jonathan A. King
Publication: Trends in Molecular Medicine
Publisher: Elsevier
Date: May 2012
Copyright © 2012 Elsevier Ltd. All rights reserved.

Logged in as:
Saleha Al-atawi
Cardiff university
Account #:
3001365711
LOGOUT

Order Completed

Thank you for your order.

This Agreement between Cardiff university -- Saleha Al-atawi ("You") and Elsevier ("Elsevier") consists of your license details and the terms and conditions provided by Elsevier and Copyright Clearance Center.

Your confirmation email will contain your order number for future reference.

printable details

| | |
|--|--|
| License Number | 4536410067727 |
| License date | Feb 26, 2019 |
| Licensed Content Publisher | Elsevier |
| Licensed Content Publication | Trends in Molecular Medicine |
| Licensed Content Title | Protein misfolding and aggregation in cataract disease and prospects for prevention |
| Licensed Content Author | Kate L. Moreau,Jonathan A. King |
| Licensed Content Date | May 1, 2012 |
| Licensed Content Volume | 18 |
| Licensed Content Issue | 5 |
| Licensed Content Pages | 10 |
| Type of Use | reuse in a thesis/dissertation |
| Portion | figures/tables/illustrations |
| Number of figures/tables/illustrations | 1 |
| Format | both print and electronic |
| Are you the author of this Elsevier article? | No |
| Will you be translating? | No |
| Original figure numbers | Computational simulation of human γ D-crystallin polymerization. Fig 3 |
| Title of your thesis/dissertation | Structural changes in the lens during accommodation |
| Publisher of new work | Cardiff University |
| Expected completion date | Mar 2019 |
| Estimated size (number of pages) | 1 |
| Requestor Location | Cardiff university cardiff cardiff, wales CF24 4HQ United Kingdom Attn: Cardiff university |
| Publisher Tax ID | GB 494 6272 12 |
| Total | 0.00 USD |

Figure 1-8 (B)

Copyright Clearance Center RightsLink®

Home Account Info Help



Title: Crystal structure of truncated human β B1-crystallin
Author: Rob L.M. van Montfort, Orval A. Bateman, Nicolette H. Lubsen, et al
Publication: Protein Science
Publisher: John Wiley and Sons
Date: Jan 1, 2009
© The Protein Society

Logged in as:
Saleha Al-atawi
Cardiff university
Account #:
3001365711
LOGOUT

Order Completed

Thank you for your order.


This Agreement between Cardiff university -- Saleha Al-atawi ("You") and John Wiley and Sons ("John Wiley and Sons") consists of your license details and the terms and conditions provided by John Wiley and Sons and Copyright Clearance Center.

Your confirmation email will contain your order number for future reference.


[printable details](#)


| | |
|---------------------------------------|---|
| License Number | 4536411497169 |
| License date | Feb 26, 2019 |
| Licensed Content Publisher | John Wiley and Sons |
| Licensed Content Publication | Protein Science |
| Licensed Content Title | Crystal structure of truncated human β B1-crystallin |
| Licensed Content Author | Rob L.M. van Montfort, Orval A. Bateman, Nicolette H. Lubsen, et al |
| Licensed Content Date | Jan 1, 2009 |
| Licensed Content Volume | 12 |
| Licensed Content Issue | 11 |
| Licensed Content Pages | 7 |
| Type of use | Dissertation/Thesis |
| Requestor type | University/Academic |
| Format | Electronic |
| Portion | Figure/table |
| Number of figures/tables | 1 |
| Original Wiley figure/table number(s) | Ribbon diagrams showing the assembly characteristics of the domains in monomeric bovine γ B-crystallin . Fig 1 |
| Will you be translating? | No |
| Title of your thesis / dissertation | Structural changes in the lens during accommodation |
| Expected completion date | Mar 2019 |
| Expected size (number of pages) | 1 |
| Requestor Location | Cardiff university cardiff cardiff, wales CF24 4HQ United Kingdom Attn: Cardiff university |
| Publisher Tax ID | EU826007151 |
| Total | 0.00 USD |


Figure 1-8 (C)



Copyright Clearance Center



[Home](#)
[Account Info](#)
[Help](#)




Title: Homology Modeling of Cephalopod Lens S-Crystallin: A Natural Mutant of Sigma-Class Glutathione Transferase with Diminished Endogenous Activity

Author: Chyh-Chong Chuang, Shih-Hsiung Wu, Shyh-Horng Chiou, Gu-Gang Chang

Publication: Biophysical Journal

Publisher: Elsevier

Date: February 1999

Copyright © 1999 The Biophysical Society. Published by Elsevier Inc. All rights reserved.

Logged in as:
Saleha Al-atawi
Cardiff university

Account #:
3001365711

LOGOUT

Order Completed

Thank you for your order.


This Agreement between Cardiff university -- Saleha Al-atawi ("You") and Elsevier ("Elsevier") consists of your license details and the terms and conditions provided by Elsevier and Copyright Clearance Center.

Your confirmation email will contain your order number for future reference.


[printable details](#)


| | |
|--|--|
| License Number | 4536420741808 |
| License date | Feb 26, 2019 |
| Licensed Content Publisher | Elsevier |
| Licensed Content Publication | Biophysical Journal |
| Licensed Content Title | Homology Modeling of Cephalopod Lens S-Crystallin: A Natural Mutant of Sigma-Class Glutathione Transferase with Diminished Endogenous Activity |
| Licensed Content Author | Chyh-Chong Chuang, Shih-Hsiung Wu, Shyh-Horng Chiou, Gu-Gang Chang |
| Licensed Content Date | Feb 1, 1999 |
| Licensed Content Volume | 76 |
| Licensed Content Issue | 2 |
| Licensed Content Pages | 12 |
| Type of Use | reuse in a thesis/dissertation |
| Portion | figures/tables/illustrations |
| Number of figures/tables/illustrations | 1 |
| Format | both print and electronic |
| Are you the author of this Elsevier article? | No |
| Will you be translating? | No |
| Original figure numbers | Overall S-crystallin dimer model along the vertical Figure 3 |
| Title of your thesis/dissertation | Structural changes in the lens during accommodation |
| Publisher of new work | Cardiff University |
| Expected completion date | Mar 2019 |
| Estimated size (number of pages) | 1 |
| Requestor Location | Cardiff university cardiff |
| | cardiff, wales CF24 4HQ United Kingdom Attn: Cardiff university |
| Publisher Tax ID | GB 494 6272 12 |

Figure 1-9



RightsLink®

[Home](#)
[Account Info](#)
[Help](#)




Title: Changes in the internal structure of the human crystalline lens with age and accommodation

Author: M. Dubbelman, G.L. Van der Heijde, H.A. Weeber, G.F.J.M. Vrensen

Publication: Vision Research

Publisher: Elsevier

Date: October 2003

Copyright © 2002 Elsevier Ltd. All rights reserved.

Logged in as:
Saleha Al-atawi
Cardiff university

Account #:
2001365711

LOGOUT

Order Completed

Thank you for your order.

This Agreement between Cardiff university -- Saleha Al-atawi ("You") and Elsevier ("Elsevier") consists of your license details and the terms and conditions provided by Elsevier and Copyright Clearance Center.


Your confirmation email will contain your order number for future reference.

[printable details](#)

| | |
|--|--|
| License Number | 4536421358121 |
| License date | Feb 26, 2019 |
| Licensed Content Publisher | Elsevier |
| Licensed Content Publication | Vision Research |
| Licensed Content Title | Changes in the internal structure of the human crystalline lens with age and accommodation |
| Licensed Content Author | M. Dubbelman, G.L. Van der Heijde, H.A. Weeber, G.F.J.M. Vrensen |
| Licensed Content Date | Oct 1, 2003 |
| Licensed Content Volume | 43 |
| Licensed Content Issue | 22 |
| Licensed Content Pages | 13 |
| Type of Use | reuse in a thesis/dissertation |
| Portion | figures/tables/illustrations |
| Number of figures/tables/illustrations | 1 |
| Format | electronic |
| Are you the author of this Elsevier article? | No |
| Will you be translating? | No |
| Original figure numbers | Schematic drawing of the zones in the lens of a 20 year-old subject Figure 7 |
| Title of your thesis/dissertation | Structural changes in the lens during accommodation |
| Publisher of new work | Cardiff University |
| Expected completion date | Mar 2019 |
| Estimated size (number of pages) | 1 |
| Requestor Location | Cardiff university cardiff |
| | cardiff, wales CF24 4HQ United Kingdom Attn: Cardiff university |
| Publisher Tax ID | GB 494 6272 12 |
| Total | 0.00 USD |

ORDER MORE
CLOSE WINDOW

Figures 1-10, 1-11 and 1-12:



Attribution-NonCommercial-NoDerivs 3.0 Unported (CC BY-NC-ND 3.0)


This is a human-readable summary of (and not a substitute for) the [license](#). [Disclaimer](#).

You are free to:


Share — copy and redistribute the material in any medium or format

The licensor cannot revoke these freedoms as long as you follow the license terms.


Under the following terms:



Attribution — You must give [appropriate credit](#), provide a link to the license, and [indicate if changes were made](#). You may do so in any reasonable manner, but not in any way that suggests the licensor endorses you or your use.



NonCommercial — You may not use the material for [commercial purposes](#).



NoDerivatives — If you [remix](#), [transform](#), or [build upon](#) the material, you may not distribute the modified material.

No additional restrictions — You may not apply legal terms or [technological measures](#) that legally restrict others from doing anything the license permits.

Notices:

You do not have to comply with the license for elements of the material in the public domain or where your use is permitted by an applicable [exception or limitation](#).

